Modeling the response of climate and precipitation stable oxygen isotopes to the Cenozoic tectonic evolution of the Himalayas and the Tibetan Plateau

Svetlana Botsyun

NNT : 2017SACLV006

THÈSE DE DOCTORAT

de

L'UNIVERSITÉ PARIS-SACLEY

préparée à

L'Université de Versailles Saint-Quentin en Yvelines

École doctorale n° 129
Sciences de l'Environnement d'Île-de-France

Spécialité : météorologie, océanographie, physique de l'environnement

par

Svetlana Botsyun

Modélisation de l'impact de l'évolution tectonique himalayennes et tibétaines sur le climat et les isotopes stable de l'oxygène au Cénozoïque

Thèse présentée et soutenue au

Laboratoire des Sciences du Climat et de l'Environnement

Le 1 Mars 2017

Devant le Jury composé de :

Yannick Donnadieu,	Chargé de Recherche (CNRS/LSCE)	Directeur de thèse
Pierre Sepulchre,	Chargé de Recherche (CNRS/LSCE)	Co-directeur de thèse
Guillaume Dupont-Nivet,	Assistant Professor (CNRS/Rennes Univ.)	Rapporteur
Christian France-Lanord,	Directeur de Recherche (CNRS/CRPG)	Rapporteur
Andreas Mulch,	Professor (BIK-F)	Examinateur
Frédéric Fluteau,	Professeur (IPGP)	Examinateur
Valerie Daux,	Professeur (UVSQ/LSCE)	Président du jury
Camille Risi,	Chargé de Recherche (CNRS/LMD)	Invitée

Ecole Doctorale Science de l'Environnement d'Île-de-France
Météorologie, océanography et physique de l'environnement

PhD

to receive the title of

DOCTEUR

de l'UNIVERSITÉ PARIS-SACLAY

prepared at

Laboratoire des Sciences du Climat et de l'Environnement

Presented for public

1 March 2017 by

Svetlana Botsyun

Modeling the response of climate and precipitation $\delta^{18}O$ to the Cenozoic tectonic evolution of the Himalayas and the Tibetan Plateau

Defends before the jury composed of:

Yannick Donnadieu,	Chargé de Recherche (CNRS/LSCE)	PhD director
Pierre Sepulchre,	Chargé de Recherche (CNRS/LSCE)	PhD co-director
Guillaume Dupont-Nivet,	Assistant Professor (CNRS/Rennes Univ.)	Reporter
Christian France-Lanord,	Directeur de Recherche (CNRS/CRPG)	Reporter
Andreas Mulch,	Professor (BIK-F)	Examiner
Frédéric Fluteau,	Professor (IPGP)	Examiner
Valerie Daux,	Professor (UVSQ/LSCE)	President of the jury
Camille Risi,	Chargé de Recherche (CNRS/LMD)	Invited

Acknowledgments

First of all I would like to express my special appreciation and thanks to my advisors Dr. Pierre Sepulchre and Dr. Yannick Donnadieu. They have been tremendous mentors for me! Firm prudence of Yannick helped me a lot to get out of the most complicated mental reasoning. The faith on Pierre in me, his scientific taste and perfectionism helped me a lot to improve my research even when have already gave up. Without grandiloquent words, I want simply to say thank you for their help and patient.

Besides my advisors, I would like to sincerely acknowledge Camille Risi for numerous discussions and kilometers of mail written. Without this collaboration my thesis would not be possible. Camille gave me an example of a scientist whom I would like to approach to become.

I would like to thank Dr. Guillaume Dupont-Nivet, Christian France-Lanord, prof. Andreas Mulch, prof. Frédéric Fluteau, prof. Valerie Daux for accepting participating my defense committee. I also thank Guillaume Dupont-Nivet, Christian France-Lanord and Frédéric Fluteau for interesting discussions at the early stage of this study.

I am grateful to Alexis Licht and Jeremy Caves for a fruitful collaboration, numerous discussions. Their valuable suggestions helped me a lot to improve the paper manuscript.

I want to thank the iTECC project for the possibility of working on a very interesting subject in a team of professionals. Multiple meetings and trainings, 29th HKT workshop, and Himalayas field-trip helped not only to develop professional skills, find new collaborations and have interesting scientific discussions, but also to learn more about people of different nationalities and find really good friends. I acknowledge PhD students and post-docs - Gwladys Govin, Natalie Vögeli, Lorenzo Gemignani, Jesse Davenport, Eric Deal, Iris van der Veen, Zakaria Ghazoui, Mohammad Sahragard Sohi, Ruben Rosenkranz, Madeleine Bohlin, Mike Kelly, Guangsheng Zhuang, Alessandro Santato and Pl's - Dr. Yani Najman, Prof. Manfred Strecker, Dr. Dirk Sachse, Dr. Christian France-Lanord, Prof. Peter van der Beek, Prof. Jan Wijbrans, Prof. Mike Bickle, Dr. Jean Braun. It was really honor for me to work in a group of such professionals.

I thank all my colleges at LSCE who helped me in my work and adaptations in a new country. I thank permanents of Clim research group - Gilles Ramstein, Christophe Dumas, Jean-Yves Peterschmitt, Didier Roche, Didier Paillard, Masa Kageyama for their support. I want particularly thank all PhD students, post-docs and trainees who was together with me at LSCE: Alexandre Pohl, Jean-Baptist Ladant, Ning Tang, Sébastien Le Clec'h, Annemiek Stegehuis, Tristan Vadsaria and others. I also thank technichiens and administrative staff of LSCE.

I want to thank my friends and family. My mother, aunt, grandmother and grandfather

for their permanent support. My granny passed away before the date of the defense, but without her support this work was impossible. I thank my husband Alexander for his support whatever I am doing.

I want to thank all teachers of French language courses, that help me to integrate into the French culture and helped a lot scientific and personal communication. Finally I want to thank France for welcoming me and just all good people that I met here.

Svetlana Botsyun,
Laboratoire des Sciences du Climat et de l'Environnement,
Gif-sur-Yvette, January 2017

Contents

Summary

Tectonics-climate interactions as well as the impact of greenhouse forcing on climate have become a major focus of paleoclimate studies. The Himalayas and Tibetan Plateau owe their current latitudinal position and height due to the Cenozoic collision between Indian and Asian plates, since ~55 Ma. However, the timing and rate of surface elevations remain controversial and their impact on Asian climate and the onset of monsoon systems in this area is highly debated.

Stable oxygen paleoaltimetry is considered to be a very efficient and widely applied technique, but has limitations from two sides: 1) the link between stable oxygen composition of precipitation and climate is not well established, 2) Cenozoic climate over Asia is poorly reconstructed. With a purpose of filling the gap in our knowledge of climate variability over Asia during the Cenozoic we use the isotope-enabled atmospheric general circulation model LMDZ-iso. Various scenarios of mountains growth have been applied together with Early Eocene, Middle Eocene, Oligocene and Miocene boundary conditions. Our results show a significant influence of paleogeography on the Asian climate. Specifically, the surface elevation of the Himalayas and Tibetan Plateau directly impact local temperatures, but also the atmosphere circulation that results in increased precipitation rates over the southern Tibet and wide-spread aridity over the northern Tibet and in central Asia.

For the purpose of understanding where and how these climatic changes linked with the growth of mountains affect $\delta^{18}O$ in precipitation we develop a theoretical expression for the precipitation composition based on the Rayleigh distillation and show that only 40 % of sampled sites for paleoaltimetry depict signal attributed to topography changes. We conclude that the Himalayas may have attained their current elevation later than expected. In contrast, we suspect that isotope-based palaeoaltimetry could underestimate surface elevation over the northern Tibet. In addition, realistic Cenozoic boundary conditions together LMDZ-iso allow reconstructing $\delta^{18}O$ in paleoprecipitation for several periods during the Cenozoic.

The focus has been put on the Eocene, since paleoelevation reconstructions are particularly controversial for this period. Wind trajectories back tracking applied to the model outputs allows to compare the moisture feeding of the Himalayas and the Tibetan Plateau regions for the present-day and the Eocene cases and shows that the Rayleigh distillation processes are not applicable for the Eocene Himalayas due to mixing of air from multiple moisture sources over this area. We show that Eocene precipitation $\delta^{18}O$ is rather insensitive to topographic height in Asia. However, carbonate $\delta^{18}O$ still records paleoelevation because the fractionation between calcite and water is sensitive to temperature,

which depends on altitude. Comparison of simulated Eocene $\delta^{18}O$ patterns with data from the carbonate archives suggest that the Himalayas and the Tibetan Plateau did not reach present-day (3000+ m) elevations during the Eocene.

Résumé étendu

Les interactions entre la tectonique et le climat ainsi que l'étude du forçage radiatif associé aux gaz à effet de serre sont devenus des axes de recherche prioritaires des sciences de la terre pour les décennies à venir. Les déplacements horizontaux et verticaux des plaques lithosphériques jouent le rôle principal dans les changements climatiques à long-terme à travers plusieurs processus. Le relief à la surface du globe terrestre a un impact direct sur le climat en modifiant le bilan radiatif mais aussi la circulation atmosphérique, les courants océaniques et le potentiel d'entrée en glaciation. De plus, la tectonique impacte indirectement le climat en affectant la dynamique du cycle du carbone et donc les compositions chimique de l'atmosphère et de l'océan. D'ailleurs, alors que l'évaluation des changements climatiques liés à l'altitude est nécessaire pour comprendre l'histoire du soulèvement d'une chaîne de montagnes, les données précises de paléo-élévation sont essentielles pour les reconstructions paléoclimatiques.

Le massif formé par l'Himalaya et le plateau tibétain (HPT) constitue la plus haute chaîne de montagnes du monde, et la barrière orographique formée par celle-ci contrôle la circulation atmosphérique en Asie. Cette région est considérée comme un véritable « laboratoire naturel » pour l'étude des interactions entre tectonique et climat, car les observations de terrain ainsi que les simulations numériques suggèrent un impact important de la formation de ces montagnes sur les changements climatiques à différentes échelles de temps. On sait que le soulèvement orographique dans cette région résulte de la collision de la plaque indienne avec la plaque eurasiatique, initiée il y a ~55 Ma, et du poinçonnement de l'Inde vers le nord-nord-est dans le continent eurasiatique. En revanche, la vitesse de surrection du HPT tout au long du Cénozoïque reste encore aujourd'hui largement débattue.

La paléo-altimétrie est une estimation quantitative de la paléo-élévation au-dessus du niveau moyen de la mer. Parmi les nombreuses techniques aujourd'hui disponibles pour reconstruire la paléo-altitude, celle reposant sur l'analyse des isotopes stables de l'oxygène (i.e., la composition isotopique d'un échantillon définie par rapport à un étalon et indiquée par la notation δ: $\delta^{18}O$) est la plus largement répandue. Cette approche se fonde sur la sensibilité du $\delta^{18}O$ des précipitations ($\delta^{18}O_p$) à la température (qui, à son tour, est contrôlée par l'altitude), selon le modèle de la distillation de Rayleigh. Les études utilisant les isotopes de l'oxygène exploitent la forte sensibilité du $\delta^{18}O_p$ aux changements d'élévation (via un lapse rate isotopique moyen global de 2,8 ‰ km^{-1}) pour reconstruire l'altitude des reliefs dans le passé lointain. Généralement, plusieurs étapes sont nécessaires pour ces paléo-reconstructions: (1) le rapport isotopique de l'oxygène $\delta^{18}O_c$ doit être mesuré dans des archives naturelles (les carbonates des sols, les carbonates la-

custres, etc.) ; (2) le rapport est ensuite calculé dans les paléo-précipitations ($\delta^{18}O_{pp}$) en tenant compte de l'équilibre entre l'eau et la calcite à une température donnée; et (3) les valeurs du $\delta^{18}O_{pp}$ sont converties en valeurs de paléo-altitude en utilisant des relations théorétiques entre $\delta^{18}O_p$ et topographie (i.e., un lapse rate isotopique).

Les reconstructions paléo-altimétrique fondées sur l'analyse des isotopes stables de l'oxygène ont été appliquées à la chaîne de l'Himalaya et du plateau tibétain pour les périodes de temps allant du Paléocène au Pléistocène (60-2 Ma). Néanmoins, cette méthode a deux limites principales: 1) les relations entre $\delta^{18}O$ et climat ne sont pas bien établies; et 2) le climat Cénozoïque en Asie est mal contraint. Dans le cadre de cette thèse, nous avons étudié le rôle de la surrection du HPT, l'influence du changement de la concentration atmosphérique en CO_2, ainsi que l'impact des modifications de la paléogéographie au cours du Cénozoïque, sur le cycle de l'eau et sur la composition isotopique des précipitations. Nous avons pour cela souhaité répondre aux questions suivantes :

1. Quels sont les processus contrôlant aujourd'hui la distribution spatiale des isotopes stables de l'oxygène ?
2. Comment a évolué le climat asiatique au cours du Cénozoïque ?
3. Est-ce que les processus qui contrôlent la distribution spatiale des isotopes stables d'oxygène étaient constants pour toutes les périodes de temps, en particulier, quand les montagnes étaient plus petites, la région de HPT était située près de l'équateur et la concentration du CO_2 dans l'atmosphère était considérablement plus élevée ?
4. La méthode classique de paléo-altimétrie du HPT, fondée sur les isotopes stables de l'oxygène, peut-elle être appliquée tout au long de l'ère Cénozoïque ?

Pour répondre à ces questions, nous avons utilisé le modèle de circulation générale atmosphérique LMDZ et sa version isotopique LMDZ-iso. Avec cet outil, nous avons évalué les changements spatiales et temporelles des variables climatiques et la composition isotopique de la vapeur et des précipitations. Pour les simulations plus « réalistes », nous avons également utilisé les températures océaniques de surface dérivées d'un modèle couplé océan-atmosphère (FOAM), ainsi que la distribution de la végétation simulée avec un modèle dédié (LPJ). L'utilisation d'une grille conçue spécifiquement pour cette étude, bénéficiant d'un zoom sur l'Asie du Sud-Est, a permis d'atteindre une résolution spatiale moyenne de l'ordre de 50 km sur l'Asie centrale, tout en conservant une taille des cellules beaucoup plus grande sur le reste du globe, ce qui fournit un bon compromis entre un temps de calcul raisonnable et une résolution spatiale permettant de représenter adéquatement toutes les caractéristiques principales de la topographie du HPT. En outre, la comparaison des résultats de nos modèles avec les données publiées de $\delta^{18}O$ mesuré dans les archives naturelles, a fourni une occasion unique de réviser l'histoire de la surrection du HPT.

Nous avons tout d'abord étudié les variations isotopiques dans la région du HPT à l'époque actuelle. D'après les mesures de $\delta^{18}O$ dans les eaux de pluie, le taux de variation du $\delta^{18}O$ en fonction de l'altitude moyenne est de 2.8 ‰ km^{-1} (Poage and Chamberlain, 2001). Cette relation a été établie empiriquement, sur la base d'échantillonnages des

eaux de surface sur le front sud de l'Himalaya (e.g Garzione et al., 2000a), et confirmée théoriquement selon l'équation de la distillation de Rayleigh (Rowley and Garzione, 2007; Rowley et al., 2001). Cependant, la composition isotopique des précipitations est également influencée par la température, l'humidité, les processus de post-condensation, la quantité de précipitations et la composition isotopique initiale des sources d'humidité. Les résultats de simulations conduites avec LMDZ-iso suggèrent que le lapse rate isotopique n'est pas constant spatialement à travers la région étudiée. Nous montrons que le modèle de la distillation de Rayleigh calibré pour l'Himalaya (Rowley and Garzione, 2007; Rowley et al., 2001) reproduit bien les données des échantillons actuels des eaux de rivières dans certains secteurs donnés de la région asiatique, mais qu'ailleurs la conformité est beaucoup plus faible. L'utilisation d'une valeur unique de lapse rate isotopique pour l'ensemble de l'Himalaya pourrait dès lors causer une sous-estimation considérable des paléo-altitudes dans les segments centraux et septentrionaux du plateau tibétain.

Dans une deuxième étape, afin de tester la validité du lapse rate pour les temps géologiques plus anciens, nous avons effectué des tests de sensibilité du climat et du $\delta^{18}O_p$ aux changements de la topographie du plateau tibétain. Nous avons réalisé des simulations dans lesquelles la topographie de l'Himalaya est réduite partiellement (i.e., de moitié), ou totalement, tout en gardant le reste des conditions aux limites identiques à celles de l'époque actuelle (i.e. la position des continents reste constante). Ces simulations révèlent que la composition isotopique des précipitations est très sensible aux changements climatiques associés à la surrection du HPT. Afin de comprendre où et comment ces changements climatiques liés à la surrection des montagnes affectent le $\delta^{18}O_p$, nous avons proposé une expression théorique de la composition isotopique des précipitations fondée sur la distillation de Rayleigh. Nous avons montré que seulement 40 % des sites échantillonnés du HPT contiennent la signature isotopique représentant la topographie. Il apparaît donc que la topographie n'est pas l'unique facteur contrôlant les valeurs du $\delta^{18}O_p$. La contribution relative des autres facteurs peut varier en fonction de l'étape de la surrection et de la région considérées. Notamment, les changements d'humidité relative, la quantité de précipitations et les processus de post-condensation en Asie ont un impact majeur sur le $\delta^{18}O_p$. Nous soulignons que les futures études portant sur les reconstructions de paléo-altitude devraient prendre en compte ces facteurs climatiques pour éviter une mauvaise estimation des altitudes d'époques anciennes. Les résultats obtenus dans cette étude montrent que l'Himalaya pourrait avoir atteint son élévation actuelle plus tardivement que précédemment proposé. En revanche, dans le nord du Tibet, la paléo-élévation pourrait avoir été sous-estimée.

Dans l'étape suivante, des simulations ont été réalisées avec le modèle LMDZ-iso en utilisant les reconstructions paléogéographiques représentatives de quatre époques du Cénozoïque (55, 42, 30, 15 Ma). Ces paléogéographies reflètent le déplacement progressif du sous-continent indien vers le nord et le retrait de la Paratéthys, ancêtre élargi de la Mer Méditerranée dont la présence pourrait avoir largement influencé les régimes de pluie sur le plateau tibétain. En général, pour toutes ces expériences, les valeurs du $\delta^{18}O_p$ dans la région himalayenne augmentent de 9 ‰ par rapport aux valeurs actuelles. Pour l'expérience avec les conditions aux limites Miocène (15 Ma), une évolution vers des valeurs de $\delta^{18}O$ moins appauvries sur la topographie élevée est compatible avec le mé-

canisme proposé par Poulsen and Jeffery (2011). Ces derniers ont montré que lors d'une augmentation des teneurs en CO_2 atmosphérique, la haute troposphère se réchauffe plus que les basses couches. Ce différentiel induit un gradient vertical de température dans la troposphère plus faible qui se traduit lui même par des valeurs de $\delta^{18}O_v$ relativement enrichies, qui sont ensuite transportées vers le surface terrestre dans les zones de subsidence. Pour les périodes plus anciennes, telles que l'Eocène et l'Oligocène, le plateau tibétain est situé à 10° de latitude plus au Sud qu'aujourd'hui. Ce déplacement de la région dans la zone de convection où de l'air enrichi de la surface est transporté jusqu'au niveau de condensation par ascendance va induire la présence de valeurs de $\delta^{18}O_v$ sur le plateau tibétain largement plus positive que de nos jours.

Dans la mesure où les reconstructions des paléo-élévations sont particulièrement controversées pour les premières étapes de l'évolution du plateau tibétain, nous avons ensuite souhaité approfondir notre étude de l'Eocène (en utilisant une paléogéographie qui correspond au 42 Ma). L'analyse des différences climatiques entre l'Eocène et l'époque actuelle a été réalisée afin de comprendre les mécanismes climatiques qui font varier le $\delta^{18}O_v$ dans la région asiatique. Dans le cadre du contexte de l'Eocène, nous avons testé la sensibilité du climat au retrait de la Paratethys, aux changements de la température de surface de l'océan (SST), à la concentration atmosphérique en CO_2, à l'albédo du surface, aux paramètres orbitaux ainsi qu'aux changements de topographie. Ces tests de sensibilité montrent que la paléogéographie joue le rôle le plus important dans les motifs spatiaux du $\delta^{18}O$. Le traçage des trajectoires du vent appliqué aux résultats des modèles a permis de comparer l'alimentation en humidité dans les régions de l'Himalaya et du plateau tibétain pour l'époque actuelle et pour l'Eocène. Cette analyse révèle que les procédés de distillation de Rayleigh ne sont pas applicables pour l'Himalaya de l'Eocène à cause du mélange d'air provenant de sources d'humidité multiples dans cette zone. Cela suggère donc que l'hypothèse de stationnarité de la relation $\delta^{18}O$-altitude à travers les temps géologiques est inexacte, et qu'elle peut conduire à des estimations trompeuses de paléo-altitude. En plus, pour le cas Eocène, nous montrons que le $\delta^{18}O_p$ lui-même est insensible à la hauteur topographique en Asie, tandis que le $\delta^{18}O_c$ enregistre le signal de la paléo-élévation puisque le fractionnement entre la calcite et l'eau est sensible à la température, qui, à son tour, dépend de l'altitude. La comparaison du $\delta^{18}O$ simulé pour l'Eocène avec les données du $\delta^{18}O$ mesuré dans les carbonates suggère que, pendant l'Eocène, l'Himalaya et le plateau tibétain n'avaient encore pas atteint leur élévation actuelle (> 3000 m).

De nombreux travaux récents de modélisation se sont intéressés à l'impact du soulèvement de l'Himalaya et du plateau tibétain sur la circulation atmosphérique, l'aridification et la mousson dans la région asiatique. Cependant, la plupart des études ont utilisé des conditions aux limites proches de celles de l'époque actuelle (y compris la configuration des continents et la concentration atmosphérique en CO_2) pour tester le rôle de la tectonique dans les caractéristiques de la mousson asiatique. Ainsi, les apports relatifs du forçage de la tectonique et des gaz à effet de serre à l'intensification de la mousson Cénozoïque et à la désertification en Asie n'étaient pas connus avec précision. D'autre part, l'acquisition de nouvelles données géologiques nécessite les bases physiques pour les exploiter et les interpréter correctement. Nous avons ici utilisé un modèle de circulation

générale (LMDZ) pour estimer la sensibilité du climat cénozoïque en Asie à la topographie et à la concentration atmosphérique en CO_2, qui changent conjointement avec la configuration des continents au cours du Paléocène, de l'Eocène, de l'Oligocène et du Miocène. Cette méthode nous a permis d'évaluer l'importance relative de chacun de ces facteurs pour les modèles climatiques. Pour les expériences plus réalistes, LMDZ a été forcé avec les SST calculées en utilisant le modèle FOAM et avec l'albédo provenant des résultats du modèle de végétation LPJ. Les résultats préliminaires illustrent parfaitement une influence significative des changements topographiques sur le climat asiatique pour toutes les périodes cénozoïques, à l'exception de l'Eocène inférieur. Nos simulations climatiques montrent que le retrait de la Paratéthys, le déplacement latitudinal de l'Inde et la hauteur du plateau tibétain contrôlent les précipitations et provoquent la variabilité de la mousson en Asie. Selon ces modèles, l'aridité à l'Asie central a persisté pendant tout le Cénozoïque, alors que l'étendue latérale des déserts était contrôlée par la topographie, la paléogéographie et la concentration atmosphérique en CO_2.

Notre recherche s'adresse non seulement à une vaste communauté de géochimistes, de climatologues, mais aussi aux géologues et aux géophysiciens qui se sont intéressés à l'histoire de la surrection des chaînes de montagnes ainsi qu'à l'évolution géodynamique de la collision entre l'Inde et l'Eurasie. Les résultats de ce travail pourraient être appliqués non seulement pour améliorer notre connaissance de l'évolution du climat pendant le Cénozoïque mais aussi pour réinterpréter l'évolution du soulèvement du plateau tibétain et de l'Himalaya, avec une application pratique possible à la géodynamique de la région.

Introduction

General context and scientific questions

Tectonics-climate interactions have been inspiring much inter-disciplinary discussion since a quarter of a century. The Himalayas and Tibetan Plateau (HTP), as the major mountain building on the Earth, serves as an important natural laboratory for investigating the coupling between topographic evolution and climate forcing. In pioneer works on this subject, Kutzbach et al. (1989); Raymo and Ruddiman (1992); Ruddiman and Kutzbach (1989) suggested that the uplift of the HTP has a profound effect on atmospheric circulation. In these works it has been also proposed that Cenozoic tectonic uplift of the HTP drives the increase in atmospheric CO_2 concentrations through the increase in the chemical weathering. Since these early studies substantial progress has been made, including studies that use modeling tools to investigate the impact of Asian topography on climate and the carbon cycle. However, a major limit in such kind of modeling is linked to the paleogeography reconstruction uncertainty, and to our limited knowledge of the scale and rate of the HTP surface uplift. In addition, the surface elevation provides important information on the geodynamic mechanisms shaping the Earth surface.

For paleoelevation reconstructions, a lot of modern techniques are available. Among them, stable oxygen paleoaltimetry is considered to be one of the most efficient and has been widely applied for reconstruction of the elevation history of the HTP. However, stable isotope paleoaltimetry has several limitation, because: 1) the link between stable oxygen composition of precipitation and climate is not established, 2) the main atmospheric factors that control atmospheric distillation and air mass $\delta^{18}O$ values may vary through time, and 3) Cenozoic climate over Asia, including the monsoon onset is poorly reconstructed.

In this thesis we aim to address the following scientific questions:

1. What processes control present-day distribution of stable water isotopes in precipitation?

2. How climate was changing under the influence of the Asian topography uplift, change of the paleogeography during the Indo-Asian collision and the drop of atmosphere pCO_2 through the Cenozoic?

3. Were the processes controlling the spatial distribution of stable oxygen isotopes in precipitation constant through the Cenozoic, especially in a case of lower elevation of Himalayas and Tibetan Plateau, their southward shift, and high atmosphere

pCO_2 concentration?

4. Could the classic stable oxygen isotopes-based paleoaltimetry technique be applied for the Cenozoic?

Dissertation format

The following work consists of 7 Chapters, connected in between and which, all together are aiming to answer the scientific questions asked.

Chapter 1 reviews the scientific background of this thesis, discussing the main forms of tectonics-climate interaction (focusing on the impact of the tectonics on climate), the geological structure and geodynamical history of the Himalayas and Tibetan Plateau as well as the main techniques of paleoelevations reconstructions (with a focus on stable oxygen isotopes paleoaltimetry). This introductory chapter is pivotal to set up for comprehension of the multidisciplinary topic of this thesis.

Climate modeling is the main tool of this work. Thus, in **Chapter 2** we provide fundamentals of climate and stable oxygen isotopes modeling and review the models and boundary conditions used in this study.

In **Chapter 3** we discuss the main factors that control of $\delta^{18}O_p$ over Asia nowadays and their variations with the HTP uplift. We suggest the possible impacts of this variations on the paleoelevations estimates accuracy. In this chapter we present our article entitled "Impacts of Tibetan Plateau uplift on atmospheric dynamics and associated precipitation $\delta^{18}O$" published in *Climate of the Past*.

Further, in **Chapter 4** we discuss the results of our experiments with realistic Cenozoic boundary conditions and exploring the isotopic processes for paleo periods. In this chapter the focus is made on the Eocene period and we present the article in preparation for *EPSL*, entitled "Controls of the Eocene stable oxygen isotopes over Himalayas and Tibetan Plateau".

In **Chapter 5** we provide a comparison of measured carbonate $\delta^{18}O$ with model simulated $\delta^{18}O$ (so-called "forward proxy modeling") in order to test the validity of existing $\delta^{18}O$-based Eocene paleoelevations reconstructions for the HTP. In this chapter we present a draft paper "Eocene stable oxygen isotopes in the Himalayas and Tibetan Plateau: A record of elevation or of climate change?", ready for submission to *Nature Communications*.

In **Chapter 6** we discuss the impact of the tectonic evolution of the Indo-Asia collision zone on the Asian monsoon circulation and test the sensitivity of Asian climate through the Cenozoic to the change of paleogeography, topography and CO_2 concentration with the numerical experiments

Finally, in **Chapter 7** we summaries our investigation, discuss possible uncertainties associated, give an idea on the work in progress and highlight the perspectives and possible applications of this study.

Chapter 1

General introduction

In this introductory chapter we define the main possible impacts of tectonics-induced horizontal displacements and vertical motions of the Earth crust on climate change, focusing on the Himalayas and Tibetan Plateau region (Section 1.1). Further, with a purpose of understanding the timing and scale of the Earth surface uplift and latitudinal displacement of land masses over this region during the Cenozoic, we provide a quick overview of tectonic evolution of Indo-Asia collision zone (Section 1.2). As the surface elevation is suspected to be one of the most crucial factor impacting regional and global climates, we provide an overview of geological, paleontological and geochemical methods typically used for paleoelevation reconstruction of mountain belts in general and the Himalayas and Tibetan Plateau in particular (Section 1.3). In the Section 1.3 we discuss the principles of the stable water isotopes-based paleoaltimetry: we give the definition of the isotopic composition of water, main properties of stable oxygen isotopes, present-day spatial distribution and application for measurements of paleoelevations. We also suggest a complete elevation history of the HTP during the Cenozoic based on published data. Finally, based on the problematic discussed in this chapter, we specify the main objectives of our work (Section 1.4).

Contents

1.1 Tectonics-climate interactions

Nowadays it becomes evident that horizontal and vertical displacements of terrains associated with plate tectonics play a fundamental role on climate (DeConto, 2009; Kutzbach et al., 1989; Raymo and Ruddiman, 1992; Ruddiman and Kutzbach, 1989). The form of the earth surface has an impact on climate through *direct effects*, modifying the surface energy balance, atmospheric circulation, oceanic currents and glaciation. Tectonics also has important *indirect effects* on climate through control of the geochemical cycles and the composition of the atmosphere and the ocean. Consequences of tectonics activity on the shape and composition of the Earth layers (lithosphere, hydrosphere, atmosphere, etc.) are complex and include a lot of interacting elements (e.g. surface elevations, form of orogens and its spatial position, land-sea distribution, sea-level, carbon dioxide emissions into the atmosphere by volcanoes, etc.). Several early reviews have treated different aspects of tectonics-climate interactions (DeConto, 2009; Hay, 1996). In the following sections we do not aim to specify the full variety of interactions between tectonics and climate, but to provide the basics for the major ones. In this quick overview we summarize the recent achievements made by climate modeling studies on tectonics-climate interactions. A particular focus is put on the HTP region.

1.1.1 Impact of orography on climate

Tectonic uplift of major mountain belts is often cited as an important factor to modify climate (Raymo and Ruddiman, 1992; Ruddiman and Kutzbach, 1989). The potential impact of mountains on climate was first inferred based on the interpretation of the geological record and then, with the development of computers, using numerical models and general circulation models in particular (see more on climate modeling methods in Chapter 2). However, it is necessary to keep in mind that the impact of an orogen on climate depends on its latitudinal position, size and elevation, thus, although general impacts are known, each particular region should be studied individually.

Orographic precipitation, barrier effect and rain shadows

Orographic precipitation occurs when moist air is forced upwards over rising terrain, such as a mountain. A rain shadow is an area on the leeward side of an orographic barrier with relatively small precipitations amount compared to adjacent regions. During an orographic ascent to the mountain tops, humid air masses cool down and reach the dew point (the point where the water vapor condenses into rain), thus most of precipitation falls on the windward side or on top of the mountain. On a leeward side, only moisture-depleted air is advected and a dry region forms, that is called "a rain shadow" (Figure 1.1).

Rain shadow effect area can extend hundreds of kilometers and is pronounced in vegetation types and sediments characteristic for dry zones (evaporates). Vegetation is of particular importance because it affects land surface roughness, atmospheric moisture, and the partitioning of sensible and latent heat fluxes between the surface and atmosphere (Dickenson and Henderson-Sellers, 1988).

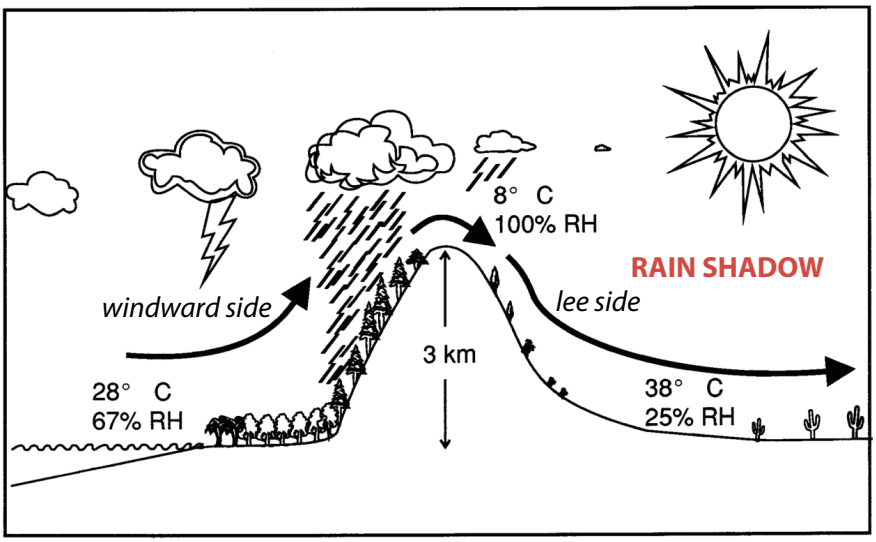

Figure 1.1 – Schematic diagram showing the orographic precipitation and formation of a rain shadow of a mountain range. Figure after from (Hay, 1996). Precipitation occurs on the windward side of the range, and a rain shadow develops on its lee. *RH* relative humidity.

Rain shadow effect is very typical for modern climates and is observed over a lot of places in the word. The most pronounced examples are: the Death Valley, a desert in North America, that is in the rain shadow of the Sierra Nevada mountain range; the South Island New Zealand, which is a rain shadow of the Southern Alps; the Atacama Desert in Chile as a rain shadow of the Andes together with moisture-blocking action of high pressure over the Pacific; the eastern part of the Pyrenean mountains in the south of France. Similarly, Karakum Desert and Kyzylkum Desert, are protected from the penetration of moist air by Caucasus in the west, Mount Elbrus in the south and the Himalayas to the east. The Tibet is one of the most remarkable rain shadows anywhere on Earth, where the Himalayas snap up moisture coming form the Bay of Bengal and the Pacific Ocean and the Tian-Shan and the Pamir have a blocking effect on the westerly moisture.

Similar to rain shadow effects may have been characteristic for ancient climates. For example, in a simulation with idealized "supercontinent" (pole-to-pole continents) more arid condition that exists today have been produced by Hay (1996). Numerous modeling efforts have been made for reproducing and explaining rain shadow effect in various domains all over the world. For example, Sepulchre et al. (2006) showed that the topographic uplift of eastern African topography impact has complex effect on regional climate, including the rain shadow effects. The orographic barrier and rainshadow effect of Tian-Shan mountains is also well known. It acts as a "trap" for the moisture coming with the westerlies thus contributing to the hyper aridity of the Taklimakan desert (Baldwin and Vecchi, 2016; Sato, 2005). Liu et al. (2015) based on numerical experiments indicates

the rain shadow effect of Tibetan Plateau as the main reason of formation of inland Asian deserts.

However, recent study of development of orographic rain shadows during orogenesis (Galewsky, 2009) have shown that rain shadow formation is nonlinear and nonunique function of both topography and atmospheric state. These conclusions indicate that geological records of orographic aridity cannot be interpreted in terms of topography elevation alone.

Mountain uplift and atmospheric planetary waves

An atmospheric wave is a periodic disturbance in the fields of surface pressure, geopotential height, temperature, or wind velocity which may either propagate (traveling wave) or not (standing or stationary wave). Large-scale planetary waves are called Rossby waves. Rossby waves form as a consequence of the conservation of absolute vorticity. When a parcel of air (or water) is displaced from its original latitude or changes its thickness as it passes over a mountain range, it responds by changing its latitude (planetary vorticity) and/or its relative vorticity (tendency to rotate). The resulting oscillations in the mean flow about a given latitude produce long planetary waves which move westward relative to the flow. In the fast flow of the upper troposphere, the waves appear to move slowly eastward relative to the Earth's surface.

Large mountain belts provide direct physical barriers to atmospheric flow, which induce these long planetary Rossby waves in the upper-level westerlies. In the Northern Hemisphere, the longest of these waves tend to become stationary or locked relative to major orographic features. Uplift of mountain chains can disrupt atmospheric circulation by deflecting the atmosphere jet stream and planetary waves (Hay, 1996).

Pioneer works on the importance of the orography of the Earth for the general character of westerlies were held by Charney and Eliassen (1949), Dorodnitsyn (1950) and Bolin (1950). In these works the atmospheric behavior in presence of an obstacle (mountain) was described with the equations of geophysical hydrodynamics.

Manabe and Broccoli (1990) provided numerical experiments with and without mountains in the northern hemisphere and showed the role of high topography on the position of the jet stream (Figure 1.2). In addition, these authors attributed the general aridity of the American interior and the Central Asia to the effect of the Rocky Mountains and the Tibetan Plateau on the planetary wave pattern. One of the main conclusions of this paper is that without mountains in the northern hemisphere, large-scale circulation is much more zonal.

Recent works investigated the relative contribution of the TP and Mongolian mountains on the westerly jet over North Pacific (Shi et al., 2014). Based on numerical experiments, these authors speculate that the Mongolian topography has a greater impact on westerlies that the TP despite its smaller size. Based on coupled atmosphere-ocean GCM experiments, Yun et al. (2016) studied the impact of the TP uplift (with experiments from 0 to 100 % of the current height) on the seasonal characteristics of the westerlies flow, the jet displacement and strength in the northern hemisphere. Authors assess the effects of the progressive uplift of the Tibetan Plateau on the atmospheric blocking (quasi-stationary

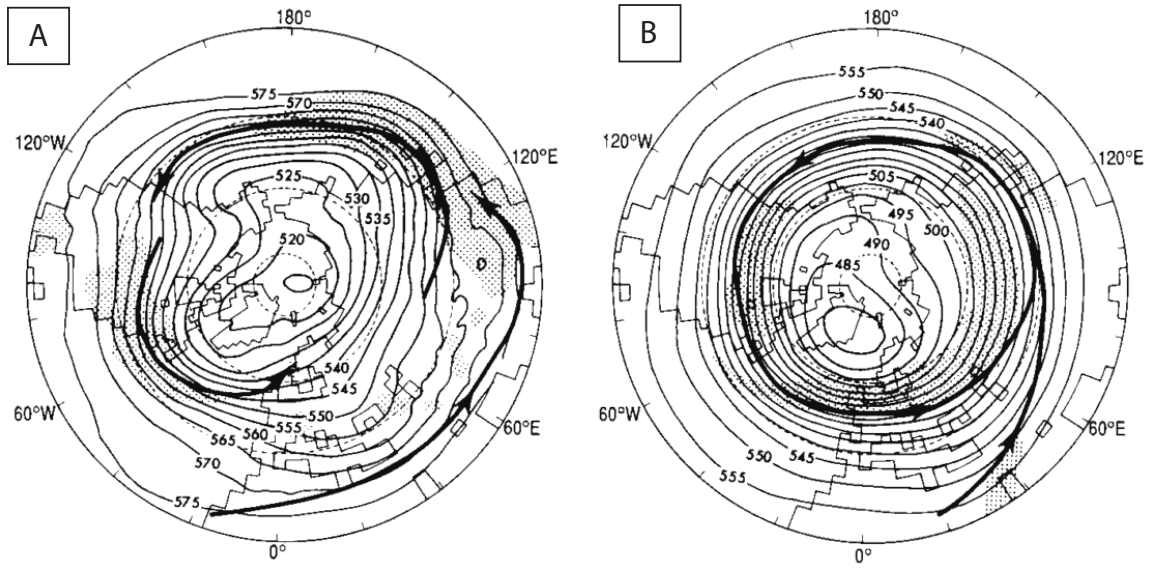

Figure 1.2 – The effect of mountains uplift on westerly wind in the northern hemisphere based on numerical experiments done by Manabe and Broccoli (1990). A) experiments with present-day topography, B) experiment with neglected topography all over the world. The 500-mb geostrophic wind speed is inversely proportional to the spacing of the height contours for March-Avril-May, and the thick arrows indicates the position of the jet-stream axis at 500 mb. Stippling indicates precipitation rate > 3 mm per day. This figure greatly illustrates that without mountains global-scale atmospheric circulation is much more zonal.

mid-latitude high pressure system blocking the westerly background flow) and show that during winter, the Tibetan Plateau uplift increases the blocking frequency over both Atlantic and Pacific oceans *via* amplifying the eddy kinetic energy of stationary waves, while during the summer this effect is larger over the Atlantic.

Mountain uplift and global monsoons

The term *monsoon* is generally defined from the seasonal reversal in both precipitation and wind fields. The monsoon circulation is characterized as a climate system with seasonal reversal in surface winds over and around the continents accompanied by highly seasonal, intense precipitation (Wang and Ding, 2006). A network of seasonally varying precipitating systems and winds reversal is called *the global monsoon* (Fasullo and Webster, 2003). The global monsoon includes all major monsoon regions: Australia, northern Africa, southern Africa, North America, South America, and Asia (Wang et al., 2014b).

Mountain uplift is known to effect the onset and intensification of the monsoonal circulations, thus it become one of the most important manifestations of tectonic-climate interactions (Huber and Goldner, 2012; Molnar et al., 1993; Roe et al., 2016). Relationship between the presence of topography and monsoon circulation has been examined in numerous studies; it has been shown that mountain ranges have significant impact on atmospheric circulation through mechanical and dynamical effects (Wu et al., 2015) (see more on the discussion about mechanical and dynamical effects of the Himalayas and Tibetan Plateau in Section 1.1.4).

Paleo-monsoon variability is commonly linked with tectonic forcing. Paleo-monsoon

variability have been studied using sedimentogical and paleontological proxies. For example, quantitative studies of the variability in the African monsoon have been based on terrestrial records of lake level changes in northern Africa (Kutzbach, 1980), marine records of eolian dust from the Atlantic (Sarnthein et al., 1981), and sapropels in the Mediterranean (Rossignol-Strick, 1983). The Indian monsoon was studied using upwelling records from the Arabian Sea (Gupta et al., 2015), cyclicity in eolian deposits (e.g. Loess Plateau of China) (An et al., 2001), analysis of Siwalik Group sediments (Sanyal et al., 2004b) and many others proxies.

Nowadays, besides sedimentological and palentological proxies, general circulation models (GCMs) are frequently used to investigate the impact of topography uplift on paleo-monsoon onset and variability (An et al., 2001; Broccoli and Manabe, 1992; Lunt et al., 2010).

Huber and Goldner (2012) using Eocene boundary conditions showed that a global monsoon distribution of precipitation exists in the Eocene regardless of Tibetan Plateau height. However, most of paleoclimate modeling studies use near-present day boundary conditions (e.g land-sea mask, atmospheric CO_2) for reconstructing paleo-monsoons.

We discuss the impact of the HTP on Asian climate based on published data in Section 1.1.4 and we bring our contribution to this subject in Chapter 6.

Mountains uplift and oceanic circulation

The effect of mountains uplift on in the context of coupled atmosphere-ocean system has been investigated since only last decade. Studies of Abe et al. (2003) and Kitoh (2004) showed that the uplift of the HTP has influence on sea surface temperatures and sea surface salinity of Pacific and Indian Oceans both, as well as on precipitation through changes in the intensity of the subtropical anticyclone and trade winds. Importantly, numerical studies have also suggested that global mountains have important effect on global-scale meridional overturning circulation (MOC) (Rind et al., 1997; Schmittner et al., 2011). The authors show that higher mountains reduce water vapor transport from the Pacific and Indian Oceans into the Atlantic Ocean and contribute to increased salinities and enhanced deep-water formation and MOC in the Atlantic and simultaneous decrease of MOC in the Pacific Ocean.

The impact of the Andes uplift on oceanic currents have been studied by Sepulchre et al. (2009b). The author show that this uplift played a crucial role in shaping the lower troposphere dynamics over the Pacific Ocean and wind stress values that results in a marked southward shift of the Humbold Current System, changing the latitudinal position of coastal upwelling areas as well as the strength of the South Pacific gyre.

Mountains uplift and glaciation

Because tropospheric temperatures generally decrease with increasing altitude (the globally averaged tropospheric lapse rate is about $6.5\,^{\circ}\mathrm{C}\cdot\mathrm{km}^{-1}$), high terrain is more likely to maintain perennial snow and ice cover. James Dana in 1856 was one of the first scientists who noticed that continental glaciations could be linked with terrestrial movements

during the past time periods (Dana, 1856). In addition, he concluded that continental glaciations existed in the geological time because of higher topographical elevations.

Numerical modeling studies in the end of the XXth century have shown that tectonic uplift of widespread land areas above the equilibrium snowline can lead to the sudden, non-linear growth of glaciers and ice sheets, possibly leading to continental-scale glaciation. The rapid non-linear response is caused mainly by albedo feedbacks (North et al., 1983) associated with the high reflectivity of snow and ice and the geometrical effect of a growing ice cap and its rapidly expanding accumulation zone.

Further investigations revealed that the spatial scale of surface uplift is a key factor in the potential response of glaciations. For example, modern ice sheet modeling studies have shown that broad uplift of an initially ice-free Antarctic interior can trigger sudden glaciation, provided the continent is already near a glaciation threshold (DeConto and Pollard, 2003).

Besides the direct effect of mountains uplift on glaciation indirect effect through increase rate of silicate weathering and reduction of atmospheric CO_2 exists (see the following section). Thus, studying of the impact of the topography on glaciations is important because glaciation itself has important feedback on climate through the albedo change (snow has high albedo).

Mountain uplift and global CO_2 level

Based on terrestrial and marine proxies (e.g. stromatal density, fossil soils, B/Ca) atmospheric CO_2 concentration lowering has been reconstructed during the Cenozoic (Figure 1.3) from more then 1000 ppm in the Early Eocene to 280 ppm in the XIXth century (pre-industrial levels). For more details on the change of pCO_2 through the Cenozoic see Section 1.1.3.

Observations infer that large uplift of mountain ranges globally results in higher erosion rates (Molnar and England, 1990; Raymo and Ruddiman, 1992). Erosion not only affects the mountains themselves, but delivers large volumes of sediment to the ocean. On a global scale, this sedimentary flux influences ocean chemistry and imposes a net draw down of atmospheric CO_2 (Raymo and Ruddiman, 1992). Following simplified equation describes the consumption of CO_2 during chemical weathering of silicates:

$$CaSiO_3 + CO_2 \leftrightarrow CaCO_3 + SiO_2 \tag{1.1}$$

According to this equation, the carbon dioxide is consumed during the chemical weathering and thus lower concentration of "free CO_2" in the atmosphere. Furthermore, burial of organic carbon in deep-sea submarine fans may also cause a reduction in CO_2 through removing large volumes of carbon from the normal carbon recycling process (Galy et al., 2007; Raymo, 1994). France-Lanord and Derry (1997) showed that at least during the Neogene, CO_2 consumption from the net burial of organic carbon during the Himalayan sediment deposition was 2-3 times higher then those from the removal of Himalayan weathered silicates.

In turn, atmospheric pCO_2 variations are known to have an impact on climate through

the temperature feedback, thus the linkage between the mountain uplift and pCO_2 become a highly discussed topic since the last decades. For more details on the impact of CO_2 on global climate, see Sections 1.1.3. We also provide some insight into the discussion on the linkage between the Himalayas and Tibetan Plateau uplift and global cooling (through reducing the atmospheric CO_2 concentration) in Section 1.1.4.

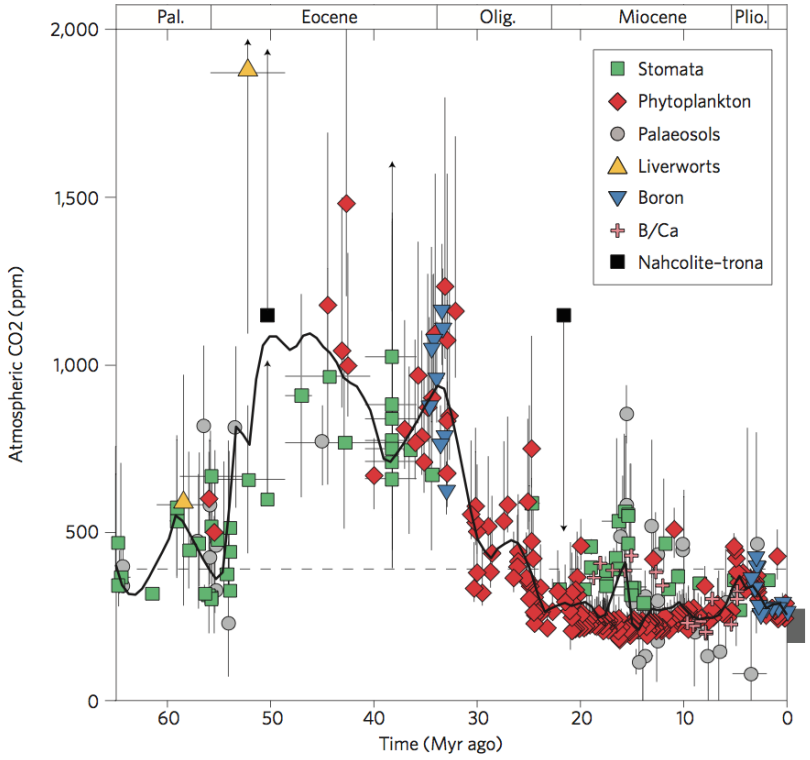

Figure 1.3 – Atmospheric CO_2 estimates reconstructed from terrestrial and marine proxies over the past 60 million years following recent revisions (see Beerling and Royer (2011) for more details). The vertical lines show the error bars. Horizontal dashed line indicates the present-day atmospheric CO_2 concentration (390 ppm). Figure modified from Beerling and Royer (2011).

1.1.2 Impact of paleogeography on climate

Term "paleogeography" implies not only paleo surface relief, but also bathymetry, paleo position of continents, land-sea distribution, opening an closing of oceanic passages. In the following section we review the impact of the paleogeography (apart from the topography) on some aspect of the Earth climate.

The consent on fundamental link between climate and land-sea distribution dates back at least to Lyell. His theory saying that a concentration of land on the pole should cool the Earth (Lyell, 1830) was born much earlier then the plate tectonics theory. Today we consider that the horizontal movement of the earth's surface reached huge scale through the geological time (up to 200 km/Ma), and the idea about the impact of continents movements on climate is widely explored.

Oceanic circulation

Recent modeling studies show that land mass distribution modifies the regional and global climate through, first of all, changes in the oceanic circulation (Donnadieu et al., 2016; Hamon et al., 2013; Hill et al., 2013; Lefebvre et al., 2012). Poulsen et al. (2003, 2001) carried out model simulations under two different Cretaceous palaeogeographies, representing conditions before and after the separation of the African and South American continents to form the Atlantic. They found that continental positions strongly influenced global ocean circulation, in particular regions of deep water formation.

Opening and closing of oceanic passages also are important consequences of plate tectonics and sea level variations. Changes in gateways have become a focus of multiple paleoclimate studies (Bijl et al., 2013; Hamon et al., 2013; Sijp et al., 2014; Yang et al., 2014). For example, it has been suggested that Late Cretaceous changes in climate and continental configuration, namely the widening of the Atlantic Ocean and the deepening of the Central Atlantic gateway, could have induced major changes in oceanic circulation that may have had an impact on the general oxygenation state of the oceanic basins and contributed to the conclusion of large-scale anoxic events in the deep ocean (Donnadieu et al., 2016). Bice and Marotzke (2002) examined the role of ocean gateways in the Eocene, and found that the configuration of polar seaways affected the sensitivity of climate to hydrological forcing, through changes in ocean overturning.

In addition, oceanic currents change may have an important consequence on CO_2 level through the change of the residence time of carbon in the ocean due to variations in ocean circulation (Lauderdale et al., 2013).

Sea surface temperatures

Land-sea distribution impacts sea surface temperatures directly and through oceanic currents. For example, Donnadieu et al. (2006) examined three paleogeographies through the Cretaceous, using the FOAM model coupled to a slab ocean. They focused on the influence of continentality on seasonality, but noted that changing paleogeography alone could give a ~4 °C global-mean warming at a constant CO_2 level. Recently, Lunt et al. (2015) provided high-resolution modeling and showed that paleogeography and solar radiation affected global mean, zonal mean, and local temperatures for periods form the Cretaceous to the Eocene.

Thermal properties of land

The land-sea distribution can have a direct effect on climate, for example, through changes in the global distribution of low-albedo characteristic for the oceans surface and high-albedo of land surfaces (Barron et al., 1980). On the other hand, the latitudinal position of continents determines vegetation distribution over land and thus, has an impact on surface albedo and roughness. In turn, the albedo has direct impact on the precipitation/evaporation balance and runoff (Otto-Bliesner, 1995). Charney et al. (1977); Sud and Fennessy (1982) provided GCM experiments with varies surface albedo and have shown that despite the evaporation scheme set, the increase in albedo causes a net decrease of

radiative flux to the ground surface and, thus, net decrease of convective clouds and precipitation.

The seasonal thermal contrast between land and ocean is generally considered to be responsible for the well-known monsoonal circulation systems driven by seasonally alternating low-level pressure patterns over land and sea (DeConto, 2009). Thus, continents position potentially impacts this contrast and, consequently, seasonality, magnitude and coverage area of monsoons.

1.1.3 Impact of atmospheric pCO_2 variations on climate

Through the geological time, CO_2 level was not constant (Figure 1.3). On long timescales, atmospheric CO_2 concentration is determined by the balance among geochemical processes including organic carbon burial in sediments, silicate rock weathering (for mode detail see 1.1.1) and volcanism with crucial contribution from Large Igneous Provinces (LIPs) (Ernst and Youbi, 2016; submitted). Since the carbon dioxide is one of the main greenhouse gases and largely contributes to the global temperature change, evaluating its impact through the Cenozoic is very important.

Variations of carbon dioxide during the Cenozoic

The pCO_2 levels throughout the Cenozoic were generally lower than during much of the Cretaceous (Goddéris et al., 2014; Wang et al., 2014c). During the **Paleocene**, pCO_2 levels was around 500 ppm[1] (Figure 1.3). For the Eocene, however, there is a wide range of estimates (e.g. Beerling and Royer, 2011; Maxbauer et al., 2014; Smith et al., 2010; Zachos et al., 2008).

During the **early Eocene** climate optimum, relatively high concentration (about 1000 ppm) was reached (Beerling and Royer, 2011; Doria et al., 2011), but according to Smith et al. (2010), in the early Eocene, pCO_2 values range from 580 ± 40 to 780 ± 50 ppm. For a climatic optimum occurred in the **middle Eocene**, the reconstructed pCO_2 is mainly between 700 and 1000 ppm, up to 1200 ppm (Beerling and Royer, 2011). In the late middle Eocene, overall estimates indicates a shift in pCO_2 towards lower values. Still, the upper branch of the estimates indicate pCO_2 up to 1000 ppm (Beerling and Royer, 2011). Simultaneously, for the same time interval, based on stomatal indices, Doria et al. (2011) indicate the declined of $pCO_2$to 450 ppm.

During the **late Eocene**, the decreasing trend of the pCO_2 level was replaced by an abrupt increase in pCO_2 up to 1000 - 1500 ppm just a few million years before the Eocene-Oligocene boundary (Figure 1.3) (Beerling and Royer, 2011).

Although various results were made by different pCO_2 reconstruction proxies at the same time, their entire decreasing tendency of pCO_2 level is remarkably consistent with each other since the Eocene. Starting from the **Oligocene**, an overall decreasing trend of the pCO_2 is reconstructed (Figure 1.3) which is consistent with appearance of ice-sheets in the Antarctic during the Late Cenozoic (Beerling and Royer, 2011; Zachos et al., 2008).

[1] parts per million

During the Oligocene mean pCO_2 was about 450-700 ppm, reaching its minimum during the **Miocene and Pliocene** (Figure 1.3).

Although growing evidences confirmed a general trend (a long-term decrease) of pCO_2 during the Cenozoic (Liu et al., 2016; Maxbauer et al., 2014; Pagani et al., 2005), the reason behind the decline of pCO_2 is still under debates. Since the Cenozoic CO_2 undergo tremendous changes, it is important to know to what extent climate is sensitive to these variations.

Cenozoic climate sensitivity on CO_2 forcing

Reconstructed based on paleotemperature proxies global temperature decreasing trend throughout the Cenozoic appeared to be consistent with the global decrease of the atmospheric pCO_2 concentration (Beerling and Royer, 2011; Zachos et al., 2008). Expectedly, a scientific efforts have been undertaken to reveal a link between these CO_2 levels and Cenozoic climate change. Thus, starting with the earliest works, atmospheric pCO_2 is considered as a major forcing factor driving the climatic oscillations over geological time scales (Walker et al., 1981).

Climate sensitivity is the equilibrium temperature change in response to the variation of the radiative forcing. The climate sensitivity specifically to CO_2 is often expressed as the global mean temperature change in °C associated with a doubling of the concentration of carbon dioxide in Earth's atmosphere. Because the CO_2 concentration constantly increases since the industrialization its impact on recent global climate warming is relatively well understood and the range is estimated to be between 2 and 4.5 °C (Stocker et al., 2014).

In a context of the Cenozoic conditions, the climate sensitivity is difficult to establish (Kürschner et al., 2008). However, experiment with increased CO_2 concentration have become the focus of paleoclimate modeling studies. For example, Barron and Washington (1985); Manabe and Bryan (1985) explored the climatic effects of large changes of CO_2 concentration in the atmosphere and show that increase in CO_2 concentration results in decrease in the meridional gradient of surface air temperature with a simultaneous increase in upper tropospheric temperature. Sensitivity experiments using general circulation models are the basis for investigation of whether changes in geography or atmospheric CO_2 concentration can explain Cenozoic global cooling detected from natural archives (Barron and Washington, 1985; Goddéris et al., 2014).

1.1.4 Himalayas and Tibetan Plateau as a natural laboratory of tectonics-climate interactions

The Himalayas and Tibetan Plateau is the largest mountain building in the world and is considered as a "natural laboratory" of tectonics-climate interactions, because observations together with numerical simulations show the important impact of its uplift on climate modifications on different time scales (see Tada et al. (2016) for complete review).

A famous example of tectonics-climate couplings is the **Asian monsoon** and the uplift of the HTP (An et al., 2001; Clift and Plumb, 2008; Molnar et al., 1993). However, still the

physical basics of such influence are disputed. For example, there are large amount of discussion about impact of Asian mountain ranges on atmosphere circulation through mechanical and thermodynamic effects (e.g. Boos and Kuang, 2010; Wu et al., 2015, 2012) and change of such effects with the growth of mountains buildings (Ramstein et al., 1997; Tang et al., 2013).

The thermal effects of TP in most cases are identified with the so-called "air pump" mechanism. The air column over the TP descends in winter and ascends in summer each year, working as an air pump and regulating the atmospheric circulation (Wu et al., 2015). The major driving source of these movements is sensible heating on elevated surfaces (Molnar et al., 2010), that contributes to heating the overlaying atmosphere. In summer the TP generates not only a heating source but also a negative vorticity source for the atmosphere, creating cyclonic circulation in the lower troposphere, which converges toward the continent and rises over the TP (Wu et al., 2015).

The opponents of "air pump" mechanism argues that the high TP affect the South Asian monsoon less by heating the overlying atmosphere, more simply acting as an obstacle to southward flow of cool, dry air (e.g. Boos and Kuang, 2010). Now, it is more or less accepted, that the large-scale orography of TP and Himalayas affects the Asia climate through thermal and mechanical forcing both. Yanai and Wu (2006) and more recently Wu et al. (2015) gave a thorough review of the past studies about the effects of the HTP and conclude that the thermal effects of these large-scale mountains are closely connected with their dynamic counterparts. However, Wu et al. (2015) also indicate that the different contributions of dynamic and thermodynamic effects of the HTP to climate, and the intrinsic dynamical processes require further investigation.

In recent modeling studies is also discussed what Plateau elevation and what part of the Plateau are crucial for the monsoon change. Different elevation scenarios (based on the geological evolution), including bulk-plateau uplift, partial or phased HTP uplift were applied (see Liu and Dong (2013) for a review). However, in most cases these experiments are not realistic because they use, except of the topography, near-present boundary condition. Our contributions on the studying of the links between the HTP and the Asian monsoon is in Chapter 6.

Another classical example of climate-tectonics interaction is the HTP uplift and the **Central Asia aridification**. Manabe and Broccoli (1990) also explored the role of mountains in maintaining extensive arid climates in the middle latitudes of the northern hemisphere (see also Broccoli and Manabe (1992)) and stressed the importance of orographically induced stationary wave troughs.

Theories suggest that the mountains uplift can result in greater rates of chemical weathering, and thus lower **atmospheric** CO_2 **concentrations** (see Section 1.1.1). The hypothesize that the Cenozoic uplift of the Himalayas and Tibetan Plateau has a crucial role in the Cenozoic cooling associated with reduction of the atmospheric CO_2 that we observe during the Cenozoic (see Section 1.1.3) was hypothesized since a quarter of century (Molnar and England, 1990; Molnar et al., 1993; Raymo and Ruddiman, 1992). Moreover, it has been also suggested that this uplift played an important role in the initiation of northern hemisphere glaciations (Ruddiman and Kutzbach, 1989).

Recent modeling of tectonic-climate feedbacks associated with increased weathering

of the Himalayas and Tibet suggests that two primary biogeochemical processes - silicate weathering and organic carbon burial - can account for the lowering of atmospheric CO_2 necessary to force global cooling Zachos and Kump (2005). However, at the time of these inferences, accurate records of both atmospheric CO_2 and the surface uplift history of the Himalaya and Tibet were lacking. Besides interactions listed here, the TP uplift has much more other effects on climate including the oceanic circulation, SSTs, etc.

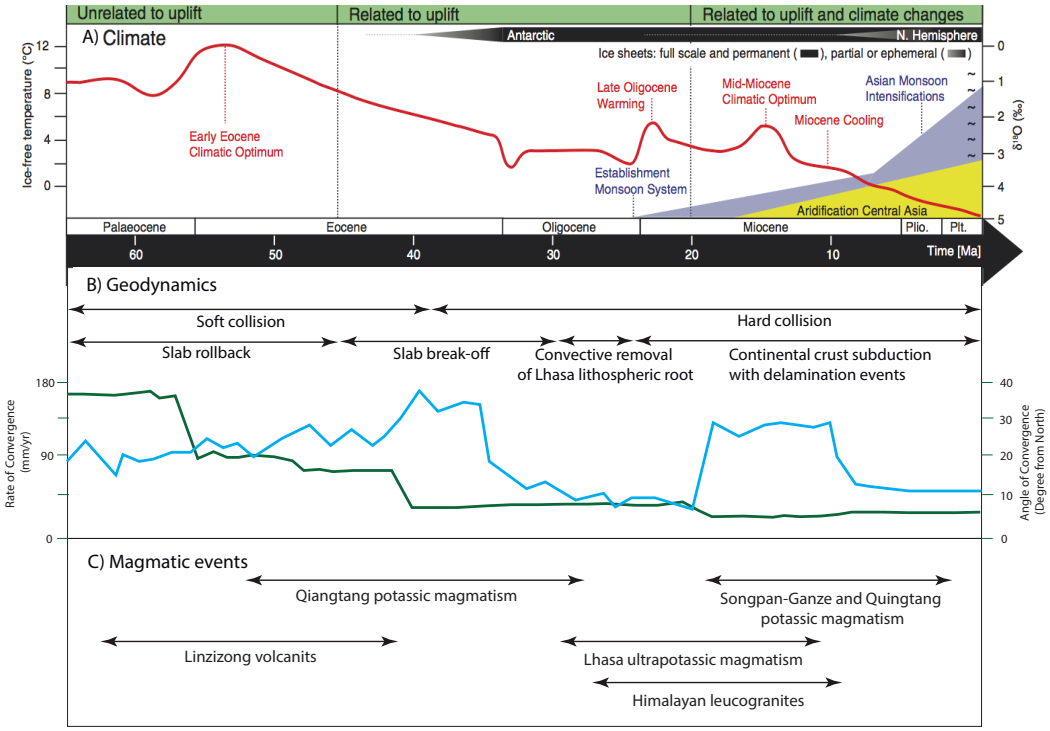

Figure 1.4 – A) Global climate evolution through the Cenozoic (from Favre et al. (2014), B) Successive geodynamical events over the Himalayas and Tibet Chung et al. (2005), rate of convergence (in mm/yr) between Indian and Asia plates and angle of convergence (in degree from the north) based on (Lee and Lawver, 1995), and C) Major magmatic events according to Chung et al. (2005).

1.2 Tectonic evolution of India-Asia collision zone

The Himalayas, the Tibetan Plateau and surrounding mountains (Figure 1.5) are the largest mountain building on the planet, stretching 3000 km from west to east with average modern elevations of ~4.5 km for Tibetan plateau with complex and heterogeneous geological structure (see Section 1.2.1).

Interpretation of the structural record, sediment accumulation history reconstruction, thermochronological and geochemical results suggest the Himalayas and Tibetan Plateau uplift was probably caused by stress and deformation linked with the convergence of Indian and Asian plates. The Himalayan-Tibetan orogen have become a focus of multidisciplinary study as an archetypical example of a collision since more then half a century, since the approval of the plate tectonics theory.

The collision of India with the Eurasian continent represents one of the most spectacular examples of continental collisions during the Cenozoic, since the northward migration velocity of India continent was extremely fast, with maximum convergence rate of ~20 cm/year (Patriat and Achache, 1984) and immense horizontal shortening. The rate of convergence and the latitudinal position of the Indian plate is relatively well constrained based on paleomagnetic data (see Section 1.2.3).

The deformations and related magmatic events in the interior and margins of the Tibetan Plateau probably occurred in late Paleocene, Eocene, Oligocene, Miocene and/or Plio-Quaternary. However, despite extensive research on the tectonic and geodynamic evolution of the HTP, the details of the timing and rate of India-Eurasia collision, timing of geological events and associated response of surface elevations remain controversial (Molnar and Stock, 2009; Najman et al., 2010; Tapponnier et al., 2001; Wang et al., 2008a, 2014a) (Section 1.2.2).

More complete overview dealing with both active tectonics and the overall geological evolution of the system can be found in numerous works, for example, Allegre et al. (1984); Burg and Chen (1984); Chang et al. (1989); Chung et al. (2005); Pan et al. (2012); Tapponnier et al. (1986, 2001); Wang et al. (2008b,c); Yin (2006); Yin and Harrison (2000) and others. The goal of the following section is to provide a coherent picture of the timing and rate of geological events over the studied region and to give an idea on the order of magnitude of the tectonics events that have been hypothesized to have an impact on climate (e.g. Molnar et al., 1993; Ramstein et al., 1997; Ruddiman and Kutzbach, 1989).

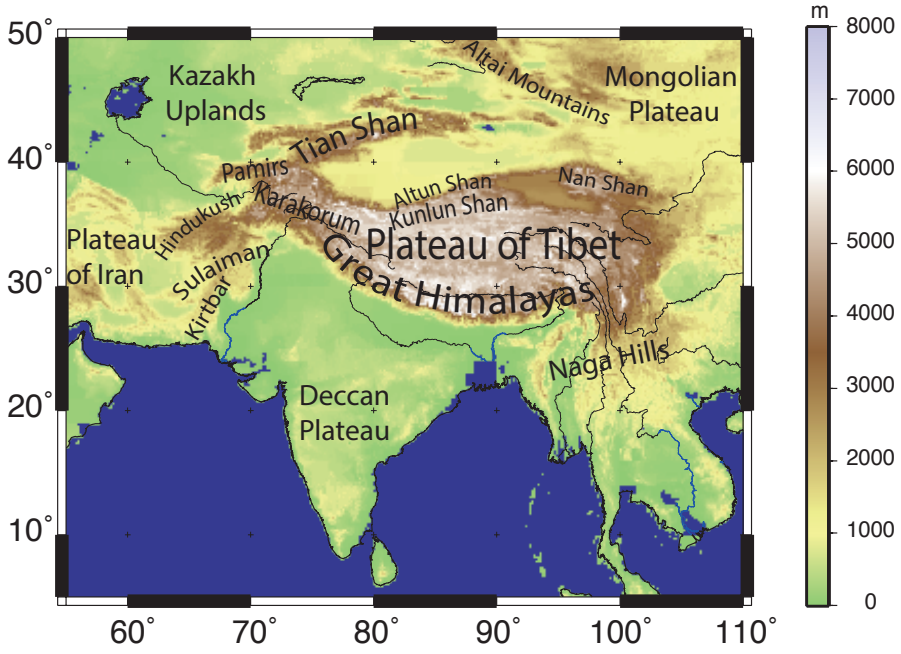

Figure 1.5 – Regional relief and orography.

1.2.1 Structural zonation, geology and manifestations of Cenozoic tectonics

Present-day Himalayan-Tibetan orogen is a collage of continental fragments assembled in Paleozoic and Mesozoic, with the latest amalgamation and tectonic reactivation during the Indo-Asia collision event in the Cenozoic. Here we suggest an overview of the geological structuring and manifestations of the Cenozoic tectonics and igneous activity that may have resulted in Cenozoic massive uplift of the region (for the uplift history reconstructions of the HTP region see Section 1.3.6).

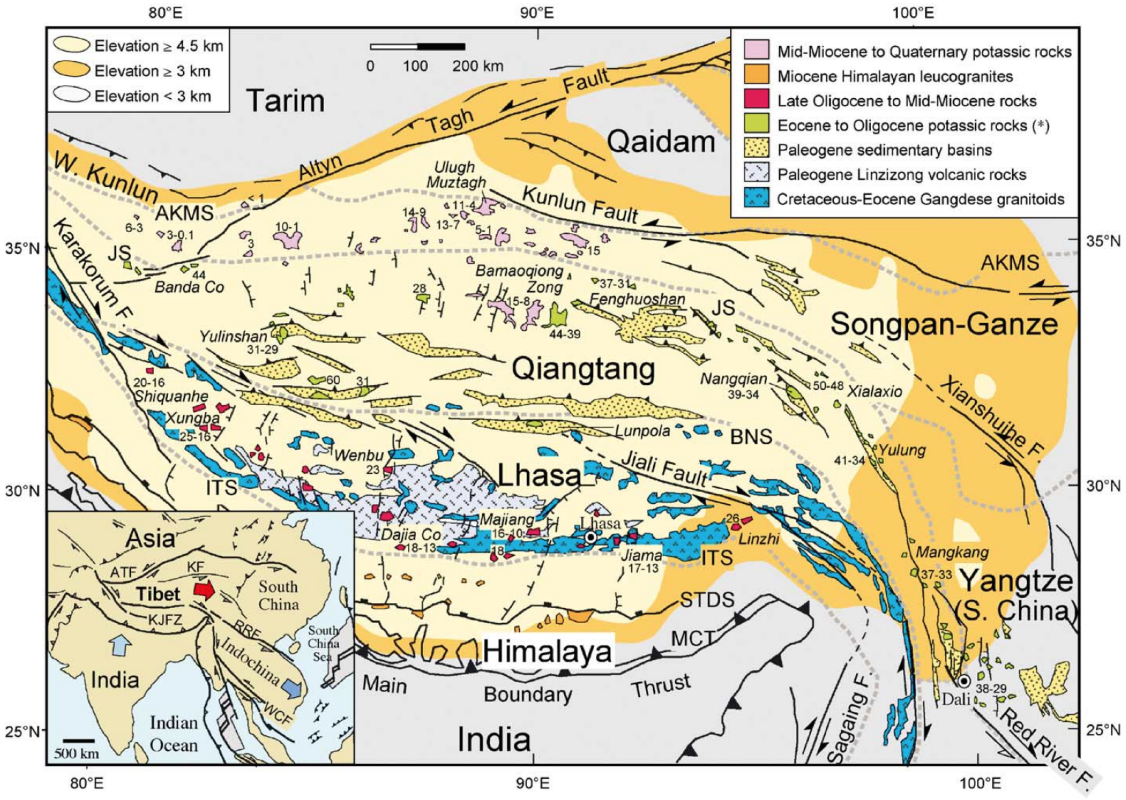

Figure 1.6 – Simplified geological map of the Tibetan plateau and surrounding areas from (Chung et al., 2005). An asterisk in the legend for magmatic rocks remarks that Paleocene (60 Ma) sodium-rich basalts emplaced in the western Qiangtang are included. Inset shows the Cenozoic tectonic extrusion in East Asia related to the India – Asia collision (after Tapponnier et al., 1982). MBT = Main Boundary Thrust; MCT = Main Central Thrust; STDS = South Tibet Detachment System; ITS = Indus – Tsangpo Suture; BNS = Bangong – Nujiang Suture; JS = Jinsha Suture; AKMS = Ayimaqin – Kunlun – Muztagh Suture; ATF = Tltyn Tagh Fault; KF = Kunlun Fault; KJFZ = Karakorum – Jiali Fault Zone; RRF = Red River Fault; WCF = Wang Chao Fault. Ages of post-collisional potassic magmas are shown in numerals, data sources are given (Chung et al., 2005).

Himalayas

The **Himalayas** lie between the Indian shield to the south and the Indus-Yalu (Indus-Tsangpo) suture to the north (Chung et al., 2005; Yin and Harrison, 2000). They consist of three tectonic slices bounded by three north-dipping Late Cenozoic fault systems of different ages: the Main Boundary Thrust (MBT), the Main Central Thrust (MCT), and the

South Tibetan Detachment System (STDS) (Figure 1.6). All three tectonic slices are considered to be parts of so-called Tethyan Himalayas - the north-facing passive continental margin, which developed from middle Proterozoic to Cretaceous times (Brookfield, 1993). The Mesozoic passive continental margin sequence of the Himalaya was developed continuously until the latest Cretaceous when the collision between India and Asia began affecting its sedimentary facies patterns and its rate of subsidence (Yin and Harrison, 2000).

The lowest slice is called **The Lesser Himalayas** and is bounded at the base by the MBT and at the top by the MCT (Yin and Harrison, 2000). This tectonic zone consists mainly of Precambrian clastic sediments and metasedimentary rocks (Brookfield, 1993).

The second slice, **The Greater (or High) Himalayas** is bounded by the MCT below and the STDS above (Burchfiel et al., 1992; Burg and Chen, 1984; Yin and Harrison, 2000) and comprises late Proterozoic to early Cambrian metasedimentary rocks (Hodges et al., 1996).

The North Himalayas lies between the South Tibetan Detachment System and the Indus-Tsangpo Suture (ITS)Indus-Tsangpo Suture zone (Yin and Harrison, 2000). It consists of late Precambrian to early Paleozoic sedimentary and metasedimentary rocks (Burchfiel et al., 1992; Yin and Harrison, 2000) and thick Permian to Cretaceous continental margin sequences (Brookfield, 1993).

Tibetan Plateau

On a large scale, the Tibetan Plateau constitutes a tectonic collage of continental blocks (terranes), separated by sutures (Wang et al., 2008c). From north to south, the interior of the Tibetan Plateau comprises the roughly east–west-trending **Kunlun, Songpan-Ganzi, Qiangtang and Lhasa blocks**, (Figure 1.6 (Chung et al., 2005; Wang et al., 2008c; Yin and Harrison, 2000). The sutures separating these blocks decrease in age from north to south (Chang et al., 1989).

The **Kunlun Block** is considered to be a broad Early Paleozoic arc that was later superposed by a Triassic arc. Together, they are referred to as the Kunlun batholith. Origin of the Triassic arc is still under much debate. Some authors interpret it as northward subduction of the Songpan-Ganze ocean beneath Paleozoic Kunlun basement (Zhang et al., 2011), while others relate this arc to south dipping subduction on the north (Burchfiel et al., 1995). In the region, the Kunlun thrust system that resulted in at least 250 km of shortening, is still active.

The **Songpan-Ganze Block** is a long, narrow belt between Kunlun and Qiangtang terrane, formed by collision during Jurassic time and completed by latest Jurassic (Dewey, 1988). This terrane is characterized by intensely deformed sequence of Triassic-Jurassic strata of deep marine deposits. This deformation was contemporaneous with collision and subsequent continued convergence between North and South China and resulted in ~250 km shortening (Burchfiel et al., 1995).

The **Qiangtang Block** is bounded by the Jinshajiang Suture (JS) to the north, and the Bangong-Nujiang Suture (BNS) to the south Yin and Harrison (2000). It is generally accepted that the suturing of the Songpan-Ganzi–Qiangtang and Qiangtang–Lhasa blocks occurred in the Middle Cretaceous (Yin and Harrison, 2000), and consequently the Qiang-

tang Block has been in an intra-continental setting since that time.

The **Lhasa Block** is bounded by the Yarlung-Zangbo and Bangong-Nujiang Sutures, collided with Qiangtang to the north in the interval from late Jurassic to middle Cretaceous depending on the longitude (Dewey, 1988; Yin and Harrison, 2000). Active collision lasted until the early Late Cretaceous within the Lhasa terrane, resulting in at least 180 km shortening (Murphy et al., 1997).

1.2.2 Timing of main events during the Cenozoic collision

The geodynamical history of the region has been derived by dating the tectono-magmatic events. Timing, volume, spatial distribution, compositions of magmatism as well as brittle and plastic deformations give an idea about the magnitude of crustal shortening over the HTP and abrupt events (such as a slab break-off) with has implications for reconstructing the elevation history of the region (see Section 1.3.6).

Collision

Since the Late Cretaceous, the migration speed of India northward was extremely fast (to a maximum of ~20cm/year, (Chatterjee et al., 2013; Patriat and Achache, 1984)). This extremely fast event was followed by a collision between moving India plate and quasi fixed Asia plate. The timing of onset of Indo-Asia collision provokes raging debates, but still remains controversial. Until now, it was generally agreed that India began to collide with the accretionary Asian margin in the early Eocene at ~55–50 Ma Clift et al. (2002, 2008); Dupont-Nivet et al. (2010); Leech et al. (2005); Meng et al. (2012); Najman et al. (2010); Yin and Harrison (2000). However, an increasing number of modern studies are calling for an earlier collision onset ~85 Ma (Chatterjee et al., 2013), ~70–65 Ma, (Cai et al., 2011; Ding et al., 2005; Yin and Harrison, 2000), ~60 Ma Hu et al. (2015); Khan et al. (2009); Wu et al. (2014), ~60–55 Ma Khan et al. (2009) and even for a later collision time of ~30 Ma (Aitchison et al., 2008) or ~40 Ma (Bouilhol et al., 2013)

Recent studies confidently show that the collision has been asymmetric and more complex than previously assumed, involving two subduction zones: 1) the first, a collision of Tibetan-Himalayan microcontinent with Asia, followed by 2) a "hard" India-Asia collision with Indian continental lithosphere at 40 Ma (Bouilhol et al., 2013; Khan et al., 2009) or ~25-20 Ma (van Hinsbergen et al., 2012)

Post-collisional history

Paleocene-Eocene Northward subduction of the Neo-Tethyan slab along the southern margin of Asia prior to the Indian indentation gave rise to an Andean-type magmatic arc, now exposed as the voluminous Gangdese batholith and Linzizong volcanic successions in the Lhasa terrane of southern Tibet (Chung et al., 2005).

After collision, intracontinental convergence and deformation continued across Tibet, reaching northward to involve a larger area than previously (Royden et al., 2008). In the central Himalaya, postcollisional deformation involved south-vergent thrusting and fold-

ing of rocks of the north Indian passive margin as it was subducted beneath Eurasia. The magnitude of this Early Cenozoic shortening is unknown; within the basins shortening is small but locally may reach more than 50 %. It has been suggested that this shortening reflects the beginning of southward underthrusting of Eurasia below Tibet (Royden et al., 2008).

The magmatism started with Na-rich basalts in the Paleocene and changed to potassic and ultrapotassic compositions in the Eocene. Similar scenarios involving slab rollback, back-arc extension, basin formation, and magmatic activity have been widely postulated for the evolution of the Mediterranean-Carpathian orogenic system (e.g. Chalot-Prat and Girbacea, 2000).

Late Eocene - Early Oligocene The Neo-Tethyan oceanic slab is suggested to have detached from the Indian continental lithosphere at ~45 Ma, in accordance with the Himalayan metamorphic record (Chung et al., 2005) and the onset of the India–Asia "hard collision". This slab breakoff would have led to cessation of the Gangdese magmatism and a substantial amount of topographic uplift (for the elevation history review see Section 1.3.6). Whereas most, if not all, workers consider the Gangdese arc magmatism to have ceased at ~40 Ma, Harrison et al. (2000) argued that the magmatism lasted longer, at least to ~30 Ma. The breakoff, which eliminated slab pull, would have prevented the Indian cratonic mantle lithosphere from moving further downward because it is more refractory and intrinsically more buoyant than the Asian mantle lithosphere (Fielding, 1996).

In the mean-time, in where is now the northern and northeastern Tibetan plateau, a different style of tectonism involving the “back-arc” lithospheric extension that began in early Tertiary time was operating. This extensional event, however, seems to have been diminished in the Oligocene when the magmatism in the region changed its compositions from Na-rich basalts to potassic and ultrapotassic, implying a gradual decrease in degrees of partial melting in the mantle source (Chung et al., 2005).

Late Oligocene - Mid-Miocene The Indian collision eventually caused the Qiangtang terrane to switch from an extensional to compressional regime in Oligocene time. This is borne out by the waning and then cessation of the potassic magmatism and the development of a major sedimentary hiatus in the Hoh Xil basin (Liu et al., 2001), both around ~30 Ma. It is hence proposed that regional crustal shortening, perhaps with concomitant topographic uplift (Liu et al., 2001), began at this time in the area far behind the collision front.

Partial melting of metasomatized lithospheric mantle to form the ultrapotassic magmatism in the Lhasa terrane can be explained by two possible mechanisms, i.e., convective removal of the lower lithosphere and breakoff of the Neo-Tethyan slab (Chung et al., 2003). Williams et al. (2001) argued with a larger scale for the lithospheric removal. The latter involves the dissipation of potential energy that would cause further consequences such as the uplift and extension of the Tibetan Plateau (Molnar et al., 1993). The work of Chung et al. (2003) is consistent with the point of Williams et al. (2001) that the widespread occurrence of post- collisional magmatism in the Lhasa terrane indicates that these small volume igneous activities are regional phenomenon. This further supports the hypothe-

sis that calls for removal of the thickened lithospheric root underneath southern Tibet. In this sense, the ultra-potassic lavas and adakites are interpreted as melts of the metasomatized lithospheric mantle. The occurrence of adakitic rocks from southern Tibet suggests that there was a thickened crust (>50 km) in the region and that its lower part consisted of mafic eclogite and/or garnet amphibolite which melted because of a major thermal perturbation caused by removal of the Lhasa lithospheric keel (Chung et al., 2005, 2003).

Chung et al. (2005) suggest as well that in southern Tibet, the lower part of the Lhasa lithosphere was removed in the late Oligocene. This interpretation, invoking two separate detachments of the Neo-Tethyan slab and thickened Lhasa lithosphere occurring at ~45 and 26 Ma.

In the Lhasa terrane, the loss of its lithospheric root and replacement by hotter asthenosphere would have greatly raised the geothermal condition, which led to generation of the ultrapotassic magmas of this stage from the remnant lithospheric mantle and the adakites from the mafic lower part of the Lhasa crust that had been thickened and hence eclogitized in its deeper levels after the slab breakoff (Chung et al., 2003).

Further evolution refers to northward underthrusting of the Indian mantle lithosphere associated with Himalayan tectonomagmatism (Chung et al., 2005).

Also located at the northern edge of the HTP, the initiation of the uplift of the West Kunlun range probably started 23 Ma due to upper crustal shortening and consequent crustal thickening (Jiang et al., 2013).

Mid-Miocene-Quaternary Magmas of this stage were divided by Yin and Harrison (2000) into a “highly potassic group” and a “calc-alkaline group”, with the former group supposedly being distributed mainly in the western Songpan – Ganze province and the latter group in the western Qiangtang province. “Diffused” destruction of the lower part of the lithospheric mantle beneath the Qiangtang and Songpan – Ganze terranes leads to reactivation of the potassic magmatism and uplift of the northern Plateau (Chung et al., 2005).

The tectonic setting of northern Tibet was transformed to an east – west extensional environment beginning at ~13 Ma, as shown by the synchronous onset of renewed potassic volcanism and north-south-striking normal faulting (Blisniuk et al., 2001).

In the west Qiangtang Block, most Cenozoic volcanic rocks have been considered to be shoshonitic and were generated only during the past 15–3 Ma (e.g. Chung et al., 2005), similar to some late (16–0 Ma) shoshonitic rocks in the east Qiangtang Block (Wang et al., 2001).

1.2.3 Latitudinal position of proto-Tibetan Plateau

After the separation from Africa in the Late Cretaceous, the Indian plate started its northward drift, accompanied with the subduction of the Tethys Ocean crust and ultrafast spreading in Southeast Indian Ridge. Analysis of Cenozoic magnetic anomalies in the Indian ocean shows that the relative velocity between the Indian and Eurasian plates decreased rapidly from ~15–25 cm/yr to ~13–18 cm/yr at ~50 Ma (Achache et al., 1984; Wu et al., 2013). This sudden decrease in plate convergent rate has been interpreted as

indicating the time for the onset of the Indo-Asian collision (Achache et al., 1984).

The latitudinal position of the Indian subcontinent is reconstructed within the uncertainty of the paleomagnetic method. Figure 1.8 shows present-day and reconstructed paleo-positions of two points on the India plate with respect to the Eurasia plate at different times according to Molnar et al. (2010). These data indicates that during the Eocene and the Oligocene, the Indian subcontinent was likely situated in the equatorial zone. Yin and Harrison (2000) synthesis shows that at least 1400 km of north-south shortening has been absorbed by the Himalayan-Tibetan orogen since the onset of the Indo-Asian collision. Thus, during the Paleogene, highly elevated terrains may have situated far south then nowadays, that is important for understanding local and global climate changes during the Cenozoic.

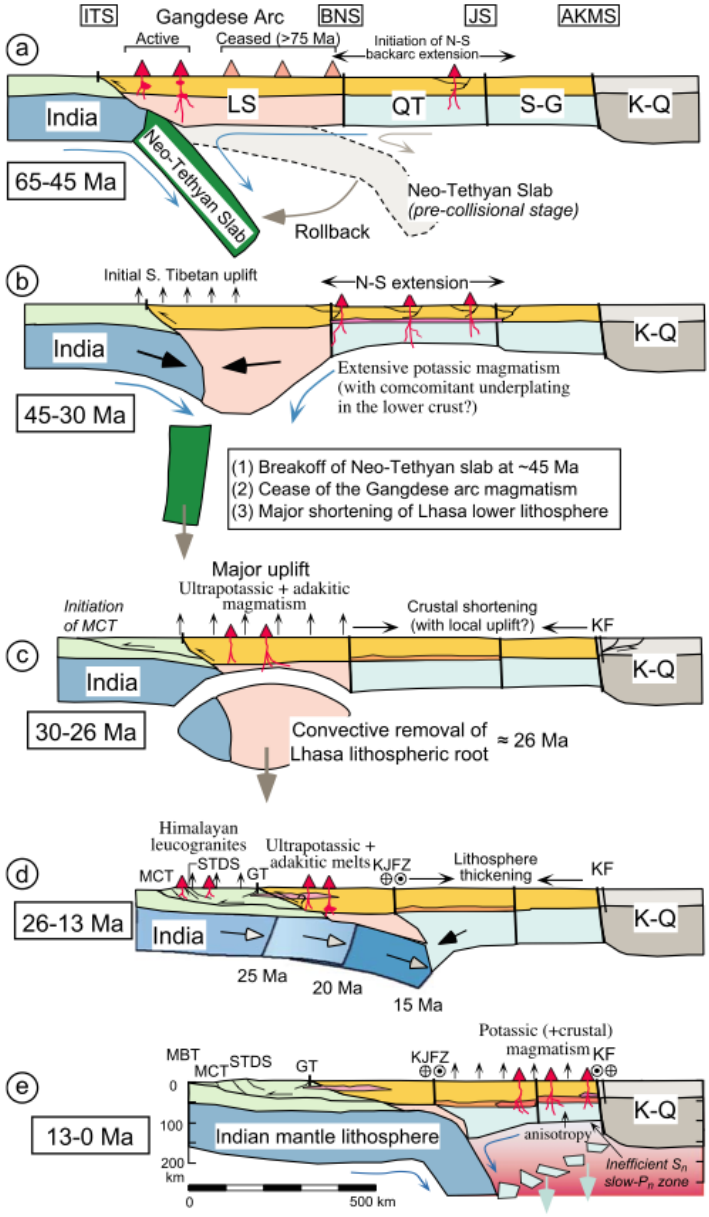

Figure 1.7 – One of numerous suggested scenarios of geodynamical evolution of Indo-Asia collision zone, according to Chung et al. (2005). Stages of Tibetan Plateau evolution illustrated by the 0° E south-north section. The Gangdese arc magmatism is related to the slab rolling back. (b) 45 – 30 Ma: Detachment of the Neo-Tethyan slab and onset of the "hard collision" particularly in the lower part of the India and Lhasa lithospheres. (c) 30–26 Ma: Removal of the gigantic Lhasa lithospheric mantle leading to the uplift and formation of the southern Tibetan plateau. (d) 26 – 13 Ma: Northward underthrusting of the Indian mantle lithosphere associated with Himalayan tectonomagmatism. The ultrapotassic and adakitic magmatisms, resulting from thermal perturbation owing to the loss of thickened Lhasa lithospheric root, ceased by the underthrusting. (e) 13 Ma to the present: "Diffused" destruction of the lower part of the lithospheric mantle beneath the Qiangtang and Songpan – Ganze terranes to reactivate the potassic magmatism and raise the northern plateau. MBT = Main Boundary Thrust; MCT = Main Central Thrust; STDS = South Tibet Detachment System; ITS = Indus-Tsangpo Suture; BNS = Bangong-Nujiang Suture; JS = Jinsha Suture; LS = Lhase Block; QT = Qiangtang Block; S-G = Songpan-Ganze Block; K-Q = Kunlun-Quadam; AKMS = Ayimaqin-Kunlun-Muztagh Suture; ATF = Tltyn Tagh Fault; KF = Kunlun Fault; KJFZ = Karakorum-Jiali Fault Zone; RRF = Red River Fault; WCF = Wang Chao Fault.

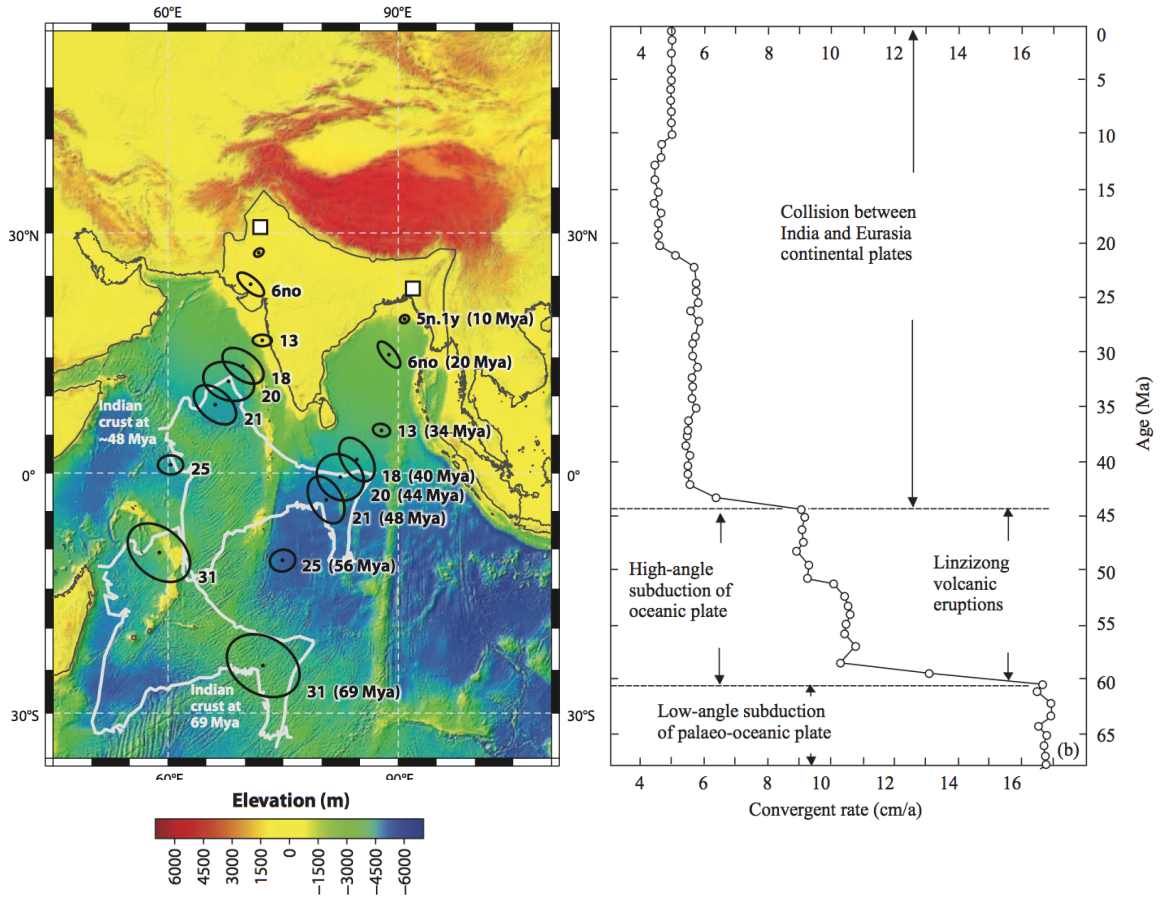

Figure 1.8 – A) Map showing present and reconstructed positions of two points on the India plate with respect to the Eurasia plate at different times in the past. Numbers identify chrons and corresponding ages. An outline of the Indian coastline and the northern edge of present-day, intact Indian crust is also reconstructed to its positions ~48 Mya, close to the time of collision, and 69 Mya, before the collision. White rectangular show present-day position of 2 selected points. Ellipses show the reconstructed position within 95 % confidence interval of these two points accordingly. Figure modified from (Molnar et al., 2010). B) The convergent rate between the Indian and Asian plates. Figure modified from (Wu et al., 2013)

1.3 Paleoelevation reconstructions methods

Paleoaltimetry is a quantitative estimate of the surface elevation above mean sea level of ancient landscape. Quantitative estimations of paleoaltitude have become a focus of Earth sciences because amplitude, lateral extent, timing and rate of growth/decay of the topographic signal provides 1) constraints on the geodynamic mechanisms shaping the Earth surface, including isostatic flexural effects linked to continental thinning or shortening (Faccenna et al., 2014), the dynamical effect of a large mantle upwelling (Burov and Gerya, 2014; Faccenna et al., 2014; Flament et al., 2014; Lithgow-Bertelloni and Silver, 1998), the delamination of the mantle part of the continental lithosphere (Chung et al., 2005; Meissner and Mooney, 1998; Schott and Schmeling, 1998), magmatic underplating or thermal expansion associated with an array of smaller mantle plumes rising beneath the continent (Murphy et al., 1998), dynamic rebound associated with the detachment of a subducting slab (Chung et al., 2005; Duretz et al., 2011), etc. and 2) reconstructions of paleoclimates, including changes on the atmospheric dynamics, oceanic circulation, temperature, hydrological cycle, etc.

Other way round, surface uplift is undoubtedly linked to the tectonic events, which reconstructions (based on spatial distribution, timing and composition of magmatism, structural analysis, sedimentary record interpretation, etc.), may give a first-order idea of paleo landscapes. However, quantitative estimates of paleoelevations are more complex to achieve and the elevation history of major orogens has been challengeable for decades. Here we overview the methods that are commonly used for the paleoelevation reconstructions of orogens.

1.3.1 Paleoelevation reconstructions based on geological evidences

Uplift in continental regions is inferred from varied geological evidences as the presence of marine sediments and terraces at altitude above present sea level, river terraces and nick points, erosional platforms, character and volume of clastic detritus in basin of sedimentation and thermal history of terrains linked with exhumation.

River and marine terraces

A terrace is a step-like landform. By studying the size, shape, and age of terraces, one can determine the geologic processes that formed them. When terraces have the same age and/or shape over a region, it is often indicative that a large-scale geologic or environmental mechanism is responsible.

Marine terraces (relatively flat, horizontal or gently inclined surface of marine origin) are common land forms in many geologic and environmental settings throughout the world that, when numerically dated, offer a means to calculate rates of uplift relative to global sea level (Gurrola et al., 2014). For example, based on marine terraces in Norway and Svalbard the isostatic domal uplift of Fennocandia (of about 1-2 km) subsequent to a melt of last Pleistocene ice cap has been inferred (Lambeck et al., 1998). However, additional caution should be applied to the elevation reconstruction based on terraces,

because of an uncertainty linked to the absence of knowledge about eustatic sea level changes.

River terraces are remnants of the former floodplain of a stream or river. River terraces evolution over region can be influenced by tectonics, climate, or erosion changes. Based on geomorphological analysis, Kuhle (1995) has suggested that during the course of the Pleistocene the Tibetan Plateau was glaciated several times so that at each time there alternated a maximum glacial isostatic depression and an interglacial uplift (with a magnitude of ~1 km).

Studies of the Earth surface uplift are abundant for Quaternary, however, for earlier time periods they are less abundant.

Sedimentary record

Increase in sedimentation rates in forland basin is commonly interpreted as an uplift of a nearby mountain region (Potter and Szatmari, 2009). However, such an increase may result from erosion rate acceleration in response to climate change. Nevertheless, ones paleoclimate change are taken into account, a material balance method can be applied. This technique is based on an assumption about the material conservation in terms of total amount of denudation and sedimentation and allows the paleotopographic restoration by transferring he materials in the sedimentation basin back to their provenance (Hay et al., 1989). For example, using this approach, Yan et al. (2015) proposed that Longmen Mountain region (eastern Tibetan Plateau) have been uplifted from 0 to 2751 m since the Late Triassic.

Thermochronology data

Using apatite fussion track and $^{4}He/^{3}He$ thermochronometry may allow to reconstruct exhumation of the mountain building which is in a direct relation with the uplift and erosion rate (Ehlers and Farley, 2003). Combined with modeling approach, thermochronometry can be applied for reconstruction of regional landscape evolution (Braun, 2003).

1.3.2 Paleontological methods of paleoelevation reconstructions

Paleobotanical methods

Fossil plants have long been used to infer paleoclimate. The most basic premise of paleobotanical theory is that plants that grow in warm climates look different from plants that grow in cold climates, and therefore if one or the other can be recognized in the fossil record we have a constraint on the climate in which the plants lived. Another basic hypothesis is that in mountains, vegetation is distributed according to altitudinal zones and thus paleobotanical method to infer paleoelevations.

At present there are two general approaches that utilize fossil plant assemblages for assessing quantitative terrestrial palaeoclimates during the paleo periods: taxonomic based

methodologies and morphological based methodologies (Chaloner and Creber, 1990; Liang et al., 2003).

Taxonomic method is based on identification of the flora in terms of modern plants and an assumption that the climatic preferences of any particular plant fossil are similar to modern "nearest living relatives". In contrast, morphological based methods assume that morphological characteristics of plants had the same relation to climate in the past as they do now, without reference to the systematic status of the plant.

The second half of the analysis involves relating the fossil flora to some climate parameter or group of parameters, and further using these parameters to infer elevation. The climatic half of the analysis may involve estimates of mean annual temperature (MAT), and growing season length, temperature lapse rate and mean annual enthalpy.

In paleobotany a lot of assumptions and inferences are used that results in huge uncertainties associated with traditional paleobotanical analyses. Forest et al. (1999) developed a technique for paleoelevations estimations from fossil leaves based on moist static energy. Recently it has been also suggested that plants could provide a direct indicator of altitude through the correlation between stomatal density in leaves and CO_2 partial pressure (McElwain, 2004). Although this approach has the advantage of being independent of global climate models, it is unclear how useful the technique will be in interpreting the fossil record given that the correlation is strongly species specific and so its application would be restricted to fossil floras comprising extant species.

Paleozoological methods

Invertebrates, fishes and mammalians fossils are used for paleoelevations reconstructions. For example, finding of rhinoceroses fossils in the Dingqing Formation of the Miocene age in the Lunpola Basin indicates modest elevations (~3000 m) of the Northern Tibet at that time, because Plesiaceratherium has been inferred to live in subtropical and warm temperate forests and the environmental reconstructions based on modern alpine vegetation vertical zones in the Himalayas and the Early Miocene global climatic conditions indicate that the highest elevation in the Lunpola Basin at the time of the deposition of the Dingqing Formation could not have exceeded 3170 m (Deng et al., 2012). In addition, mountains may also be considered as a physical barrier for species migration. Separated habitats of mammalians may, for example, attest existence of high enough mountains.

1.3.3 Stable isotopes as a proxy for paleoelevation reconstructions

Stable isotopes are widely used for paleoelevations reconstructions. This method is applied for reconstructing topographic histories of many of the world's largest mountain ranges including the Andes and the Altiplano region (e.g. Garzione et al., 2014, 2008, 2006; Kar et al., 2016; Mulch et al., 2010; Rohrmann et al., 2014), the North American Cordillera (e.g. Chamberlain et al., 2012; Gébelin et al., 2012; Lechler and Galewsky, 2013; Mix et al., 2011; Mulch and Chamberlain, 2007), the Alps Campani et al. (2012), the Southern Alps of New Zealand (e.g. Chamberlain et al., 1999), central Asia mountains (Caves et al., 2014) and, of course, the Himalaya and Tibetan Plateau (e.g. Ding et al., 2014; Garzione et al.,

2000b; Hoke et al., 2014; Rowley and Currie, 2006; Xu et al., 2013, see more in Section 1.3.6).

In this section for better understanding the technique of paleoelevation reconstructions of mountains belts that relies on stable oxygen isotopes measurements, first, we introduce the physical bases that govern distribution of stable water isotopes, then show basic principles of application of stable water isotopes for reconstruction the elevations of mountains belts during the past using classical "inverse proxy modeling". Finally we show how "forward proxy modeling" takes advantage of recent development of isotopes-enabled general circulation model (GCM)s.

Stable oxygen isotopes: definition, fractionation and distribution

Definition and notations. Isotopes are variants of a particular chemical element, which differ in neutron number, while the number of protons in each atom is the same. Each isotope of a given element has a different mass number, but has no difference in gross chemical properties, which are determined by the number of electrons.

The mass number of oxygen isotopes ranges from ^{12}O to ^{24}O, among which only three are naturally occurring and stable: ^{16}O, ^{17}O, and ^{18}O. Other oxygen isotopes are radioactive and unstable. Water consists mainly from the molecules of $H_2{}^{16}O$, but at the same time there are some molecules with heavy oxygen isotopes: $H_2{}^{17}$ and $H_2{}^{18}O$. These different molecules are called isotopologues or commonly just "stable water isotopes".

A deviation from the ocean reservoir of different oxygen molecules called the isotopic composition and is expressed in ‰ using the δ-notation:

$$\delta = \left(\frac{R_{sample} - R_{stand}}{R_{stand}} \right) \cdot 1000 \tag{1.2}$$

where R is the ratio of the heavy to light isotope, and R_{sample} and R_{stand} are the ratios in the sample and standard, respectively. For oxygen isotopes in water R_{stand} references to Standard Mean Ocean Water (SMOW), that is equal to $2.0052 \cdot 10^{-3}$ and for oxygen in carbonates to Pee Dee Belemnite (PDB), that is equal to $11.2372 \cdot 10^{-3}$ (Gonfiantini, 1978)[2]. In this thesis we are focused on one stable isotopologue of water - $H_2{}^{18}O$, because it is used in the classical paleoaltimetry approach (see Section 1.3.3). We define $\delta^{18}O$ for quantifying the relative enrichment of water in $H_2{}^{18}O$.

Isotopic fractionation. The isotopic fractionation is an enrichment of one isotope relative to another in a chemical or physical process. The isotopic fractionation is a consequence of differences in mass of isotopic species. The extent of which can be expressed by a fractionation factor, alpha (α). Isotopic fractionation, mainly occurs during a phase transition, when the ratio of light to heavy isotopes in the involved molecules changes. There are two types of isotopic fractionation: equilibrium and kinetic.

Equilibrium fractionation is a result of differences of isotopologues mass. The saturation vapor pressures $H^{18}O$ slightly differ from most abundant isotopologue $H^{16}O$. An

[2]To transfer $\delta^{18}O$(PDB) to $\delta^{18}O$(SMOW) use following equation: $\delta^{18}O(SMOW) = 30.92 + 1.03092 \cdot \delta^{18}O(PDB)$

example of equilibrium fractionation: when water vapor condenses (an equilibrium fractionation), the heavier water isotopes (^{18}O) become enriched in the liquid phase while the lighter isotopes (^{16}O) tend toward the vapor phase. This fractionations depends mainly from the temperature.

Differences of molecules diffusivity (linked to mass and symmetry differences between the isotopologues) induce another type of fractionation – kinetic. Heavy molecules have less diffusivity comparable to lighter ones. Kinetic fractionation depends on relative humidity of the ambient environment Merlivat and Jouzel (1979). Thus, fractionation takes place in such process as evaporation, condensation to both liquid and ice, re-evaporation of precipitation in atmosphere, and plant transpiration from land surface.

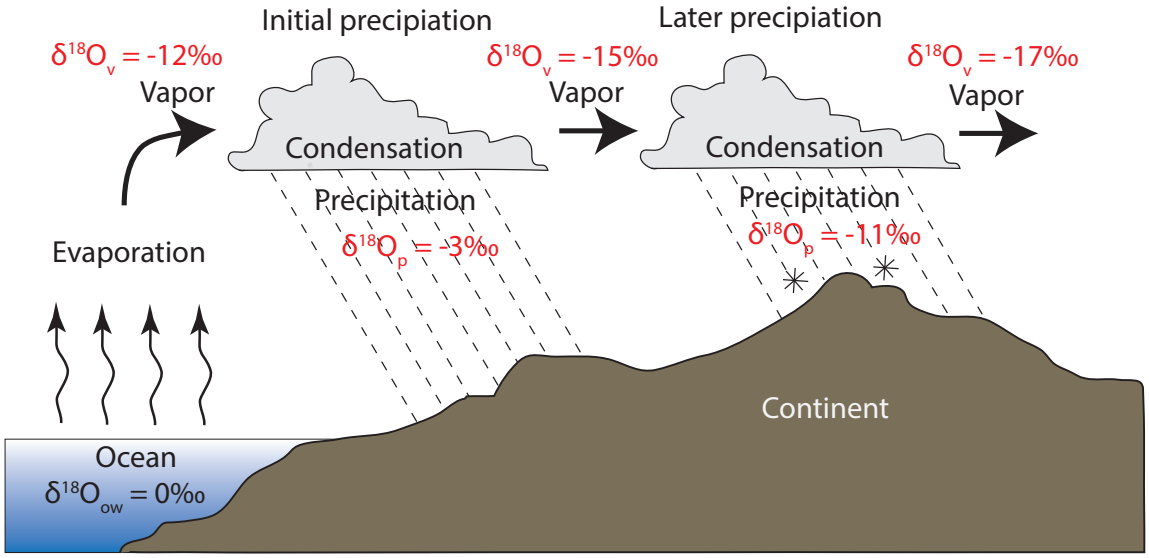

Figure 1.9 – Illustration of $^{18}O_p$ and $^{18}O_v$ depletion through the rainout process. Based on Hoefs and Hoefs (1997) and Coplen et al. (2000).

Rayleigh distillation. Isotopic fractionation that occurs during condensation in a moist air mass can be described by Rayleigh distillation. The Rayleigh distillation considers an isolated ascending air parcel with prescribed initial temperature, relative humidity, and a reference value for composition of the vapor before the rainout process:

$$R_v = R_{v0} \cdot f^{\alpha-1} \tag{1.3}$$

where R_v is the isotope ratio of remaining vapor, R_{v0} - isotope ratio in initial vapor, f - the fraction of vapor remaining and α - the isotopic fractionation coefficient.

A fractionation coefficient α depends from the water phase (Majoube, 1971; Merlivat and Nief, 1967). The fraction f reflects temperature T*, that occurred during the last condensation event (Galewsky and Hurley, 2010; Galewsky et al., 2005; Sherwood, 1996):

$$f = q_s(T^*)/q_0 \tag{1.4}$$

where q_0 is the initial humidity of air parcel in the air source and q_s is the saturation

specific humidity, function of temperature following the Clausius-Clapeyron relationship. The temperature during the last condensation event is not easy to estimate directly, because it depends on the altitude of the last cloud that the air mass has encountered. It can be deduced from the specific humidity at the surface, q, assuming that the air subsides adiabatically from the altitude of last condensation down to the surface. In this case, $q_s(T^*) = q$. The specific humidity at the surface is a function of relative humidity, *rh*, and of saturation specific humidity at the surface temperature:

$$q = rh \cdot q_s(T_s) \tag{1.5}$$

where T_s is the surface air temperature.

The saturation specific humidity $q_s(T_s)$ can be calculated using saturation vapor pressure of water es and pressure p (in hPa):

$$q_s(T_s) = 0,622 \cdot es(T_s)/p \tag{1.6}$$

The saturation vapor pressure (es) is calculated using August-Roche-Magnus formula, using temperature T_s in Celsius:

$$es(T_s) = 6.1094 \cdot exp((17.625 * T_s)/(T_s + 243.04)) \tag{1.7}$$

These equations show that the final isotopic composition of vapor largely depends on the initial composition of vapor, but also on the initial specific humidity (q_0). According to the Rayleigh distillation, the main factor controlling the isotopic composition is *f*, which is controlled by temperature according to the Clausius-Clapeyron relation. This explains, in first order, the zonal distribution of the isotopic composition, but also precipitations depletion that is observed at high altitude (altitude effect) (see Section 3.1).

Figure 1.10 shows the isotopic composition of vapor and precipitation during simple Rayleigh distillation process.

In Section 3.1 we give more details on the present-day controlling factors on $\delta^{18}O_p$. In our article published in *Climate of the Past* (Section 3.4) we investigate the factors controlling $\delta^{18}O_p$ over Asia through the Cenozoic, in particular, we aim to answer the question to what instant the Rayleigh distillation (and the temperature) may explain paleo isotopic variations.

Observations of present-day spatial distribution of $\delta^{18}O$

Stable water isotopes have been measured in water samples (rain, ocean surface, polar snow, lakes or rivers) since the early 1950s (Dansgaard, 1953, 1964). The Global Network of Isotopes in Precipitation (GNIP) was initiated in 1958 by International Atomic Energy Agency (IAEA) and World Meteorological Organization (WMO), and became operational in 1961. Global annual mean $\delta^{18}O_p$ in precipitation interpolation from about 700 GNIP stations is shown on Fig. 1.11.

In order to augment the number of GNIP stations, regional networks for $\delta^{18}O_p$ measurements have been created. For example, The Institute of Tibetan Plateau Research in

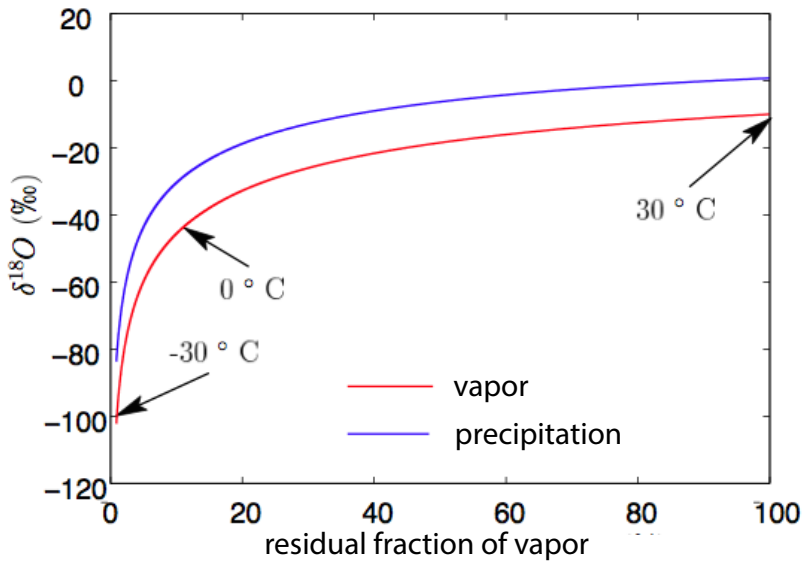

Figure 1.10 – Evolution of $\delta^{18}O$ in vapor and precipitation in a single air mass following the Rayleigh distillation. Figure modified from (Risi, 2009).

China has established a continuous observation network of $\delta^{18}O_p$ on the Tibetan Plateau (eg. Liu et al., 2010; Tian et al., 2007).

Isotopic composition of tropospheric water vapor is also available from satellite observations, such as Tropospheric Emission Spectrometer (TES) aboard the Aura spacecraft.

Application of stable oxygen isotopes

"Classical" paleoaltimetry based on stable oxygen isotopes in precipitation. Among the methods developed to constrain the altitudinal history of orogenic areas, stable isotope-based paleoaltimetry is probably the most widely used. This approach is based on the sensitivity of $\delta^{18}O_p$ on the temperature (elevation) according the Rayleigh distillation. Studies using oxygen isotopes take advantage of strong sensitivity of $\delta^{18}O_p$ values to elevation change to reconstruct paleoelevation.

For reconstructing paleoelevation usually two steps are required:

First, oxygen isotopic ratios are measured in so-called paleoaltimetry archives, lactrusine or soil carbonates ($\delta^{18}O_c$) and are related to $\delta^{18}O$ in paleoprecipitation ($\delta^{18}O_{pp}$) using Kim and O'Neil relationship (Kim and O'Neil, 1997)[3]:

$$\delta^{18}O_{pp}(\text{SMOW}) = \delta^{18}O_c(\text{PDF}) - 18.03(10^3 * T^{-1}) + 32.42 \quad (1.8)$$

where T is the temperature of carbonate formation. This equation admit an assumption of equilibrium between water and calcite:

[3]this equation is commonly used for lacustrine and paleosols carbonate, for biogenic carbonate (for example, from shells of gastropods or bivalves) fractionation factors from Grossman and Ku (1986) should be applied

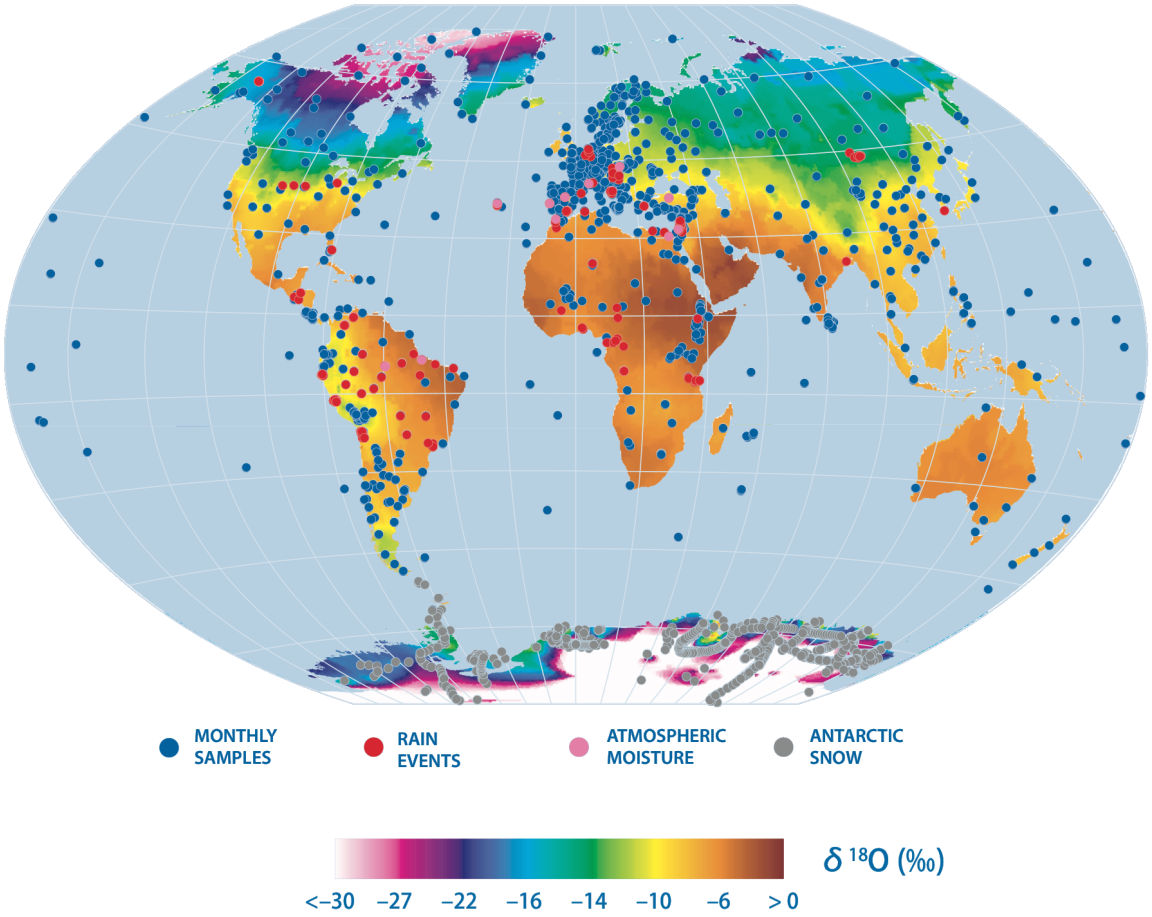

Figure 1.11 – Global distribution of $\delta^{18}O$ (per mil, ‰) in precipitation produced by interpolation of long-term annual means from about 700 GNIP stations. Figure retrieved from (Elbaradei, 2013)

$$1000 ln\alpha(Calcite - H_2O) \simeq \delta^{18}O_c(\text{SMOW}) - \delta^{18}O_w(\text{SMOW}) \tag{1.9}$$

where α is the fractionation factor.

Second, this $\delta^{18}O$-elevation relationship is related to reference isotopic values from low-elevated point. $\delta^{18}O$-elevation relationships have been calibrated both empirically (e.g. Garzione et al., 2000a; Poage and Chamberlain, 2001) and theoretically using basic thermodynamic principles that govern isotopic fractionation of an ascending vapor mass (Rowley and Garzione, 2007; Rowley et al., 2001). Present-day meteoric water $\delta^{18}O$ measured in major mountain regions has a good correlation with the mean global lapse rate of 2.8‰ km^{-1} (Poage and Chamberlain, 2001) (for more details see Section 3.2).

However, this "classic" paleoaltimetry technique has some limitations, because $\delta^{18}O_c$ is not a simple temperature proxy and reflects the isotopic interaction between dissolved carbonate species and water, $CaCO_3$ actually records the isotopic signature of the water with a temperature-dependent offset, reflecting the isotopic fractionation in this reaction. Thus, for relevant paleoaltimetry reconstruction the temperature of carbonate formation should be known. See Section 1.3.5 for more on limits of stable oxygen-based paleoaltimetry approach, including limits associated with with paleotemperature uncertainty and uncertainty of processes that govern the $\delta^{18}O_p$ in the past.

Use of silicates for stable isotopes paleoaltimetry. In addition to carbonate archives, modern studies widely use silicate rocks (such as smectite, kaolinite, chert, as well as metamorphic minerals that grow in the presence of meteoric waters) for stable isotopes paleoaltimetry (Mulch and Chamberlain, 2007). This technique has several advantages: 1) silicate rocks provide both a hydrogen and oxygen isotope records that allows to estimate the evaporative effects on meteoric waters prior to mineral formation and 2) hydrogen ratios, derived from micas of shear zones which reflect the isotopic composition of waters infiltrated into this weak zone during the last stage of orogenesis. This technique allows to use the isotopic ratios and age constrains from the same mineral grain.

Clumped isotope thermometry. Traditionally, paleoclimate reconstructions have been based on oxygen isotopes ($\delta^{18}O$) in the calcium carbonate ($CaCO_3$) form paleosoils, laces or shells, as we have shown in previous sections. Carbonate clumped isotope thermometry is a relatively new technique based on measurements of the degree of order of ^{13}C and ^{18}O into bonds with each other (making the $^{13}C\ ^{18}O\ ^{16}O_2{}^{-2}$ ion group) in carbonate minerals (Eiler, 2011). Clumped isotope thermometry allows to reconstruct isotopic ratios and the temperature of carbonate formation at the same time (Huntington and Lechler, 2015).

1.3.4 Other techniques of paleoelevation reconstructions

Besides paleoaltimetry technique listed previously, there are some other methods, less abundant, but perspective. There are new techniques based on vesicular basalt (e.g. Sahagian and Proussevitch, 2007), hydrous silicates and glass (e.g. Mulch and Chamberlain, 2007), biogenic apatite (e.g Kohn and Dettman, 2007) or molecular biomarkers (Polissar et al., 2009).

1.3.5 Limits in paleoelevations reconstructions

Whereas paleoaltimetry techniques using different terrestrial archives are widely applied, these methods have their own limits. For example, uncertainty of paleobotanic methods is mainly linked with the large geographic variation in mean annual temperature (MAT) and lapse rates (Forest et al., 1999).

However, in this thesis we are interested mainly in stable oxygen isotopes-based techniques. In addition to analytical uncertainties linked with measuring of $\delta^{18}O$ (which are relatively small (Blisniuk and Stern, 2005)), the physical interpretation of stable oxygen isotopic signal is complicated by several factors:

- **Isotopic lapse rates spatial and temporal variations.** Present-day meteoric water $\delta^{18}O$ measured in major mountain regions has a good correlation with the mean global lapse rate of 2.8 ‰ km^{-1} (Poage and Chamberlain, 2001). However, in more detail consideration, precipitation $\delta^{18}O$ lapse rate shows significant spatial variations. For example, the isotopic lapse rates on the windward side of the Sierra Nevada are 3.1 ‰ km^{-1} in the Southern Sierra, but deviate to 0.9 ‰ km^{-1} in the

lee side and to 0.2 ‰ km^{-1} in the interior of the Great Basin (Mulch, 2016). On the other hand, carbonate $\delta^{18}O$ is usually related to topography change using modern isotopic lapse rates (either from modern measurements or theory) because of the absence of knowledge about past isotopic lapse rates (e.g. Currie et al., 2005; Cyr et al., 2005; Garzione et al., 2000b; Hoke et al., 2014; Rowley and Currie, 2006). In the absence of direct measurements of "paleo" lapse rate *in situ*, using stable isotopes paleoaltimetry methods have potential issues on two fronts: (i) the presumed constancy of isotopic lapse rates through time, and (ii) the consequences of global climate change on regional climate variables (Kohn and Dettman, 2007).

- **Uncertainties in paleoclimate**. Since the isotopic ratios in precipitation and their lapse rates are controlled by such factors as temperature, precipitation amount, relative humidity, provenance and mixing of moisture, etc. (see Chapter 3), our limited knowledge on paleoclimate may have a significant impact on paleoelevations reconstructions relevance. For example, knowledge about paleotemperatures and temperature lapse rates is important not only for paleoprecipitation isotopic composition reconstruction (applying temperature-dependent Kim and O'Nail equation (Kim and O'Neil, 1997)), but also for reconstructing paleo lapse rates. For the Andes, not considering the impact of uplift on climate dynamics and related $\delta^{18}O$ values has been shown to produce errors in paleoelevation reconstruction reaching up to ± 50 % (Ehlers and Poulsen, 2009; Poulsen et al., 2010). In regions characterized by monsoonal climates, the predominance of the amount effect on the isotopic composition of precipitation may lead to increasing isotopic lapse rates as the result of higher precipitation rates (Gonfiantini et al., 2001), thus paleo-monsoons studies are indispensable.

- **Robustness of processes that govern $\delta^{18}O$ today in application for paleo epochs.** One of the major limitations linked with empirical paleoelevations reconstructions is the assumption that the isotopic signal is controlled by climate variables (e.g. temperature) in a uniform way throughout the entire proxy record (Sturm et al., 2010). For example, the isotopic fractionation efficiency and since isotopic distributions in warm environment may be notably different from present-day one (See the Chapter 4).

- **Potential diagenetic alteration of carbonates.** Diagenesis of carbonate minerals can significantly alter both carbon and oxygen isotope values during recrystallization, shifting $\delta^{18}O_c$ to less negative values (Kent-Corson et al., 2009). However, degree of alteration is difficult to evaluate, that increase the uncertainty in paleoelevation studies.

In order to reduce uncertainties associated, multiproxy approaches should be applied. For example, paleotemperature uncertainty in paleo $\delta^{18}O$ may be reduced if independent constraints on paleotemperatures are available, such as paleotemperature estimates based on studies of leaf physiognomy (Spicer et al., 2003) or clumped isotope thermometry (Eiler, 2011), which allows retrieving $\delta^{18}O_c$ and temperature of carbonate formation at the same time. In addition, numerical modeling may help to increase reconstructions

reliability. In this thesis we address several issues linked with stable oxygen based paleoaltimetry and use model-data approach in order to increase relevance of paleoaltimetry estimates (see the main purposes of this thesis in Section 1.4 and Chapter 5 in particular).

1.3.6 Paleoaltimetry of Himalayas and Tibetan Plateau

Here we review Cenozoic paleoelevations of the HTP inferred from quantitative and semi-quantitative approaches. Those studies that do not present quantitative paleoelevation estimates that are cited in this section do provide constraints on the evolution of the monsoon climate as indirect evidence for the presence of a large and highly elevated Tibetan Plateau. Summary of these studies could be found in the Table 1.1. Locations of paleoelevation studies based on different natural archives for various periods through the Cenozoic are presented on Figure 1.12. Spatial and temporal variations of reconstructed paleoelevations from published data are summarized on Figure 1.13.

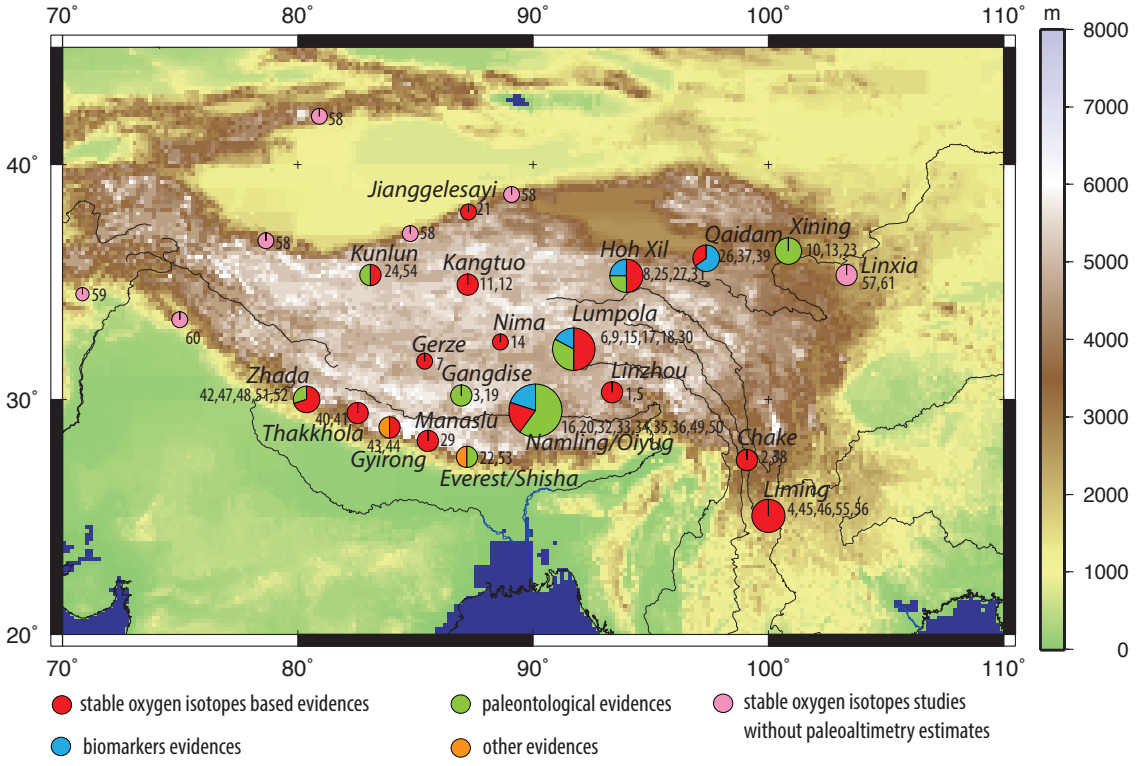

Figure 1.12 – Topographic map of the Himalayas and Tibetan Plateau with locations for which quantitative paleoelevations studies have been published for different periods through the Cenozoic (see the Table 1.1). The color of circles shows the method of paleoelevations reconstructions. The size of circles represent the number of studies for a particular location. Numbers correspond to cited in the Table 1.1 papers. Additional numbers (57-60) correspond to stable oxygen isotopes studies without attempts to reconstruct paleoelevations: 57) (Fan et al., 2007); 58) (Kent-Corson et al., 2009); 59) (Quade and Cerling, 1995; Quade et al., 1992; Stern et al., 1997); 60) (Dettman et al., 2001; Sanyal et al., 2004a), 61) (Dettman et al., 2003)

Late Cretaceous - Paleocene

Elevations of the TP prior to the collision are uncertain and quantitative studies are lacking. Timing of the collision onset in the region is uncertain (see Section 1.2.2) and the magnitude of syn-collisional uplift has never been estimated quantitatively. However, for this time period, presence of Andes-type orogen in the south of Asia over Tethyan subduction zone was hypothesized. Yin and Harrison (2000) also indicate that it is unlike that such spectacular event as Indo-Asian collision would not result in significant surface uplift. Ding et al. (2014) infer high elevation (4500 ± 500 m) of the TP at 60-54 Ma, based on lacustrine carbonates of Linzhou Basin (Figure 1.13, Table 1.1).

Eocene

Most geological studies suggest a massive uplift of the HTP started shortly after the collision (Mulch and Chamberlain, 2006). However, quantitative studies show a wide range of paleoelevations estimates (Figure 1.13, subplot A).

Paleoelevations reconstruction of the Lunpola basin, in the center HTP, indicate that this part of Tibet reached 4000 m at latest ~35 Ma (Rowley and Currie, 2006). A similar result (elevations of 4000 ± 500) was found in the Linzhou basin in central Tibet based on $\delta^{18}O$ from paleosoils and fossil ostracodes (Ding et al., 2014). Extremely high Eocene elevations (~5000 m) are also reported for the Northern Tibet (Xu et al., 2013). However, (Cyr et al., 2005) infer elevations of 2000 +850/-1050 for Fenghuoshan group in the Northern Tibet at ~37 Ma. Interestingly, in a recent study, Wei et al. (2016) report close to sea-level elevations for Gerze Basin (Central Tibet) at ~39 Ma based on stable oxygen isotopic evidences.

Eocene elevations of about 3000 m are reported by (Song et al., 2010) based on fossil pollen records. Nevertheless, these elevations are significantly lower than those predicted by $\delta^{18}O$-paleoaltimetry (e.g. Ding et al., 2014; Rowley and Currie, 2006). Note, however, that the pollen used here represents only one location in the Lunpola Basin and the age constraint cannot be resolved more precisely than to assign an Eocene age. Palynological assemblages in lacustrine sediments from the Xining basin (north-eastern HTP) show the presence of high-altitude (2000-3000 m) vegetation, confirming the occurrence of regional uplift as early as 38 Ma (Dupont-Nivet et al., 2008). Pollen evidences from Xining basin from 33-46 Ma sediments also show near present-day (~2000 m) elevations at that time (Hoorn et al., 2012).

In general, an early uplift of the HTP (~40 to 35 Ma) is in agreement with the shift in ocean global geochemistry ($^{87}Sr/^{86}Sr$ isotope ratio) in marine carbonate records, that is interpreted as an enhanced silicate weathering in a response of massive orogenic uplift (Raymo and Ruddiman, 1992). Also, a significant increase in clastic sedimentation offshore around south-eastern Asia corresponds to this time frame (Potter and Szatmari, 2009).

Modest Eocene elevations (not higher than 3000 m) are consistent with the hypothesis that uplift of at least some parts of the HTP followed two pulses of tectonic activity in the Oligocene (around 30-25 Ma) (Wang et al., 2012a) and Miocene (10-15 Ma) (Blis-

niuk et al., 2001; Harris, 2006), reflecting distinct mechanisms of crustal thickening (Wang et al., 2012a) and the convective removal of the lower portion of the thickened Asian lithosphere (Chung et al., 2005; Molnar et al., 1993).

Thus, the early uplift history of the HTP remains controversial: from a near sea surface Plateau to high Eocene elevations, consequently the early uplift history of the HTP need to be reviewed.

Oligocene

There are few quantitative estimates of Oligocene elevation over the HTP. However, most of them indicate high elevations at this time period. DeCelles et al. (2007) rapport Oligocene (26 Ma) elevations of 4500-5000 for the Nima basin in the central Tibet. Similar high topography (4100 +1200/-1600 m) has been induced based on isotopic proxies for the Oiyug basin (Currie et al., 2016). However, paleoelevations retrieved based on biomarkers (Jia et al., 2015) and paleontological evidences (Sun et al., 2014) for the Lumpola basin are lower (~3000 m) (Figure 1.13, Table 1.1).

DeCelles et al. (2007) found that central Tibet had reached a high paleoelevation of 4.5–5 km by 26 Ma through stable isotope analyses of paleosol carbonate. By presenting geologic and geophysical data from north-central TP, including magnetostratigraphy, sedimentology, paleocurrent measurements, $^{40}Ar/^{39}Ar$ and fission-track studies, (Wang et al., 2008b) show that the central Plateau was elevated 40 Ma ago, and the regions south and north of the central Plateau gained a high elevation significantly later.

It is widely accepted, that during the Oligocene the uplift progressed particularly northward and southward causing the extension of the TP (e.g. Mulch and Chamberlain, 2006). Among other evidence, a magnetostratigraphic study of Tertiary sediments indicates that the start of the uplift of the north Qaidam Block at ~30 Ma (Sun et al., 2005).

Miocene

Number of paleoelevations estimates increases for recent time periods and for the Miocene a lot of paleoelevations estimates from various natural archives are available (Figure 1.13, Table 1.1). Quantitative studies for the southern HTP evidence, with few exceptions, that southern parts of this orogen likely reached an elevation comparable to present-day one by Mid to Late Miocene (between 15 and 5 Ma) (Figure 1.13).

Direct evidence of the Miocene high surface elevation (5300 +430/-520) comes from the oxygen isotope composition of carbonates deposited in the Thakkhola graben as early as 11 Ma in the southern part of the Tibetan plateau (Garzione et al., 2000b). This is also consistent with the results of work by Rowley et al. (2001), where the changes in the isotopic composition of Himalayan precipitation with elevation using one-dimensional model based on Rayleigh distillation process are modeled and elevations of ~4500 m for Thakkhola graben at 10 Ma have been inferred.

There is an evidence (inferred from a multiproxy study based on $\delta^{18}O$ from fossil molusks and paleobotanical estimates) that the elevation of the Zhada basin, located near the southern margin of the HTP, reached a mean elevation of ~4000 - 4500 m. during the

Miocene (Saylor et al., 2009). Based on this results Saylor et al. (2009) indicates a potential 'collapse' of certain areas of the HTP due to crustal extensions or other (relaxing) tectonic processes. However, Murphy et al. (2009) based on measurement of $\delta^{18}O$ from gastropod shells reconstruct late Miocene elevations of Zhada basin of about 1500 m.

Further east in the Himalayan foreland of Nepal, Dettman et al. (2001) estimated the $\delta^{18}O$ of paleoprecipitation from authigenic minerals contained in 13 Ma to recent fluvial and flood-plain deposits of Siwalik Group sediments. Assuming a broad range of reasonable paleotemperature estimates from floral assemblages, Dettman et al. (2001) estimated that the shells formed in water with $\delta^{18}O$ values from 12 to 7 ‰. This high variability has been interpreted as evidence for strong seasonal $\delta^{18}O$ variations in surface waters due to a pronounced monsoon climate, implying the presence of a high and broad Tibetan plateau by 10.7 Ma.

This increase in the $\delta^{18}O$ values of authigenic minerals at ~8 Ma has been interpreted as the result of rapid uplift of the Himalayas and Tibetan Plateau, leading to increased aridity and greater soil water evaporation due to monsoon strengthening (Quade et al., 1989; Quade and Cerling, 1995), or to a change in the main moisture source area for the studied region by the rising orogen cutting off low-$\delta^{18}O_p$ from the North (Quade and Cerling, 1995; Stern et al., 1997). The earliest stable isotope studies used to infer climate changes related to the evolution of the TP are from Neogene Siwalik Group molasse deposits in the Himalayan foreland of NW-Pakistan. The $\delta^{18}O$ values of pedogenic carbonate nodules and smectite show to 4 permil increase at ~8 Ma (Quade et al., 1989; Quade and Cerling, 1995; Stern et al., 1997).

Estimates for the Gyirong Basin of the Himalayas are also controversial. Rowley and Garzione (2007) report high elevations of 5000 +480/-600 for at leas 7 Ma, while Wang and Ding (2006) infer much more modest elevations (2900-3400 m) for the same time period. Nearby Manaslu Basin shows high elevations of ~6000 m already at 20 Ma (France-Lanord et al., 1988; Rowley and Garzione, 2007) which are similar to the elevations reported for the Mount Everest region (Gébelin et al., 2013).

The research on the Oiyug basin indicates that the southern TP achieved paleoelevations of 5200 +1330/–630 m at least 15 Ma (Currie et al., 2005). This result is consistent with elevations reported in recent multiproxy research of Currie et al. (2016), where elevations of 5100-5400 m are reported. Miocene elevations of nearby Namling basin are also reconstructed to be high (4689 ± 895 m or 4838 ± 847 m) based on paleobotanic and climate modeling study (Spicer et al., 2003). However, Zhou et al. (2007) reveal lower (2500-3000 m) Miocene elevations for the same locations based on fossil floras.

Isotopic analysis of the Miocene Lunpola Basin (central Tibet) lacustrine marles and limestones yielded altitude estimates of 4260 +475/-575 m (Rowley and Currie, 2006). However, Deng et al. (2012) report elevations of 3000 m for the Lumpola Basin for 18-16 Ma based on mammalians fossils analysis.

Song et al. (2010) derive the mid Miocene (10 Ma) altitudes of Gangdise-Nyainquntanglha Area in the central Tibet between 3000 m and 3150 m based on pollen evidence. These Miocene altitude estimates were lower than those obtained from both leaf physiognomy (Spicer et al., 2003) and oxygen isotopes (Currie et al., 2005) by around 1500 m.

For the northern Tibet,the Miocene elevations have been reconstructed from the Hoh Xil Basin. Based on isotopic evidence from lacustrine carbonates, Wu et al. (2007a) reconstruct Early-Middle Miocene elevations of ~3500 m. This value is consistent with that reported for the same location by Polissar et al. (2009). However, based on paleobotanical evidence Sun et al. (2015) report much lower (1395-2931 m) elevation for this locations at ~17 Ma.

Qaidam Eocene Basin have been shown to have modest elevations since at least Miocene (Wu et al., 2007a). These authors report elevations of ~2500 m based on isotopic evidence. Zhuang et al. (2014) based on leaf wax stable isotopes reveal elevations of 1900 m from 15 Ma sediments and ~4000 m elevations fro ~10.4 Ma, that indicated a rapid uplift of Qaidam Block in the Miocene. However, analysis of pollen from nearby Xining basin show that this terrain was highly elevated since the Early Miocene (Deng et al., 2012).

Dettman et al. (2003) studied the stable isotope composition of authigenic minerals in a nearly continuous sequence of fluvial and lacustrine deposits covering an age range from 29 Ma into the Holocene from the Linxia Basin. These authors do not directly reconstruct paleoelevations, but indicate a shift in a contineous carbonate record to higher $\delta^{18}O$ values at approximately 13 to 12 Ma. This shift is interpreted as an increase in aridity at that time resulting from the uplift of the Tibetan Plateau, or some portion of it, to elevations high enough to limit the supply of moisture from the Indian or the Pacific Ocean (Dettman et al., 2003).

The elevations reconstructions from the Kunlun mountains are particulary important for understanding the evolution of the Northern Tibet. Deng et al. (2012) indicate that in the Early Eocene, Kunlun has been already high, with mean elevations of 3500-4000 m.

Pliocene-Quaternary

Latest geologic records show that, the central and southern TP probably had approached to the modern height before the Pliocene. Since the Pliocene, the uplift has mainly occurred in the northern Plateau (Mulch and Chamberlain, 2006).

Most studies report near present-day elevations in the Zhada Basin of the western Himalayas (Huntington and Lechler, 2015; Wang et al., 2013), with an exception of Deng (2013), in most investigations lower elevations (~4000) are reported. Hsu et al. (1973) reveal abrupt uplift (of about 3000 m) in the Shisha Mount regions since middle-late Pliocene.

In the Pliocene, the Oiyug Basin was highly elevated (~5500 m) (Currie et al., 2016), however, estimated uncertainty of this measurement is high (of about 1500-2000 m). For the Namling Basin, Zhou et al. (2007) report modest elevations of 2500-3500 m, which corresponds to 2200-3400 m regional uplift since the Pliocene.

Significant uplift of the northern Tibet during the last ~2-3 Ma has been reconstructed with stable oxygen isotopes measurements from fossil fauna (Wang et al., 2008d). Over the Naga Hills Pliocene elevations are similar to those of present-day (Hoke et al., 2014).

Table 1.1 – Cenozoic elevations reconstructions for the Himalayas and Tibetan Plateau region from published data

No [4]	Locality	Age	Method used	Paleoelevation reconstructed [5]	Reference
			Paleocene		
(1)	Linzhou Basin, Nianbo Formation	60-54 Ma	$\delta^{18}O$ from lacustrine and paleosoil carbonates	4500+400/-400 m	Ding et al. (2014)
			Eocene		
(2)	Chake	Eocene	$\delta^{18}O$ from pedogenic carbonates	121 ± 700 m	Hoke et al. (2014)
(3)	Gangdise-Nyainqentanglha Area	Eocene	pollen and climate modeling	3295–3495 m	Song et al. (2010)
(4)	Liming	Eocene	$\delta^{18}O$ from pedogenic carbonates	2650 ± 300 m	Hoke et al. (2014)
(5)	Linzhou Basin, Pana Formation	51-48 Ma	$\delta^{18}O$ from paleosoils and ostracodes	4000 ± 500 m	Ding et al. (2014)
(6)	Lumpola basin, middle Niubao Formation	~39 Ma	$\delta^{18}O$ from lacustrine and paleosoil carbonates	4050+510/-620 m	Rowley and Currie (2006)
(7)	Gerze Basin	~39 Ma	$\delta^{18}O$ from limestone and foraminifera fossil	close to sea level	Wei et al. (2016)
(8)	Fenghuoshan Group	~37 Ma	$\delta^{18}O$ from lacustrine carbonates	2000+850/-1050 m	Cyr et al. (2005)
(9)	Lumpola basin, upper Niubao Formation	~35 Ma	$\delta^{18}O$ from lacustrine and paleosoil carbonates	4850+380/-460 m	Rowley and Currie (2006)
(10)	Xining Basin	33-36 Ma	pollen	~2000 m (near present-day elevations)	Hoorn et al. (2012)
(11)	Kangtuo	28-51 Ma	$\delta^{18}O$ from lacustrine and paleosoil carbonates	5165 ± 593 m	Xu et al. (2013)
(12)	Saonahu	28-51 Ma	$\delta^{18}O$ from lacustrine and paleosoil carbonates	4923 ± 361 m	Xu et al. (2013)

[4] Numbers correspond to those on Figure 1.12

[5] here we refer to the peleoelevation and error estimates from the original paper and does not ague where these reconstructions are correct

(13)	Xining Basin	prior to Oligocene	pollen	2000-3000 m	Dupont-Nivet et al. (2008)
			Oligocene		
(14)	Nima basin of central Tibet	26 Ma	$\delta^{18}O$ from paleosol carbonate	4500-5000 m	DeCelles et al. (2007)
(15)	Lunpola basin	25.5 to 21.6 Ma	$\delta^{13}C$ and δD from leaf wax n-alkanes	~3000 m	Jia et al. (2015)
(16)	Oiyug Basin	Late Oligocene-middle Miocene	$\delta^{18}O$ and δD multi-proxy	4100 +1200/-1600 m	Currie et al. (2016)
(17)	Lunpola basin	Late Oligocene-early Miocene	fossil pollen records	~3190 ± 100 m	Sun et al. (2014)
			Miocene		
(18)	Lumpola basin, Dingquig Formation	Miocene	$\delta^{18}O$ from lacustrine marles and limestones	4260+475/-575 m	Rowley and Currie (2006)
(19)	Gangdise-Nyainqentanglha Area	Miocene	pollen and climate modeling	3000–3150 m	Song et al. (2010)
(20)	Namling Basin	Miocene	fossil floras	2500-3000 m, (1300 m uplift)	Zhou et al. (2007)
(21)	Jianggelesayi	Early Miocene	$\delta^{18}O$ and $\delta^{13}O$ in fluvial and lacustrine carbonates	< 1500 m	Chen et al. (2002)
(22)	Mount Everest region	Early Miocene	δD of hydrous minerals	elevations similar to modern	Gébelin et al. (2013)
(23)	Xining-Minhe basin	Early Miocene	pollen	4000-4500 m	Deng et al. (2012)
(24)	Kunlun Mountains	Early Miocene	pollen	3500-4000 m	Deng et al. (2012)
(25)	Wudaoliang Basin and Kunlun Mts.	Early-Middle Miocene	$\delta^{18}O$ and $\delta^{13}C$ from lacustrine carbonates	~3500 m	Wu et al. (2007b)

(26)	Qaidam Basin	Early-Middle Miocene	$\delta^{18}O$ and $\delta^{13}C$ from lacustrine carbonates	~2500 m	Wu et al. (2007b)
(27)	Wudaoliang	20 Ma	D/H from biomarkers	~4000 m	Polissar et al. (2009)
(29)	Manaslu and Chokang Arm (Himalayas)	20 Ma	$\delta^{18}O$ and δD from igneous and metamorphic rock	2500-6000 m	France-Lanord et al. (1988)
(30)	Lunpola Basin	18–16 Ma	based on mammalian fossils	3000 m	Deng et al. (2012)
(31)	Wudaoliang Basin	~17 Ma	palaeobotanical evidences	1395-2931 m (2000-3000 m uplift)	Sun et al. (2015)
(32)	Oiyug Basin	15,1	$\delta^{18}O$ from carbonates	5200+340/-390 m	Currie et al. (2005)
(33)	Namling basin	15 Ma	Paleobotanic and climate modeling study	4689 ± 895 m	Spicer et al. (2003)
(34)	Namling basin	15 Ma	Paleobotanic and climate modeling study	4838 ± 847 m	Spicer et al. (2003)
(35)	Oiyug Basin	~15 Ma	plant-wax *n*-alkenes δD and $\delta^{18}O$ from lacustrine siderite	5100 +1300/-1900 m	Currie et al. (2016)
(36)	Oiyug Basin	~15 Ma	fossil-floral physiognomy	5400 m	Currie et al. (2016)
(37)	Qaidam basin	~15 Ma	leaf wax stable isotopes	1900 m	Zhuang et al. (2014)
(38)	Juanchuan	Middle Miocene	$\delta^{18}O$ from pedogenic carbonates	3300 ± 500 m	Hoke et al. (2014)
(39)	Qaidam basin	~ 10.4 Ma	leaf wax stable isotopes	~4000 m	Zhuang et al. (2014)
(40)	Takkhola Graben	0-10 Ma	$\delta^{18}O$ from paleosoils	5300 +430/-520 m	Garzione et al. (2000b)
(41)	Thakkhola Graben	10 Ma	$\delta^{18}O$ from carbonates	~4500 m	Rowley et al. (2001)
(42)	Zhada Basin	9 Ma	$\delta^{18}O$ from fossil mollusks and paleobotanical	4000-4500 m	Saylor et al. (2009)
(43)	Gyirong Basin (High Himalayas)	~7 Ma	$\delta^{13}C$ from fossil fauna	2900–3400 m	Wang et al. (2006)

(44)	Gyirong (Himalayas)	≤ 7 Ma	$\delta^{18}O$ from carbonates	5000 +480/-600	Rowley et al. (2001)
(45)	Luhe	Late Miocene	$\delta^{18}O$ from pedogenic carbonates	1000 ± 800 m	Hoke et al. (2014)
(46)	Lanping	Late Miocene	$\delta^{18}O$ from pedogenic carbonates	3300 ± 450 m	Hoke et al. (2014)
(47)	Zada basin	Late Miocene	$\delta^{18}O$ from gastropod shells	1500 m	Murphy et al. (2009)
			Pliocene-Quaternary		
(48)	Zhada Basin	late Miocene-Pliocene	carbonate clumped isotope thermometry	5400 ± 500 m	(Huntington et al., 2015)
(49)	Xixabangma and Namling Basin	Pliocene	fossil floras	2500-3500 m, (2200-3400 uplift)	Zhou et al. (2007)
(50)	Oiyug Basin	~5 Ma	plant-wax *n*-alkenes	5500 +1400/-2000 m	Currie et al. (2016)
(51)	Zanda Basin	4.6 Ma	based on mammalian fossils	~4000	Deng (2013)
(52)	Zanda (Zhada) Basin	4.2–3.1 Ma	$\delta^{13}C$ from fossil fauna	similar to present-day elevations	Wang et al. (2013)
(53)	Mount Shisha Pangma	middle-late Pliocene	paleobotany	2500 m (3000 uplift)	Hsu et al. (1973)
(54)	Kunlun Mountain Pass area	~2–3 Ma	$\delta^{18}O$ from fossil fauna	2000 ± 1600 m (2600 ± 1600 m uplift)	Wang et al. (2008d)
(55)	Yanyuan	Pliocene-Quaternary	$\delta^{18}O$ from pedogenic carbonates	2400 ± 1100 m	(Hoke et al., 2014)
(56)	Eryuan	Pliocene-Quaternary	$\delta^{18}O$ from pedogenic carbonates	2750 ± 700 m	(Hoke et al., 2014)

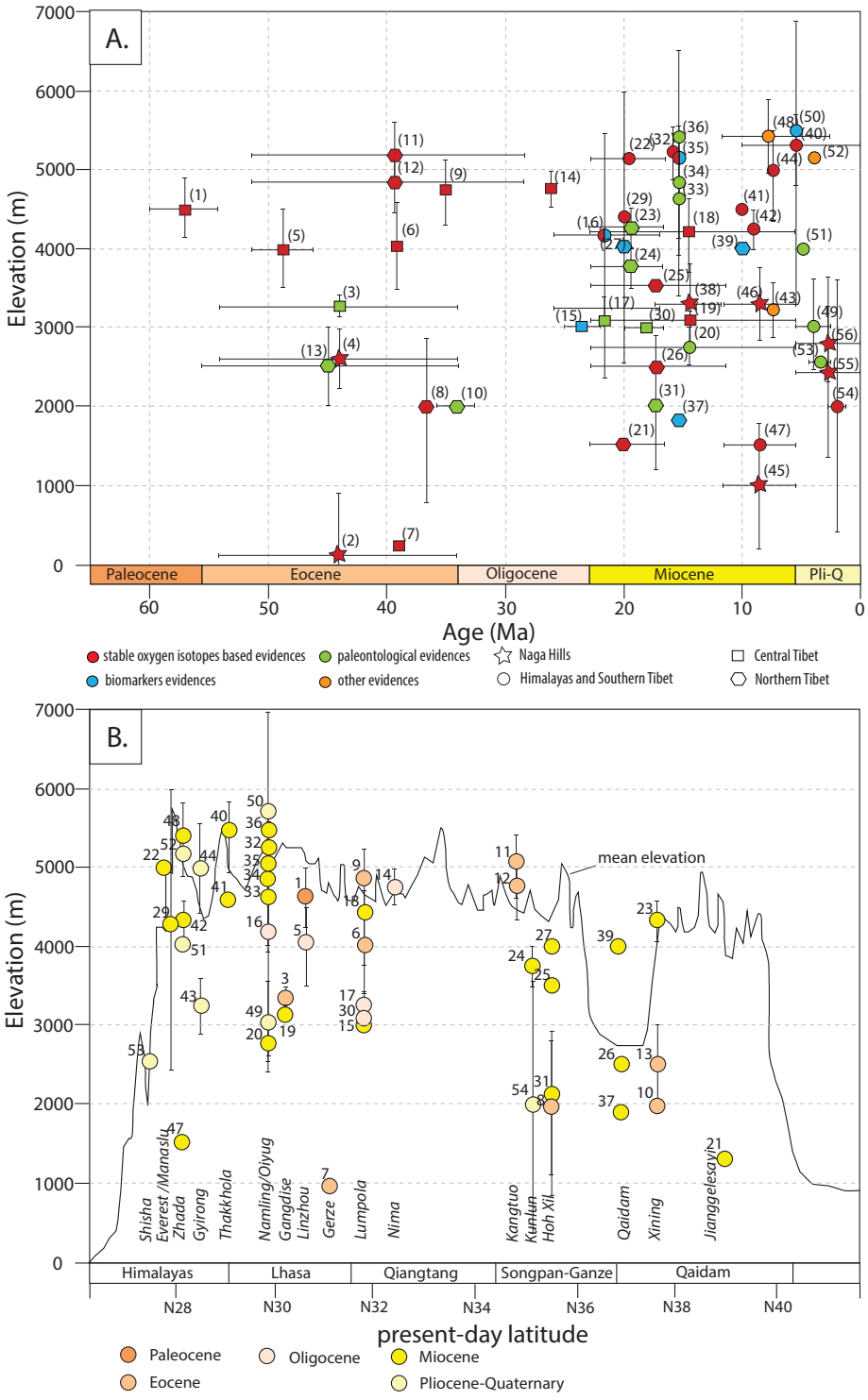

Figure 1.13 – A) Summary of paleoelevaition evolution of the Himalayas and Tibetan Plateau region based on published quantitative estimates (see the compilation in the Table 1.1). Color shows the type of archive: red - stable oxygen isotopes evidences, green - palentological evidences, blue - biomarkers evidences, orange - other evidences. Geometry shows the location of sampling: stars - the Naga Hills (Liming and Chake basins), circles - the Himalayas and the Southern Tibet (Nanling, Oiyug, Zhada, Thakkhola, Gyirong, Everest, and Shisha basins); rectangles - the Central Tibet (Gangdise, Linzhou, Gerze, Nima, and Lumpola basins) polygons - the Northern Tibet (Kunlun, Kangtuo, Hoh Xil, Qaidam, Xining, Linxia, and Jianggelesayi basins). B) The S-N trending transect of the Himalayas and Tibetan Plateau. Ages are shown with different colors. Numbers on both figures corresponds to those in the Table 1.1 and on Figure 1.12.

1.4 Summary and main purpose of the thesis

In this introductory section, we show, first, to what extant geological evolution of the Earth surface may impact climates. It has been shown that the uplift of mountain belts has strong effects on global and regional climate patterns and processes including glaciation, rain shadow effect, stationary waves, monsoon circulation, oceanic currents and even the chemical composition of the atmosphere. Shifting of continents and land-sea distribution has also been hypothesized to have major influence on the climate patterns, despite the lack of studies on this subject.

The Himalayas and Tibetan Plateau are the most spectacular mountain building in the world with mean elevation of about 5000 meters and area of more then 1,3 million km^2. Based on geological evidence, high Asian topography has been formed as a response to multiple tectonic events during the Cenozoic, which timing and rate are widely discussed are the literature.

The Himalayas and Tibetan Plateau region has long been a focus of numerous studies, especially linked with extreme topography-climate interaction. Quantitative constraints on topographic development could, on the one hand, serve as direct means of testing tectonic models for Tibetan Plateau, and on the other, could be used as a boundary condition for climate models as and the uplift of the HTP is supposed to be responsible on major climate changes, including the appearance of the monsoonal system in East Asia, the onset of central Asian desertification as well as the global cooling through reducing the atmospheric CO_2 concentration by chemical weathering through the Cenozoic.

Quantitative estimation of the role of the HTP in Cenozoic climate change is still challengeable. In order to shed light on this subject, the timing and scale of the HTP uplift should be estimated first. For this purpose a wide range of methods are available, including stable oxygen based paleoaltimetry, which is considered to be one on the most efficient techniques and have been applied to the HTP region for time periods from early Eocene to the Pliocene.

However, paleoelevation reconstruction techniques have some serious limitation, particularly associated with our limited knowledge about paleoclimates. For correct paleoaltimetry estimates using stable oxygen-based technique, the relationships between paleoclimates and paleo $\delta^{18}O_p$ should be established first.

In this thesis two types of approaches have been used with following aims:

- Numerical modeling:

  - Provide modeling experiments testing the impact of the HTP uplift on atmospheric circulation and $\delta^{18}O_p$;

  - Provide modeling experiments with realist Cenozoic boundary conditions in order to reconstruct paleo $\delta^{18}O_p$ variations and its main controlling factors during different periods during the past;

  - Provide modeling experiments, testing the impact of Cenozoic paleogeographies, topography and atmospheric CO_2 concentration evolution on the Asian monsoons and aridification.

- Model-data comparison:

  - Estimate the possibility of using $\delta^{18}O$ based approach for relevant paleoelevation studies;

  - Review the elevation history of the Himalayas and Tibetan Plateau.

Chapter 2

Climate and stable oxygen isotopes modeling

Modeling is widely accepted to be a very powerful technique for reconstructing paleo, modern and future climates. For taking challenge of current study (see Section 1.4) we have chosen numerical climate modeling as our main instrument. In this chapter we provide a short introduction to climate modeling (Section 2.1): give an overview of the modeling principles of the Earth climate system components, main climate models types and the history of their development. We also suggest an introduction to the basics of implementation of stable water isotopes to numerical models (Section 2.2), focusing on general circulation models. We finish with an overview of models and modeling strategy (Section 2.3), as well as boundary condition (Section 2.4) used in this study.

Contents

2.1 Fundamentals of climate modeling

2.1.1 Modeling of the Earth climate system components

A model in geosciences is an attempt to reproduce processes that happen in nature. A climate model is a simplified representation of processes of the Earth climate system. In order to understand, reproduce these processes and predict the effects of changes and interactions, first of all, the climate system should be divided into several components. According to the definition from World Meteorological Organization (WMO), the following interacting components of the climate system should be defined (see also Figure 2.1):

- the atmosphere, i.e., the layer of gases surrounding the Earth of a complex composition (oxygen, nitrogen, carbon dioxide, water vapor, ozone, etc.), which affects the transfer of solar radiation, coming to the atmosphere's upper boundary, to the earth's surface. The atmosphere is the most unstable and variable component of the climate system (Baede et al., 2001);
- the ocean, i.e., the main water reservoir in the climate system, consisting of the saline water of the world ocean and the seas adjacent to it, absorbing the main part of solar radiation that comes to its surface, and representing, owing to the high heat capacity of the water, a powerful energy accumulator (Dymnikov et al., 2012);
- the land, i.e., the surface of the continents above the sea level with its hydrological system (rivers, lakes and swamps) and the soil (including ground waters);
- the biosphere (biota), i.e., the vegetation on land and in the ocean, as well as organisms in the air, sea, and land, including man;
- and the cryosphere, i.e., continental and marine ice, mountain glaciers, the snow cover, and the cryolithozone (permafrost).

Due to its huge size and long time scales, the climate system cannot be studied by direct experimental methods. Owing to specific characteristics of the climate system (for example, very small thickness of the atmosphere and ocean in comparison to the Earth radius), laboratory experiments are also very problematic. For a detailed investigation of the real climate system and its behavior in the past and future climate models - theory-based representations that characterize or simulate essential features and mechanisms - are available today.

Climate models represent either one or many components of the climate system, trying to get closer to "realist" representation of the real world and to understanding the processes controlling climate. Climate models are quantitative methods and describes the climate system in terms of basis physical, chemical and biological principles.

From the mathematical point of view, climate can be defined as a statistical ensemble of states taken on by the climate system during a sufficiently large time interval (Dymnikov et al., 2012). "The classical averaging period is 30 years", according to the WMO. In parallel, decadal averages have been successfully used in the IPCC report (Stocker et al., 2014). In the general case, an "ensemble" is understood not only as a set of states but also

as a certain probabilistic measure assigned over this set that determines the probability of the system to stay within a certain subset of the given set (Stocker et al., 2014).

Nowadays climate modeling is developing extensively. However, despite improvements in human knowledge and in computation resources, a numerical model is still a considerable simplification of real world, thus the results of such modeling can only be approximations.

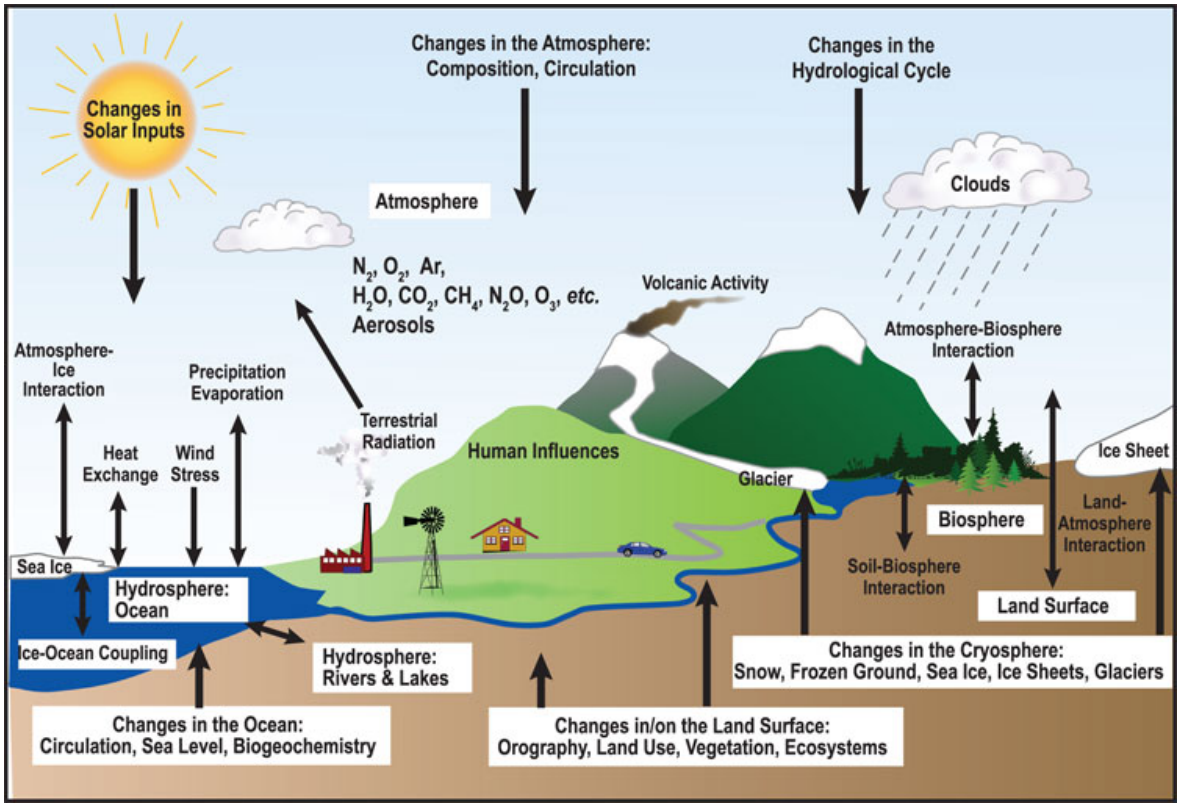

Figure 2.1 – Schematic representation of the Earth climate system's components, their interactions, and main processes. Figure from IPCC report (2007),FAQ 1.2 Solomon et al. (2007)

2.1.2 History of climate modeling

The history of climate modeling have been reviewed in details in Lorenz (1983); McGuffie and Henderson-Sellers (1997) and more recently in Edwards (2011). Here we provide a short overview of the development of scientific ideas in Meteorology and Climatology starting from ancient times and conceptual models to modern isotopes enabled general circulation models.

Conceptual models

The earliest attempts to understand climate phenomena and to explain the weather conditions were expressed in conceptual models (Figure 2.2). In its infancy, people faced with adverse weather conditions, attempted to explain climate phenomenon and atmo-

spheric processes with a divine providence (for example, Stribog [1], Boreas, Zephyrus [2]). With the development of civilization in China, India, the Mediterranean countries, attempts to regular meteorological observations and some guesses about the causes of atmospheric processes have been made. During this time, the foundations of scientific understanding of climate have been laid.

The first treatise on climate phenomena was made by Aristotle in his *Meteorology* at about 350 BC. By meteorology, Aristotle didn't simply mean the study of weather. His more expansive definition of meteorology included "all the affectations we may call common to air and water, and the kinds and parts of the earth and the affectations of its parts." In *Meteorology*, Aristotle identified the water cycle and discussed topics ranging from natural disasters to astrological events. The Aristotle's *Meteorology* determined the understanding of the climate for a long time. Starting with Aristotle, the Earth was divided into five zones. These portions of the spherical Earth determined by the geographic latitude in Greco-Roman geography and astronomy are called "climes".

Eratosthenes was a Greek expert in many disciplines, including astronomy, geography, and mathematics. At 3rd century BC Eratosthenes deduced the Earth's spherical shape and he was the first to calculate the tilt of the Earth's axis. In a now-lost work entitled *Geographika*, Eratosthenes following Aristotle divided the planet into climate zones (climes).

Five centuries latter, Ptolemy (2nd century AD) connected climate to the inclination of the sun and divided the planet (according to the lengths of the longest day) into climatic zones more precisely than it was done by Aristotle and Eratosthenes. Ptolemy gave a list of parallels, starting with the equator, and proceeding north at intervals, chosen so that the longest day (summer solstice) increases in steps of a quarter of an hour from 12 hours at the equator to 18 hours at 58° N, and then, in larger steps, to 24 hours at the arctic circle. Ptolemy's system of seven climes was later adopted in Arabo-Persian astronomy and meteorology.

Modern scientific meteorology dates back to the XVII century, flowing the formation of modern physics basics. Invention of thermometer and barometer made possible instrumental observations and contributed to new conceptual models. In 1686, seeking to understand the physics of the trade winds, Edmond Halley published one of the first theories to go beyond the Ptolemaic view of climate as a function of latitude. Halley suggested that solar heating caused air to rise near the equator. This 'rareified' air caused denser air from higher latitudes to 'penetrate in', creating the trade winds. Halley's term 'circulation', as well as his notion that the atmosphere must 'preserve the Equilibrium', remains in use today. Fifty years later, George Hadley modified Halley's explanation, taking into account the Coriolis effect. Thomson (1857) and Ferrel (1859) revised the Hadley's theory, invoking north-south Coriolis force. These conceptual models explained the prevailing winds over the globe and captured the fundamental energy-transport function of the climate system. At the end of the IXXth century the first works on climate sensitivity started. Based on observed correlation of CO_2 concentration in the atmosphere and global temperature, Svante Arrhenius (Arrhenius, 1896) theorized the impact of CO_2 on global temperature.

[1] a deity associated the wind in Slavic mythology
[2] Gods of winds in Greek mythology

His calculations allowed to conclude that the level of CO2 acted as a regulator of water vapor, and ultimately determined the planet's long-term equilibrium temperature.

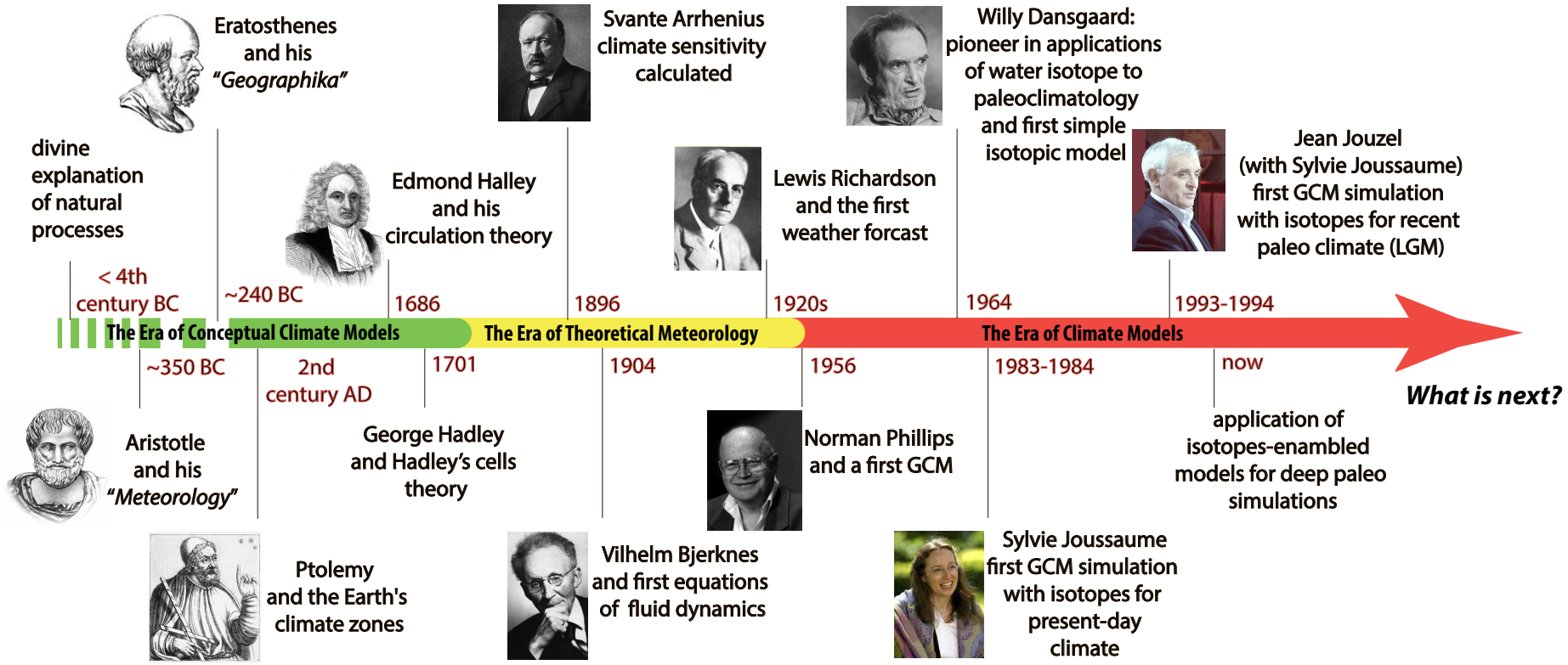

Figure 2.2 – From ancient times to modern isotopes enabled general circulation models. Key persons and a progress made.

Analog models

Analogical models are a method of representing a phenomenon of the world by another, more understandable or analysable system. In geoscienses analog models are difficult to perform because of long timescales and enormous size. However, simple physical models, such as bowls or globes filled with viscous fluids were constructed at least from the early XXth century, as was reviewed by Richardson (2007), in order to reproduce turbulent flows. With some approximation such a system presents atmospheric motions. Later analog models used a rotating tank heated at the rim and cooled in the center, thus simulating equatorial solar heating and polar cooling (Hide, 1953). Despite their very limited capabilities, such analog models demonstrated fundamental principles of fluid motion and probably inspired the numerical modelers (Lewis, 1998).

Numerical models

In the second half of the XIXth century the foundation of dynamic meteorology have been laid, in other worlds the application of fluid mechanics and thermodynamics principles to the study of atmospheric processes have been started. Mathematical modeling in atmospheric physics started with stating and solving the problem of hydrodynamic numerical weather prediction. For the first time, a weather forecast problem like that of mathematics and mechanics was formulated in Vilhelm Bjerknes' article, published in 1904 (Bjerknes, 1904), where it was treated as a problem with initial conditions for the equations of the dynamics of a baroclinic fluid.

In the early 1920s, Richardson proposed a method of numerical weather report (Richardson, 1922). Since the information about real state of the whole atmospheric column is necessary as the initial condition, he designed instruments for atmospheric measurements at altitudes of several kilometers above the surface. When constructing the theory of numerical weather prediction, Richardson studied the turbulence of the atmospheric boundary layer, radiation processes, and atmospheric thermodynamics.

Soon after the Ward War II an extensive development of numerical climate models started. At 1956 Norman Phillips developed a numerical code which could realistically represent monthly and seasonal patterns in the troposphere. This model is now considered as the first successful general circulation model of climate. The basis for EBMs was introduced by both Budyko (1969) and Sellers (1969). Radiative-convective models (RCMs) were introduced by Manabe and Wetherald (1967) and reviewed in Ramanathan and Coakley (1978).

2.1.3 Types of numerical climate models

"Simple" climate models

Energy balance models (EBMs) It is the oldest and the simplest type of climate models. These models attempt to account for all energy coming in and all energy going out of some system (e.g. the Earth). The term "balance" suggests that the system is at equilibrium, thus no energy is accumulated. EBMs are usually one-dimensional (the latitude

as one dimension) or even zero-dimensional (globally-averaged values only) and the atmospheric dynamics are not modeled in EBMs. Although EBMs are simple-constructed, it is a valuable tool for studying paleo and future climates both (McGuffie and Henderson-Sellers, 1997). This kind of models allows to access long-term variability linked with change of the Earth glaciation and insolation (e.g. Peltier et al., 2004).

Radiative-convective models (RSMs) These models have one or two-dimensions, with height as the dimension that is invariably present. RCMs simulate in detail the transfer of energy through the depth of the atmosphere, including a) the radiative transformations that occur as energy is absorbed, emitted and scattered, and b) the role of convection, energy transfer *via* vertical atmospheric motion, in maintaining stability. Two-dimensional RCMs also simulate horizontally-averaged energy transfers (McGuffie and Henderson-Sellers, 1997).

Earth system models of intermediate complexity (EMICs)

Up to now, there is no concise definition of an Earth system Models of Intermediate Complexity (EMIC). Perhaps, this will presumably never be achieved, because the border between EMICs and comprehensive models will change with time and computer capacity. A table of EMICs which are currently in operation have been published and discussed in Claussen et al. (2002). A revised description of all EMICs in operation can be found in Claussen (2005) and EMICs intercomparison is discussed in Brovkin et al. (2006) and more recently in Eby et al. (2013). EMICs and simple climate models differ much more. For example, EMICs realistically represent the large-scale geographical structures of the Earth, like the shape of continents and ocean basins, which is not the case for simple climate models.

General circulation models (GCMs)

A general circulation model (GCM) is a computer code that reproduce the dynamics of planetary outer layers such as ocean and atmosphere. Different climatic systems such as oceans, atmosphere, vegetation and land ice could be coupled in a single model model (couple GCM - CGCM) or be separated (e.g. ocean GCM – OGCM, atmosphere GCM - AGCM).

The GCM **dynamical core** resolves the primitive equations governing the atmosphere thermodynamics, expressing the conservation of momentum by the Navier-Stokes equation under the assumption of hydrostatic equilibrium (i.e. vertical acceleration is neglected). Conservation of energy expressed in an energy budget, accounting for radiative processes through the atmosphere and on the Earth surface. The conservation of mass is expressed by the continuity equation, for all considered components of the atmosphere (air, water in vapor, liquid and ice phase) (Bjerknes, 1921; McGuffie and Henderson-Sellers, 1997; Sturm et al., 2010). GCMs use different discretizations (e.g. longitude-latitude grids or spherical harmonics, pressure or sigma vertical levels) and optimized algorithms to resolve the primitive equations.

Many processes occurring in the nature cannot be resolved explicitly in the dynamical core, because they happen at much smaller scales. For these processes the **physical parametrization** part of GCMs code is responsible. For example, for AGCMs, convective cloud systems develop over an area of a few kilometers, which is two orders of magnitude less than the grid resolution (even using a zoomed grid). Convection needs thus to be parameterized, in order to represent the mean precipitation and energy release over the entire grid cell. The changes in prognostic hydrological variables (e.g. atmospheric liquid and vapor content, temperature) related to convection are fed back to the dynamical core, so that the next iteration is computed with updated variables. In Section 2.2.4 we will focus on parameterization relevant for the inclusion of stable water isotopes tracers in GCMs.

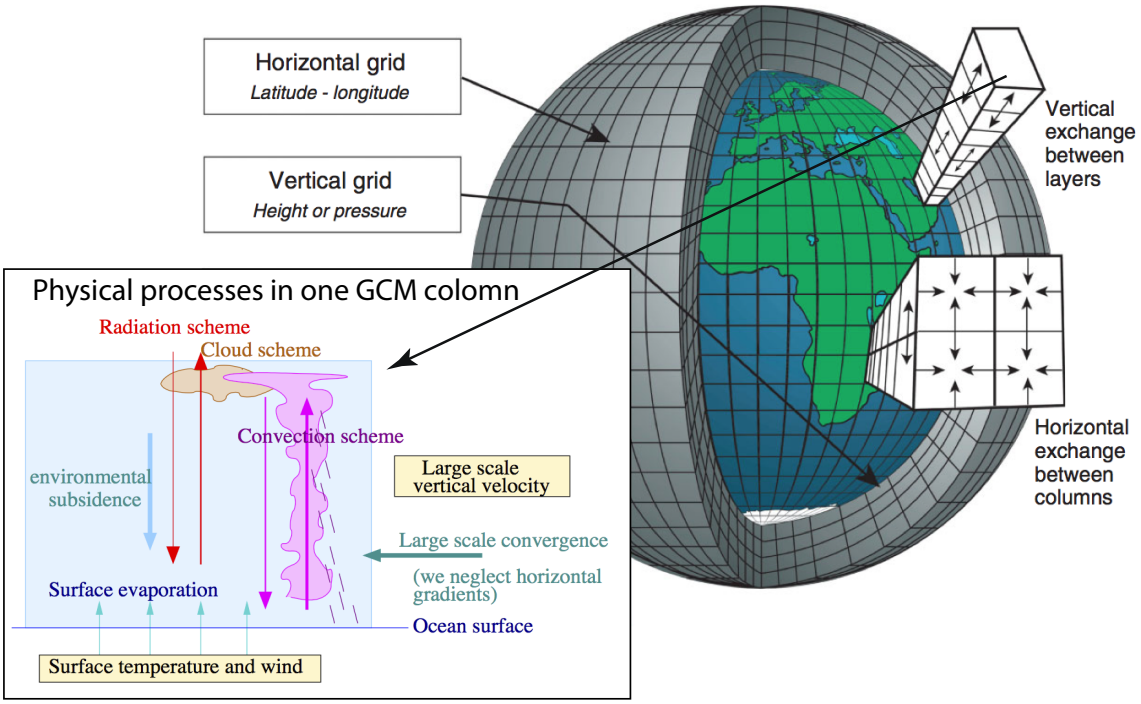

Figure 2.3 – Schematic representation of the grid structure of a GCM components and limit conditions (boxed in yellow)for its one column. Compiled from (Risi, 2009) and Edwards (2011).

2.2 Modeling of stable oxygen isotopes in precipitation

Over the last decades, empowered by more expertise and computational resources, water isotopes have been implemented not only to "simple" one-dimensional models, but also to a dozen of atmosphere general circulation models. In a first review on SWI-enabled models published by Hoffmann et al. (2000) only few studies on isotopes modeling were cited, while according to more recent reviews made by Sturm et al. (2010) and by Xi (2014) the isotope modeling community has been significantly expanded. In following sections we describe main principles and advances in water isotopes modeling and point out the peculiar properties of LMDZ-iso as a main instrument of isotopes modeling used in this thesis.

2.2.1 Purposes of implementation of stable water isotopes in numerical models

Early works on principles of stable water isotopes distribution on the Earth and their potential applications in paleoclimatology (e.g. Dansgaard, 1964) have become a catalyst for implementation of isotopes into numerical models. First of all, numerical models allow to reproduce observed isotopic distribution and to understated its controlling factors (first-order controlling factors at least) and to reveal a sensitivity of stable water isotopes to the climate change. Another important application of numerical models with stable water isotopes is a reconstruction of paleoclimates and paleo isotopes distribution with a purpose of interpretation geological proxy data (Jouzel et al., 1994).

2.2.2 Isotopes in "simple" models

Rayleigh-type distillation models

Since much of spatial and temporal isotopic variations can be explained by the Rayleigh distillation, most isotopic "simple" models are based on the Rayleigh distillation (for more details on the Rayleigh distillation see Section 1.3.3 and Chapter 3). Rayleigh distillation models have been widely used to interpret the isotopic composition of ice in Antarctica (e.g. Vimeux et al., 2002) and Greenland (Jouzel et al., 2000). These models simulate the evolution of the composition of the vapor and precipitation along the path of air masses from low latitudes to high latitudes. Such models requare the initial composition of vapor (before the orographic ascend), as well as initial temperature and humidity.

An example of Rayleigh-type distillation model is a model developed by Rowley et al. (2001) and validated in Rowley and Garzione (2007). This is a 1-D model that use thermodynamic principles and Rayleigh distillation processes to reproduce the isotopic composition of an air mass during its orographic uplift. This model considers an isolated ascending air parcel with prescribed initial temperature (T_0), relative humidity (Rh_0), and a reference value for composition of the vapor before the rainout process (R_{v0}). Although this model was validated against data for the Himalayas region and the southern Tibetan Plateau, Rowley et al. (2001) and other authors (Blisniuk and Stern, 2005) stressed the caution required for its application for paleoaltimetry (see Section 1.3.3). Specifically, the choice of unique reference-values for T_0, Rh_0 and R_{v0} implies an exclusive southern origin of vapor for entire region of destination.

However, the Rayleigh distillation is not a unique processes controlling $\delta^{18}O$. In the work of Risi (2009) possible complications of the Rayleigh distillation are listed:

- kinetic effects during the formation of ice crystals (Jouzel and Merlivat, 1984);
- partial condensate retention before the precipitation and coexistence of liquid and solid phase in some clouds (Ciais and Jouzel, 1994);
- realistic evolution of temperature, pressure and humidity of air mass along its trajectory (Helsen et al., 2007);

- recharging of an air parcel by the evaporation (Helsen et al., 2007; Worden et al., 2007);
- mixing of multiple air masses (Worden et al., 2007);

In addition, even if a Rayleigh model can successfully reproduce the observed modern behavior of stable water isotopes for certain regions, it may be inadequate in the context of a very different climate.

2.2.3 Isotopes in models of intermediate complexity

Doubling of the hydrological cycle (in case of only 2 stable isotopes simulated), results in increased the simulation cost in terms of computing resources. Earth system Models of Intermediate Complexity have an evident advantage on more complex models in computation time. Another benefit of EMICs is a possibility of simultaneous representation of several climate systems, because these models are coupled.

Up to now, SWI are implemented in several EMICs, for example, oxygen isotopes have been implemented in the three-dimensional model of intermediate complexity called iLOVECLIM (version 1.0), allowing fully coupled atmosphere–ocean simulations. The detailed implementations of oxygen isotopes in iLOVECLIM can be found in Roche (2013).

2.2.4 Isotopes in atmospheric general circulation models

For implementation of stable water isotopes in a AGCM model, the hydrological cycle needs to be duplicated, i.e. every variable should to be accompanied by its isotopic counterpart (for $H_2{}^{18}O$, HDO, $H_2{}^{17}O$). The dynamical core of a GCM can advect and mix isotopic tracers from different air masses, while in the physical parametrization the equilibrium and kinetic fractionations are computed on each time stem when a phase change of water takes place. This technique allows a modification of the isotopic composition of different reservoirs across the globe. Modern AGCMs include processes of fractionation due to phase change in process evaporation, condensation both to liquid and ice, and re-evaporation of precipitation in atmosphere. The isotopic modeling allows to calculate the isotopic composition of water content (in vapor and precipitation both) according to climate conditions and to assess the sensitivity of water composition to the variations of these conditions.

Due to a large amount of physical processes present in GCMs, they become an ideal tool for understanding the processes that govern the isotopic distribution for the present-day and paleo case. Pioneers in this approach was the work of Joussaume et al. (1984) who implemented the SWI in a GCM of Laboratoire de Météorologie Dynamique and produced a global isotope field for present-day January climate (Figure 2.2). Nowadays, stable isotopes have been implemented in a large number of GCMs: GCM GISS (Jouzel et al., 1987; Schmidt et al., 2007), ECHAM (Hoffmann et al., 1998), MUGCM (Noone and Simmonds, 2002), GENESIS (Mathieu et al., 2002), NCAR CAM (Lee et al., 2007), GSM (Yoshimura et al., 2008), HadCM3 (Tindall et al., 2009), LMDZ (Risi et al., 2010) and others. Table 2.1 lists selected isotopes-enabled AGCMs and some their characteristics.

Also we need to mention that SWI are implemented in number of regional circulation models like REMO-iso or RegCM3. Here we are not discussing these models in detail.

Table 2.1 – Selected isotopes-enabled AGCMs and their standard characteristics

Isotope-enabled AGCM	Standard resolution	Timestep	References	Examples of paleo studies
GISS	4° × 5°, 23 vertical levels	0.5 hrs (adjustible)	(Jouzel et al., 1987; Schmidt et al., 2007)	(Charles et al., 2001; Jouzel et al., 1994)
ECHAM	~ 3.8° × 3.8°, 19 vertical levels	40min (adjustible to 4min)	(Hoffmann et al., 1998)	(Roe et al., 2016; Sturm et al., 2007)
MUGCM	3.25° × 3.625°, 9 vertical levels	20min	(Noone and Simmonds, 2002)	NA
GENESIS	~ 3.75° × 3.75°, 18 vertical levels	0.5hrs	(Mathieu et al., 2002)	(DeConto et al., 2008)
CAM	~ 2.8° × 2.8°, 26 vertical levels	20min	(Lee et al., 2007)	(Sewall and Fricke, 2013; Tharammal et al., 2013)
GSM	1.85° × 1.85°, 17 vertical levels	NA	(Yoshimura et al., 2008)	NA
HadCM3	2.5° × 3.75°, 19 vertical levels	0.5hrs	(Tindall et al., 2009)	(Tindall et al., 2010; Tindall and Haywood, 2015)
LMD			(Joussaume et al., 1984)	(Joussaume and Jouzel, 1993)
LMDZ-iso	2.5° × 3.75° or 1.27° × 2.5° or zoomes grid, 19 or 39 vertical levels	3min	(Risi et al., 2010)	Joussaume and Jouzel (1993) using LMD
MIROC 3.2		20min	(Kurita et al., 2011)	NA

2.2.5 Use of isotopes-enabled models for paleoclimate simulations

A common purpose of isotopic modeling is a reconstruction of paleoclimatic isotopic field in order to help the paleodata interpretation. The most frequently modeled period of the past is the Last Glacial Maximum (LGM) because 1) the glacial climate is very different from the present-day one and 2) the LGM boundary conditions a sufficiently well known (Jouzel et al., 1994). The first simulation of paleo $\delta^{18}O$ with a GCM was made in 1993 by Joussaume and Jouzel (1993) using LMD model (Figure 2.2). These authors managed to reproduce isotopic distribution for August and January for LGM climate. The first full annual cycle simulation has been made for LGM climate with GISS GCM (Jouzel et al., 1994). In more recent studies, the isotopic distribution for the Last Glacial Maximum was

also simulated by Charles et al. (2001); Li et al. (2016); Tharammal et al. (2013). Later SWI-enabled GCMs have been successfully used for paleoclimate studies, concerned whole Paleozoic and Cenozoic eras (Table 2.1).

To quantify how different aspects of climate changes influence $\delta^{18}O_p$ isotopes-equipped AGCMs have been used. Results highlight the sensitivity of $\delta^{18}O_p$ to climate change associated with variations in pCO_2 (Poulsen and Jeffery, 2011; Poulsen et al., 2007), sea surface temperatures (Sturm et al., 2007), sea level changes (Poulsen et al., 2007), and uplifts of major orogens (Botsyun et al., 2016; Ehlers and Poulsen, 2009; Poulsen et al., 2010). Isotopes-enabled GCMs have been also used to produce "realistic" simulations of paleo climates, for example, Tindall and Haywood (2015) - for the Pliocene, Roe et al. (2016) - for Eocene and Tindall et al. (2010) for early Eocene, DeConto et al. (2008) for Eocene-Oligocene, Sewall and Fricke (2013) for the Cretaceous. At the exception of a few studies (Roe et al., 2016; Sewall and Fricke, 2013; Tindall et al., 2010), these works were based on sensitivity experiments using present-day continental positions and could not aim at simulating $\delta^{18}O_p$ for a particular period in the past.

2.3 Models used in this study

2.3.1 FOAM fully coupled General Circulation Model

Fast Ocean Atmosphere Model (FOAM) is a fully coupled, mixed-resolution, general circulation model developed by Jacob (1997). FOAM uses the combination of a low resolution atmosphere model and a highly efficient medium-resolution ocean model. Atmosphere component resolution is 7.5° longitude by 4.5° latitude (48 x 40 cells) on a regular latitude-longitude grid. Here we use a version with 18 vertical levels. Ocean component has a resolution of 2.4° by 1.8° (128 x 128 cells) on a regular grid longitude-latitude and 24 vertical levels, including 12 in the first thousand meters.

The atmospheric component of FOAM, Parallel Community Climate Model version 3 - University of Wisconsin (PCCM3-UW) is mainly composed of PCCM2 code, which is a parallelized version of Community Climate Model version 2 (CCM2), developed in collaboration of National Center for Atmospheric Research (NCAR) at Oak Ridge National Laboratory (ORNL) and Argonne National Laboratory (ANL), with atmospheric physics upgraded following CCM3 (Tobis et al., 1997).

The ocean component called OM3, is very similar to Modular Ocean Model (MOM), developed at Geophysical Fluid Dynamics Laboratory (GFDL) and to some extent to the model Parallel Ocean Program (POP), which version 2 is the ocean component of the model Community Earth System model (CESM) of NCAR. The atmospheric and oceanic components are linked by a coupler, which calculates and interpolates fluxes between the two components (Tobis et al., 1997).

FOAM incorporates a simple continental surface model, based on those of CCM2. There are 5 vegetation classes, distributed in a form of latitude bands. The temperautre over continents is calculated using a diffusion model with 4 layers, which properties depend on the type of vegetation. Hydrology is calculated by a simple "bucket" model. This

means that the soil can store up to 15 cm of water, the amount of which will alter evaporation. Above this height, water is routed to the ocean by a parallel routing model specifically developed by Robert Jacob. The presence of snow changes the soil temperature values as well as its albedo. The resolution of this biospheric component is identical to that of the ocean. The sea ice model is based on the thermodynamic model code of Community Sea Ice Model version 2.2.6 (CSIM2.2.6) developed at NCAR. This component also has the same resolution as the ocean model.

In FOAM reasonable resolution and calculation time are balanced. This allows to use this model for studying long-term climate variability and paleoclimates. FOAM compares well with other generalised climate models for present-day climate (Jacob, 1997) and has also proven to be useful in the study of past climates (e.g. Donnadieu et al., 2006; Hamon et al., 2013; Lefebvre et al., 2012; Pohl et al., 2016, 2014, 2015; Poulsen et al., 2001).

More detail on FOAM could be found on-line:

http://www.mcs.anl.gov/research/projects/foam/

2.3.2 LPJ vegetation model

The Lund-Potsdam-Jena dynamic global vegetation model (LPJ) (Sitch, 2000; Sitch et al., 2003) is the model of vegetation and vegetation-soil biogeochemistry. Different modules describe key ecosystem processes, including vegetation establishment, resource competition, growth and mortality. Vegetation structure and composition are described by nine plant functional types (PFTs), which are distinguished according to their plant physiological (C3, C4 photosynthesis), phenological (deciduous, evergreen) and physiognomic (tree, grass) attributes. Each grid cell is divided into fractions covered by the PFT and bare ground. The presence and fractional coverage of an individual PFT depends on its specific environmental limits, and on the outcome of resource competition with the other PFTs. The two-layer soil–water balance model is based on Haxeltine and Prentice (1996) model. LPJ is run on a grid cell basis with inputs of soil texture, monthly fields of temperature, precipitation and percentage sunshine hours.

2.3.3 LMDZ atmospheric general circulation model

Atmospheric General Circulation model developed at Laboratoire de Météorologie Dynamique (LMD), Paris, France with a zoomed grid LMDZ (Hourdin et al., 2006) is an atmospheric component of Institute Pierre Simon Laplace (IPSL) fully coupled GCM (Marti et al., 2010), participating to Coupled Model Intercomparison Projects (CMIPs) (Meehl et al., 2007; Taylor et al., 2012). This is a complex model that incorporates many processes decomposed into a dynamic part, calculating the numerical solutions of general equations of atmospheric dynamics, and a physical part, calculating the details of the climate in each grid point and containing parameterizations processes such as the effects of clouds, convection, orography.

In LMDZ, water vapor is advected by the Van Leer advection scheme Van Leer (1977). In the version of LMDZ used in this work, the land surface is represented as a simple bucket model, and land surface evaporation is calculated as a single flux: no distinction

is made between transpiration, bare soil evaporation, or evaporation of intercepted water by the canopy.

However, despite limitations, the ability of this model to simulate atmospheric dynamics and reproduce rainfall patterns over Asia was shown in numerous studies (Day et al., 2015; Krishnan et al., 2015; Ladant et al., 2014; Lee et al., 2012; Licht et al., 2014; Zhou and Li, 2002).

Resolutions In this study we use three different model resolutions: 1) 96 grid points in longitude, 95 in latitude and 19 vertical layers without zoom, 2) 96 grid points in longitude, 95 in latitude and 19 vertical layers with a stretched grid (with a zoom center in 89° E 31° N) and 3) 144 grid points in longitude, 142 in latitude and 39 vertical layers (with a zoom center in 89° E 31° N). The first configuration of LMDZ in resolution 96×95×19 without zoom was used for the study of Asian monsoon (Chapter 6). For studying the oxygen stable isotopes over Asia with sensitivity experiments (Chapter 3) the isotopic version of LMDZ was used in the resolution of 96×95×19. Experiments with realistic boundary conditions (Chapter 4 and Chapter 5) were run in a resolution 144 ×142×39. For resolutions 96×95×19 and 144×142×39 a zoomed grid were used with a zoom center set over the Himalayas and Tibetan Plateau (Figure 2.4).

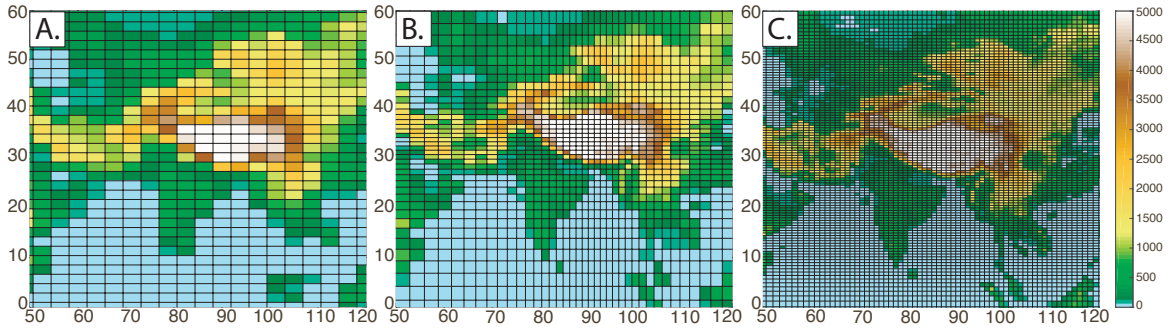

Figure 2.4 – Spatial resolutions of present-day geography over Asia used in this study: A) Non-stretched grid, resolution of 96×95×19 , B) Stretched grid, resolution of 96×95×19 with a zoom over the Tibetan Plateau, and C) Stretched grid, resolution of 144×142×39 with a zoom over the Tibetan Plateau. Center of zoom for case A) and C) is in 89° E 31° N.

2.3.4 Isotopes in LMDZ

In this thesis we use LMDZ-iso GCM as a main tool for studying paleo variations of stable oxygen isotopes over Asia. LMDZ-iso is an isotopic version of the LMDZ model (Risi et al., 2010). Isotopic processes in LMDZ-iso are documented in (Risi et al., 2010) and (Risi, 2009). The implementation of water isotopes in the convection scheme is described in (Bony et al., 2008). Here we present only a short summary of the isotopic processes that are reproduced in LMDZ-iso model:

- Water species are transported and mixed passively by large-scale advection (Van Leer advection scheme (Van Leer, 1977)) and various air masses fluxes;

- Equilibrium fractionation coefficient are calculated after Merlivat and Nief (1967) and Majoube (Majoube, 1971) and kinetic effects are taken into account following Merlivat and Jouzel (1979) and Jouzel and Merlivat (1984);
- The relative proportion of evaporative enrichment and diffusive equilibration is calculated depending on relative humidity following Stewart (1975);
- The model takes into account the evolution of the compositions of both the rain and surrounding vapor as the rain drops re-evaporate (Bony et al., 2008). However, the model is not accounting for the rain-drop size while rain-drop evaporation, like it is described in Lee and Fung (2008);
- Evaporation over land is assumed not to fractionate, given the simplicity of the model surface parameterization (Risi, 2009). Without ORCHIDEE (a specific model, that contributes to the processes over land), no fractionation is taken into account during evapo-transpiration from land. As a consequence, the enriching effect of continental recycling is overestimated (Risi et al., 2013);
- LMDZ-iso is also equipped with water tagging capabilities, allowing to quantify different moisture contributions from continental and oceanic evaporation sources. The advantage of this technique compared to typical back-trajectories methods is that it tracks the water rather than air masses, thus taking into account effects of phase changes (Risi et al., 2010).

Validation of LMDz-iso model

LMDZ-iso has been evaluated for present-day climates on different time scales (from synoptic to interannual) (Risi et al., 2010). Yao et al. (2013) have provided a precise description of rainfall patterns over the HTP, and showed LMDZ-iso ability to simulate atmospheric dynamics and reproduce rainfall and $\delta^{18}O$ patterns consistent with data over this region. Botsyun et al. (2016) provided a detailed validation of LMDZ-iso ability to simulate atmospheric dynamics and to reproduce rainfall and $\delta^{18}O$ patterns over the HTP region (for more details see Chapter 3). In addition, it has been shown that LMDZ-iso reproduces reasonably well spatial and seasonal variations of $\delta^{18}O$ and has been validated for two past climates: Last Glacial Maximum (21 ka) and Mid-Holocene (5 ka) (Risi, 2009).

2.3.5 FOAM-LPJ-LMDz coupling

In our study we focus on climate variations over Asia, using LMDZ and its isotopic version. As LMDZ is an AGCM, thus we needed to prescribe sea surface temperature (SST) as boundary conditions. For increasing the realism of simulations, SSTs were obtained by using the fully coupled model FOAM. After 2000 model years of FOAM simulation (we need to give some tome time for the ocean to be equilibrated), the surface temperatures averaged over the last 100 years are used to force the LMDZ or LMDZ-iso models. This technique is a good trade-off between reasonable computing time and a spatial resolution that adequately represents the main features of topography. This technique has been validated in numerous paleoclimate studies (e.g. Ladant et al., 2014; Pohl et al., 2016)

As it was shown in Section 2.3.1 the representation of the surface processes, including the vegetation is quite poor in the FOAM model. However, vegetation distribution directly impacts (1) the albedo of each grid cell, (2) its thermal properties, (3) its roughness, and (4) its potential evaporation (Lefebvre et al., 2013). Thus, we have run LPJ model "off-line" based on FOAM simulation outputs. In other words, we have used the climatology obtained with FOAM simulation to force LPJ model with fields of temperature, precipitation and humidity. Then, the vegetation distribution simulated by LPJ has been used to build albedo and roughness spatial distributions which are necessary for LMDZ initial and boundary conditions.

Thus, LMDZ boundary conditions consist of: 1) continental topography (same for all steps), 2) sea ice and sea surface temperature retrieved directly from FOAM simulation, and 3) albedo and roughness of the ground calculated using PFTs from LPJ, forced with FOAM outputs. LMDZ model is then run for 10 or 20 years, depending on the resolution, that is enough to be in equilibrium with surface conditions and capture model internal variability (Ladant, 2015).

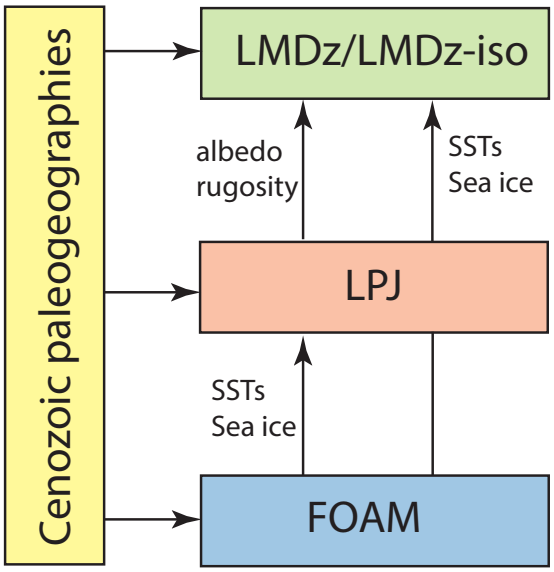

Figure 2.5 – Modeling strategy in this study

2.4 Boundary conditions used in this study

We provide 1) sensitivity experiments using present-day paleogeography with varied height of the HTP, as well as 2) "realistic" paleogeographies for the early Eocene (Herold et al., 2014), the middle Eocene (Licht et al., 2014), the Oligocene (Zhang et al., 2014) and the Miocene (Herold et al., 2008) (Figure 2.6). We summarize the experiments done for this study on the Table 2.2. For mode details see corresponding Chapters.

Table 2.2 – Summary of numerical experiments made for this study

Models used[3]	Period [4]	Geography [5]	Topography [6]	Atmospheric CO_2 concentration (in ppm)	Experiment name
Sensitivity experiments (Chapter 3)					
LMDz-iso	Actual	present-day	present-day	280	MOD
LMDz-iso	Actual	present-day	50 % of present-day topography over the HTP	280	INT
LMDz-iso	Actual	present-day	1 % of present-day topography over the HTP	280	LOW
Realist experiment with isotopes (Chapter 4 and Chapter 5)					
FOAM-LPJ-LMDz-iso	Actual	present-day	present-day	280	CTR-1X
FOAM-LPJ-LMDz-iso	Actual	present-day	present-day	1120	CTR-4X
FOAM-LPJ-LMDz-iso	Miocene	Herold et al. (2008)	Herold et al. (2008)	280	MIOC
FOAM-LPJ-LMDz-iso	Oligocene	Zhang and Liu (2010)	Zhang and Liu (2010)	840	OLI-3X
FOAM-LPJ-LMDz-iso	Oligocene	Zhang and Liu (2010)	50 % of TP compared with OLI-3X	840	OLI-3X
FOAM-LPJ-LMDz-iso	Oligocene	Zhang and Liu (2010)	150 % of TP compared with OLI-3X	840	OLI-XL
FOAM-LPJ-LMDz-iso	Oligocene	Zhang and Liu (2010)	1 % of TP compared with OLI-3X	840	OLI-S
FOAM-LPJ-LMDz-iso	Eocene	Licht et al. (2014)	Licht et al. (2014)	280	EOC-1X

[3] See modeling strategy (Section 2.3.5)

[4] Here periouds indicated corresponds to: Actual - 0 Ma, Miocene - 15 Ma, Oligocene - 30 Ma, Eocene - 42 Ma, Early Eocene - 55 Ma

[5] For details on geography and paleogeographical reconstructions used see Section 2.4.1

[6] See corresponding Chapters for mode details

FOAM-LPJ-LMDz-iso	Eocene	Licht et al. (2014)	Licht et al. (2014)	1120	EOC-4X
FOAM-LPJ-LMDz-iso	Eocene	Licht et al. (2014)	150 % of TP compared with EOC-4X	1120	EOC-XL
FOAM-LPJ-LMDz-iso	Eocene	Licht et al. (2014)	50 % of TP compared with EOC-4X	1120	EOC-M
FOAM-LPJ-LMDz-iso	Eocene	Licht et al. (2014)	1 % of TP compared with EOC-4X	1120	EOC-S
FOAM-LPJ-LMDz-iso	Eocene	Licht et al. (2014) with reduces Tethys	Licht et al. (2014)	1120	EOC-S
FOAM-LPJ-LMDz-iso	Eocene	Licht et al. (2014)	Eocene pale-ogeography with high "Himalayas"	1120	EOC-Him
FOAM-LPJ-LMDz-iso	Early Eocene	Herold et al. (2014)	Herold et al. (2014)	1120	EOC-Early
Realist experiment without isotopes (monsoon study) (Chapter 6)					
FOAM-LPJ-LMDz	Actual	present-day	present-day	280	RT0Ma1x
FOAM-LPJ-LMDz	Miocene	Herold et al. (2008)	Herold et al. (2008)	280	RT15Ma1x
FOAM-LPJ-LMDz	Oligocene	Zhang and Liu (2010)	Zhang and Liu (2010)	280	RT30Ma1x
FOAM-LPJ-LMDz	Eocene	Licht et al. (2014)	Licht et al. (2014)	280	RT42Ma1x
FOAM-LPJ-LMDz	Early Eocene	Herold et al. (2014)	Herold et al. (2014)	280	RT55Ma1x
FOAM-LPJ-LMDz	Actual	present-day	present-day	1120	RT0Ma4x
FOAM-LPJ-LMDz	Miocene	Herold et al. (2008)	Herold et al. (2008)	1120	RT15Ma4x
FOAM-LPJ-LMDz	Oligocene	Zhang and Liu (2010)	Zhang and Liu (2010)	1120	RT30Ma4x
FOAM-LPJ-LMDz	Eocene	Licht et al. (2014)	Licht et al. (2014)	1120	RT42Ma4x

FOAM-LPJ-LMDz	Early Eocene	Herold et al. (2014)	Herold et al. (2014)	1120	RT55Ma4x
FOAM-LPJ-LMDz	Actual	present-day	≤ 200 m worldwide	280	FE0Ma1x
FOAM-LPJ-LMDz	Miocene	Herold et al. (2008)	≤ 200 m worldwide	280	FE15Ma1x
FOAM-LPJ-LMDz	Oligocene	Zhang and Liu (2010)	≤ 200 m worldwide	280	FE30Ma1x
FOAM-LPJ-LMDz	Eocene	Licht et al. (2014)	≤ 200 m worldwide	280	FE42Ma1x
FOAM-LPJ-LMDz	Early Eocene	Herold et al. (2014)	≤ 200 m worldwide	280	FE55Ma1x

2.4.1 Geography, topography and bathymetry forcing

In Section 1.1 we have shown the importance of planet surface configuration on atmospheric dynamics and climate in general. The use of paleogeographies reconstruction has several pitfalls. While reconstructions provide global coverage of land elevation, the readers should keep in mind that there are several regions which suffer from large topographic uncertainty, linked to lack of paleoelevation reconstructions, uncertainty of paleoelevation reconstructions methods and an extrapolation method it self. The concerned regions are the HTP and proto-HTP region (see Section 1.3.6 for details on paleoelevation of HTP region), North American Cordillera and the Andes. The topography of Africa and Antarctica may also serve as a subject for discussions. The land-sea distribution highly depends on the results of paleomagnetic reconstructions which have their own error 1.2.3 and as well on applied sea level reconstruction. In addition, position and opening of oceanic passages (e.g. the Drake Passage, the Panama Passage, the Bering Passage) is also highly debated and for most reconstructions is based on broadly accepted theories. However, despite evident complexity and large uncertainty in used here maps, their use is justified as gives a sufficient approximation for current state of human knowledges.

Early Eocene

The early Eocene paleogeography (~55 Ma) used in this study (Herold et al., 2014) approximately corresponds to the time of starting of hard India-Asia collision. Volcanic arcs that are hypothesized to separate Indian continent form Asia on a given reconstruction have been already collided with southern Asian margin. Northern part of Greater India is covered by an epicontinental sea, forming a passage between India and Asia. The most southern part of India is situated on ~5° S.

In this paleogeography the topography is remarkably improved in comparison with those of Williams (2007) due to application of new broadly accepted regional palaeogeographic reconstructions (Herold et al., 2014). The height of the HTP region was set to 1500 m following the reconstruction of Markwick in Williams (2007), which represents an inter-

mediate solution for different competing uplift histories of the region (see section 1.3.6). Overall, in used paleogeography, the maximum elevation is less than 3000m.

Middle Eocene

The middle Eocene reconstruction corresponds approximately to 42 Ma (Licht et al., 2014), include a southward shift of the Asian continent, as well as the presence of a large Paratethys Sea covering the region between 30° N and 47° N in latitude and extending to 80° E. In the middle Eocene case TP is considerably shifted to the south (situated between 15° N and 27° N) comparable to the present-day geography and its altitude rich up to 3500 m (Figure 2.6). This middle Eocene paleogeography have been successfully used in previous paleoclimate modeling studies (Licht et al., 2014). However, with a goal of isolating the effect of topography on climate we have modified the elevation of the HTP for the Eocene case, as well as the boundaries of the Paratethys Sea (see Chapter 4 and Chapter 5).

Oligocene

The Oligocene paleogeography (~30 Ma) is performed by (Zhang et al., 2014). Latitudinal position of India is similar to those for the middle Eocene case. The Paratethys Sea is more restricted then for the middle Eocene one and larger part of Asia that is not covered by water (Figure 2.6). Turgai Strait still connected Arctic and Tethys Oceans, which divided the Eurasian continent into two parts.

Miocene

The Miocene paleogeography (Herold et al., 2008) is quite similar to the present-day case, with some exceptions, including the latitudinal position and the surface elevation of the Indian subcontinent. Compared to the present-day, the Miocene paleogeography has lower topography globally (Figure 2.6).

2.4.2 Other forcings

Except for the tectonic forcings (the geography, topography and bathymetry as a result of tectonic activity), other forcings are applied to the climate system. In our simulations, atmospheric CO_2 concentration have been changed (Figure 2.2) in order to 1) study direct and indirect effect of CO_2 on $\delta^{18}O$ and 2) obtain more realistic paleo experiments. For example, for Eocene simulation with varied topography we have used pCO_2 set to 1120 ppm, that lies within pre-industrial values approximations and the higher hand of Eocene estimates consequently (Beerling and Royer, 2011). For control ("present-day") experiments pCO_2 was kept equal to pre-industrial values of 280 ppm (Table 2.2). The orbital parameters were kept equal to present-day values for all experiments, except two addition simulations for the Eocene period, where we have test the impact of orbital forcing on the Eocene climate and stable oxygen isotopes in precipitation.

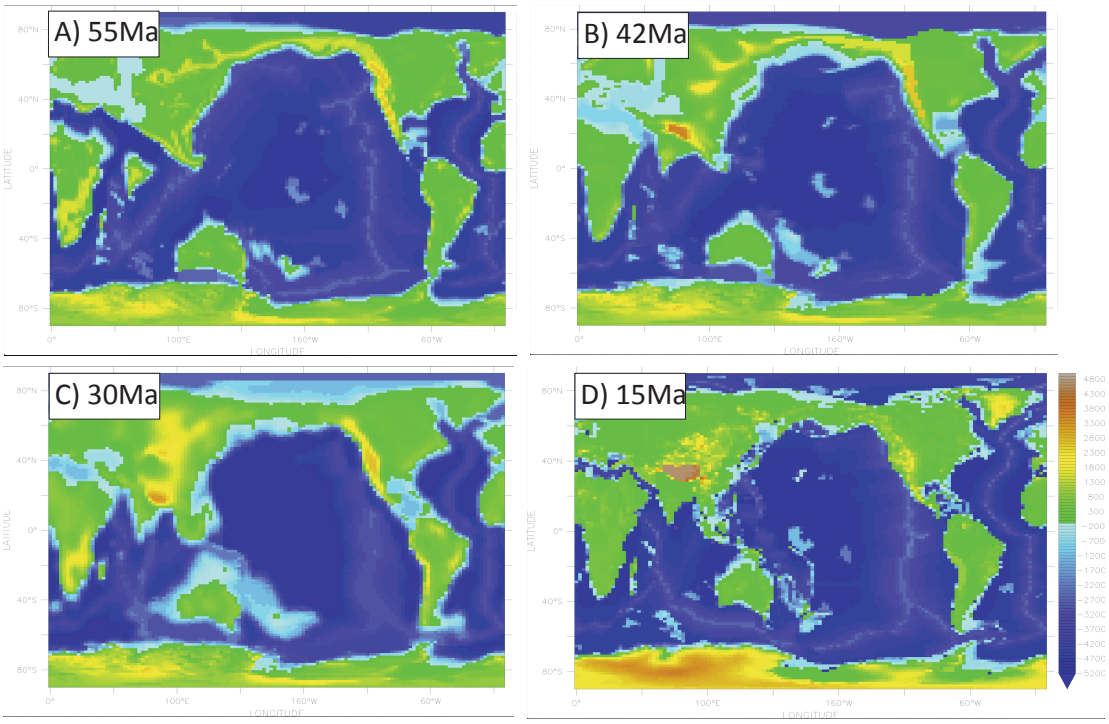

Figure 2.6 – Cenozoic paleogeographies used as boundary conditions for modeling in this study A) Paleocene-Eocene from (Herold et al., 2014), B) Eocene from (Licht et al., 2014), C) Oligocene from (Zhang et al., 2014) and D) Miocene from (Herold et al., 2008). See the text for the description.

2.5 Summary and conclusions

A climate model is a theoretical or mathematical representation (now typically involving computer simulation) of physical processes of the Earth climate system, which consists of several interconnected components, such as atmosphere, ocean, biosphere, etc. Conceptual models of climate are rooted in antiquity, while invention of electronic computer in the XXth century contributed to development of numerical models. There are multiple types of climate models, that allow solving different scientific tasks. General circulation models are the most complex and “realistic” climate models and allow providing equilibrium climate simulations. Implementation of stable water isotopes in different kind of climatic models allow coming closer to 1) understanding how different climatic processes impact the distribution of stable water isotopes and 2) decoding the information about climatic variability that is recorded by water stable isotopes in geological archives. For achieving the main purposes of this study (see Section 1.4) and answering the scientific questions asked (see Introduction) we have chosen LMDZ atmosphere general circulation model, off-line coupled with FOAM and LPJ models. This modeling strategy is a good trade-off between reasonable computation time and a high resolution. For studying stable water isotopes in precipitation we have used an isotopic version of LMDZ - LMDZ-iso. We provide sensitivity and "realistic" experiments both for different time periods during the Cenozoic.

Chapter 3

Controls of $\delta^{18}O$ in precipitation: elevation vs. climate change

Stable oxygen isotopes paleoaltimetry is considered to be a very efficient technique for reconstruction of the elevation history of mountains belts, including Tibetan Plateau and the Himalayas. However, adequate understanding of $\delta^{18}O$ signal is indispensable for this technique. In this chapter, first, we review present-day controls of $\delta^{18}O_p$: we discuss the effect of the surface elevation itself, but also the influence of temperature, humidity, post-condensational processes, precipitation amount, the initial isotopic composition of a moisture source and others climatic parameters on $\delta^{18}O_p$ (Sections 3.1). In addition, based on our numerical simulations, we show that $\delta^{18}O$-elevations gradients ("isotopic lapse rates") are spatially heterogeneous (Sections 3.2). However, although reconstruction of the controls of $\delta^{18}O$ during the past is critical for reliable paleoelevations reconstructions, our knowledge about the controls of $\delta^{18}O$ in paleo precipitation is limited (Section 3.3). In Section 3.4 we introduce our article published in the *Climate of the Past*, entitled "Impacts of Tibetan Plateau uplift on atmospheric dynamics and associated precipitation $\delta^{18}O$". This paper shed a new light on the main processes that control $\delta^{18}O$ during the Tibetan Plateau uplift. Finally, we discuss possible consequences for interpretation of stable-oxygen based paleoaltimetry studies outcomes (Section 3.5).

Contents

3.1 Present-day controls of $\delta^{18}O$ in precipitation

Spatial and temporal distribution of stable oxygen isotopes has been studied since more then half a century. Since the early works of Dansgaard (1964) and Craig (1961), progress on understanding the processes controlling the isotopic composition of water has been made (e.g. He et al., 2015; Lee and Fung, 2008; Risi et al., 2008, 2013; Wang et al., 2016; Worden et al., 2007; Yao et al., 2013). However, at low latitudes, the paleoclimatic interpretation of isotopic records may be complicated (Risi et al., 2010), because of numerous complex processes that influence $\delta^{18}O_p$ and $\delta^{18}O_v$.

Present-day controls of stable oxygen isotopes in the atmosphere have been derived from observation and climate modeling both. In the Introductory Chapter we provide the basics for the isotopic fractionation, which is an enrichment of one isotope relative to another in a chemical or physical process and the Rayleigh distillation that describes the isotopic composition of vapor during the air ascend (Section 1.3.3). Here, we review in more details the key factors that contribute to present-day spatial and seasonal ^{18}O ratios changes.

3.1.1 Temperature effect

Based on global observations it was shown that $\delta^{18}O_p$ has a zonal distribution, with more depleted composition when latitude increases (Figure 1.11). This dependence has been called "temperature effect": lower the temperature, more depleted is precipitation. An explanation of such an effect is given, for example, in Risi (2009) (a translation): "Imagine an air mass that head from low latitudes to the poles. Gradually as the temperature decreases, the saturation specific humidity decreases and therefore a part of the vapor condenses and precipitates. Since the heavy isotopes are concentrated in the most condense phase, vapor lose through the condensation a part of its heavy isotopes. Thus, successive events of condensation and precipitation result in progressive depletion of an air mass through its transport towards the poles." As a consequence, present-day latitudinal variations in $\delta^{18}O_p$ distribution is observed. Such depletion during condensation is modeled by Rayleigh distillation (see Section 1.3.3), that considers an isolated ascending air parcel with prescribed initial temperature, relative humidity, and a reference value for composition of the vapor before the rainout process (e.g Rowley et al., 2001).

The present-day spatial $\delta^{18}O_p$-temperature relationship is well documented worldwide, with slopes ranging from - 1.1 ‰/°C in high-latitude areas to virtually zero in tropical regions (where $\delta^{18}O_p$ is more strongly correlated to the amount of precipitation) (Rozanski et al., 1993). The temperature effect on $\delta^{18}O_p$ values is also manifested on a seasonal basis, with typically lower values during winter and higher values during summer (Rozanski et al., 1993).

Over northern TP and Tianshan Mountains, data and modeling results evidence an obvious relationship between $\delta^{18}O_p$ and temperature with strong seasonal cycle: i.e. maximum values in summer and minimum values in winter (Yao et al., 2013). However, over other regions of HTP this correlation is less pronounced (Yao et al., 2013).

3.1.2 Elevation effect

"Elevation effect" (or altitude effect) is a particular case of the temperature effect, as $\delta^{18}O_p$ decreases with elevation following the decrease of the temperature. When air masses are orographically uplifted they cool and precipitate preferentially the heavier isotopes. This vertical isotopic gradient sometimes is called the "isotopic lapse rate" (e.g. Bershaw et al., 2012; Ehlers and Poulsen, 2009; Poulsen et al., 2010). In mid-latitudes measured present-day isotopic lapse rates generally ranges between 0.15 ‰ and 0.30 ‰ for each 100 m of altitude gained, with an averaged in the most regions of the world of 0.28 ‰/100 m. (Poage and Chamberlain, 2001)

Over the HTP, relationships between $\delta^{18}O_p$ and elevation have been determined both empirically (e.g. Garzione et al., 2000b; Poage and Chamberlain, 2001) and theoretically using thermodynamic principles and Rayleigh distillation processes (Rowley and Garzione, 2007; Rowley et al., 2001) (see more in the Section 3.2).

Now it is widely accepted (e.g. Bershaw et al., 2016; Mulch, 2016; Schemmel et al., 2013) that the isotopic lapse rates may change spatially and temporally depending on the precipitation history, the degree of cooling and the precipitable moisture left and other climatic parameters. However, neither the impact of different climate parameters on isotopic lapse rates (even for present-day!) nor its regional values (example for the HTP) have been evaluated.

3.1.3 Continental effect

A particular case of the Rayleigh distillation, so-called the continental effect, describes the decrease in $\delta^{18}O_p$ with distance from the ocean along the trajectory of an air masses (Dansgaard, 1964; Rozanski et al., 1993). This effect is present in both high-latitude and low-latitude regions (Gat, 1996).

However, implication of the continental effect for interpretation of observed isotopic distribution has several limits:

- this principle implies a presence of a single air mass that undergoes successive events of condensation and precipitation, but not a mixture of different air masses (often the case in nature);
- it may be counteracted by injection of enriched recycled continental moisture back to the atmosphere from evaporation of soil water, lakes, and rivers (Risi et al., 2013).

In addition the continental effect may be overprinted by other factors, such as the amount effect or raindrop evaporation (see below). For example, Araguás-Araguás et al. (1998) have shown that over Asia, the continental effect is observed for dry season only, while for the season with heavy monsoon, stronger correlation of $\delta^{18}O_p$ with precipitation amount is observed. In our simulation of present-day $\delta^{18}O_p$, the continental effect is well pronounced over India and China, expressed in gradual decrease of $\delta^{18}O_p$ with increased distance from the coast (Figure 3.1).

3.1.4 Evaporation and continental water recycling

Continental water recycling is the return of land surface evaporation water to the land surface as precipitation. Continental recycling has an enriching effect on the vapor $\delta^{18}O$: surface waters are enriched in heavy isotopes due to preferable evaporation of lighter isotopes and thus consentration of heavy isotopes in liquid phase. Water evaporated from land surface is more enriched in heavy isotopes than water evaporated from the ocean (Gat, 1996). Without continental recycling, the precipitation, which is more enriched in heavy isotopes than the vapor, would be lost in the surface runoff. Integrated along a trajectory, continental recycling has an enriching effect on both downstream vapor and precipitation (Lee et al., 2012; Risi et al., 2013). Evaporation from soil and surface waters as well as plants evapo-transpiration contributes to enriched $\delta^{18}O$. In addition, direct evaporation of rain impact $\delta^{18}O$.

Quade et al. (2011) with an analysis of surface water samples have shown a gradual increase in $\delta^{18}O$ values to the north of Himalayas crest and reduced isotope-elevation gradient in the northernmost TP that reflects the diminishing contribution of summer monsoon, together with increased influence of westerlies and local moisture recycling. Similar increase in $\delta^{18}O$ in stream-water and precipitation samples north of the Himalayan crest was also reported by Tian et al. (2001) and Zhang et al. (2002). Tian et al. (2001) highlight a particular role of continental recycling to the north of the Tanggula mountains. Bershaw et al. (2012) using backtracking trajectories analysis (HIPSPLIT) suggest that local moisture recycling has a crucial impact on isotopic signature of precipitation regardless the origin of air mass.

However, studying the contribution from evaporation from soil and surface waters as well as plants evapo-transpiration to isotopic composition of vapor and precipitation is complicated because precipitation is strongly affected by postcondensational processes (Lee and Fung, 2008; Risi et al., 2010) and the vapor more directly reflects the moisture origin (Gat, 1996; Risi et al., 2013).

Our experiments show that for present-day case up to 40-80 % of moisture over the TP have been recycled (Figure 3.3, see more in Section 3.2 and Section 3.4). However, these values should be considered carefully because of the uncertainty in land-atmosphere feedbacks linked with the representation of surface processes in the model (see Section 7.1.1).

3.1.5 Moisture sources and mixing of air masses

Changes in moisture sources have been shown to influence $\delta^{18}O_p$, since different vapor transport pathways affect $\delta^{18}O_v$ (Ehlers and Poulsen, 2009; Gat, 1996; Quade et al., 2007). Increasing distance between the water vapor source and the precipitation region induces stronger distillation of water vapor and more negative values of precipitation $\delta^{18}O$ (Rozanski et al., 1993), explaining the negative $\delta^{18}O$ gradient simulated from coastlines to continent interiors over most regions (see earlier, the "continental effect"). Thus, air masses originated from the nearby water reservoirs have higher $\delta^{18}O$ values that from distant precipitation sources (LeGrande and Schmidt, 2009).

In a series of studies, Tian et al. (Tian, 2003; Tian et al., 2007, 2001) isolate three distinct regions where stable water isotopes patterns appears to be different: (1) south of Himalayas, (2) southern TP, between Himalayas and Tanggula mountains and (3) TP north of Tanggula mountains. In these studies, moisture origin, vapor transport, as well as the "amount effect" (see Section 3.1.6) of monsoon precipitation have been hypothesized to influence the final $\delta^{18}O$ signal of precipitation. Based on the isotopic composition of surface waters and soil carbonates, Quade et al. (2011) suggest a gradual increase in $\delta^{18}O$ values to the north of Himalayas crest and reduced isotope-elevation gradient in the northernmost TP that reflects the diminishing contribution of summer monsoon. In addition to the restricted influence of the Indian Ocean-derived moisture on the northern Plateau, Hren et al. (2009) showed an enriching impact of western-sourced air masses on moisture signature of the northern TP. Bershaw et al. (2012) used back-trajectories to estimate moisture sources contributing to the hydrological budget of Asia and suggests that air mass mixing varies from east to west across the Plateau, but moisture recycling has an overprinting effect on isotopic composition over the TP, regardless of origin of air masses.

In a very recent work Li et al. (2016) use an isotope tracking general circulation model to estimate modern $\delta^{18}O$ variations across the TP and conclude that during the summer, monsoon vapor transport from the north and southwest of the plateau generally corresponds to more enriched $\delta^{18}O_p$, whereas vapor transport from the Indian Ocean in average corresponds to more depleted $\delta^{18}O_p$.

The major assumption of most Rayleigh distillation-type models (e.g. model of (Rowley et al., 2001) is that an air parcel is isolated and has no exchange with surrounding air. Worden et al. (2007) described processes of "injections of moisture from the surface evaporation into the atmosphere" that results in more enriched $\delta^{18}O_p$. This injection is called "mixing" of two air masses, and the authors show that $\delta^{18}O_p$ in this process is less depleted in heavy oxygen isotopes that expected from simple Rayleigh distillation. A mixing may be also a result of mixture between air masses of different source such as monsoonal source and westerlies for the HTP. Li et al. (2016) show that air mixing over present-day Himalayas is small (0.2 %). However, these authors indicated that over the HTP the mixing ratio is not clear and requires additional verification.

3.1.6 Amount effect and aridity

The amount effect is the observed decrease in $\delta^{18}O_p$ values with increased rainfall amount (Dansgaard, 1964; Rozanski et al., 1993). The ^{18}O content in precipitation decreases not only with higher precipitation intensity in a single storm (Miyake and Matsubaya, 1968), but also at seasonal scale. Lee and Fung (2008), following the earlier works of Dansgaard (1964) and Rozanski et al. (1993), provided complete explanations on the "amount effect":

- $H_2^{18}O$ has slightly higher vapor pressure. As a consequence, during intense precipitation, fractional removal of heavy isotopes in the condensate, or the initial rain within the cloud, is high. This results in low $\delta^{18}O$ in the remaining vapor and ensuing condensate;

- High precipitation rate implies large raindrops and numerous raindrops interacting with the vapor, significantly lowering the isotopic composition of the vapor and the ensuing raindrops;
- In heavy showers, the isotopic composition of the vapor, and hence of the precipitation, decreases with time because of the continuous isotopic exchange with falling raindrops.

In contrast to the amount effect, aridity (low RH, less intensive showers, smaller rain drops) has following competitive effects:

- Water vapor near the surface has higher $\delta^{18}O_p$ because of the effect of enriched vapor from the surface evaporation and little condensation. Thus, small raindrops would adjust to the high $\delta^{18}O_p$ surface water vapor, and "forget" their isotopic composition at the cloud layer (Lee and Fung, 2008);
- High relative loss of light isotopes (which results in more ^{18}O-enriched values for raindrops) associate with raindrops evaporate below the cloud base in arid regions (Lee and Fung, 2008).

In other words, because lighter isotopes evaporate more easily, rain reevaporation leads to an isotopic enrichment of precipitation. Therefore, the more reevaporation, the greater the difference between $\delta^{18}O_p$ and $\delta^{18}O_v$. The effects described here which happens after condensation are commonly called "post-condensational effects". In a model, it mainly associates with raindrop reevaporation that can occur after initial condensation. We refer to the study of (Lee and Fung, 2008), where post-condensation effects are explained in details. The contribution of such processes increases dramatically for very dry areas, where the relative humidity is less than 40 %.

Over the Himalayas and South TP observations show a negative correlation between the precipitation amount and $\delta^{18}O_p$, during the monsoonal season in particular (Tian et al., 2001; Yao et al., 2013). In contrast, over Northern Tibet and Tarim Basin arid conditions predominate, that results in bigger difference between $\delta^{18}O_p$ $\delta^{18}O_v$, and less depleted $\delta^{18}O_p$.

3.1.7 Other effects

In addition to the processes listed above, other climatic variable may contribute to resulting $\delta^{18}O_p$ signal. Large-scale atmospheric circulation impact $\delta^{18}O_p$: 1) through the convective processes that strongly affect the isotopic composition of both vapor and precipitation and have negative isotopic signature (Bony et al., 2008; He et al., 2015; Risi et al., 2008), and 2) through a strong isotopic depletion that occurs in the subsiding branch of the Hadley circulation (Frankenberg et al., 2009).

Relative humidity has an impact on $\delta^{18}O_v$ through two steps 1) during condensation through Rayleigh distillation and 2) after condensation, because of raindrop evaporation, as degree of isotopic enrichment of precipitation compared to vapor is higher with lower relative humidity (Lee and Fung, 2008).

The HTP snow cover and albedo change is known to change atmospheric circulation and spatial and temporal radiative budget variations that have their consequences for $\delta^{18}O_p$ (Poulsen and Jeffery, 2011). High surface albedo associated to the snow cover contributes to an extra cooling of air masses and thus to lower $\delta^{18}O_v$.

Blisniuk and Stern (2005) highlighted that change in sea surface temperatures is a challenging aspect of paleoelevation estimates as it controls the initial moisture content of an air mass. With some exceptions, this effect has been ignored in all the studies summarized above, but can be relatively important, because it has a direct impact of the surface air pressures and thus the atmospheric circulation (Blisniuk and Stern, 2005).

GCMs represent most processes that have potential effect on $\delta^{18}O_p$, that make it possible to use numerical modeling tool for the purpose of our study. We discuss the uncertainties associated with the use of GCMs for studying paleo isotopic composition in Section 7.1.1.

3.2 Spatial variations of isotopic "lapse rates" over the Tibetan Plateau and the Himalayas

In this section we present the study that we have done on the variations of $\delta^{18}O$-elevation relationships over the HTP. Results presented in this section we obtain using a model configuration with 96 grid points in longitude, 72 in latitude and 19 vertical layers, with the first four layers in the first kilometer above the surface and a zoom over the HTP that allows increased spatial resolution over at ~100 km over central Asia. In our simulations 4 potential moisture sources are considered: (1) continental sources, (2) Indian Ocean, (3) Atlantic Ocean and Mediterranean Sea, and (4) Pacific Ocean. All boundary conditions are set to pre-industrial values.

Introduction and study motivation

The thermodynamic model (in 1-D) of Rowley et al. (2001) (R_1) considers an isolated ascending air parcel with prescribed initial temperature (T_0), relative humidity (Rh_0), and a reference value for composition of the vapor before the rainout process (V_0, New Delhi value for most studies). Accounting for adiabatic ascent and Rayleigh distillation, a relationship between decreasing $\delta^{18}O$ values and increasing elevation can be computed and approximated with a second-order polynomial. Although this model was validated against data for the Himalayas region and the southern Tibetan Plateau, Rowley et al. (2001) and other authors (Blisniuk and Stern, 2005) stressed the caution required for its application for paleoaltimetry. Specifically, the choice of unique reference-values for T_0, Rh_0 and V_0 implies an exclusive southern origin of vapor for the entire HTP region. If precipitation results from mixed air-masses originating from different moisture sources, this model is not valid for remote regions. Still, this $\delta^{18}O$-elevation relationship is widely used with common T_0, V_0 and Rh_0 for all HTP sub-regions (Currie et al., 2005; Cyr et al., 2005; Ding et al., 2014; Hoke et al., 2014; Rowley and Currie, 2006; Rowley et al., 2001; Xu et al., 2013). Furthermore other climatic parameters that control $\delta^{18}O$, such as precipita-

tion amount (Risi et al., 2008), climate aridity (Frankenberg et al., 2009) and non-adiabatic temperature changes (Ehlers and Poulsen, 2009) were not taken into account in this one-dimensional model (Rowley and Garzione, 2007; Rowley et al., 2001).

Results

Simulated $\delta^{18}O$ values are consistent with sparse observations from the International Atomic Energy Agency (IAEA) Global Network of Isotopes in Precipitation that allow us to use the model for the purpose of this study (see Figure 8 in Section 3.4). The modern annual averaged isotopic distribution is characterized by very depleted (down to -18 ‰) values over the Himalayas and the southern Tibet and a shift to more positive values (ranging from -10 to -8 ‰) over northern TP and Kunlun, from 30° N to 35° N. Precipitation $\delta^{18}O$ over Tarim Basin and northern margins of TP experiences an abrupt decrease, with values down to -16 ‰ (Figure 3.1). Based on observations of modern $\delta^{18}O$ in precipitation and its relationship with temperature and precipitation amount, TP and Himalayas were divided into three regions (Yao et al., 2013): the southern one located between 25° N and 30° N, the central one located between 30° N and 35° N and the northern one located between 35° N and 40° N (Figure 3.1). Below we provide a comparison of the isotopic lapse rates for these regions, obtained by considering simulated precipitation $\delta^{18}O$ against associated gridpoint elevation.

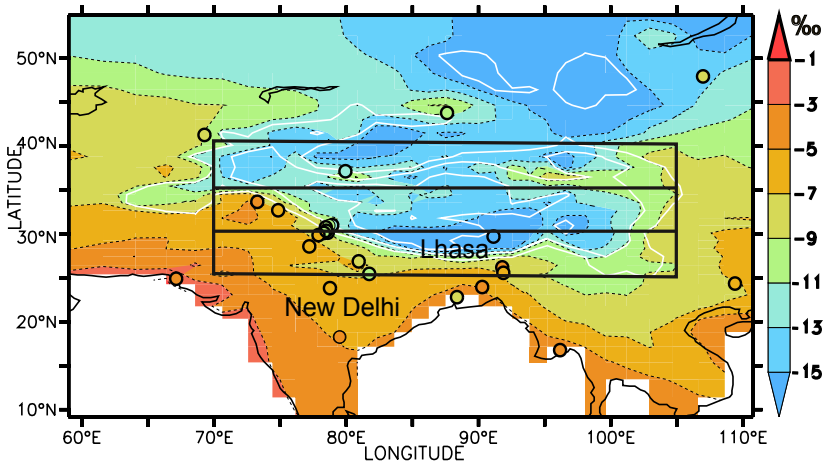

Figure 3.1 – LMDZ-iso simulated $\delta^{18}O$ in precipitation. Colored points show data from Global Network of Isotopes in Precipitation observations data set. For more detailed model-data comparison see Section 3.4

For the southern region, a second order polynomial approximation of simulated $\delta^{18}O_p$ as a function of altitude is in reasonable agreement with the relationship proposed by Rowley (2007); Rowley et al. (2001)(Figure 3.2a). Still, residuals from this polynomial regression do not have a constant variance as one may expect from a classical regression scheme. This implies that a more complex statistical model is needed to accurately capture variability changes. A flexible and statistically convenient approach is to postulate a change point (a discontinuity) that leads to two possibly non-linear behaviours for two different altitude ranges. This statistical strategy can be implemented by fitting two cubic

smoothing splines, low and high altitudes, respectively. Statistically the optimal breaking point is found by using square residuals method and corresponds to -6 ‰ for the southern region and 5 ‰ for the central. Constrained with a method described in (Hastie et al., 2009) relationships for high (that exceeds 4000 m) and low (less then 4000 m) elevations of the HTP appeared to be very close to linear (Figure 3.2a,b). For the central region and for a fixed $\delta^{18}O_p$, the Rowley's relationship provides an elevation systematically underestimated compared with the likely range of elevations obtained with our GCM isotope enabled simulation (Figure 3.2b). In the northern part of TP, simulated $\delta^{18}O$ values are highly scattered and no relationship between $\delta^{18}O$ and elevation can be constructed, compromising $\delta^{18}O$-based paleoaltimetry for this specific region (Figure 3.2c).

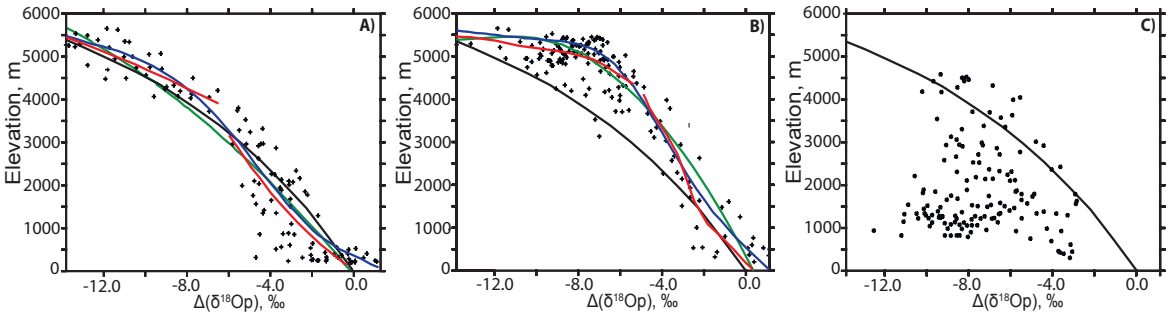

Figure 3.2 – Isotopic lapse rates for A) southern region (between 25° N and 30° N), B) central part (between 30° N and 35° N) and C) northern part (between 35 ° N and 40° N) of the TP and Himalayas. Points - model derived $\delta^{18}O$ in precipitation. Black line shows relationship from the empirical model (Rowley and Garzione, 2007; Rowley et al., 2001). Green line shows second order polynomial approximation of simulated $\delta^{18}O$ values. Blue line shows cubic-spline approximation. Red lines show independent cubic-spline approximation for two altitudinal ranges.

For the Himalayas and southern TP, air masses mainly originate from the Indian Ocean and get advected to this region via the Indian plain by the monsoon circulation. Therefore, taking a low reference point (with T_0, Rh_0, V_0) located in New Delhi together with a Rayleigh-based model (Rowley and Garzione, 2007; Rowley et al., 2001) is an appropriate assumption for this region. Deviations from this model in some localities can be explained by the «amount effect», the empirical relationship largely known for oceanic tropical conditions Risi et al. (2008) and for Asia monsoonal areas (Yang et al., 2011).

Water-tagging capabilities of the model allow us to estimate the relative contribution of different moisture sources to the water budget of the HTP (Figure 3.3a). Only the southeastern part of the HTP is mainly controlled by the Indian Ocean precipitation. In the central and northern parts of the TP, moisture comes from a complex mixture of air masses originating from different sources. At least three air masses feed the area, one coming from the South associated with the Indian monsoon, one coming from the southeast linked with the East-Asian monsoon, and one coming from the West associated to the westerlies. Besides this complex mixing of various water vapor sources, the isotopic composition of the water vapor also changes due to the contribution of the local continental recycling over the plateau (Figure 3.3a). The TP also is more isolated from ocean basins northward which results in an increase in local recycling contribution to precipitation balance. Extremely depleted $\delta^{18}O$ values over Tarim Basin and northern margins of

TP are probably due to strong large-scale subsidence of air that has undergone thorough distillation in these desert regions (Frankenberg et al., 2009).

We discuss these results together with the conclusions of the study presented in our paper published in the *Climate of the Past* in Section 3.5.

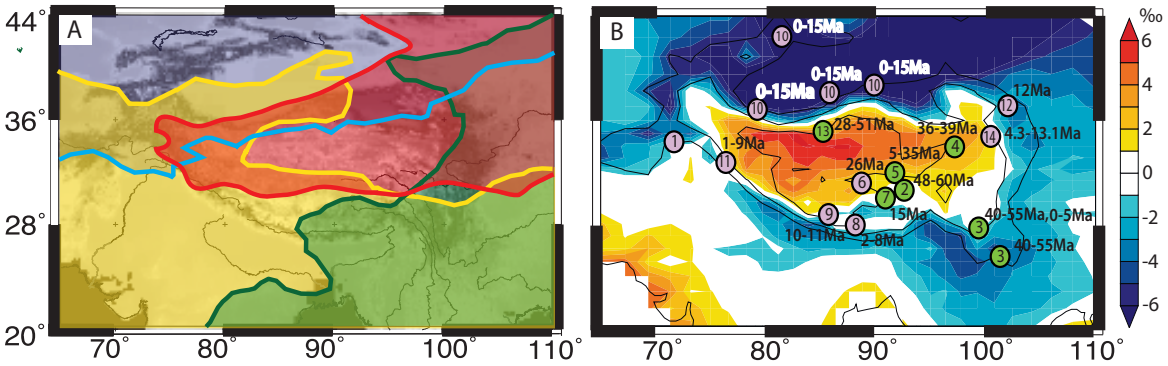

Figure 3.3 – A) Mean annual relative contributions of Indian (more then 15 % of total precipitation - yellow shade), the Atlantic Ocean and Mediterranean Sea (more then 15 % of total precipitation - blue shade), continental recycling (more then 40 % of total precipitation - red shade) and the Pacific Ocean (more then 15 % - green shade) moisture sources. B) Difference between the $\delta^{18}O$ simulated by LMDZ-iso and the $\delta^{18}O$ predicted by the Rowley polynomial. Numbered circles show existing studies isotopic studies of paleoelevations from: 1) Quade and Cerling (1995); Stern et al. (1997); 2)Ding et al. (2014); 3)Hoke et al. (2014); 4) Cyr et al. (2005); 5) Rowley and Currie (2006); 6) DeCelles et al. (2007); 7) Currie et al. (2005); 8) Dettman et al. (2001); Quade and Cerling (1995); 9) Garzione et al. (2000b); 10) Kent-Corson et al. (2009); 11) Sanyal et al. (2004a); 12) Dettman et al. (2003); 13) Xu et al. (2013); 14) Fan et al. (2007). Green cycles correspond studies that use Rowley's polynomial for paleoelevation reconstructions.

3.3 Controls of paleo delta $\delta^{18}O$

Nowadays it is quite well understood that climate changes through past may be crucial for paleo $\delta^{18}O_p$ (Sturm et al., 2010). However, empirical paleoclimate reconstructions using oxygen stable isotopes are based on the assumption of stationarity of $\delta^{18}O$-elevation relationship through geological time (Sturm et al., 2010), because paleo $\delta^{18}O$ and its link with paleoclimate is uncertain. Although theoretic present-day $\delta^{18}O$-elevation relationship was validated against data for the Himalayas region and the southern Tibetan Plateau, Rowley et al. (2001) and other authors (Blisniuk and Stern, 2005) stressed the caution required for its application for paleoaltimetry.

To avoid limitation linked with uncertainty of paleo $\delta^{18}O$ and paleo $\delta^{18}O$-elevation relationships, isotopes-equipped AGCMs have been used for reconstructing paleo spatial distribution of $\delta^{18}O$ in meteoric waters under external forcing of increased atmospheric pCO_2 (Poulsen and Jeffery, 2011; Poulsen et al., 2007), increased sea surface temperatures (SSTs) (Sturm et al., 2010), sea level variations (Poulsen et al., 2007), and elevation variations of major orogens (Ehlers and Poulsen, 2009; Poulsen et al., 2010).

The HTP is particularly sensitive to climate change (Yao et al., 2013), and given the impact of paleoclimate changes to $\delta^{18}O$, especial caution should be exercised in case of

oxygen stable isotopes-based paleoelevations reconstructions for this region and studies of paleo $\delta^{18}O$ and its controls over the region are essential.

3.4 Article published in *Climate of the Past*: Impacts of Tibetan Plateau uplift on atmospheric dynamics and associated precipitation $\delta^{18}O$

In our article published in *Climate of the Past* we study the sensitivity of $\delta^{18}O$ to paleoclimate changes over Asia linked with the growth of the Himalayas and Tibetan Plateau. Our main goal is to understand to what extent topography changes explain the precipitation $\delta^{18}O$ signal over Himalayas and Tibetan Plateau (i.e. the direct topography effect) and what part of this signal depends on other climate processes. Based on the Rayleigh distillation we developed a theoretical expression of $\delta^{18}O$ with a purpose of numerical estimation of each controlling factors of total oxygen isotopic signal.

Clim. Past, 12, 1401–1420, 2016
www.clim-past.net/12/1401/2016/
doi:10.5194/cp-12-1401-2016

Climate of the Past
Open Access
EGU

Impacts of Tibetan Plateau uplift on atmospheric dynamics and associated precipitation $\delta^{18}O$

Svetlana Botsyun[1], Pierre Sepulchre[1], Camille Risi[2], and Yannick Donnadieu[1]

[1]Laboratoire des Sciences du Climat et de l'Environnement, LSCE/IPSL, CEA-CNRS-UVSQ, Université Paris-Saclay, Gif-sur-Yvette, France
[2]Laboratoire de Météorologie Dynamique, LMD/IPSL, UPMC, CNRS, Paris, France

Correspondence to: Svetlana Botsyun (botsyun.svetlana@gmail.com)

Received: 15 December 2015 – Published in Clim. Past Discuss.: 15 January 2016
Revised: 8 May 2016 – Accepted: 3 June 2016 – Published: 28 June 2016

Abstract. Palaeoelevation reconstructions of mountain belts have become a focus of modern science since surface elevation provides crucial information for understanding both geodynamic mechanisms of Earth's interior and the influence of mountain growth on climate. Stable oxygen isotopes palaeoaltimetry is one of the most popular techniques nowadays, and relies on the difference between $\delta^{18}O$ of palaeoprecipitation reconstructed using the natural archives, and modern measured values for the point of interest. Our goal is to understand where and how complex climatic changes linked with the growth of mountains affect $\delta^{18}O$ in precipitation. For this purpose, we develop a theoretical expression for the precipitation composition based on the Rayleigh distillation and the isotope-equipped atmospheric general circulation model LMDZ-iso outputs. Experiments with reduced height over the Tibetan Plateau and the Himalayas have been designed. Our results show that the isotopic composition of precipitation is very sensitive to climate changes related to the growth of the Himalayas and Tibetan Plateau. Specifically our simulations suggest that only 40 % of sampled sites for palaeoaltimetry depict a full topographic signal, and that uplift-related changes in relative humidity (northern region) and precipitation amount (southern region) could explain absolute deviations of up to 2.5 ‰ of the isotopic signal, thereby creating biases in palaeoelevation reconstructions.

1 Introduction

Despite ongoing debates regarding the thermal and mechanical nature of mechanisms involved (Boos, 2015; Chen et al., 2014), the Himalayas and the Tibetan Plateau (hereafter TP) have long been considered to exert major influences on Asian atmospheric dynamics, notably by reinforcing South Asian monsoon and driving subsidence ultimately leading to onsets of deserts over central Asia (Rodwell and Hoskins, 2001; Broccoli and Manabe, 1992). Thus, reconstructing the history of Himalayas and TP uplift appears crucial to understand the long-term climate evolution of Asia. In addition, understanding the timing and scale of surface elevation growth is crucial for reconstructing the rate and style of this tectonic plates convergence (e.g. Royden et al., 2008; Tapponnier et al., 2001).

Elevation reconstructions for the Tibetan Plateau and Himalayas are based on fossil-leaf morphology (e.g. Antal, 1993; Forest et al., 1999; Khan et al., 2014; Sun et al., 2015), pollen (Dupont-Nivet et al., 2008), correlation between stomatal density and the decrease in CO_2 partial pressure with altitude (McElwain, 2004), and carbonate oxygen isotopic compositions (Currie et al., 2005; DeCelles et al., 2007; Garzione et al., 2000a; Li et al., 2015; Rowley and Currie, 2006; Saylor et al., 2009; Xu et al., 2013). In contrast to palaeobotanical methods, oxygen isotope palaeoaltimetry has been widely applied to the Cenozoic. Carbonate $\delta^{18}O$ is related to topography change using $\delta^{18}O$-elevation relationship. These relationships have been calibrated both empirically (Garzione et al., 2000b; Gonfiantini et al., 2001; Poage and Chamberlain, 2001) and theoretically, using ba-

sic thermodynamic principles, including Rayleigh distillation, that govern isotopic fractionation processes (Rowley and Garzione, 2007; Rowley et al., 2001).

The difference between palaeoprecipitation $\delta^{18}O$ detected from natural archives and modern values of the site of interest has been used to identify the effect of the surface uplift in numerous recent studies (Currie et al., 2005; Cyr et al., 2005; Ding et al., 2014; Hoke et al., 2014; Mulch, 2016; Rowley and Currie, 2006; Rowley et al., 2001; Xu et al., 2013). In the absence of direct measurements of "palaeo" altitude-$\delta^{18}O$ relationship in situ, stable isotope palaeoaltimetry is potentially hampered by the fact that the presumed constancy of altitude–$\delta^{18}O$ relationships through time might not be valid. For instance for the Andes, not considering the impact of uplift on climate dynamics and related $\delta^{18}O$ values has been shown to produce errors in palaeoelevation reconstruction reaching up to $\pm 50\,\%$ (Ehlers and Poulsen, 2009; Poulsen et al., 2010). Regional climate variables and associated isotopic signal in precipitation can also be affected by global climate change (Battisti et al., 2014; Jeffery et al., 2012; Poulsen and Jeffery, 2011). Moreover, it has been suggested that climate-driven changes in surface ocean $\delta^{18}O$ through the Cenozoic can also influence recorded values of precipitation $\delta^{18}O$ over the continent and corrections has been applied in some studies (Ding et al., 2014). Over TP, mismatches between palaeoelevation estimations from palynological and stable isotope data (e.g. Sun et al., 2014) could be related to complex climatic changes and associated variations of altitude-$\delta^{18}O$ relationship linked to the uplift, but still a detailed assessment of the consequences of topographic changes on precipitation $\delta^{18}O$ is lacking.

Spatial distribution of isotopes in precipitation was described using various types of models, from one-dimensional to three-dimensional general circulation (Craig, 1961; Dansgaard, 1964; Gedzelman and Arnold, 1994; Risi et al., 2010; Stowhas and Moyano, 1993). Such modelling studies show how large-scale Asian monsoon circulation influences precipitation $\delta^{18}O$ (He et al., 2015; LeGrande and Schmidt, 2009; Pausata et al., 2011; Vuille et al., 2005). At the global scale, precipitation $\delta^{18}O$ has been shown to be affected by several factors other than elevation, including mixing between air masses (Ehlers and Poulsen, 2009; Gat, 1996), large-scale subsidence (e.g. Frankenberg et al., 2009), continental recycling (Lee et al., 2012; Risi et al., 2013), deep convection (Risi et al., 2008), and enrichments linked to global warming (Poulsen and Jeffery, 2011). Numerous studies have investigated the impact of Asian topography on climate change, including the monsoon intensification (e.g. An et al., 2015; Harris, 2006; Kutzbach et al., 1989; Ramstein et al., 1997; Raymo and Ruddiman, 1992; Zhang et al., 2015) and Asian interior aridification onset (Broccoli and Manabe, 1992; Liu et al., 2015). Nonetheless, the linkage between these "climatic parameters" altered by the growth of TP and their influence on the isotopic signal remain unclear. In this article we use numerical modelling to provide some insights.

2 Methods

2.1 Model simulations

We use an atmospheric general circulation model (GCM) developed at Laboratoire de Météorologie Dynamique, Paris, France with isotopes-tracking implement, called LMDZ-iso (Risi et al., 2010). LMDZ-iso is derived from the LMDz model (Hourdin et al., 2006) that has been used for numerous future and palaeoclimate studies (Ladant et al., 2014; Pohl et al., 2014; Sepulchre et al., 2006). Water in a condensed form and its vapour are advected by the Van Leer advection scheme (Van Leer, 1977). Isotopic processes in LMDZ-iso are documented in (Risi et al., 2010). Evaporation over land is assumed not to fractionate, given the simplicity of the model surface parameterisation (Risi et al., 2010). Yao et al. (2013) have provided a precise description of rainfall patterns over the TP, and showed LMDZ-iso ability to simulate atmospheric dynamics and reproduce rainfall and $\delta^{18}O$ patterns consistent with data over this region.

LMDZ-iso is also equipped with water tagging capabilities, allowing us to quantify different moisture contributions from continental and oceanic evaporation sources. The advantage of this technique compared to typical back-trajectories methods is that it tracks the water rather than air masses, thus taking into account effects of phase changes. In our simulations five potential moisture sources are considered: (1) continental sources, (2) Indian Ocean, (3) Atlantic Ocean, (4) Mediterranean Sea, and (5) Pacific Ocean.

We use a model configuration with 96 grid points in longitude, 72 in latitude and 19 vertical layers, with the first four layers in the first kilometre above the surface. LMDZ-iso has a stretchable grid that allows increased spatial resolution over a defined region. In our case, it gives an averaged resolution of ~ 100 km over central Asia, which is a good trade-off between a reasonable computing time and a spatial resolution that adequately represents main features of TP topography.

Here we report results from three experiments designed to isolate the influence of Asian topography on climate and isotopic composition of precipitation. Topography is derived from a 10 min US Navy dataset and interpolated to the model grid. The control run (MOD) is a pre-industrial run, i.e. initialised with boundary conditions (insolation, greenhouse gases, sea surface temperatures (SSTs), topography) kept at pre-industrial values. For the two other experiments, we keep all boundary conditions (including albedo, rugosity, and vegetation distribution) similar to those in MOD run, except for the topography. We reduce the altitude over the area covering the Tibetan Plateau, Himalayas and a part of surrounding mountains: Tian Shan, Pamir, Kunlun and Hindu Kush to 50 % of modern elevations (intermediate, INT case) and to 250 m elevation (low, LOW case) (Fig. 1). SSTs for all runs come from the AMIP dataset (monthly SSTs averaged from 1979 to 1996; Taylor et al., 2000). Each experiment has been

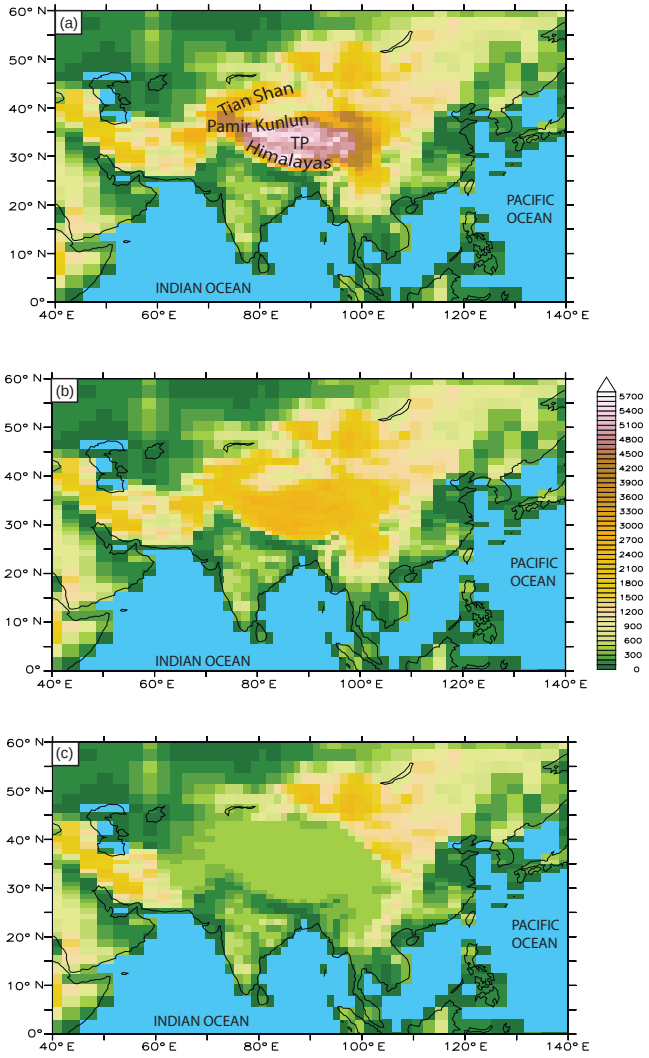

Figure 1. Models design **(a)** 100 % of modern topography – MOD case; **(b)** Tibetan Plateau, Himalayas, Tian Shan, Pamir, Kunlun and Hindu Kush elevations reduced to 50 % of modern elevation – INT case; **(c)** Tibetan Plateau, Himalayas, Tian Shan, Pamir, Kunlun and Hindu Kush elevations reduced to 250 m – LOW case.

run for 20 years. We analyse seasonal means over the last 18 years, as the two first years are extracted for spin-up.

2.2 Theoretical framework for the precipitation composition

Our goal is to understand to what extent topography changes explain the precipitation δ^{18}O signal over TP (i.e. the direct topography effect) and what part of this signal depends on other climate processes. To do so, we develop a theoretical expression for the precipitation composition.

To the first order, the δ^{18}O composition of the precipitation R_p follows that of the vapour R_v. Deviations from the vapour composition, $\varepsilon = R_p - R_v$, are associated with a local

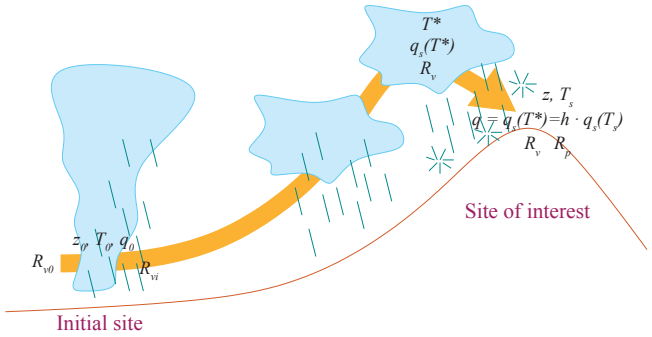

Figure 2. Idealized framework of an isolated air parcel transported from an initial site at low altitude to the site of interest. Most notations are illustrated.

condensational or post-condensational process.

$$R_p = R_v + \varepsilon \quad (1)$$

In an idealized framework of an isolated air parcel transported from an initial site at low altitude to the site of interest (Fig. 2), the vapour composition can be predicted by Rayleigh distillation:

$$R_v = R_{v0} \times f^{\alpha - 1} + dR_v, \quad (2)$$

where R_{v0} is the initial composition of the vapour at the initial site; α is the fractionation coefficient that depends on temperature and on the water phase (Majoube, 1971; Merlivat and Nief, 1967); and f is the residual fraction of the vapour at the site of interest relatively to the initial site of an air mass ascent. We take the initial site as characterised by a temperature and humidity T_0 and q_0. Under these conditions, R_{v0} is the theoretical isotopic composition of vapour that it would have if all the vapour originated from the local evaporation over quiescent oceanic conditions. Depending on the atmospheric circulation, on deep convective and mixing processes and on the source region of water vapour, the isotopic composition of vapour may deviate from the Rayleigh distillation by dR_v.

The residual fraction f depends on the specific humidity q at the site of interest:

$$f = q/q_0. \quad (3)$$

The air is not always saturated near the surface, therefore:

$$q = h \times q_s(T_s), \quad (4)$$

where h and T_s are the relative humidity and air temperature near the surface of the site of interest. The air can be under-saturated because it can be considered as air that has been transported adiabatically from the area of minimum condensation temperature, T^* (Galewsky and Hurley, 2010; Galewsky et al., 2005; Sherwood, 1996): $q = q_s(T^*)$.

The surface temperature can be predicted to first order by the adiabatic lapse rate, Γ, and is modulated by the non-adiabatic component dT_s that represents processes such as large-scale circulation or radiation:

$$T_s = T_0 + \Gamma \times (z - z_0) + dT_s, \quad (5)$$

where z and z_0 are the altitudes at the site of interest and at the initial site. We use an adiabatic lapse rate equal to $-5\,km^{-1}$ based on the measurements of modern observed mean temperature lapse rate on the southern slope of the central Himalayas, that ranges from -4.7 to $-6.1\,km^{-1}$ for the monsoon season and from -4.3 to $-5.5\,km^{-1}$ for the rest of the year (Kattel et al., 2015).

If we combine Eqs. (1) to (5), we get that R_v is a function of ε, dR_v, h, dT_s and z:

$$R_p = R_{v0} \times \left[h \times q_s (T_0 + \Gamma \times (z - z_o) + dT_s)/q_0\right]^{\alpha - 1} + dR_v + \varepsilon. \quad (6)$$

Or in a simpler form:

$$R_p = R_p(\varepsilon, dR_v, h, dT_s, z). \quad (7)$$

Parameters z_0, q_0, T_0 are reference values that are common to all sites of interest, all climates and geographies. Even if initial conditions for the Rayleigh distillation vary depending on the atmosphere circulation, on deep convective processes and on the site of interest, we keep the same reference values and we consider all variations in initial conditions are accommodated by dR_v.

This model is equivalent to that of Rowley et al. (2001) for $dR_v = 0$ (i.e. neglecting the effects of mixing and deep convection on the initial water vapour), $\varepsilon = (\alpha - 1) \times R_v$ (i.e. neglecting post-condensational effects), and $h = 1$ (i.e. assuming the site of interest is inside the precipitating cloud).

2.3 Decomposing precipitation composition differences

Our goal is to understand why R_p varies from one climatic state to another. We refer to these climatic states using subscript 1 and 2 and to their difference using the Δ notation. Differences between INT and LOW and between MOD and INT climatic states correspond to the initial and the terminate stages of the TP uplift respectively. We decompose $\Delta R_p = R_{p2} - R_{p1}$ into contribution from ΔdR_v, $\Delta\varepsilon$, Δh, ΔdT_s, and Δz:

$$\Delta R_p = \Delta R_{p,\Delta\varepsilon} + \Delta R_{p,\Delta dR_v} + \Delta R_{p,\Delta h} + \Delta R_{p,\Delta dT_s} + \Delta R_{p,\Delta z} + N, \quad (8)$$

where $\Delta R_{p,\Delta\varepsilon}$, $\Delta R_{p,\Delta dR_v}$, $\Delta R_{p,\Delta h}$, $\Delta R_{p,\Delta dT_s}$, and $\Delta R_{p,\Delta z}$ are the contributions of ΔdR_v, $\Delta\varepsilon$, Δh, ΔdT_s, and Δz to ΔR_p. Non linear terms of decomposition are gathered into the residual term N. Contributions are estimated using Eq. (7) (see also Table 1):

$$R_{p,\Delta\varepsilon} = R_p(\varepsilon_2, dR'_v, h', dT'_s, z') - R_p(\varepsilon_1, dR'_v, h', dT'_s, z') \quad (9)$$

$$R_{p,\Delta dR_v} = R_p(\varepsilon', dR_{v2}, h', dT'_s, z') - R_p(\varepsilon', dR_{v1}, h', dT'_s, z') \quad (10)$$

$$R_{p,\Delta h} = R_p(\varepsilon', dR'_v, h_2, dT'_s, z') - R_p(\varepsilon', dR'_v, h_1, dT'_s, z') \quad (11)$$

$$R_{p,\Delta dT_s} = R_p(\varepsilon', dR'_v, h', dT_{s2}, z') - R_p(\varepsilon', dR'_v, h', dT_{s1}, z') \quad (12)$$

$$R_{p,\Delta z} = R_p(\varepsilon', dR'_v, h', dT'_s, z_2) - R_p(\varepsilon', dR'_v, h', dT'_s, z_1). \quad (13)$$

In order to decrease the sensitivity of the decomposition to the state at which it has been calculated we take z', dT'_s, h', dR'_v, and ε' as centred differences:

$$z' = (z_2 + z_1)/2 \quad (14)$$

$$dT'_s = (dT_{s2} + dT_{s1})/2 \quad (15)$$

$$h' = (h_2 + h_1)/2 \quad (16)$$

$$dR'_v = (dR_{v2} + dR_{v1})/2 \quad (17)$$

$$\varepsilon' = (\varepsilon_2 + \varepsilon_1)/2. \quad (18)$$

Note that ε' in Eqs (10) to (13) and dR'_v in Eqs. (9) and (11) to (13) can be replaced by 0 without changing the result. Parameters z, dT_s, h, dR_v, and ε are diagnosed for the climatic states 1 and 2 from LMDZ-iso simulations (e.g. for pairs of experiments, MOD and INT cases). Parameter ε is estimated as $\varepsilon = R_p - R_v$, where R_p and R_v are isotopic ratios simulated by LMDZ-iso. Parameter h is the relative humidity simulated by LMDZ-iso. Altitude z is a prescribed boundary condition of the simulations. Parameter dR_v is estimated by calculating the difference between the water vapour isotopic ratio simulated by LMDZ-iso ($R_{v,LMDZ}$) and that predicted by Rayleigh distillation if the initial water vapour isotopic ratio is R_{v0}:

$$dR_v = R_{v,LMDZ} - R_{v0} \times (q/q_0)^{\alpha - 1}, \quad (19)$$

where q is the specific humidity simulated by LMDZ-iso and α is the isotopic fractionation as a function of the near-surface air temperature T_s simulated by LMDZ-iso. Parameter dT_s is estimated from Eq. (5) by calculating the difference between the near-surface air temperature simulated by LMDZ-iso and that predicted by the adiabatic lapse rate:

$$dT_s = T_s - T_0 - \Gamma \times (z - z_0). \quad (20)$$

All the isotopic decomposition terms computed are weighted by the precipitation amount.

Table 1. Table detailing how the different terms of the decomposition for ΔR_p, as written in Eq. (7), are estimated.

Term written with differential format	Estimate of these terms	Physical meaning
ΔR_p	$R_p(dR_{v2}, \varepsilon_2, h_2, dT_{s2}, z_2) - R_p(dR_{v1}, \varepsilon_1, h_1, dT_{s1}, z_1)$	Total isotopic difference between state 2 and state 1
$\Delta R_{p,\Delta z}$	$R_p(\varepsilon', dR'_v, h', dT'_s, z_2) - R_p(\varepsilon', dR'_v, h', dT'_s, z_1)$	Direct effect of topography change
$\Delta R_{p,\Delta dT_s}$	$R_p(\varepsilon', dR'_v, h', dT_{s2}, z') - R_p(\varepsilon', dR'_v, h', dT_{s1}, z')$	Effect of lapse rate change, associated with non-adiabatic effects, possibly due to changes in surface energy budget or in large-scale atmospheric stratification
$\Delta R_{p,\Delta h}$	$R_p(\varepsilon', dR'_v, h_2, dT'_s, z') - R_p(\varepsilon', dR'_v, h_1, dT'_s, z')$	Effect of local relative humidity change, possibly due to large-scale circulation changes
$\Delta R_{p,\Delta \varepsilon}$	$R_p(\varepsilon_2, dR'_v, h', dT'_s, z') - R_p(\varepsilon_1, dR'_v, h', dT'_s, z')$	Effect of changes in condensational and post-condensational effects, possibly due to changes in rain reevaporation processes
$\Delta R_{p,\Delta dR_v}$	$R_p(\varepsilon', dR_{v2}, h', dT'_s, z') - R_p(\varepsilon', dR_{v1}, h', dT'_s, z')$	All other effects, including effects of deep convection, mixing, water vapour origin, continental recycling on the initial water vapour

2.4 Robustness of the decomposition

First, to check whether the linear decomposition is a good approximation of the total R_p change, we estimate the non-linear term N as a residual, i.e. for each pair of states, we calculate the deviation of $\Delta R_p = R_p(\varepsilon_2, dR_{v2}, h_2, dT_{s2}, z_2) - R_p(\varepsilon_1, dR_{v1}, h_1, dT_{s1}, z_1)$ from LMDZ-simulated isotopic differences between the two experiments. N represents less than 17 % of the total R_p change for both stages of TP uplift.

Our method to estimate the terms in Eq. (7) is equivalent to first order approximation of partial derivatives, i.e. we neglect the sensitivity of the partial derivatives to the state at which they are calculated. We tested this sensitivity by using Eqs. (9) to (13) changing z' to z_1 or z_2, dT'_s to dT_{s2} or dT_{s1} and so on. For example, in Eq. (13), replacing h' with h_1 changes the resulting $R_{p,\Delta z}$ by 0.03 ‰, replacing h' with h_2 has an impact of 0.09 ‰. In the same equation, replacing dT'_s with dT_{s1} and with dT_{s2} contributes to $R_{p,\Delta z}$ with 0.005 and 0.039 ‰ respectively. As it was highlighted earlier, replacing ε' and dT'_s with ε_1 or ε_2 and dR_{v1} or dR_{v2} respectively has no impact to the resulting $R_{p,\Delta z}$ Thus, our method shows low sensitivity to the state.

Second, to check the influence of initial conditions R_{v0}, T_0 and q_0 on the decomposition, we estimate the sensitivity of the different contributions to changes in R_{v0}, T_0, and q_0, of 1 %, 1 K and 10 % respectively (Table 2). R_{v0} is the parameter that influences most of the decomposition terms, with a maximal sensitivity of 0.9 ‰ obtained for $\Delta R_{p,\Delta z}$ for a change of 1 ‰ in R_{v0}. Sensitivity to temperature and humidity is lower, ranging from 0 to 0.6 ‰. Overall, all the decomposition terms show a sensitivity < 1 ‰ with most (82 %) of them < 0.5 ‰, making our decomposition method robust.

3 Results

3.1 Model validation in terms of simulated climate variables

LMDZ has been used for numerous present-day climate and palaeoclimate studies (Kageyama et al., 2005; Ladant et al., 2014; Sepulchre et al., 2006), including studies of monsoon region (e.g. Lee et al., 2012; Licht et al., 2014). Yao et al. (2013) showed that LMDZ-iso has the best representation of the altitudinal effect compared to similar GCM and RCM models. These authors have also provided a detailed description of rainfall patterns over the Tibetan Plateau, and showed LMDZ-iso ability to simulate atmospheric dynamics and reproduce rainfall and $\delta^{18}O$ patterns consistent with data over this region. For the purpose of our experiments validation, we compare MOD experiment outputs with rainfall data from the Climate Research Unit (CRU) (New et al., 2002) (Fig. 3a, b, c). When compared to CRU dataset, MOD annual rainfalls depict an overestimation over the high topography of the Himalayas and the southern edge of the Plateau, with a rainy season that starts too early and ends too late in the year. Over central Tibet (30–35° N), the seasonal cycle is well captured by LMDz-iso, although monthly rainfall is

Table 2. INT-LOW and MOD-INT sensitivity of the decomposition terms (in ‰) to the changes of R_{v0}, T_0, q_0, of 1 ‰, 1 K and 10 % respectively.

	Northern region			Southern region		
	T_0	q_0	R_{v0}	T_0	q_0	R_{v0}
INT-LOW experiment						
$\Delta R_{p,\Delta z}$	0.08	0.33	0.67	0.07	0.25	0.51
$\Delta R_{p,\Delta dT_s}$	0.01	0.02	0.04	0.07	0.06	0.13
$\Delta R_{p,\Delta h}$	0	0.35	0.66	0	0.19	0.83
$\Delta R_{p,\Delta dR_v}$	0	0	0.05	0	0	0.52
$\Delta R_{p,\Delta \varepsilon}$	0	0	0	0	0	0
MOD-INT experiment						
$\Delta R_{p,\Delta z}$	0.21	0.6	0.8	0.17	0.59	0.9
$\Delta R_{p,\Delta dT_s}$	0.2	0.09	0.18	0.19	0.02	0.05
$\Delta R_{p,\Delta h}$	0	0.58	0.6	0	0.37	0.27
$\Delta R_{p,\Delta dR_v}$	0	0	0.65	0	0	0.67
$\Delta R_{p,\Delta \varepsilon}$	0	0	0	0	0	0

always slightly overestimated (+0.5 mm day^{-1}). CRU data show that the northern TP (35–40°N) is drier with no marked rainfall season and a mean rainfall rate of 0.5 mm day^{-1}. In MOD experiment, this rate is overestimated (1.5 mm day^{-1} on annual average). Despite these model data mismatches, the ability of LMDZ-iso to represent the seasonal cycle in the south and the rainfall latitudinal gradient over the TP allows its use for the purpose of this study.

Our MOD simulation is pre-industrial, consequently a comparison with modern data is expected to provide differences driven by the pre-industrial boundary conditions. Still comparing LMDZ-iso outputs with mean annual temperatures from CRU dataset (New et al., 2002) (Fig. 3d, e, f) and relative humidity from NCEP-DOE Reanalysis (Kanamitsu et al., 2002) (Fig. S1 in Supplement) shows that LMDZ-iso model captures these variables reasonably well.

3.2 Impact of TP uplift on Asian climate

Theoretically, the Tibetan Plateau has both mechanical and thermal effects on atmospheric dynamics that induce increased monsoon activity to the south and drive arid climate to the north (Broccoli and Manabe, 1992; Sato and Kimura, 2005). Thus, modifying TP height is expected to alter these large-scale atmospheric dynamics and associated climate variables (namely temperature, precipitation, relative humidity (hereafter RH), cloud cover), and in turn to affect the isotopic signature of rainfall.

In LOW experiment, strong summer heating leads to the onset of a "Thermal Low" at the latitude of maximal insolation (ca. 32° N), similar to the present-day structure existing over the Sahara (Fig. S2). This structure is superimposed by large-scale subsidence linked to the descending branch

Table 3. Values of isotopic changes due to decomposed terms for two uplift stages and for two regions (see the text).

Term	Isotopic change (‰)			
	Initial stage		Terminal stage	
	South	North	South	North
$\Delta R_{p,\Delta z}$	−1.40	−2.00	−3.96	−4.55
$\Delta R_{p,\Delta dT_s}$	0.4	−0.09	0.76	−0.25
$\Delta R_{p,\Delta h}$	2.40	1.97	1.38	2.50
$\Delta R_{p,\Delta \varepsilon}$	−1.30	−1.73	−0.41	0.01
$\Delta R_{p,\Delta dR_v}$	−1.10	−0.14	−2.38	−0.54
Total ΔR_p	−1.00	−1.99	−4.61	−3.16

of the Hadley cell, and both factors act to drive widespread aridity over the TP area between ca. 30 and 40° N, associated with very low (< 40 %) RH values (Fig. S2). Subsidence also prevents the development of South Asian monsoon over the north Indian plane and favours aridity over this region. In winter, large-scale subsidence induces high surface pressures and creates an anticyclonic cell that prevents convection and humidity advection, resulting in low RH and annual rainfall amount ranging from 50 to 500 mm over the TP area (Fig. 4f).

Uplifting TP from 250 m above sea level (ASL) to half of its present-day altitude (INT case) initiates convection in the first tropospheric layers, restricting large-scale subsidence to the upper levels (Fig. 4c, e). In turn, South Asian monsoon is strengthened and associated northward moisture transport and precipitation increase south of TP (Figs. 5, 6). As a consequence the hydrological cycle over TP is more active, with higher evaporation rates (Fig. 7d). Together with colder temperatures linked to higher altitude (adiabatic effect) (Fig. 7b), the stronger hydrological cycle drives an increase in RH (Fig. 7a) and cloud cover (Fig. S3). Another consequence of increased altitude is higher snowfall rates in winter and associated rise of surface albedo (Fig. S4). When added to the increased cloud cover effect, this last process contributes to an extra cooling of air masses over the Plateau. To the north of TP, the initial stage of uplift results in increased aridity (i.e. lower RH and rainfall) over the Tarim Basin region (Fig. 6). This pattern can be explained both by a barrier effect of southern topography and by stationary waves strengthening, which results in subsidence to the north of TP. This latter mechanism is consistent with pioneer studies which showed that mountain-related activation of stationary waves prevented cyclonic activity over Central Asia and induced aridity over this region (Broccoli and Manabe, 1992).

The impact of the terminal stage of TP uplift also drives an increase in RH over the Plateau, especially during summer time, when a very active continental recycling (Fig. S6) makes RH rise from 40 (INT) to 70 % (MOD). Precipitation

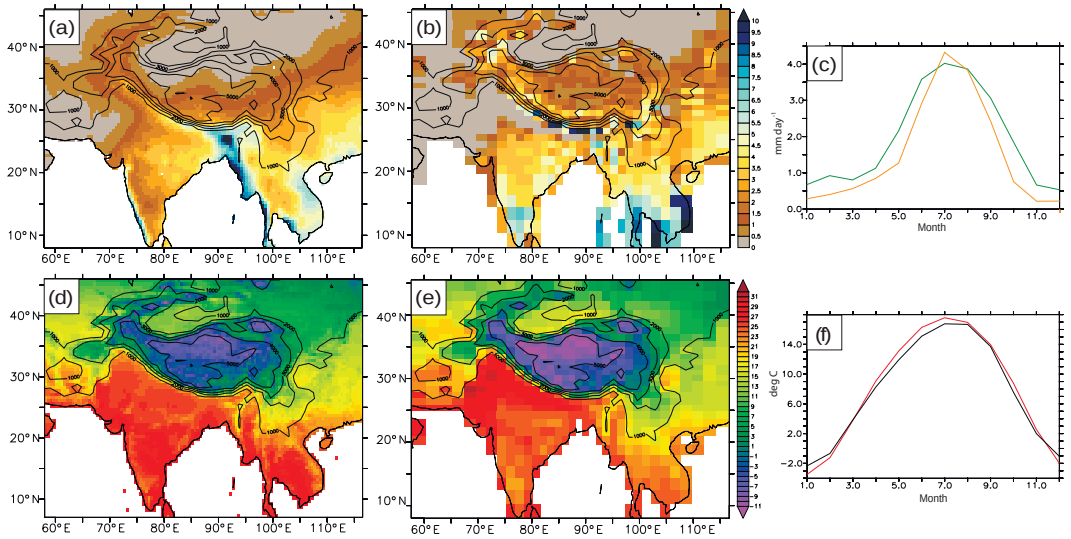

Figure 3. CRU dataset annual mean rainfall (mm/day) **(a)** and annual mean temperature (°C) **(d)** compared to simulated annual mean rainfall for MOD experiment **(b)** and simulated annual mean temperature for MOD experiment **(e)**. The seasonal cycles of averaged from 25 to 40° N and from 75 to 100° E for the MOD experiment precipitation **(c)** and temperature **(f)**. Green and red lines of figures **(c)** and **(f)** corresponds to MOD experiment, orange and black to the CRU dataset respectively.

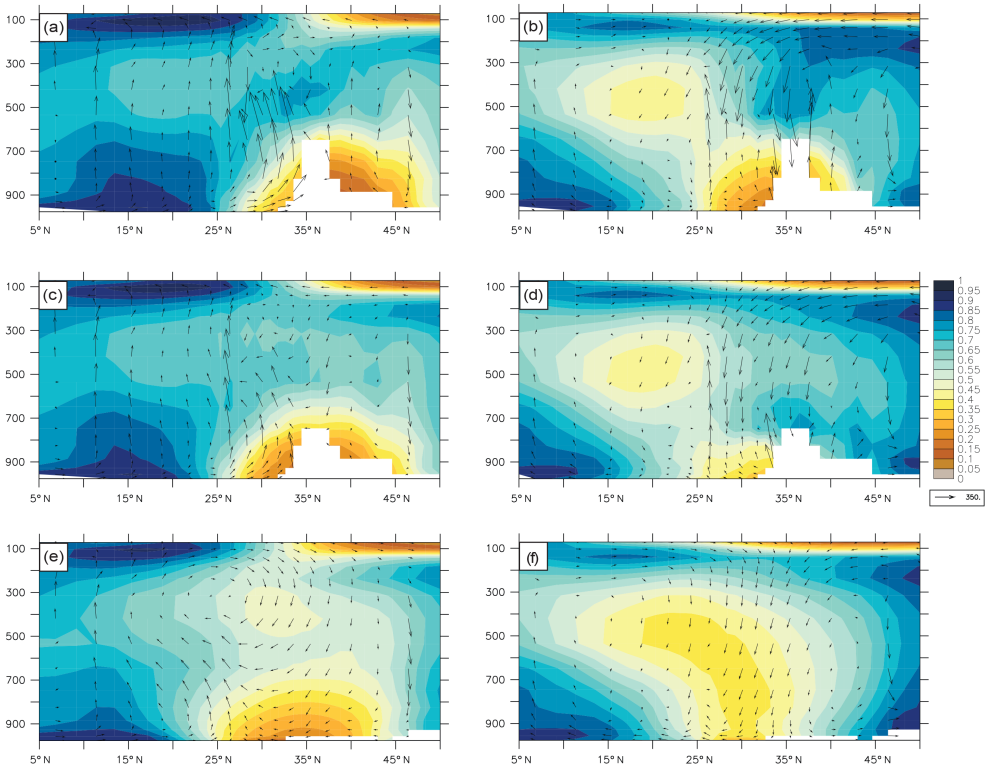

Figure 4. Cross-TP profiles (averaged between 70 and 90° E) showing the relative humidity and moisture transport for seasons **(a, c, e)** MJJAS and **(b, d, f)** ONDJFMA and for three simulations: **(a, b)** MOD, **(c, d)** INT, **(e, f)** LOW cases.

amount also increases significantly (Fig. 6), driven both by increased evaporation and water recycling during summer, and intense snowfall during winter. The latter contributes to the increase in the surface albedo and associated surface cooling during winter. Conversely, the uplift to a modern-like Plateau reduces RH (down to 30 %) north of the Plateau,

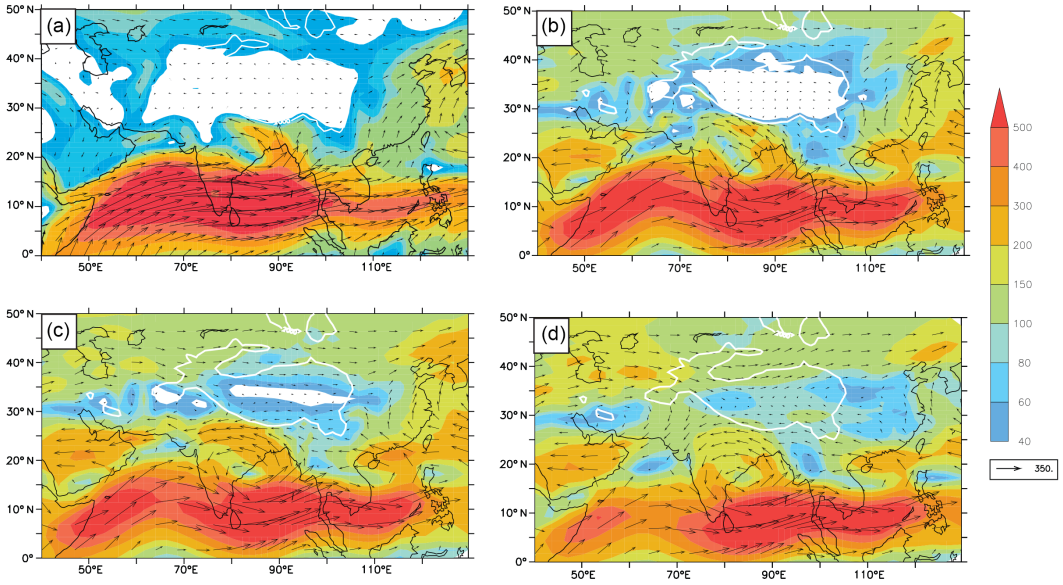

Figure 5. Directions and intensity of JJA vertically integrated humidity transport for: **(a)** averaged from ERA-40 re-analysis and for **(b)** MOD case, **(c)** INT case, **(d)** LOW case.

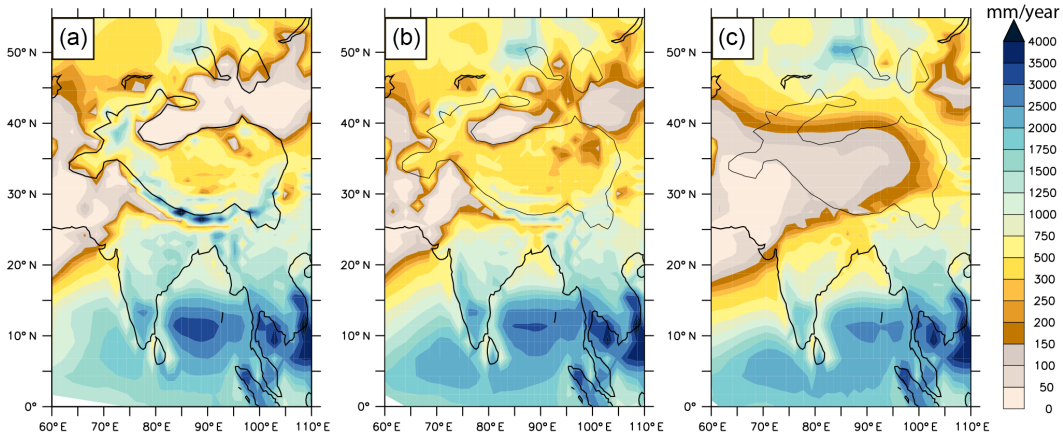

Figure 6. Annual mean precipitation amount (absolute values, mm yr^{-1}) for the following: **(a)** MOD case, **(b)** INT case, **(c)** LOW case.

and allows the onset of large arid areas. We infer that this aridification is linked to a mechanical blocking of moisture transport, both by Tian Shan topography for the winter westerlies, and the eastern flanks of TP for summer fluxes; despite changes in stationary waves structure and sensible heat (not shown), no marked shift in subsidence between INT and MOD experiments is simulated. This result is consistent with recent studies (Miao et al., 2012; Sun et al., 2009) that have suggested the potential contribution of Pamir and Tian Shan rainshadow effect to aridification in Qaidam Bassin and the creation of Taklamakan Desert.

3.3 Response of precipitation $\delta^{18}O$ to TP uplift

3.3.1 Model validation in terms of simulated precipitation $\delta^{18}O$

The modern mean annual isotopic distribution is characterised by very depleted values of $\delta^{18}O$ over the Himalayas and southern Tibet (down to $-18\,‰$) and a shift to more positive values (ranges from -11 to $-13\,‰$) over northern TP and Kunlun from 30 to 35° N. Precipitation $\delta^{18}O$ over Tarim Basin experiences an abrupt decrease compared to northern TP, with values down to $-16\,‰$ (Fig. 8a). Overall, simulated annual mean $\delta^{18}O_p$ are consistent with sparse observations from the International Atomic Energy Agency (IAEA) Global Network of Isotopes in Precipitation and $\delta^{18}O$ in precipitation measurements compiled from Quade et al. (2011),

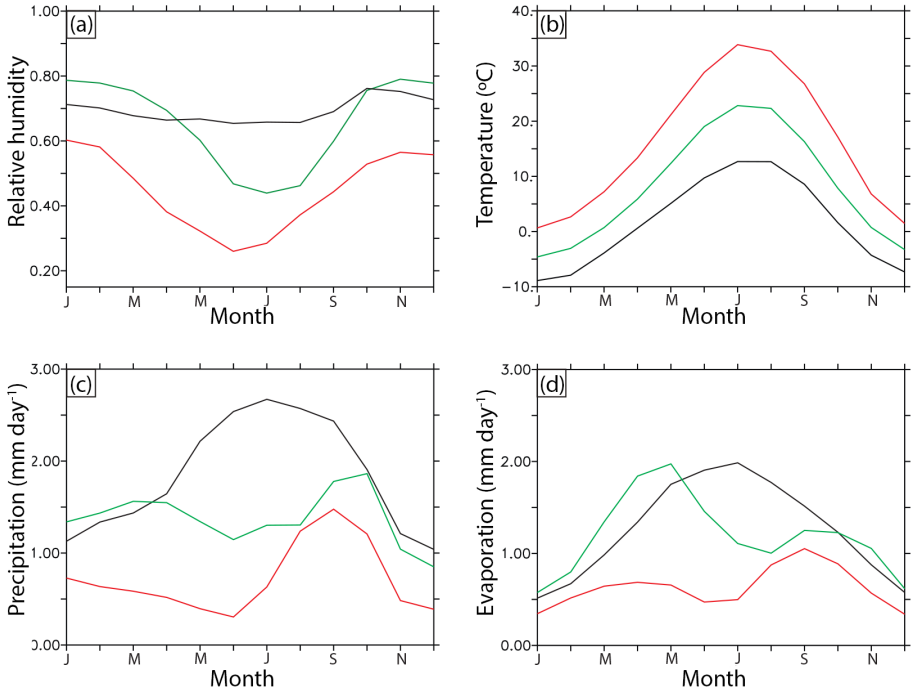

Figure 7. Intra-annual variations in **(a)** low level relative humidity, **(b)** near-surface temperature, **(c)** precipitation amount and **(d)** evaporation amount. All variables are averaged for TP with the altitude over 1500 m. Black colour corresponds to MOD experiment, green – for INT experiment and red – for LOW experiment.

Bershaw et al. (2012), Hren et al. (2009) and Caves et al. (2015) (Fig. 8a, b). In general, the model shows a good agreement with precipitation and VSMOW-weighted modern surface waters $\delta^{18}O$, including stream, lake and spring waters (data from Bershaw et al., 2012; Hren et al., 2009; Quade et al., 2011), as testified by a Pearson coefficient of 0.86 between modelled and observed precipitation $\delta^{18}O$ (Fi. 8c). This comparison shows the ability of LMDZ-iso to reproduce the decrease in $\delta^{18}O$ from the Indian subcontinent to the Himalayan foothills and with minimum values over the Himalayas. Simulated increase in $\delta^{18}O$ over the TP with the distance from the Himalayas is also consistent with data sampled along a southwest–northeast transect across the Plateau (Bershaw et al., 2012). However, over the northern margins of the TP, LMDZ-iso underestimates simulated $\delta^{18}O$ in precipitation (Fig. 8a). This model data mismatch may result from two types of uncertainties. First despite the high resolution obtained with a zoomed grid, restricted topographic features could not be well-captured over some parts of the TP, which could lead our simulations to miss local processes affecting $\delta^{18}O$ in rainfall. Second, overestimating the westerlies fluxes (see the comparison with the ERA moisture transport on Fig. 5a) could lead to underestimate $\delta^{18}O$ over the northern part of the TP, through advection of depleted air masses. Nevertheless, despite our model not capturing the absolute maximal values well, the regional latitudinal gradient is correctly represented, and most observed values are within the range of simulated $\delta^{18}O$ (Fig. 8b). We consider that the ability of LMDZ-iso to represent this gradient makes it reliable to carry out this study, which is focusing on sensitivity experiments with large changes in topography and associated anomalies in $\delta^{18}O$.

3.3.2 Simulated isotopic changes and signal decomposition

To first order, increasing topography over TP leads to more negative $\delta^{18}O$ over the region (Fig. 9). In the absence of topography, precipitation $\delta^{18}O$ follows a zonal pattern and undergoes a weak latitudinal depletion on the way to the continental interior, except from slight deviations over India, central China and the eastern part of the TP (Fig. 9b). At 40° N, i.e. the northern edge of modern TP, $\delta^{18}O$ values reach -9 ‰ in LOW case, compared to -14 ‰ in MOD case. For the INT case the latitudinal depletion from south to north is stronger (ca. 0.4 ‰ per latitudinal degree), with $\delta^{18}O$ values ranging from -6 ‰ for the lowered Himalayas foothills to -11 ‰ for northern and eastern margins of TP (Fig. 9a).

The total difference in isotopic composition of precipitation, ΔR_p, between pairs of experiments (INT-LOW, MOD-INT) is significant beyond the areas where the topography was reduced by the experimental design (Figs. 10a, 11a). Substantial differences in $\delta^{18}O$ between MOD and INT experiments are simulated over the southern TP (up to 10 ‰)

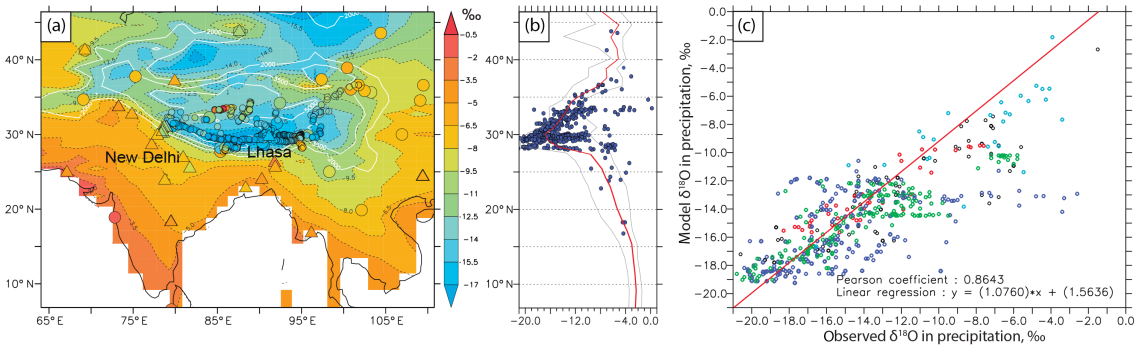

Figure 8. **(a)** Annual mean $\delta^{18}O$ in precipitation simulated by LMDZ-iso for MOD case. Triangles show $\delta^{18}O$ in precipitation from GNIP stations, big circles – $\delta^{18}O$ in precipitation from Caves et al. (2015) compilation (annual mean and JJA values respectively), small circles represent $\delta^{18}O$ in streams, lakes and springs compiled from Quade et al. (2011), Bershaw et al. (2012), Hren et al. (2009). **(b)** S-N profiles of model simulated $\delta^{18}O$ for the MOD case. Blue points correspond to the same measured data as on **(a)**. The $\delta^{18}O$ profile is averaged between 75 and 105° E. Grey lines show minimum and maximum values for the selected range of longitudes. **(c)** Observed vs. modelled $\delta^{18}O$ in precipitation. The colour of circles corresponds to the data set: red – Bershaw et al. (2012), blue – Quade et al. (2011), green – Hren et al. (2009), black – Caves et al. (2015); light blue shows mean annual data from GNIP stations. Red line shows a linear regression.

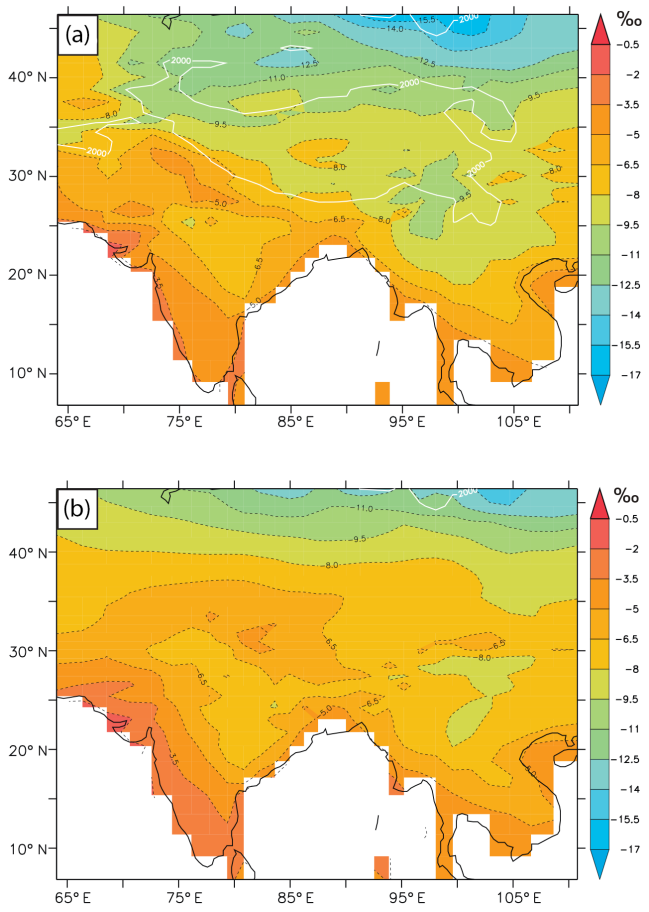

Figure 9. Annual mean $\delta^{18}O$ in precipitation simulated by LMDZ-iso for **(a)** INT case and **(b)** LOW case.

and over the Tarim Basin (up to 7 ‰). Between INT and LOW cases, the differences are over the margins of the TP, over Pamir, Tian Shan and Nan Chan. We should note that the isotopic difference becomes more important for the later stage of the plateau uplift. For clarity, we define two boxes, over the northern (from 34 to 38° N and from 88 to 100° E) and southern (from 27 to 33° N and from 75 to 95° E) part of TP (Fig. 12).

Direct topography effect on $\delta^{18}O$

The direct effect of topography change is determined as the decomposition term $\Delta R_{p,\Delta z}$ in Eq. (7). For the initial stage of the uplift, the altitude effect produces a decrease in precipitation $\delta^{18}O$ ranging from −1 to −3 ‰ (Fig. 10b). For the terminal stage of the uplift, the isotopic decrease linked with altitude goes up to −7 ‰ (Fig. 11b). Differences between both stages are linked to the non-linear relationship between $\delta^{18}O$ and elevation. Also for both stages, the difference between ΔR_p and $\Delta R_{p,\Delta z}$ is non-zero (Figs. 12a, 13a). These differences are particularly marked for the terminal stage, for which $\Delta R_{p,\Delta z}$ averages −5.5 ‰ over the northern part of TP (Fig. 13a, b), whereas the total isotopic change averages −3 ‰. Locally, the difference between $\Delta R_{p,\Delta z}$ and ΔR_p can reach +4 ‰. When averaged over the southern box, $\Delta R_{p,\Delta z}$ is less negative (−4 ‰) than ΔR_p (−4.6 ‰), with localised maximum differences reaching −4 ‰ (Table 3). Offsets between $\Delta R_{p,\Delta z}$ and ΔR_p are also detected for the initial stage of the uplift (Fig. 12a, b), but are lower: they reach +2 ‰ over central TP but barely reach 1 ‰ when averaged over southern and northern boxes. These offsets are related to additional effects of uplift on $\delta^{18}O$ that are discussed in the following sections.

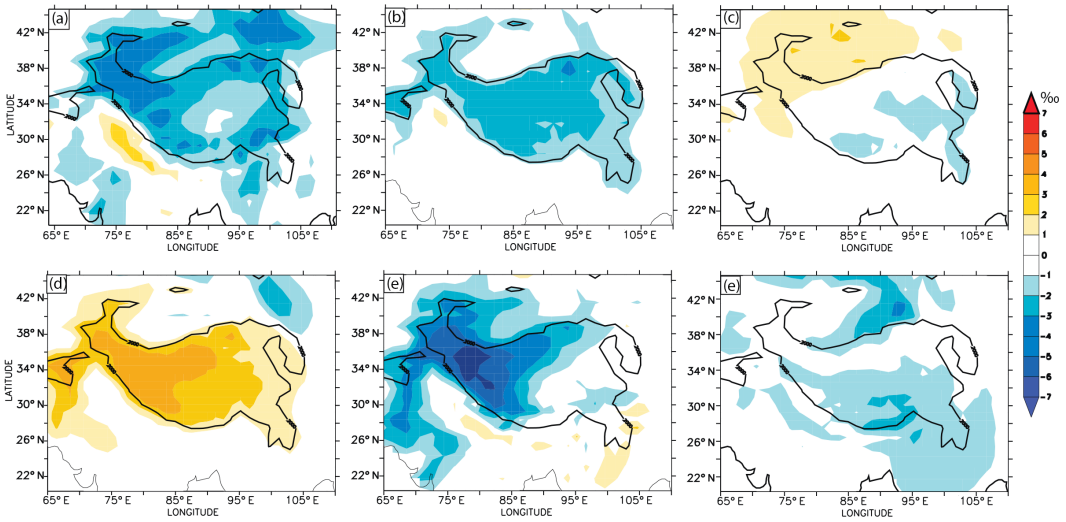

Figure 10. **(a)** Total isotopic difference between INT and LOW experiments (ΔR_p) and spatial isotopic variations related to the following: **(b)** direct effect of topography changes, **(c)** effect of lapse rate change, associated with non-adiabatic effects, **(d)** effect of local relative humidity change, **(e)** effect of changes in post-condensational processes, **(f)** all other effects (see Table 1).

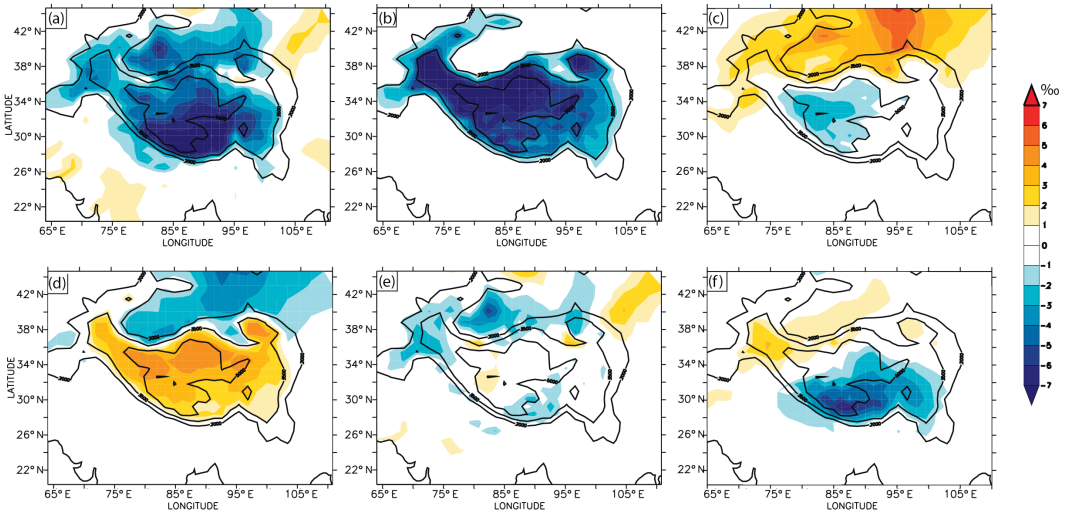

Figure 11. **(a)** Total isotopic difference between MOD and INT experiments (ΔR_p) and spatial isotopic variations related to the following: **(b)** direct effect of topography changes, **(c)** effect of lapse rate change, associated with non-adiabatic effects, **(d)** effect of local relative humidity change, **(e)** effect of changes in post-condensational processes, **(f)** all other effects (see Table 1).

Non-adiabatic temperature changes impact

Besides the adiabatic temperature effects linked with the TP uplift, non-adiabatic temperature changes can be identified, in relation with surface albedo and cloud cover changes depicted in Sect. 3.2.1. The term $\Delta R_{p,\Delta dT_s}$ in Eq. (7) (Table 1, line 3) is associated with these non-adiabatic effects, i.e. spatial variations of the temperature lapse rate. Figures 10c and 11c show the portion of the total isotopic signal that is linked to this effect. It plays a modest role for the early phase of uplift (+1–2 ‰ locally), but is more important for the second stage. It contributes to 2–5 ‰ of total isotopic difference, with a positive sign over southeast TP interior, TP northern margins and Asia interior. Negative anomalies have a magnitude of 2–3 ‰, but are less widespread, localised over the TP interior (Fig. 11c). Positive isotopic anomalies are associated with a steeper lapse rate than expected based on adiabatic processes. Conversely, negative $\delta^{18}O$ anomalies that are observed over northern TP and over Pamir are explained by a weaker lapse rate than adiabatic. Overall, these variations represent between 10 and 19 % (4–10 % for the initial stage) of the processes that are not linked to topography (Figs. 12d, e and 13d, e).

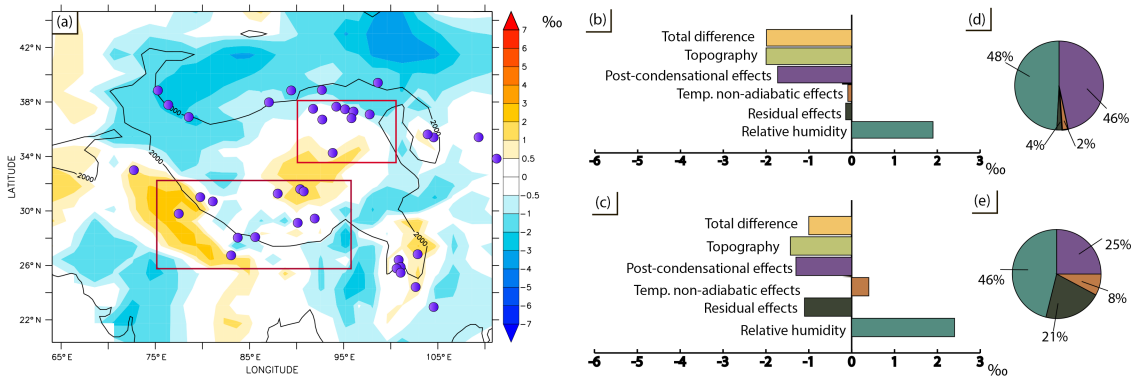

Figure 12. **(a)** Difference in $\delta^{18}O_p$ between INT and LOW experiments that is not related to direct effect of topography changes. Violet points show Cenozoic palaeoelevation study locations (compiled from Caves et al., 2015). Red rectangles show regions for that averaged values decomposed terms are shown: **(b)** northern region, **(c)** southern region. Pie diagrams show portion of total isotopic difference related to processes other then topography: **(d)** northern region, **(e)** southern region.

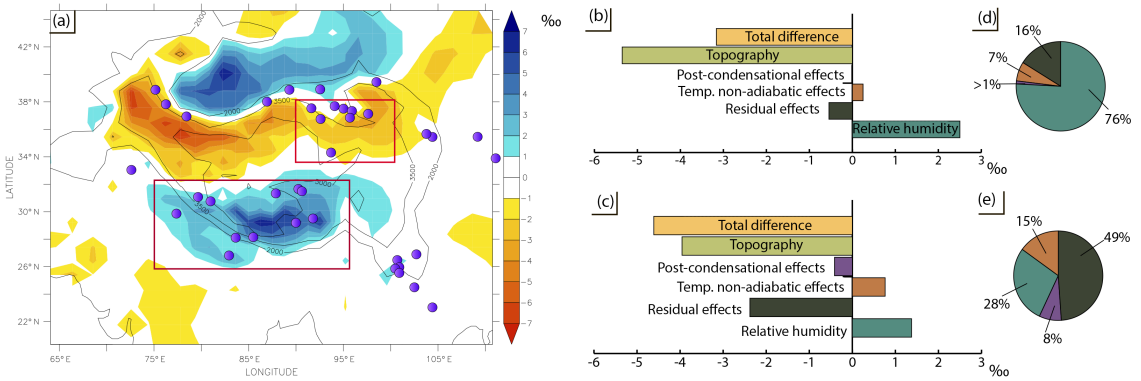

Figure 13. **(a)** Difference in $\delta^{18}O_p$ between MOD and INT experiments that is not related to direct effect of topography changes. Violet points show Cenozoic palaeoelevation study locations (compiled from Caves et al., 2015). Red rectangles show regions for that averaged values decomposed terms are shown: **(b)** northern region, **(c)** southern region. Pie diagrams show portion of total isotopic difference related to processes other then topography: **(d)** northern region, **(e)** southern region.

Impact of RH changes during condensation process

The term $\Delta R_{p,\Delta h}$ in Eq. (7) depicts the portion of total isotopic signal ΔR_p linked to local RH change during condensation process (Table 1, line 4). Over TP, $\Delta R_{p,\Delta h}$ is positive for both uplift phases, and RH changes act as a counterbalance to the topography effect. $\Delta R_{p,\Delta h}$ reaches $+4\,‰$ for the late stage (Fig. 11d), and maxima are located over the western part and northern part of TP for both stages of the uplift. Equation (4) shows that this positive anomaly is directly related to the increase in RH described in Sect. 3.2.1. For the initial stage, $\Delta R_{p,\Delta h}$ depicts also positive values (up to $+3\,‰$) to the southwest of TP. When averaged over northern and southern boxes, the counterbalancing effect of RH on ΔR_p ranges from 1.5 to $+3\,‰$, and this effect represents up to 76 % of all non-topographic processes (Figs. 12, 13). Interestingly, an opposite signal is simulated over the Tarim basin, where topography was kept constant in the three experiments. This signal is consistent with the previously-depicted decrease in RH over this region, in relation with rain-shadow effects and large-scale subsidence.

Post-condensation processes impact

The difference between $\delta^{18}O_v$ and $\delta^{18}O_p$ is linked to the post-condensation effects, mainly associated with raindrop reevaporation that can occur after initial condensation. Because lighter isotopes evaporate more easily, rain reevaporation leads to an isotopic enrichment of precipitation. Therefore, the more reevaporation, the greater the difference between $\delta^{18}O_p$ and $\delta^{18}O_v$. We refer to the study of (Lee and Fung, 2008), where post-condensation effects are explained in detail. The contribution of such processes increases dramatically for very dry areas, where the relative humidity is less than 40 %. Estimation of term $\Delta R_{p,\Delta\varepsilon}$, i.e. the change in isotopic difference between vapour and precipitation, allows to quantify the contribution of post-condensational processes to total ΔR_p signal (Figs. 10e, 11e) without appealing

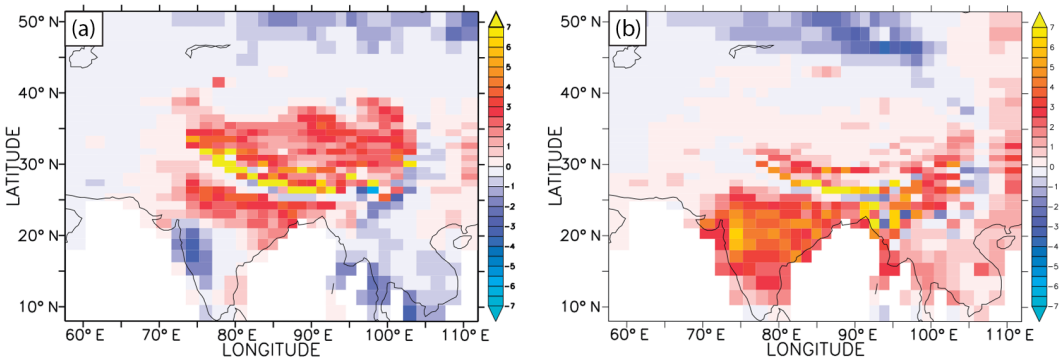

Figure 14. Precipitation change (mm day^{-1}) for **(a)** MOD-INT **(b)** INT-LOW cases.

to the d-excess. For both stages of uplift, $\Delta R_{p,\Delta\varepsilon}$ is mostly negative, indicating a depletion of R_p relative to R_v with the uplift. Over the Plateau, contribution of post-condensational effects for the initial stage of uplift ranges from 25 % to 46 % of total non-topographic effects, whereas it represents less than 10 % for the terminal stage (Figs. 12a, 13a). The most significant signal is simulated over the northern part of the Plateau and over its western margin and adjacent areas. Post-condensational effects during the initial stage lead to up to a −5 ‰ anomaly over the western margin of TP (Fig. 12e) whereas the terminal stage creates a substantial negative anomaly only over northern TP margin and Tarim Basin (Fig. 13e).

Residual processes effect

The last term of Eq. (7), $\Delta R_{p,\Delta dR_v}$, corresponds to the part of the total isotopic signal that could not be explained by previously mentioned processes. These residual anomalies are rather weak for the initial stage of the uplift, explaining less than 1 ‰ of the signal over the northern plateau, and around 1 ‰ over the southern TP and adjacent parts of Asia and India (Fig. 10f). Contribution of these effects to the initial stage is 4 and 21 % to the northern and southern box respectively (Fig. 12d, e). Conversely, for the terminal stage of the TP uplift this anomaly reaches up to −4 ‰ over the southern part of the TP (Fig. 11f) and contributes to 49 % of the non-topographic processes signal (Fig. 13d, e). In the next sections we propose several mechanisms that could contribute to this residual anomaly.

4 Discussion

Our results suggest that TP uplift affects precipitation $\delta^{18}O$ through direct topographic effect, but that a significant part of the signal is related to several other processes. These processes alter the isotopic signal not only over TP, but also over adjacent regions, where topography was kept the same by the experiment design. A second result is that despite a similar altitudinal change of TP between the two uplift stages, the topographic effect on $\delta^{18}O$ is more perturbed by other processes during the terminal stage than during the initial one.

For the terminal stage, the residual effects change over the southern region dominates (49 %) the isotopic signal that is not linked to the direct topographic effect. The RH change and non-adiabatic temperature changes also have an important counterbalancing impact, together contributing to 43 % of the isotopic signal (Fig. 13e). For the northern region, the topographic effect is mainly counterbalanced by the RH change effect (2.5 ‰), ultimately leading to a 2.3 ‰ offset between ΔR_p and what is expected from topography. Here RH contributes to 76 % of the isotopic signal not linked with the topography change, while non-adiabatic temperature changes, residual effects change and post-condensational processes have an impact of 16, 7 and < 1 % respectively (Fig. 13d).

4.1 Impact of RH variations

RH alters rainfall isotopic signature through two steps, during and after condensation. As mentioned earlier, the first effect of RH, as shown in Eq. (4) and expressed as $\Delta R_{p,\Delta h}$, occurs during condensation through Rayleigh distillation and induces that R_p increases with increasing RH. Our model shows that RH increases over TP with the initial stage of uplift, driving precipitation $\delta^{18}O$ towards less negative values. This mechanism is more efficient for the terminal stage of uplift, when RH is increased in summer as a response of a more active water cycle. South of TP, RH direct effect on $\delta^{18}O$ is noticeable, as efficient moisture transport is activated with the uplift-driven strengthening of monsoon circulation (Fig. 4). Interestingly, this mechanism is not active for the second stage of the uplift, during which rainfall increases through more effective convection, not through higher advection of moisture. As a consequence, negligible RH and R_p changes are simulated south of the Plateau when it reaches its full height. This suggests that an altitudinal threshold might trigger South Asian monsoon strengthening, and ultimately precipitation $\delta^{18}O$ signature, a hypothesis that should be explored in further studies. Conversely, the negative values of

$\Delta R_{p,\Delta h}$ over and northeast of the Tarim basin are related to a decrease in RH during both stages. Our analysis suggests that the first uplift stage is sufficient to create both barrier effects to moisture fluxes and large-scale subsidence that ultimately drive aridity over the region.

The second effect of RH on $\delta^{18}O$ concerns very dry areas (ca. $<40\,\%$), where raindrop re-evaporation can occur after initial condensation, leading to an isotopic enrichment of precipitation compared to water vapour (Lee and Fung, 2008) (Fig. S2). Such an effect is implicitly included in the post-condensational term of our decomposition that shows opposite sign when compared to $\Delta R_{p,\Delta h}$. Over the Plateau, this mechanism is effective only for the first uplift stage, where TP area transits from very low precipitation amounts and very low RH values to wetter conditions (Fig. S7).

Over TP, the opposed effects of RH almost compensate each other for the early stage of the uplift (Fig. 10d, e), but this is not the case for the final stage, since RH post-condensational effect is similar between INT and MOD experiments. Since absolute values of the impact of RH through condensation and post-condensational processes can reach $5\,‰$, it is crucial to consider RH variation when inferring palaeoaltitudes from carbonates $\delta^{18}O$.

4.2 "Amount effect" and monsoon intensification

Our results also show a substantial increase in precipitation amount over northern India, the Himalayas and TP with the growth of topography for both uplift stages (Fig. 14). The inverse relation between the enrichment in heavy isotopes in precipitation and precipitation amount, named the "amount effect" (Dansgaard, 1964) is largely known for oceanic tropical conditions (Risi et al., 2008; Rozanski et al., 1993) and for Asia monsoonal areas (Lee et al., 2012; Yang et al., 2011). Over South Tibet recent studies have shown the role of deep convection in isotopic depletion (He et al., 2015). For the two stages of uplift, the residual component of the isotopic signal depicts negative values over southern TP, where annual rainfall amount is increased. Thus we infer that this anomaly can be driven, at least partly, by the amount effect that increases with growing topography.

Various climate studies have suggested that the appearance of the monsoonal system in East Asia and the onset of central Asian desertification were related to Cenozoic Himalayan–Tibetan uplift and withdrawal of the Paratethys Sea (An et al., 2001; Clift et al., 2008; Guo et al., 2002, 2008; Kutzbach et al., 1989, 1993; Ramstein et al., 1997; Raymo and Ruddiman, 1992; Ruddiman and Kutzbach, 1989; Sun and Wang, 2005; Zhang et al., 2007), although the exact timing of the monsoon onset and its intensification remains debated (Licht et al., 2014; Molnar et al., 2010). Although our experimental setup, which does not include Cenozoic palaeogeography, was not designed to assess the question of monsoon driving mechanisms nor its timing, our results suggest that uplifting the Plateau from 250 m ASL to half of its present height is enough to enhance moisture transport towards northern India and strengthen seasonal rainfall. Nevertheless, massive increase of rainfall over TP between INT and MOD experiments indicates that the second phase of uplift might be crucial to activate an efficient, modern-day-like, hydrological cycle over the Plateau. The decrease in simulated precipitation north of the Plateau also suggests that terminal phase of TP uplift triggered modern-day arid areas.

4.3 Other effects

Although precipitation amount change explains well the residual isotopic anomaly (Figs. 10f, 11f), additional processes could interplay. Continental recycling can overprint original moisture signature and shifts the isotopic ratios to higher values due to recharging of moisture by heavy isotopes from soil evaporation (Lee et al., 2012; Risi et al., 2013). In our simulation, we detect an increasing role of continental recycling in the hydrological budget of the TP (Fig. S6), especially in its central part, that likely shifts the $\delta^{18}O$ to more positive values and partially compensates for the depletion linked to the "amount effect" over the central plateau. Another process frequently invoked to explain the evolution of precipitation $\delta^{18}O$ patterns over TP is changes in moisture sources (Bershaw et al., 2012; Dettman et al., 2003; Quade et al., 2007; Tian et al., 2007). Except for the continentally recycled moisture, southern Himalayas precipitation moisture originates mainly from the Indian, the Atlantic and the Pacific oceans (Fig. S6). Proximate oceanic basins are known to be sources of moisture with a more positive signature than remote ones (Chen et al., 2012; Gat, 1996). Supplemental analyses with water-tagging feature of LMDZ-iso show that contribution of continental recycling to rainfall over TP increases with the uplift, at the expanse of Pacific and Indian sources (Fig. S6). Although we have no mean to decipher between sources and amount effect in the residual anomaly, it seems that the change of sources is not sufficient to yield a strong offset of $\delta^{18}O$ values.

4.4 Relevance of palaeoelevation reconstructions based on palaeo $\delta^{18}O$

Quantitative palaeoelevation reconstructions using modern altitude-$\delta^{18}O$ relationship will succeed only if ΔR_p corresponds mainly to the direct topography effect. Modern palaeoaltimetry studies cover almost all regions of the Plateau for time periods ranging from Palaeocene to Pleistocene-Quaternary (see data compilation in Caves et al., 2015). Most of these studies consider changes in $\delta^{18}O$ as a direct effect of the topography uplift. Palaeoelevation studies locations (see Caves et al., 2015 for a synthesis) plotted over the anomaly maps (Figs. 12a, 13a) show for what geographical regions restored elevations should be used with an additional caution. Numerous palaeoelevation data points were located either over the northern part of the TP (from 34

Table 4. Impact of the different terms of the decomposition on the isotopic signal for the terminal stage of HTP uplift in the location where palaeoelevation studies have been done.

Locality	Latitude	Longitude	ΔR_p (‰)	$\Delta R_{p,\Delta z}$ (‰)	$\Delta R_{p,\Delta dT_s}$ (‰)	$\Delta R_{p,\Delta\varepsilon}$ (‰)	$\Delta R_{p,\Delta h}$ (‰)	$\Delta R_{p,\Delta dR_v}$ (‰)	Palaeoelevation studies at this locality
Aertashi	37.97	75.55	−1.619	−2.859	0.999	−0.294	−0.268	0.803	Kent-Corson et al. (2009)
Biger Noor	45.90	96.78	−1.169	−0.004	2.673	−0.702	−4.419	1.283	Caves et al. (2014)
Chake Basin	23.80	103.10	−0.252	0.006	−0.030	0.042	0.263	−0.533	Hoke et al. (2014)
Dzereg	47.14	93.06	−1.006	−0.004	2.216	−0.372	−4.313	1.466	Caves et al. (2014)
Eryuan	26.20	99.80	−1.356	−1.574	0.634	0.171	0.497	−1.083	Hoke et al. (2014)
Ganchaigou	37.69	91.04	−3.195	−2.780	0.836	−1.292	0.610	−0.570	Kent-Corson et al. (2009)
Gyirong Basin	28.70	85.25	−7.017	−3.850	1.073	−1.089	0.409	−3.559	Wang et al. (1996)
Hexi Corridor	39.52	97.52	−2.907	−0.279	1.732	−1.985	−2.293	−0.083	Kent-Corson et al. (2009)
Hoh Xil Basin	34.60	93.00	−3.972	−6.529	0.660	0.037	3.375	−1.514	Cyr et al. (2005)
Huaitoutala	37.30	96.70	−5.998	−4.418	−1.473	−3.620	3.104	0.409	Zhuang et al. (2011)
India Siwaliks	30.35	77.60	−1.862	0.006	0.103	−0.303	0.183	−1.851	Ghosh et al. (2004)
India Siwaliks	30.34	77.60	−1.862	0.006	0.103	−0.303	0.183	−1.851	Sanyal et al. (2005)
Janggalsay	38.15	86.62	−4.487	−2.406	1.026	−2.347	−0.952	0.192	Kent-Corson et al. (2009)
Jianchuan Basin	26.60	99.80	−1.356	−1.574	0.634	0.171	0.497	−1.083	Hoke et al. (2014)
Jingou	44.75	85.40	1.073	−0.031	1.270	1.435	−2.054	0.453	Charreau et al. (2012)
Kailas Basin	31.20	81.00	−6.705	−7.181	0.401	0.799	3.162	−3.886	DeCelles et al. (2011)
Kuitun	45.00	84.75	1.073	−0.031	1.270	1.435	−2.054	0.453	Charreau et al. (2012)
Lake Mahai	37.66	94.24	−0.964	−0.003	2.737	0.423	−4.188	0.066	Kent-Corson et al. (2009)
Lanping	26.50	99.40	−1.356	−1.574	0.634	0.171	0.497	−1.083	Hoke et al. (2014)
Lao Mangnai	36.94	91.96	−1.133	−3.998	0.447	0.356	2.233	−0.171	Kent-Corson et al. (2009)
Lenghu	37.84	93.36	−0.964	−0.003	2.737	0.423	−4.188	0.066	Kent-Corson et al. (2009)
Linxia Basin	35.69	103.10	0.443	−0.961	1.079	0.364	−0.410	0.371	Dettman et al. (2003)
Linzhou Basin	30.00	91.20	−6.756	−5.956	2.337	−0.057	0.886	−3.965	Ding et al. (2014)
Luhe	25.20	101.30	−0.242	0.009	0.317	0.411	−0.236	−0.742	Hoke et al. (2014)
Lulehe	37.50	95.08	−0.061	−0.987	1.724	1.950	−3.326	0.578	Kent-Corson et al. (2009)
Lulehe	37.50	95.08	−0.061	−0.987	1.724	1.950	−3.326	0.578	Kent-Corson et al. (2009)
Lunpola Basin	32.06	89.75	−6.763	−6.073	1.920	−0.652	1.561	−3.520	Rowley and Currie (2006)
Miran River	38.98	88.85	−4.786	−1.387	1.069	−2.683	−2.068	0.283	Kent-Corson et al. (2009)
Nepal Siwaliks	27.42	82.84	−1.370	0.006	−0.016	0.203	0.025	−1.588	Quade et al. (1995)
Nima Basin	31.75	87.50	−5.897	−7.724	−0.205	1.312	4.078	−3.359	DeCelles et al. (2011)
Oiyug Basin	29.70	89.50	−10.39	−7.842	2.634	−2.598	1.151	−3.735	Currie et al. (2005)
Oytag	38.98	75.51	−0.499	−0.716	1.320	0.719	−1.975	0.152	Bershaw et al. (2011)
Pakistan Siwaliks	33.39	73.11	0.645	0.008	0.380	0.407	0.379	−0.529	Quade et al. (1995)
Puska	37.12	78.60	−2.598	0.006	0.896	−0.472	−3.909	0.882	Kent-Corson et al. (2009)
Taatsin Gol	45.42	101.26	−0.731	−0.003	1.600	−0.364	−3.087	1.123	Caves et al. (2014)
Thakkhola	28.70	83.50	−4.018	−1.529	0.802	−0.310	−0.572	−2.409	Garzione et al. (2000)
Thakkhola−Tetang	28.66	83.50	−4.018	−1.529	0.802	−0.310	−0.572	−2.409	Garzione et al. (2000)
Xiao Qaidam	37.03	94.88	1.614	−1.376	1.772	3.117	−2.581	0.681	Kent-Corson et al. (2009)
Xifeng	35.70	107.60	0.245	0.00	0.522	0.173	−0.010	−0.440	Jiang et al. (2002)
Xorkol	39.01	91.92	−3.218	−0.871	1.871	−1.302	−2.970	0.054	Kent-Corson et al. (2009)
Xunhua Basin	35.90	102.50	0.443	−0.961	1.079	0.364	−0.420	0.371	Hough et al. (2010)
Yanyuan	27.50	101.50	−0.350	−1.152	0.657	0.539	0.373	−0.767	Hoke et al. (2014)
Zhada Basin	31.50	79.75	−3.983	−4.818	−0.046	0.831	2.708	−2.657	Saylor et al. (2009)

to 38° N and from 88 to 100° E) or over the southern region (from 27 to 33° N and from 75 to 95° E).

Our model results show that when TP altitude is increased from half to full, considering topography as an exclusive controlling factor of precipitation δ^{18}O over the southern (northern) region likely yields overestimations (underestimations) of surface uplift, since the topography effect is offset by RH and amount effects. Projecting our modelling results to each locality where palaeoelevation studies have been published (Table 4) reveals that topography change explains simulated total isotopic change reasonably well for only few locations (Linzhou Basin, Lunpola Basin, Kailas Basin, Huaitoutala). Indeed topography appears to be the main controlling factor for only 40 % of the sites, while 30 % is dominated by RH effects, 20 % by residual effects and 5 % by post-condensational and non-adiabatic temperature changes, respectively. Nevertheless such figures have to be taken carefully, since we ran idealized experiments testing only the impact of uplift, neglecting other factors like horizontal palaeogeography or pCO_2 variations, the latter being known to influence δ^{18}O as well (Jeffery et al., 2012; Poulsen and Jeffery, 2011).

For the initial uplift stage apparent consistency occurs between the topography impact and the total isotopic composition, in relation to counteracting effects RH and post-condensational processes. For the southern region RH impact appears to be the main controlling factor for the isotopic composition of precipitation, surpassing the direct to-

pography impact. Nevertheless, these processes have a different contribution for initial and terminal stages of uplift. Precipitation changes lead to overestimating altitude changes for both stages, but for the terminal stage its contribution is bigger. This effect dominates in the southern part, and more generally where the isotopic composition of precipitation strongly depends on convective activity. RH changes dominate over the western part of TP and Northern India for initial uplift stage and over the northern TP for the terminal. Differences between both stages could be partly explained by non-linearities in q_s – temperature relationships, as well as in Rayleigh distillation processes (Fig. S8). Determining whether other processes contribute to this difference would be of interest, but it is out of the scope of the present study.

5 Conclusions

Previous studies focusing on the Andes (Ehlers and Poulsen, 2009; Poulsen et al., 2010) or North American cordillera (Sewall and Fricke, 2013) have inferred that the impact of uplift of mountain ranges on $\delta^{18}O$ could be altered by the consequences of the uplift on atmospheric physics and dynamics. Our modelling results show that it is also the case for the Tibetan Plateau uplift. Additionally, we designed a decomposing analysis to quantify for the first time the different processes that can alter precipitation $\delta^{18}O$ changes with uplift. As suggested for the Andes, the onset of convective rainfall plays an important role in shifting $\delta^{18}O$ towards more negative values. Nevertheless this process is not the main factor, as we show that saturation of air masses, quantified by RH have two to three-time bigger effects on the final $\delta^{18}O$. We infer that increase in precipitation linked with the TP uplift would lead to overestimation of the topography uplift at sites over Himalayas and Southern TP, whereas increase in RH leads to underestimating the uplift at sites in Northern Tibet.

Our results could be applied to interpret palaeoclimate records and to reconstruct the region uplift history. Palaeoelevation reconstructions suggest the Himalayas attained their current elevation at least by the late Miocene or even earlier (Garzione et al., 2000a, b; Rowley et al., 2001; Saylor et al., 2009). Our results show overestimation of the topography impact over this region, thus the Himalayas may have attained their current elevation later than expected. In contrast, isotope-based palaeoaltimetry could underestimate surface elevation over the northern TP. This could explain why available isotope-based palaeoelevation estimates for the northern TP (Cyr et al., 2005), which estimates surface elevation at about 2 km, contradict palynological assemblages in lacustrine sediments from the Xining Basin, which show the presence of high-altitude vegetation at the same time period (Dupont-Nivet et al., 2008; Hoorn et al., 2012).

Still, our decomposition methods reveal that even if the impact of the TP uplift phases are rather straightforward (monsoon enhancement to the South, increase in continental recycling over TP, moisture fluxes deflection and increased aridity to the North), the consequences in terms of $\delta^{18}O$ are extremely complex, since interplays and compensation occur amongst all the processes. Limitations in our approach are related to a perfectible hydrological cycle in LMDZ-iso, and idealized boundary conditions (topography uplift scenarios, modern land–sea mask, SSTs and pCO_2). Model data comparison show that mean annual precipitation amount is slightly overestimated by the model for the northern TP, thus could result in underestimation of the amount effect contribution for the northern TP. On the contrary, the model overestimates the precipitation over the southern edge of the Himalayas. If it was more realistic, the contribution of the amount effect estimated by the decomposing method could be less important. Changes in vegetation cover, by altering albedo and persistence of snow cover, could affect the impact of non-adiabatic temperature changes on $\delta^{18}O$. Vegetation over Asia was shown to have a major variation through Cenozoic based on pollen (Dupont-Nivet et al., 2008; Miao et al., 2011; Song et al., 2010; Zhao and Yu, 2012) and palaeobolanical data (An et al., 2005; De Franceschi et al., 2008; Kohn, 2010) and future studies would benefit to explore its impact on precipitation $\delta^{18}O$. Also it is widely known that during the Cenozoic air temperature was higher due to a higher concentration of greenhouse gases in the atmosphere (Zachos et al., 2008). Studies taking into account this feedback inferred that it could lead to even larger inaccuracy in surface uplift estimations during the Cenozoic (Poulsen and Jeffery, 2011). Thus the field of palaeoaltimetry would benefit from future studies focusing on (1) using palaeoclimate proxies to constrain specifically relative humidity, surface temperature and precipitation amount in deep time and (2) applying a decomposition method to isotope-enabled GCM simulations forced by constrained palaeogeography (land-sea mask and different scenarios for orogens) and atmospheric pCO_2 for specific geological time period. The combination of both could help refine calibration for palaeo $\delta^{18}O$-elevation relationships and refining palaeoelevation estimates.

The Supplement related to this article is available online at doi:10.5194/cp-12-1401-2016-supplement.

Acknowledgements. We would like to thank three anonymous reviewers for their valuable comments and suggestions which helped improve the quality of the paper. This work is a part of iTECC (interaction Tectonics-Erosion-Climate-Coupling) project funded by the European Union. Computational resources were provided by IDRIS-GENCI (project 0292), France.

Edited by: D.-D. Rousseau

References

An, Z., Kutzbach, J. E., Prell, W. L., and Porter, S. C.: Evolution of Asian monsoons and phased uplift of the Himalaya-Tibetan plateau since Late Miocene times, Nature, 411, 62–66, 2001.

An, Z., Huang, Y., Liu, W., Guo, Z., Stevens, C., Li, L., Prell, W., Ning, Y., Cai, Y., Zhou, W., Lin, B., Zhang, Q., Cao, Y., Qiang, X., Chang, H., and Wu, Z.: Multiple expansions of C_4 plant biomass in East Asia since 7 Ma coupled with strengthened monsoon circulation, Geology, 33, 705–708, doi:10.1130/G21423.1, 2005.

An, Z., Wu, G., Li, J., Sun, Y., Liu, Y., Zhou, W., Cai, Y., Duan, A., Li, L., Mao, J., Cheng, H., Shi, Z., Tan, L., Yan, H., Ao, H., Chang, H., and Feng, J.: Global Monsoon Dynamics and Climate Change, Annu. Rev. Earth Pl. Sc., 43, 29–77, 2015.

Antal, J. S. and Awasthi, N: Fossil flora from the Himalayan foot hills of Darjeeling foothills of Darjeeling District, West Bengal and its palaeoecological and phytogeographical significance, Palaeobotanist, 42, 14–60, 1993

Battisti, D. S., Ding, Q., and Roe, G. H.: Coherent pan-Asian climatic and isotopic response to orbital forcing of tropical insolation, J. Geophys. Res. Atmos., 119, 11997–12020, 2014.

Bershaw, J., Penny, S. M., and Garzione, C. N.: Stable isotopes of modern water across the Himalaya and eastern Tibetan Plateau: Implications for estimates of paleoelevation and paleoclimate, J. Geophys. Res. Atmos., 117, 1–18, 2012.

Boos, W. R.: A review of recent progress on Tibet's role in the South Asian monsoon, CLIVAR Exch., 19, 23–27, 2015.

Broccoli, A. J. and Manabe, S.: The Effects of Orography on Midlatitude Northern Hemisphere Dry Climates, J. Climate, 5, 1181–1201, 1992.

Caves, J. K., Winnick, M. J., Graham, S. A., Sjostrom, D. J., Mulch, A., and Chamberlain, C. P.: Role of the westerlies in Central Asia climate over the Cenozoic, Earth Planet. Sc. Lett., 428, 33–43, 2015.

Chen, B., Xu, X. De, Yang, S., and Zhang, W.: On the origin and destination of atmospheric moisture and air mass over the Tibetan Plateau, Theor. Appl. Climatol., 110, 423–435, 2012.

Chen, G.-S., Liu, Z., and Kutzbach, J. E.: Reexamining the barrier effect of the Tibetan Plateau on the South Asian summer monsoon, Clim. Past, 10, 1269–1275, doi:10.5194/cp-10-1269-2014, 2014.

Clift, P. D., Hodges, K. V., Heslop, D., Hannigan, R., Van Long, H., and Calves, G.: Correlation of Himalayan exhumation rates and Asian monsoon intensity, Nat. Geosci., 1, 875–880, 2008.

Craig, H.: Isotopic variations in meteoric waters, Science, 133, 1702–1703, 1961.

Currie, B. S., Rowley, D. B., and Tabor, N. J.: Middle Miocene paleoaltimetry of southern Tibet: Implications for the role of mantle thickening and delamination in the Himalayan orogen, Geology, 33, 181–184, 2005.

Cyr, A. J., Currie, B. S., and Rowley, D. B.: Geochemical Evaluation of Fenghuoshan Group Lacustrine Carbonates, North-Central Tibet: Implications for the Paleoaltimetry of the Eocene Tibetan Plateau, J. Geol., 113, 517–533, 2005.

Dansgaard, W.: Stable isotopes in precipitation, Tellus, 16, 436–468, doi:10.3402/tellusa.v16i4.8993, 1964.

DeCelles, P. G., Quade, J., Kapp, P., Fan, M., Dettman, D. L., and Ding, L.: High and dry in central Tibet during the Late Oligocene, Earth Planet. Sc. Lett., 253, 389–401, 2007.

Dettman, D. L., Fang, X., Garzione, C. N., and Li, J.: Uplift-driven climate change at 12 Ma: A long δ^{18}O record from the NE margin of the Tibetan plateau, Earth Planet. Sc. Lett., 214, 267–277, 2003.

Ding, L., Xu, Q., Yue, Y., Wang, H., Cai, F., and Li, S.: The Andean-type Gangdese Mountains: Paleoelevation record from the Paleocene-Eocene Linzhou Basin, Earth Planet. Sc. Lett., 392, 250–264, 2014.

De Franceschi, D., Hoorn, C., Antoine, P. O., Cheema, I. U., Flynn, L. J., Lindsay, E. H., Marivaux, L., Métais, G., Rajpar, A. R., and Welcomme, J. L.: Floral data from the mid-Cenozoic of central Pakistan, Rev. Palaeobot. Palynol., 150, 115–129, 2008.

Dupont-Nivet, G., Hoom, C., and Konert, M.: Tibetan uplift prior to the Eocene-Oligocene climate transition: Evidence from pollen analysis of the Xining Basin, Geology, 36, 987–990, 2008.

Ehlers, T. A. and Poulsen, C. J.: Influence of Andean uplift on climate and paleoaltimetry estimates, Earth Planet. Sc. Lett., 281, 238–248, 2009.

Forest, C. E., Wolfe, J. A., Molnar, P., and Emanuel, K. A.: Paleoaltimetry incorporating atmospheric physics and botanical estimates of paleoclimate, Geol. Soc. Am. Bull., 111, 497–511, 1999.

Frankenberg, C., Yoshimura, K., Warneke, T., Aben, I., Butz, A., Deutscher, N., Griffith, D., Hase, F., Notholt, J., Schneider, M., Schrijver, H., and Röckmann, T.: Dynamic Processes Governing Lower-Tropospheric HDO/H_2O Ratios as Observed from Space and Ground, Science, 325, 1374–1377, 2009.

Galewsky, J. and Hurley, J. V: An advection-condensation model for subtropical water vapor isotopic ratios, J. Geophys. Res. Atmos., 115, D16116, doi:10.1029/2009JD013651, 2010.

Galewsky, J., Sobel, A., and Held, I.: Diagnosis of subtropical humidity dynamics using tracers of last saturation, J. Atmos. Sci., 62, 3353–3367, 2005.

Garzione, C. N., Dettman, D. L., Quade, J., De Celles, P. G., and Butler, R. F.: High times on the Tibetan Plateau: Paleoelevation of the Thakkhola graben, Nepal, Geology, 28, 339–342, 2000a.

Garzione, C. N., Quade, J., DeCelles, P. G., and English, N. B.: Predicting paleoelevation of Tibet and the Himalaya from δ^{18}O vs. altitude gradients in meteoric water across the Nepal Himalaya, Earth Planet. Sc. Lett., 183, 215–229, 2000b.

Gat, J. R.: Oxygen and hydrogen isotopes in the hydrologic cycle, Annu. Rev. Earth Pl. Sc., 24, 225–262, 1996.

Gedzelman, S. D. and Arnold, R.: Modeling the isotopic composition of precipitation, New York, J. Geophys. Res. Atmos., 99, 10455–10471, 1994.

Gonfiantini, R., Roche, M. A., Olivry, J. C., Fontes, J. C., and Zuppi, G. M.: The altitude effect on the isotopic composition of tropical rains, Chem. Geol., 181, 147–167, 2001.

Guo, Z. T., Ruddiman, W. F., Hao, Q. Z., Wu, H. B., Qiao, Y. S., Zhu, R. X., Peng, S. Z., Wei, J. J., Yuan, B. Y., and Liu, T. S.: Onset of Asian desertification by 22 Myr ago inferred from loess deposits in China, Nature, 416, 159–163, 2002.

Guo, Z. T., Sun, B., Zhang, Z. S., Peng, S. Z., Xiao, G. Q., Ge, J. Y., Hao, Q. Z., Qiao, Y. S., Liang, M. Y., Liu, J. F., Yin, Q. Z., and Wei, J. J.: A major reorganization of Asian climate by the

early Miocene, Clim. Past, 4, 153–174, doi:10.5194/cp-4-153-2008, 2008.

Harris, N.: The elevation history of the Tibetan Plateau and its implications for the Asian monsoon, Palaeogeogr. Palaeoecol., 241, 4–15, 2006.

He, Y., Risi, C., Gao, J., Masson-delmotte, V., Yao, T., Lai, C., Ding, Y., Worden, J., Frankenberg, C., Chepfer, H., and Cesana, G.: Impact of atmospheric convection on south Tibet summer precipitation isotopologue composition using a combination of in situ measurements, satellite data, and atmospheric general circulation modeling, J. Geophys. Res. Atmos., 120, 3852–3871, doi:10.1002/2014JD022180, 2015.

Hoke, G. D., Liu-Zeng, J., Hren, M. T., Wissink, G. K., and Garzione, C. N.: Stable isotopes reveal high southeast Tibetan Plateau margin since the Paleogene, Earth Planet. Sc. Lett., 394, 270–278, 2014.

Hoorn, C., Straathof, J., Abels, H. A., Xu, Y., Utescher, T., and Dupont-Nivet, G.: A late Eocene palynological record of climate change and Tibetan Plateau uplift (Xining Basin, China), Palaeogeogr. Palaeoecol., 344/345, 16–38, 2012.

Hourdin, F., Musat, I., Bony, S., Braconnot, P., Codron, F., Dufresne, J. L., Fairhead, L., Filiberti, M. A., Friedlingstein, P., Grandpeix, J. Y., Krinner, G., LeVan, P., Li, Z. X., and Lott, F.: The LMDZ4 general circulation model: Climate performance and sensitivity to parametrized physics with emphasis on tropical convection, Clim. Dynam., 27, 787–813, 2006.

Hren, M. T., Bookhagen, B., Blisniuk, P. M., Booth, A. L., and Chamberlain, C. P.: $\delta^{18}O$ and δD of streamwaters across the Himalaya and Tibetan Plateau: Implications for moisture sources and paleoelevation reconstructions, Earth Planet. Sc. Lett., 288, 20–32, 2009.

Jeffery, M. L., Poulsen, C. J., and Ehlers, T. A.: Impacts of Cenozoic global cooling, surface uplift, and an inland seaway on South American paleoclimate and precipitation $\delta^{18}O$, Geol. Soc. Am. Bull., 124, 335–351, 2012.

Kageyama, M., Nebout, N. C., Sepulchre, P., Peyron, O., Krinner, G., Ramstein, G., and Cazet, J.-P.: The Last Glacial Maximum and Heinrich Event 1 in terms of climate and vegetation around the Alboran Sea: a preliminary model-data comparison, Comptes Rendus Geosci., 337, 983–992, 2005.

Kanamitsu, M., Ebisuzaki, W., Woollen, J., Yang, S. K., Hnilo, J. J., Fiorino, M., and Potter, G. L.: NCEP-DOE AMIP-II reanalysis (R-2), Bull. Am. Meteorol. Soc., 83, 1631–1643, 2002.

Kattel, D. B., Yao, T., Yang, W., Gao, Y., and Tian, L.: Comparison of temperature lapse rates from the northern to the southern slopes of the Himalayas, Int. J. Climatol., 35, 4431–4443, 2015.

Khan, M. A., Spicer, R. A., Bera, S., Ghosh, R., Yang, J., Spicer, T. E. V, Guo, S. X., Su, T., Jacques, F., and Grote, P. J.: Miocene to Pleistocene floras and climate of the Eastern Himalayan Siwaliks, and new palaeoelevation estimates for the Namling-Oiyug Basin, Tibet, Global Planet. Change, 113, 1–10, 2014.

Kohn, M. J.: Carbon isotope compositions of terrestrial C_3 plants as indicators of (paleo)ecology and (paleo)climate, P. Natl. Acad. Sci., 107, 19691–19695, 2010.

Kutzbach, J. E., Guetter, P. J., Ruddiman, W. F., and Prell, W. L.: Sensitivity of climate to late Cenozoic uplift in southern Asia and the American west: numerical experiments, J. Geophys. Res. Atmos., 94, 18393–18407, 1989.

Kutzbach, J. E., Prell, W. L., and Ruddiman, W. F.: Sensitivity of Eurasian climate to surface uplift of the Tibetan Plateau, J. Geol., 177–190, 1993.

Ladant, J., Donnadieu, Y., Lefebvre, V., and Dumas, C.: The respective role of atmospheric carbon dioxide and orbital parameters on ice sheet evolution at the Eocene-Oligocene transition, Paleoceanography, 29, 810–823, 2014.

Lee, J. and Fung, I.: "Amount effect" of water isotopes and quantitative analysis of post-condensation processes, Hydrol. Process., 22, 1–8, 2008.

Lee, J. E., Risi, C., Fung, I., Worden, J., Scheepmaker, R. A., Lintner, B., and Frankenberg, C.: Asian monsoon hydrometeorology from TES and SCIAMACHY water vapor isotope measurements and LMDZ simulations: Implications for speleothem climate record interpretation, J. Geophys. Res. Atmos., 117, 1–12, 2012.

LeGrande, A. N. and Schmidt, G. A.: Sources of Holocene variability of oxygen isotopes in paleoclimate archives, Clim. Past, 5, 441–455, doi:10.5194/cp-5-441-2009, 2009.

Li, S., Currie, B. S., Rowley, D. B., and Ingalls, M.: Cenozoic paleoaltimetry of the SE margin of the Tibetan Plateau: Constraints on the tectonic evolution of the region, Earth Planet. Sc. Lett., 432, 415–424, 2015.

Licht, A., van Cappelle, M., Abels, H. A., Ladant, J.-B., Trabucho-Alexandre, J., France-Lanord, C., Donnadieu, Y., Vandenberghe, J., Rigaudier, T., Lécuyer, C., Terry Jr., D., Adriaens, R., Boura, A., Guo, Z., Soe, A. N., Quade, J., Dupont-Nivet, G., and Jaeger, J.-J.: Asian monsoons in a late Eocene greenhouse world, Nature, 513, 501–506, 2014.

Liu, X., Sun, H., Miao, Y., Dong, B., and Yin, Z.-Y.: Impacts of uplift of northern Tibetan Plateau and formation of Asian inland deserts on regional climate and environment, Quaternary Sci. Rev., 116, 1–14, 2015.

Majoube, M.: Fractionnement en oxygene-18 et en deuterium entre l'eau et sa vapeur, J. Chim. phys, 68, 1423–1436, 1971.

McElwain, J. C.: Climate-independent paleoaltimetry using stomatal density in fossil leaves as a proxy for CO_2 partial pressure, Geology, 32, 1017, doi:10.1130/G20915.1, 2004.

Merlivat, L. and Nief, G.: Fractionnement isotopique lors des changements d'état solide-vapeur et liquide-vapeur de l'eau à des températures inférieures à 0 °C, Tellus, 19, 122–127, 1967.

Miao, Y., Fang, X., Herrmann, M., Wu, F., Zhang, Y., and Liu, D.: Miocene pollen record of KC-1 core in the Qaidam Basin, NE Tibetan Plateau and implications for evolution of the East Asian monsoon, Palaeogeogr. Palaeoecol., 299, 30–38, 2011.

Miao, Y., Herrmann, M., Wu, F., Yan, X., and Yang, S.: What controlled Mid-Late Miocene long-term aridification in Central Asia? – Global cooling or Tibetan Plateau uplift: A review, Earth-Sci. Rev., 112, 155–172, 2012.

Molnar, P., Boos, W. R., and Battisti, D. S.: Orographic Controls on Climate and Paleoclimate of Asia: Thermal and Mechanical Roles for the Tibetan Plateau, Annu. Rev. Earth Pl. Sc., 38, 77–102, 2010.

Mulch, A.: Stable isotope paleoaltimetry and the evolution of landscapes and life, Earth Planet. Sc. Lett., 433, 180–191, 2016.

New, M., Lister, D., Hulme, M., and Makin, I.: A high-resolution data set of surface climate over global land areas, Clim. Res., 21, 1–25, 2002.

Pausata, F. S. R., Battisti, D. S., Nisancioglu, K. H., and Bitz, C. M.: Chinese stalagmite δ^{18}O controlled by changes in the Indian monsoon during a simulated Heinrich event, Nat. Geosci., 4, 474–480, 2011.

Poage, M. A. and Chamberlain, C. P.: Empirical relationships between elevation and the stable isotope composition of precipitation and surface waters: Considerations for studies of paleoelevation change, Am. J. Sci., 301, 1–15, 2001.

Pohl, A., Donnadieu, Y., Le Hir, G., Buoncristiani, J.-F., and Vennin, E.: Effect of the Ordovician paleogeography on the (in)stability of the climate, Clim. Past, 10, 2053–2066, doi:10.5194/cp-10-2053-2014, 2014.

Poulsen, C. J. and Jeffery, M. L.: Climate change imprinting on stable isotopic compositions of high-elevation meteoric water cloaks past surface elevations of major orogens, Geology, 39, 595–598, 2011.

Poulsen, C. J., Ehlers, T. A., and Insel, N.: Onset of convective rainfall during gradual late Miocene rise of the central Andes, Science, 328, 490–493, 2010.

Quade, J., Garzione, C., and Eiler, J.: Paleoelevation Reconstruction using Pedogenic Carbonates, Rev. Mineral. Geochem., 66, 53–87, 2007.

Quade, J., Breecker, D. O., Daëron, M., and Eiler, J.: The paleoaltimetry of Tibet: An isotopic perspective, Am. J. Sci., 311, 77–115, 2011.

Ramstein, G., Fluteau, F., Besse, J., and Joussaume, S.: Effect of orogeny, plate motion and land–sea distribution on Eurasian climate change over the past 30 million years, Nature, 386, 788–795, 1997.

Raymo, M. E. and Ruddiman, W. F.: Tectonic forcing of late Cenozoic climate, Nature, 359, 117–122, 1992.

Risi, C., Bony, S., and Vimeux, F.: Influence of convective processes on the isotopic composition (δ^{18}O and δD) of precipitation and water vapor in the tropics: 2. Physical interpretation of the amount effect, J. Geophys. Res. Atmos., 113, 1–12, 2008.

Risi, C., Bony, S., Vimeux, F., and Jouzel, J.: Water-stable isotopes in the LMDZ4 general circulation model: Model evaluation for present-day and past climates and applications to climatic interpretations of tropical isotopic records, J. Geophys. Res. Atmos., 115, 1–27, 2010.

Risi, C., Noone, D., Frankenberg, C., and Worden, J.: Role of continental recycling in intraseasonal variations of continental moisture as deduced from model simulations and water vapor isotopic measurements, Water Resour. Res., 49, 4136–4156, 2013.

Rodwell, M. J. and Hoskins, B. J.: Subtropical anticyclones and summer monsoons, J. Climate, 14, 3192–3211, 2001.

Rowley, D. B. and Currie, B. S.: Palaeo-altimetry of the late Eocene to Miocene Lunpola basin, central Tibet, Nature, 439, 677–681, 2006.

Rowley, D. B. and Garzione, C. N.: Stable Isotope-Based Paleoaltimetry, Annu. Rev. Earth Pl. Sc., 35, 463–508, 2007.

Rowley, D. B., Pierrehumbert, R. T., and Currie, B. S.: A new approach to stable isotope-based paleoaltimetry: Implications for paleoaltimetry and paleohypsometry of the High Himalaya since the late Miocene, Earth Planet. Sc. Lett., 188, 253–268, 2001.

Royden, L. H., Burchfiel, B. C., and Van Der Hilst, R. D.: The Geological Evolution of the Tibetan Plateau, Science, 321, 1054–1058, 2008.

Rozanski, Kazimierz Araguás-Araguás, L., and Gonfiantini, R.: Isotopic patterns in modern global precipitation, in: Climate Change in Continental Isotopic Records, Geophys. Monogr., 78, 1–36, 1993.

Ruddiman, W. F. and Kutzbach, J. E.: Forcing of late Cenozoic northern hemisphere climate by plateau uplift in southern Asia and the American West, J. Geophys. Res. Atmos., 94, 18409–18427, 1989.

Sato, T. and Kimura, F.: Impact of diabatic heating over the Tibetan Plateau on subsidence over northeast Asian arid region, Geophys. Res. Lett., 32, 1–5, doi:10.1029/2004GL022089, 2005.

Saylor, J. E., Quade, J., Dettman, D. L., DeCelles, P. G., Kapp, P. A., and Ding, L.: The late Miocene through present paleoelevation history of southwestern Tibet, Am. J. Sci., 309, 1–42, 2009.

Sepulchre, P., Ramstein, G., Fluteau, F., Schuster, M., Tiercelin, J.-J., and Brunet, M.: Tectonic uplift and Eastern Africa aridification, Science, 313, 1419–1423, 2006.

Sewall, J. O. and Fricke, H. C.: Andean-scale highlands in the Late Cretaceous Cordillera of the North American western margin, Earth Planet. Sc. Lett., 362, 88–98, 2013.

Sherwood, S. C.: Maintenance of the free-tropospheric tropical water vapor distribution, Part II: Simulation by large-scale advection, J. Climate, 9, 2919–2934, 1996.

Song, X. Y., Spicer, R. A., Yang, J., Yao, Y. F., and Li, C. Sen: Pollen evidence for an Eocene to Miocene elevation of central southern Tibet predating the rise of the High Himalaya, Palaeogeogr. Palaeoecol., 297, 159–168, 2010.

Stowhas, L. and Moyano, J. C.: Simulation of the Isotopic Content of Precipitation, Atmos. Environ., 27, 327–333, 1993.

Sun, B., Wang, Y.-F., Li, C.-S., Yang, J., Li, J.-F., Li, Y.-L., Deng, T., Wang, S.-Q., Zhao, M., Spicer, R. A., Ferguson, D. K., and Mehrotra, R. C.: Early Miocene elevation in northern Tibet estimated by palaeobotanical evidence, Sci. Rep., 5, 10379, doi:10.1038/srep10379, 2015.

Sun, J., Zhang, Z., and Zhang, L.: New evidence on the age of the Taklimakan Desert, Geology, 37, 159–162, 2009.

Sun, J., Xu, Q., Liu, W., Zhang, Z., Xue, L., and Zhao, P.: Palynological evidence for the latest Oligocene-early Miocene paleoelevation estimate in the Lunpola Basin, central Tibet, Palaeogeogr. Palaeoecol., 399, 21–30, 2014.

Sun, X. and Wang, P.: How old is the Asian monsoon system? – Palaeobotanical records from China, Palaeogeogr. Palaeoecol., 222, 181–222, 2005.

Tapponnier, P., Zhiqin, X., Roger, F., Meyer, B., Arnaud, N., Wittlinger, G., and Jingsui, Y.: Oblique stepwise rise and growth of the Tibet plateau, Science, 294, 1671–1677, 2001.

Taylor, K. E., Williamson, D., and Zwiers, F.: The sea surface temperature and sea-ice concentration boundary conditions for AMIP II simulations, Program for Climate Model Diagnosis and Intercomparison, Lawrence Livermore National Laboratory, University of California, 2000.

Tian, L., Yao, T., MacClune, K., White, J. W. C., Schilla, A., Vaughn, B., Vachon, R., and Ichiyanagi, K.: Stable isotopic variations in west China: A consideration of moisture sources, J. Geophys. Res. Atmos., 112, 1–12, 2007.

Van Leer, B.: Towards the ultimate conservative difference scheme, IV. A new approach to numerical convection, J. Comput. Phys., 23, 276–299, 1977.

Vuille, M., Werner, M., Bradley, R. S., Chan, R. Y., and Keimig, F.: Stable isotopes in East African precipitation record Indian Ocean zonal mode, Geophys. Res. Lett., 32, 1–5, 2005.

Xu, Q., Ding, L., Zhang, L., Cai, F., Lai, Q., Yang, D., and Liu-Zeng, J.: Paleogene high elevations in the Qiangtang Terrane, central Tibetan Plateau, Earth Planet. Sc. Lett., 362, 31–42, 2013.

Yang, X., Yao, T., Yang, W., Yu, W., and Qu, D.: Co-existence of temperature and amount effects on precipitation $\delta^{18}O$ in the Asian monsoon region, Geophys. Res. Lett., 38, 1–6, 2011.

Yao, T., Masson-Delmotte, V., Gao, J., Yu, W., Yang, X., Risi, C., Sturm, C., Werner, M., Zhao, H., He, Y., Ren, W., Tian, L., Shi, C., and Hou, S.: A review of climatic controls on $\delta^{18}O$ in precipitation over the Tibetan Plateau: Observations and simulations, Rev. Geophys., 51, 525–548, 2013.

Zachos, J. C., Dickens, G. R., and Zeebe, R. E.: An early Cenozoic perspective on greenhouse warming and carbon-cycle dynamics, Nature, 451, 279–283, 2008.

Zhang, R., Jiang, D., Zhang, Z., and Yu, E.: The impact of regional uplift of the Tibetan Plateau on the Asian monsoon climate, Palaeogeogr. Palaeoecol., 417, 137–150, 2015.

Zhang, Z., Wang, H., Guo, Z., and Jiang, D.: What triggers the transition of palaeoenvironmental patterns in China, the Tibetan Plateau uplift or the Paratethys Sea retreat?, Palaeogeogr. Palaeoecol., 245, 317–331, 2007.

Zhao, Y. and Yu, Z.: Vegetation response to Holocene climate change in East Asian monsoon-margin region, Earth-Sci. Rev., 113, 1–10, 2012.

Supplement of Clim. Past, 12, 1401–1420, 2016
http://www.clim-past.net/12/1401/2016/
doi:10.5194/cp-12-1401-2016-supplement

Climate of the Past
Open Access
EGU

Supplement of

Impacts of Tibetan Plateau uplift on atmospheric dynamics and associated precipitation δ^{18}O

Svetlana Botsyun et al.

Correspondence to: Svetlana Botsyun (botsyun.svetlana@gmail.com)

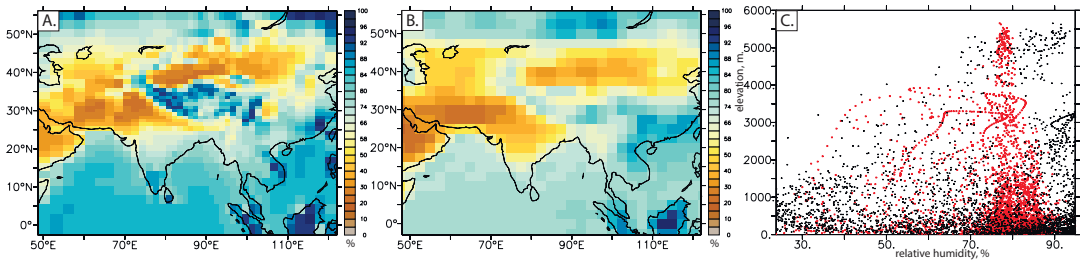

Figure S1. Mean annual relative humidity for A) LMDZ-iso simulated for the MOD experiment and B) NCEP-DOE Reanalysis. C) Scatter plot of global mean annual relative humidity versus elevation.

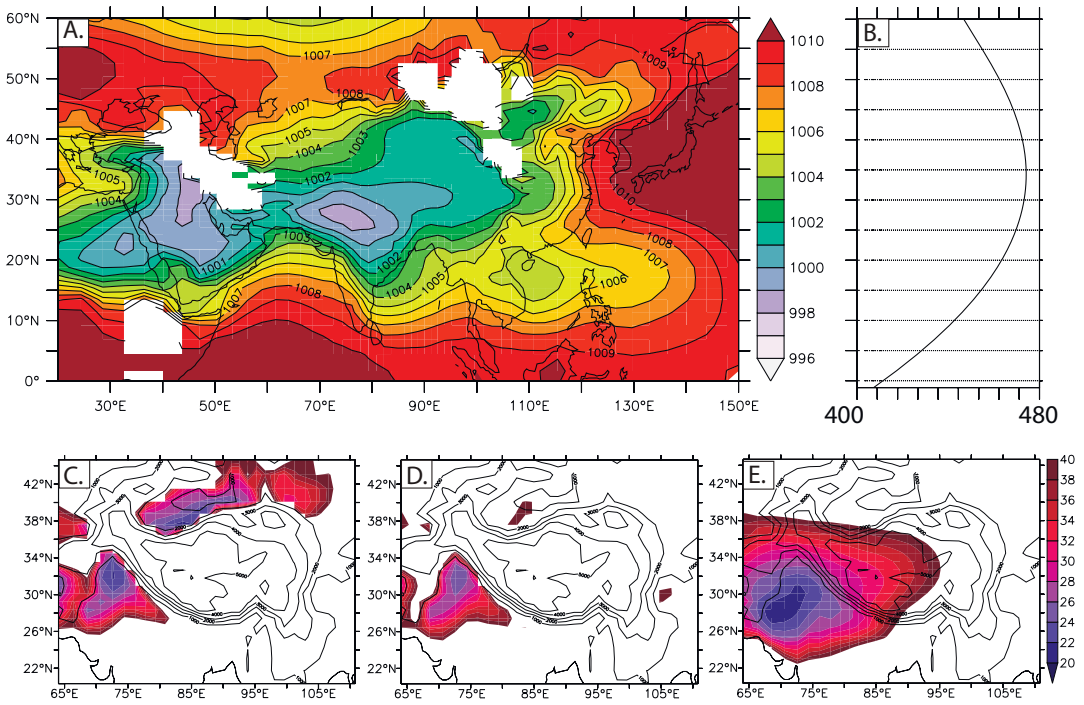

Figure S2. (A) Mean annual sea level pressure (hPa) for the LOW simulation, (B) Meridional transect of the insolation an the top of atmosphere (W m^{-2}), averaged for 90 °E, (C, D, E) Regions where relative humidity is under 40% for (C) MOD, (D) INT and (E) LOW experiment.

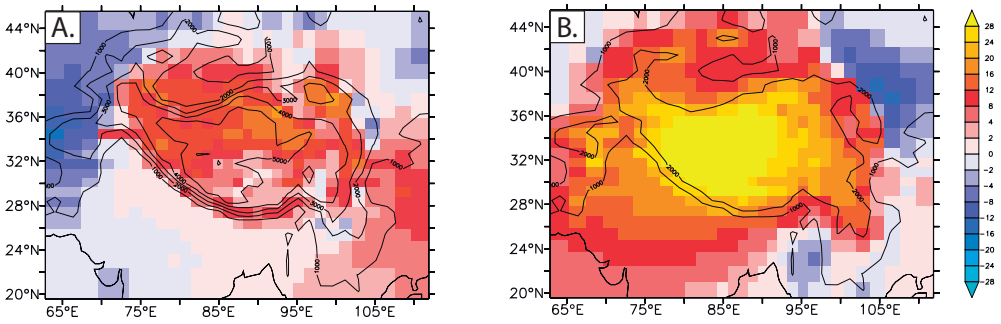

Figure S3. Total cloudiness change for A) MOD-INT B) INT-LOW cases.

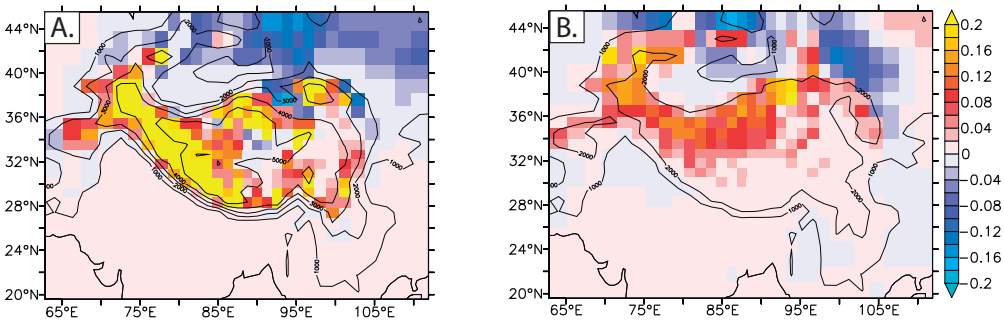

Figure S4. Surface albedo change for (A) MOD-INT (B) INT-LOW cases

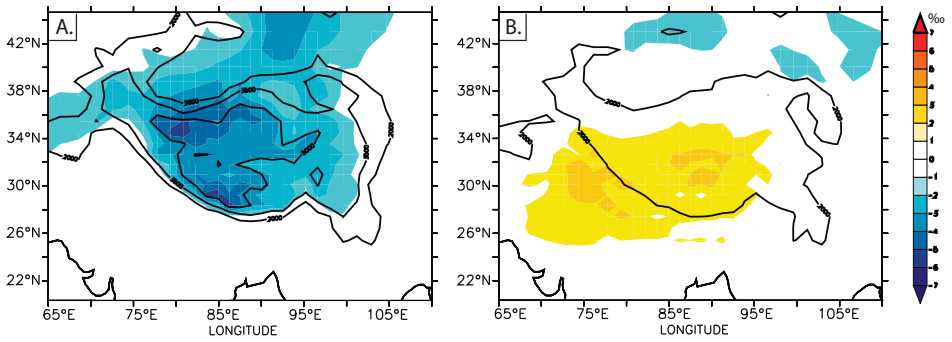

Figure S5. Spatial isotopic variations related to the change of spatial humidity for A) MOD-INT and B) INT-LOW cases.

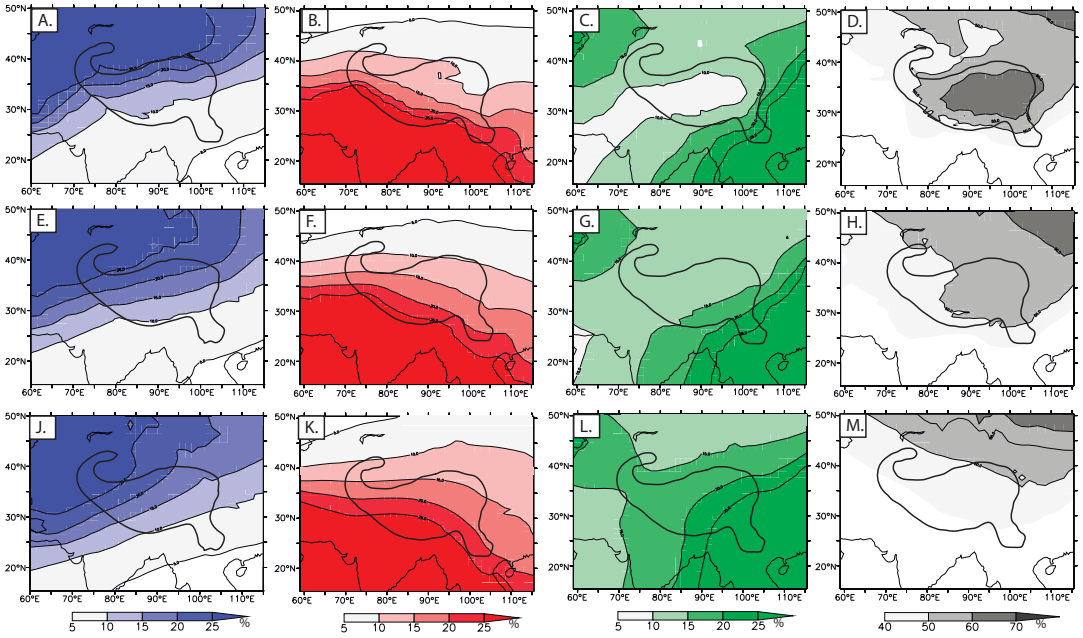

Figure S6. Moisture sources changes, illustrated by vertically integrated portion of vapour having evaporated over different regions. Blue shade - the Atlantic Ocean and Mediterranean sea source, red - the Indian Ocean moisture source, green - the Pacific Ocean source, grey - continental recycling source . (A, B, C, D) - MOD case, (E, F, G, H) - INT case, (J, K, L, M) - LOW case.

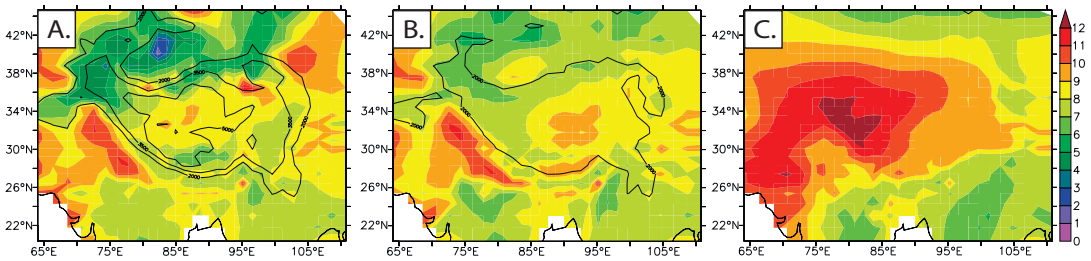

Figure S7. Deviations of precipitation $\delta^{18}O$ from the vapour composition, $\varepsilon = Rp - Rv$ for (A) MOD, (B) INT and (C) LOW cases

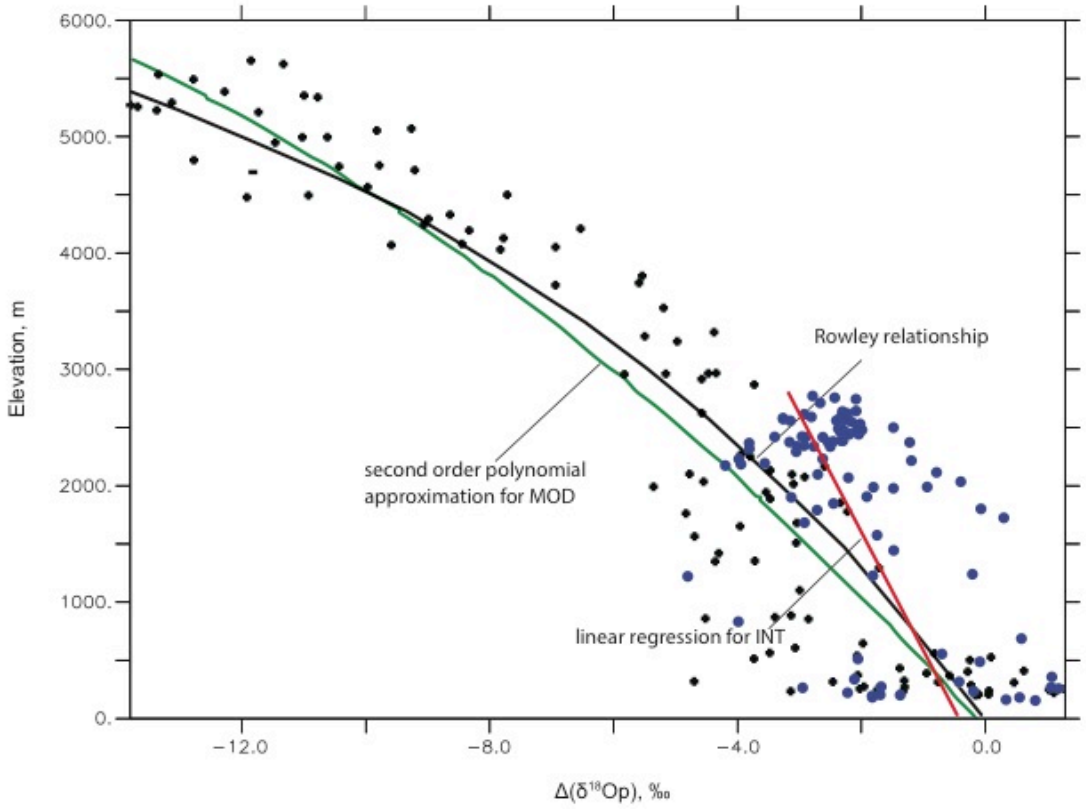

Fig. S8. $\Delta(\delta^{18}O)$ vs. elevation for MOD (black points) and INT (blue points) cases. The isotopic gradients are shown for the southern region (between 25°N and 30°N). Black line shows relationship from the empirical model (Rowley, 2001; Rowley and Garzione, 2007). Green line shows second order polynomial approximation of simulated MOD $\delta^{18}O$ values. Red line shows a linear regression for the INT $\delta^{18}O$ values.

3.5 Consequences for paleoaltimetry estimates

Modern paleoaltimetry studies cover almost all regions of the plateau for time periods ranging from the Palaeocene to the Pleistocene. These studies either directly simple $\delta^{18}O$-elevation realtionship from Rowley et al. (2001) (Cyr et al., 2005; Ding et al., 2014; Hoke et al., 2014; Rowley and Currie, 2006; Xu et al., 2015, 2013) or construct isotopic ratios in carbonates or paleosoil waters (DeCelles et al., 2007; Dettman et al., 2001; Fan et al., 2007; Garzione et al., 2000b; Kent-Corson et al., 2009; Quade et al., 1989; Quade and Cerling, 1995,?; Sanyal et al., 2004a; Stern et al., 1997; Wang et al., 2006), that could potentially be used for paleoelevation reconstructions. However, this approach has potential limitations from two sides: 1) possible spatial variations of climatic controls of $\delta^{18}O$ and their vertical gradients and 2) stationary of these gradient through time.

Comparing the simulated present-day isotopic signal with $\delta^{18}O$ obtained using the R1 (see Section 3.2) model reveals significant differences across the plateau (Figure 3.3). Rowley's relationship describes well isotopic distribution for a limited area of southern plateau and for some parts of margins. The offset from this relationship increases towards the interior part of the TP and reaches up to 5 ‰ for the northern part and even more than -6 ‰ for the northern margins, Taklamakan desert and the Tian-Shan.

When using the isotopic lapse rate from the Rowley polynomial to reconstruct Eocene paleoelevations for the central part of the plateau, we underestimate elevation by 1000-1200 meters compared to when using the lapse rate simulated by LMDZ-iso (Figure 3.26). With the latter lapse rate, we estimate the elevation of Lumpola Basin at 39 Ma at ~5400 m, compared to ~4050 m that obtained by (Rowley and Currie, 2006). Likewise our estimation for Fenghuoshan Group at 39 Ma is at 3100 m, instead of 2100 m from Cyr et al. (2005). Appearance of high-altitude vegetation and aridification in the Xining Basin (Dupont-Nivet et al., 2008) during the Eocene support the suggestion of high elevation of the central TP in the Eocene. The event of Neo-Tethyan oceanic slab detachment at ~45 Ma tracked by the metamorphic record (e.g. Kohn and Dettman, 2007) and arc magmatism, similar to the modern Central America example (Chung et al., 2005) probably resulted in accelerated uplift of the plateau and absolute altitudes comparable with the present-day.

Northern TP has been noted to be complicated for oxygen isotope paleoaltimetry. Our results show that a 1-D model based on Rayleigh distillation cannot be applied to this region because the air masses have different origin and various V_0, T_0 and Rh_0 as well as different conditions for the post-condensation processes and maximized evaporative enrichment of $\delta^{18}O$ in rain and surface waters.

We suspect that spatial variations of vapor mass origin, temperature (adiabatic and non-adiabatic), relative humidity and as well as large scale aridity and amount affect drive spatial variation in isotopic lapse rates. A particular lapse rate for each region of the Plateau should be taken into account for consistent paleoelevation reconstructions. In addition to spatial variations, isotopic lapse rates may have varied through geological time, since external forcing factors such as atmospheric CO_2 concentration, land-sea distribution and TP uplift itself likely have affected air masses trajectories, isotopic composition of initial moisture source and the distance from moisture source to precipitation. Future studies will benefit from a combined approach involving isotopic data and fully

coupled GCM simulation with well-constrained paleo boundary conditions.

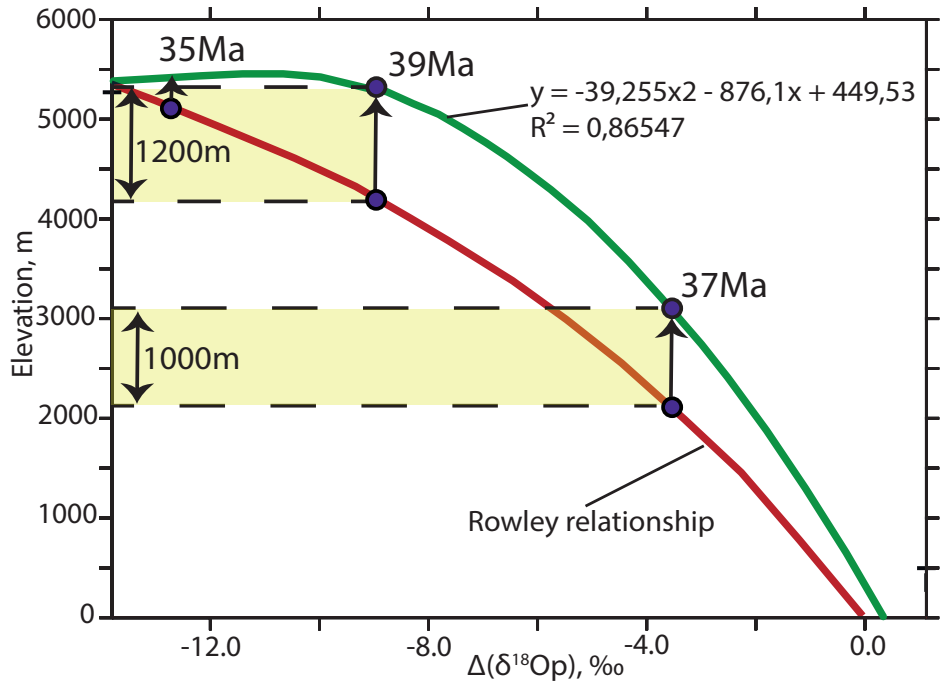

Figure 3.26 – Paleoaltimetry estimations using the theoretical relationship (Rowley et al., 2001) (red line) and LMDZ-iso established relationship (green line) for the central Tibetan Plateau. Circles show $\delta^{18}O$ of paleo soil water from paleoelevation studies: 37 Ma - Cyr et al. (2005); 35 Ma, 39 Ma – Rowley and Currie (2006). Yellow bars show possible error in paleoelevations due to spatial variations of isotopic lapse rates.

In addition to described spatial variation in the isotopic lapse rates over the HTP, $\delta^{18}O$ appeared to be highly sensitive to the elevation of mountains over this region (see Section 3.4, Supplementary figure 8).

However, we want to pay attention that in this section we aim to show a possible causes and error range associated with paleoaltimetry studies, but not to provide alternative isotopic lase rates. For realist paleo isotopic lapse rates, simulations with realist paleo boundary conditions are indispensable (See more in the Sections 4). In addition, we should stress that for relevant paleoelevations estimates paleoclimate changes must be evaluated and take into account.

3.6 Summary and conclusions

Stable-isotope paleoaltimetry is potentially hampered by the fact that the presumed constancy of altitude-$\delta^{18}O$ relationships spatially and through time might not be valid and climate changes affects $\delta^{18}O$ in precipitation.

Nowadays it is well understood that $\delta^{18}O_p$ is controlled by multiple factors, including the temperature, elevation, precipitation amount, relative humidity, and others (see Section 3.1). Given the variety of this factors over the HTP and using LMDZ-iso outputs for present-day simulation, we show how isotopic lapse rates vary spatially over the region. Presumed constancy of the isotopic lapse rate in paleoelevations studies may have crucial impact on paleoelevations estimates accuracy (Section 3.5).

We also use the isotope-equipped atmospheric general circulation model LMDZ-iso for modeling Asia climate variations and associated $\delta^{18}O$ in precipitation linked with the Himalayas and Tibetan Plateau uplift. Experiments with reduced height over the Tibetan Plateau and the Himalayas have been designed. For the purpose of understanding where and how simulated complex climatic changes linked with the growth of mountains affect $\delta^{18}O$ in precipitation we develop a theoretical expression for the precipitation composition.

Our results show that modifying Tibetan Plateau height alters large-scale atmospheric dynamics including monsoon circulation and subsidence and associated climate variables, namely temperature, precipitation, relative humidity and cloud cover. In turn, $\delta^{18}O$ signal decomposition results show that the isotopic signature of rainfall is very sensitive to climate changes related with the growth of the Himalayas and Tibetan Plateau, notably changes in relative humidity and precipitation amount. Topography itself appears to be the main controlling factor for only 40 % of the sites where previous paleoelevations studies have been performed. Change of moisture sources linked with Asian topography uplift is shown to be not sufficient to yield a strong offset of $\delta^{18}O$ values. However, the relative contribution of $\delta^{18}O$ controlling factors and their magnitude differ depending on the uplift stage and the region considered. We highlight that future paleoaltimetry studies should take into account constraints on climatic factors to avoid misestimating ancient altitudes.

We pay particular attention on necessity of paleoclimate and paleoisotopic simulations with realist boundary conditions.

Chapter 4

Cenozoic $\delta^{18}O$ in precipitation

In this Chapter, first we overview previously published works which provide paleo $\delta^{18}O_p$ simulations (Section 4.1). In Section 4.2 we discuss climatic and $\delta^{18}O_p$ patterns obtained in our numerical experiments with Eocene, Oligocene and Miocene boundary conditions. Eocene $\delta^{18}O_p$ controls over the HTP appeared to be dramatically different from those of present-day. In Section 4.3 we explore Eocene controls of precipitation $\delta^{18}O$ and present the article in preparation for *EPSL*, entitled "Controls of the Eocene stable oxygen isotopes over Himalayas and Tibetan Plateau", where we discuss the results of our experiments with Eocene boundary conditions. Finally, in Sections 4.4 we provide additional experiments that we have performed in order to test the impact of orbital parameters variations, albedo, sea surface temperatures, Paratethys retreat and topography uplift on Eocene $\delta^{18}O_p$.

Contents

4.1 Introduction: modeling for paleo $\delta^{18}O$

Given recent advances in climate modeling (see Section 2.2), one of the most straightforward methods for integrating the complex feedbacks between climate, tectonics, and the isotopic composition of precipitation is to simulate past climates with an atmosphere general circulation model (AGCM) enabled with the stable water isotopes together with paleo boundary conditions. Results of such experiments highlight the sensitivity of $\delta^{18}O_p$ to climate change associated with CO_2, SST variations and changes in elevations of major orogens.

Thus, Poulsen et al. (2007) have investigated Cretaceous $\delta^{18}O_p$ over the Western Cordillera and have shown a systematic increase of nearly 3 ‰ due to warming associated with an increase in CO_2 from 2 to 12 times pre-industrial levels. The authors have also shown that the sea level, which was eustaticaly changed during the Cretaceous, as well as the surface elevation of the Western Cordillera lowers precipitation $\delta^{18}O_p$ locally by 7 ‰. Poulsen and Jeffery (2011) using GENESIS GCM have shown that the isotopic composition of precipitation in high-elevation regions, including the Tibetan Plateau, Rocky Mountains, European Alps, and Andean Plateau, increases by 3 ‰ – 6 ‰ relative to that at low elevations with 2 times increased CO_2, due to reduction in the surface to upper troposphere $\delta^{18}O_p$ gradient.

Sturm et al. (2007) using REMO-iso model and various sea surface temperature (SST) forcings investigate the seasonal variation of the amount effect on $\delta^{18}O_p$ and the anomalous $\delta^{18}O_p$ continental gradient across the Amazon basin. They show that the amount effect define $\delta^{18}O_p$ during the wet season, while during the dry season, the $\delta^{18}O_p$ is controlled by isotopic reequilibration of rain droplets with surrounding vapor, reflecting the impact of nonfractionating transpiration by the vegetation.

The influence of the uplift of major orogens on the isotopic composition of precipitation has become a focus of recent studies. Ehlers and Poulsen (2009); Poulsen et al. (2007) focused their research on the South America region and designed numerical experiments with reduced elevation of the Andes. These authors show that South American and Andean climate have been changed significantly in response to the growth of the Andean Plateau. More specifically, their results suggest up to a 900 mm increase in rainy season precipitation over the plateau and a decrease in non-adiabatic surface temperature of up to 6.5 °C. More importantly, they have shown that the prevailing wind direction and the vapor source for precipitation switch from the South Pacific Ocean to the equatorial Atlantic as the Plateau elevation increases above ½–¾ of its present-day height. This has substantially depleting effect on $\delta^{18}O_p$ through the Cenozoic and leads to potential errors on paleoaltimetry, because changing atmospheric dynamics modify isotopic lapse rates.

Sewall and Fricke (2013) used a GCM with integrated oxygen isotope tracers (isoCAM3) in order to predict $\delta^{18}O_p$ along the North American Cordillera with the increase of elevation from 1200 m to 3975 m. They show that the increase in mean elevation is consistent with a decrease in highland temperatures and an exchange of monsoonal circulation along the eastern front of the Cordillera. These authors also show that simulated oxygen isotopic ratios in that precipitation are comparable to those obtained from natural

archives and derive mean Cretaceous elevations of Cordillera to be approaching 4000 m.

In our article published in *Climate of the Past* (Botsyun et al., 2016) we have used a GCM model with reduced elevation over the HTP region and shown to what instant climate changes associated with the uplift of the Plateau impact $\delta^{18}O_p$ signal (see Chapter 3). With the exception of (Sewall and Fricke, 2013) for the Cretaceous, all studies listed here were based on sensitivity experiments using present-day continents positions. In a recent study of (Roe et al., 2016) an isotopes enabled GCM has been used for paleoclimate simulations with paleogeographies different from those of present-day. In contrast to previous studies, in this chapter we discuss the results of experiments with realistic boundary conditions for various time periods for the Cenozoic.

4.2 LMDZ-iso simulated $\delta^{18}O$ evolution during the Cenozoic

To quantify the influence of paleogeography changes on climate and precipitation $\delta^{18}O_p$ over Asia, the atmospheric general circulation model LMDZ-iso, with embedded stable oxygen isotopes, was used. For more realistic experiments, sea surface temperatures were calculated with the fully coupled model FOAM (for more details on Method see Chapter 2). Various scenarios of HTP growth have been applied together with Early Eocene, Middle Eocene, Oligocene and Miocene boundary conditions. Here we use a model configuration with 144 grid points in longitude, 142 in latitude and 39 vertical layers. LMDZ-iso stretchable grid allows increasing regional spatial resolution and gives an averaged resolution of ~50 km over central Asia.

4.2.1 Model validation for present-day case

The modern annual averaged isotopic distribution is characterized by very depleted (down to -18 ‰) values of $\delta^{18}O_p$ over the Himalayas and the southern Tibet and a shift to more positive values (ranging from -13 to -11 ‰) over northern TP and Kunlun, from 35° N to 40° N. Precipitation $\delta^{18}O_p$ over Tarim Basin experiences an abrupt decrease, with values down to -16 ‰ (Figure 4.1, A).

On the S-N profile (Figure 4.1, B) simulated modern MJJAS isotopic distribution is characterized by a northward decrease in $\delta^{18}O_p$ from the Himalayas foothills (27° N) to the southern Tibet (with values down to -17 ‰) linked to the Rayleigh distillation during rainout and ascent of air masses along the southern flanks of the HTP. This mechanism is consistent with what has been shown from data and 1-D models (Rowley and Garzione, 2007; Rowley et al., 2001). Between 30° N and 40° N a shift to more positive values (ranging from -8 to -14 ‰) is simulated, consistent with observations from earlier studies (Bershaw et al., 2012; Quade et al., 2007). Observed isotopic enrichment is commonly related to active continental recycling (through evaporation) that contributes to the increase in lower troposphere humidity and shifts of $\delta^{18}O_p$ to an "air masses mixing" regime (Worden et al., 2007).

In general, simulated present-day $\delta^{18}O$ values are consistent with sparse observations

from the International Atomic Energy Agency (IAEA) Global Network of Isotopes in Precipitation (GNIP). However, over the India plane, simulated $\delta^{18}O$ more depleted that the observed values that is a direct consequence of overestimated amount of precipitation during the summer. Over the Himalayan foothills LMDZ-iso (in the resolution used) simulate $\delta^{18}O$ that are too enriched with are consisted with relatively dry pattern that is simulated for this area. This low precipitation over the foothills regions could be linked with backward air subsidence compensating too strong orographic air uplift parameterized in the model (Camille Risi, personal communication).

Over the elevated topography, simulated $\delta^{18}O$ shows a good agreement with annual averaged modern precipitation and rivers $\delta^{18}O$ (Bershaw et al., 2012; Caves et al., 2015; Hren et al., 2009; Quade et al., 2011) that allows us to use the model for the purpose of this study (Figure 4.1). Some model-data discrepancies over the northern and central part of the Plateau and over Mongolia could be probably explained by: i) correspondence of measured date to MJJAS $\delta^{18}O$ signal (season when rain events happen) that is much more positive that annual averaged one (not shown), ii) comparison with measurement of lake water $\delta^{18}O$, which is enriched in heavy isotopes due to evaporation processes, while currently used version of LMDZ-iso does not include lakes simulation.

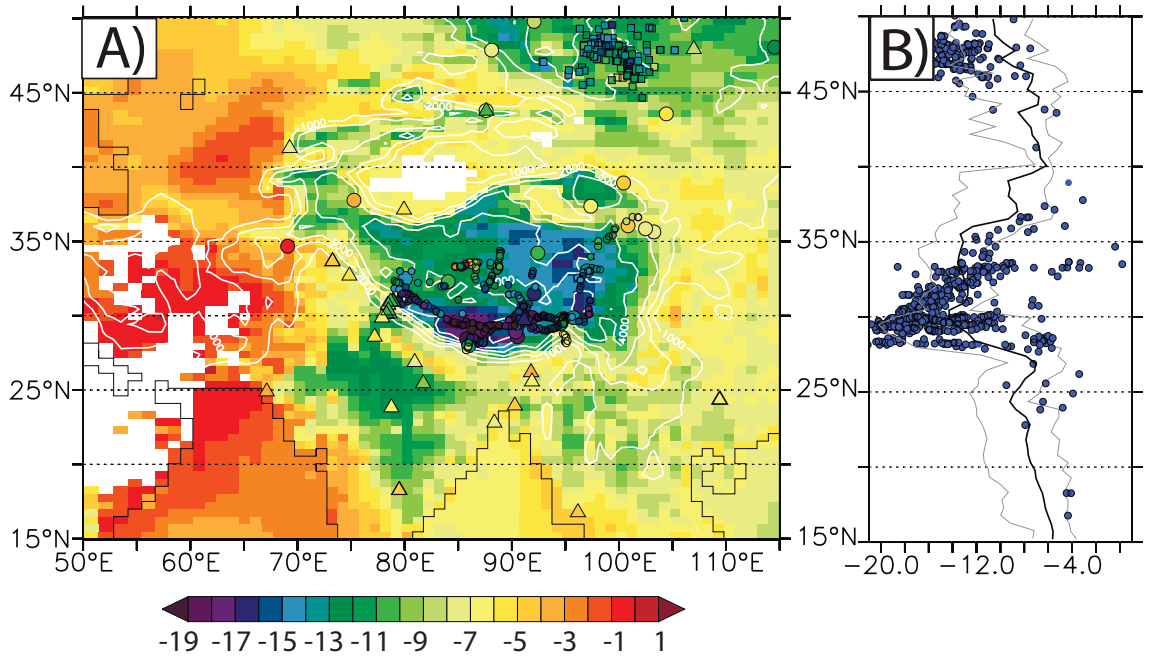

Figure 4.1 – Maps and S-N profiles of model simulated MJJAS precipitation-weighted $\delta^{18}O_p$ for control(CTR, pre-industrial) case. Triangles show $\delta^{18}O_p$ from GNIP stations, big circles – $\delta^{18}O_p$ from Caves et al. (2015) compilation, small circles represent $\delta^{18}O_p$ in streams, lakes and springs compiled from (Bershaw et al., 2012; Hren et al., 2009; Quade et al., 2011). The $\delta^{18}O_p$ profiles are averaged between 70° E and 90° E. Grey lines show minimum and maximum values for the selected range of longitudes.

4.2.2 Simulated paleo $\delta^{18}O_p$

In general, Early Eocene, Middle Eocene, Oligocene and Miocene simulated $\delta^{18}O_p$ over Asia are much more positive that present-day values (compare Figure 4.1, A and Figure 4.2). $\delta^{18}O_p$ values are ranging from -14 to 1 ‰. In our paleo experiments, values below -14 ‰ are not simulated. Further we provide some hypothesis about physical mechanisms that may contribute to the shift in paleo $\delta^{18}O_p$ towards values less negative then present-day.

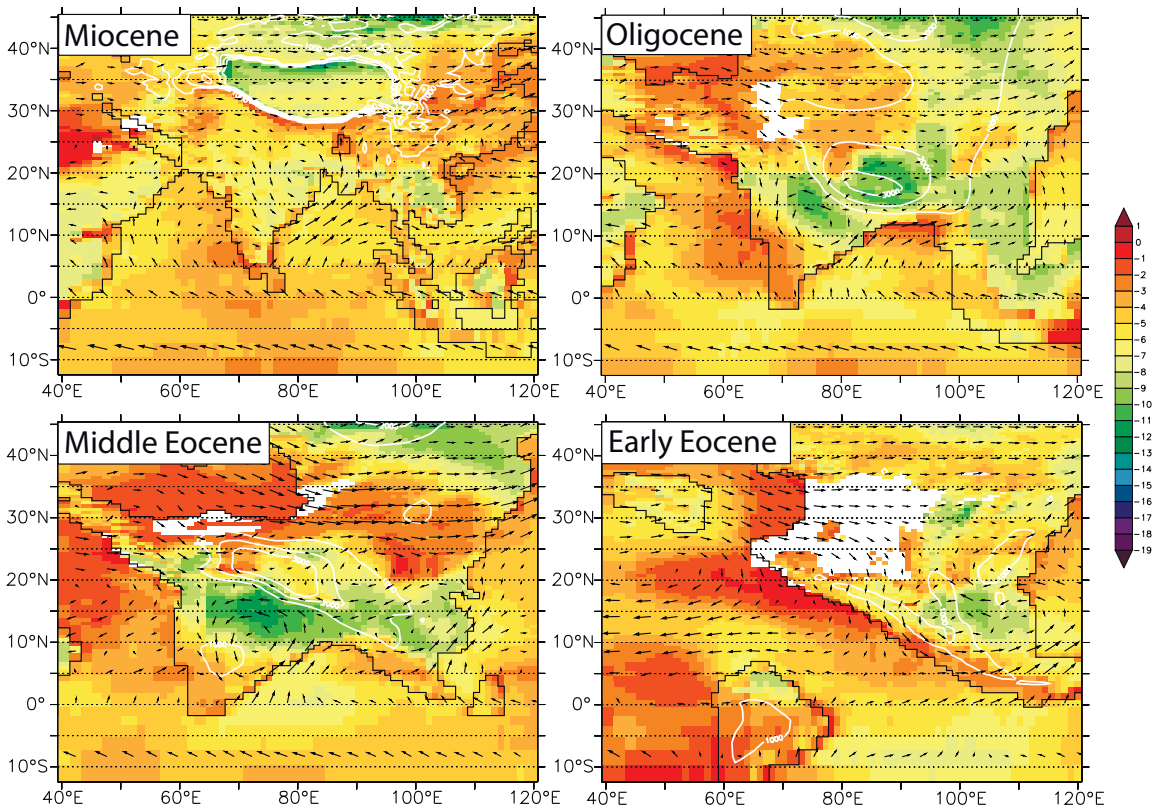

Figure 4.2 – LMDZ-iso simulated mean MJJAS $\delta^{18}O_p$ (precipitation-weighted) for: A) Miocene, B) Oligocene, C) Middle Eocene and D) Early Eocene cases. White shade corresponds to areas where precipitation is under 0.05 mm/month. Vectors show MJJAS mean moisture transport directions.

Isotopic lapse rates during the Cenozoic

In Section 3.2 we discuss spatial variations of $\delta^{18}O_p$-elevation gradients for present-day simulation. Our results suggest that the isotopic lapse rate is not constant spatially and support the statement that the empirical model based on the Rayleigh distillation calibrated for the Himalayas (Rowley and Garzione, 2007; Rowley et al., 2001) is consistent with simulated isotopic gradients over the Himalayas and the Southern Tibet, but fails over the Northern Plateau. With our realistic experiments we are able to investigate temporal variations of $\delta^{18}O_p$-relationships as well.

On the figure 4.3, $\delta^{18}O_p$ from Cenozoic realistic experiments are plotted against elevations in corresponding paleogeography. This plot clearly shows that no reliable $\delta^{18}O_p$-

elevation relationship over the HTP can be detected for the paleo case. In the absence of $\delta^{18}O_p$-elevation relationship, paleoelevations could not be reconstructed based on classic paleoaltimetry approach (see Section 1.3.3). Further we hypothesis possible mechanisms that impact this distribution and in Chapter 5 suggest how this limitation may be avoid using a GCM-simulated paleo $\delta^{18}O$.

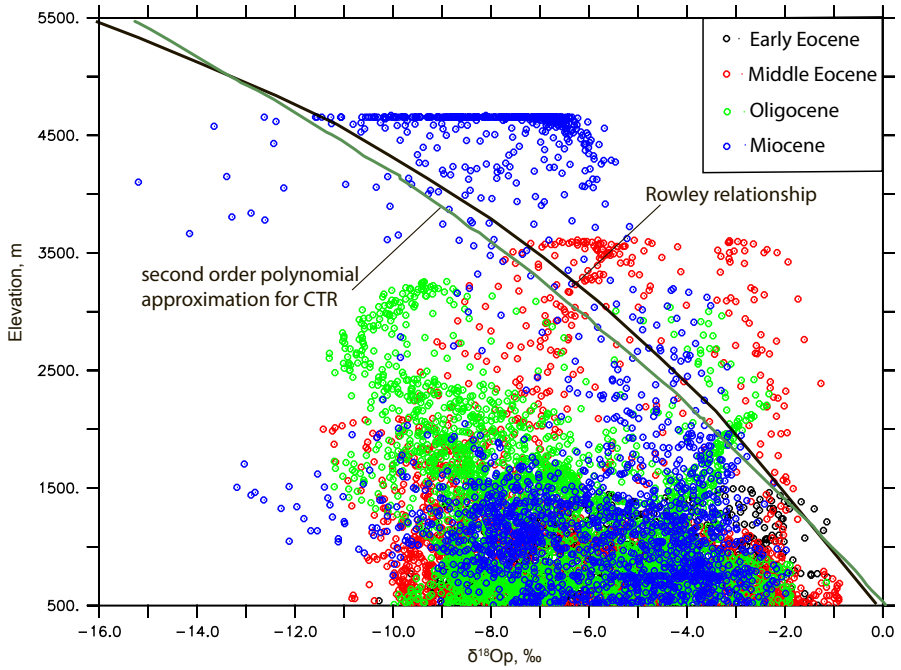

Figure 4.3 – $\delta^{18}O_p$ vs. elevation for Early Eocene, Eocene, Oligocene and Miocene experiments. Values are plotted for elevated regions (over 500 m), between 10° N and 40° N and 60° E and 100° E. Solid black line shows relationship from empirical model (Rowley and Garzione, 2007; Rowley et al., 2001). Green line shows second order polynomial approximation of simulated $\delta^{18}O_p$ for CTR (present-day) experiment. This plot clearly shows that simulated $\delta^{18}O_p$- elevation gradients ("isotopic lapse rates") for paleo cases are different from those of present-day.

Why paleo isotopic patterns over Asia are different from those of present-day?

Simulated Cenozoic $\delta^{18}O_p$ values are evidently different form those of present-day (compare Figure 4.1, A and Figure 4.2), with a shift towards less negative values for paleo epochs. Absence of $\delta^{18}O_p$-elevations relationship (Figure 4.3) contradicts models based on Rayleigh distillation widely used for reconstruction of paleoprecipitation $\delta^{18}O_p$ over Asia (e.g. Rowley et al., 2001). Here we hypothesize several possible mechanisms that contribute to simulated isotopic signal for the Cenozoic based on the preliminary analysis of the results of our simulations.

First, mean annual global warming following the increase in pCO2 in our realistic Cenozoic experiments together with the change of the latitudinal position of the HTP region during the collision between India and Eurasia causes increase in mean annual temperature over HTP from 5 to 9 °C for paleo cases. Consequently, this temperature increase cause a shift in $\delta^{18}O_p$ towards less negative values according to the Rayleigh distillation

processes.

The HTP is fed by three major air masses: the westerlies, Indian monsoon system and East-Asia monsoon (Figure 4.4) for all Cenozoic simulations, except for the Early Eocene. For all Cenozoic simulation MJJAS precipitation is high over India, South-East Asia and southern slopes of the Himalayas (Figure 4.4). High precipitation rates are known to impact $\delta^{18}O_p$ through the amount effect, however, this effect is consistent between all the simulations (Figure 4.6, 1st column). More importantly, relative contribution of evaporation and precipitation significantly changes during the Cenozoic (Figure 4.6, 3rd column). For CTR and Miocene simulations, precipitation amount dominant on evaporation over the Himalayas and the southern TP, while for the Eocene and Oligocene cases evaporation plays a more important role in the hydrological cycle of the HTP (Figure 4.6, 3rd column).

Simulated less negative paleo $\delta^{18}O_p$ over elevated topography of the HTP for the Miocene case and for the CTR case are consistent with the mechanism suggested by Poulsen and Jeffery (2011) based on their global simulations with increased pCO_2: increased concentration of greenhouse gases in the atmosphere leads to a reduction in the surface to upper troposphere $\delta^{18}O_v$ gradient and less negative values over regions with strong subsidence. However, for Oligocene and Eocene periods elevated topography is shifted from the zone of prevailing subsidence to a convection zone (Figure 4.5), making this mechanism unrealizable even for high atmospheric pCO_2 concentrations. On the contrary, emplacement of the paleo HTP in the convection zone contributes to simulated enriched values of $\delta^{18}O_p$ over highly elevated topography. The mechanism of this shift towards less negative values if following: ^{18}O-rich vapor (due to higher contribution of evaporation in the hydrological cycle, Figure 4.6, 3rd column) from the surface is mechanically transported up to the lifted condensation level where it contributes to ^{18}O-enriched condensate and precipitation.

Another effect that is responsible for simulated less negative $\delta^{18}O_p$ over the northern TP and the central Asia is high aridity associated with the subsidence zone and, as a consequence, high contribution of post-condensation effect to resulting $\delta^{18}O_p$ (Figure 4.6, 1st column). In the following Section we investigate in details the mechanism that influence $\delta^{18}O_p$ for the Eocene case.

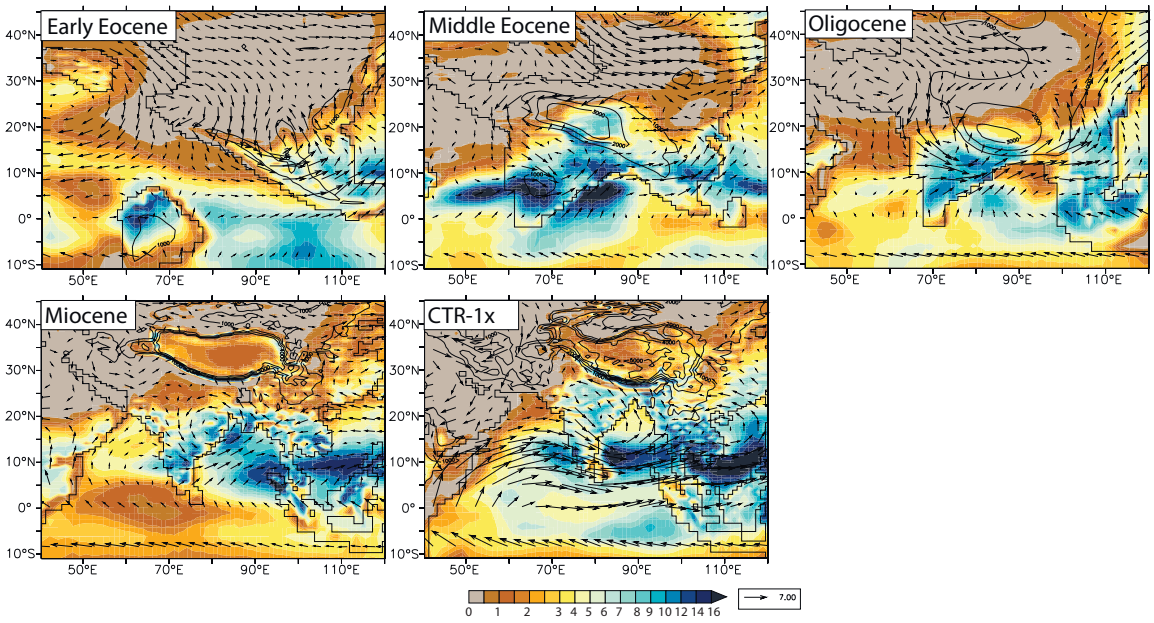

Figure 4.4 – MJJAS mean rainfall (mm/day) and surface winds for Early Eocene, Middle Eocene, Oligocene, Miocene and Control cases.

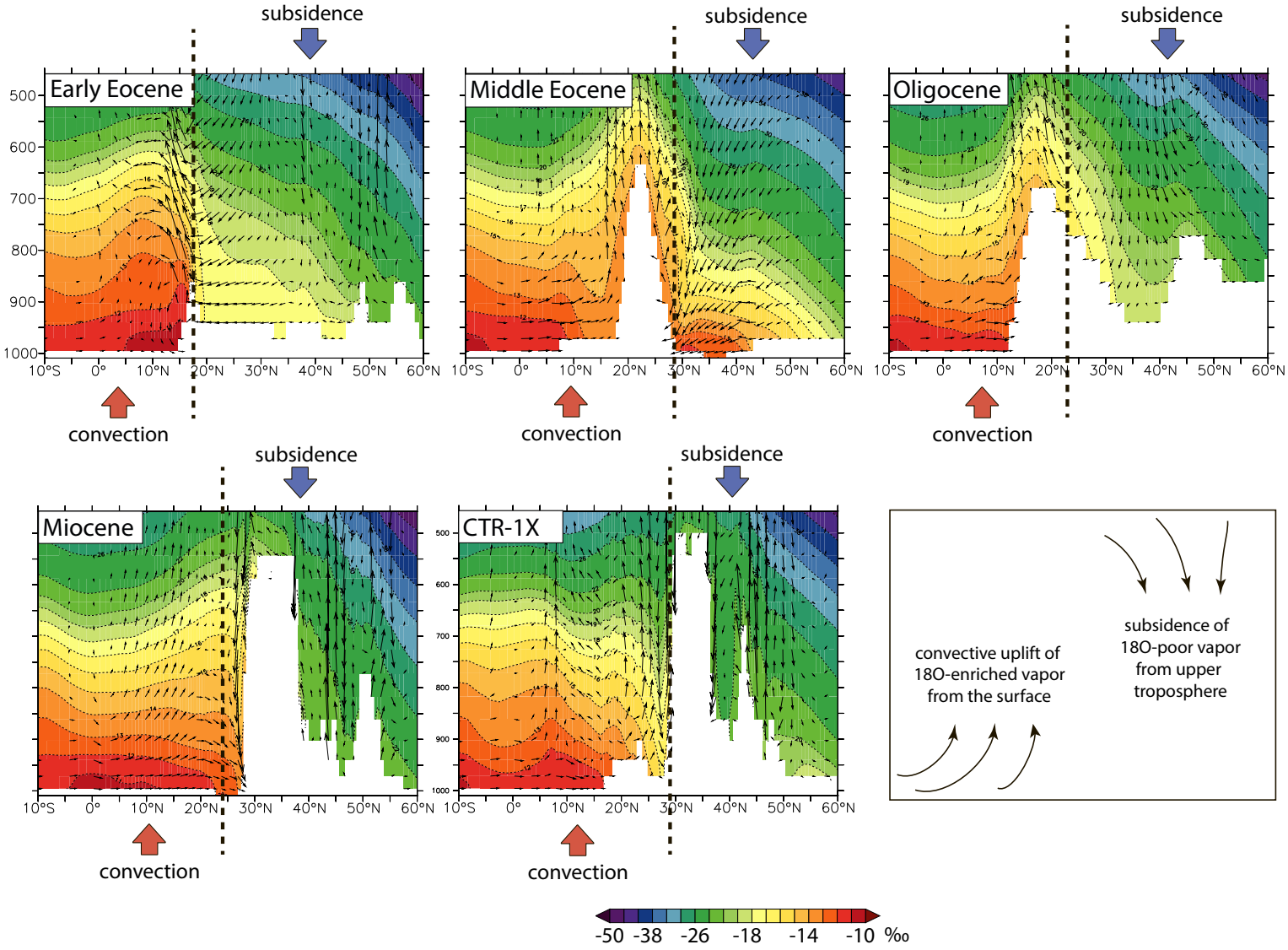

Figure 4.5 – MJJAS $\delta^{18}O_v$ and meridional-vertical wind velocities for Early Eocene, Middle Eocene, Oligocene, Miocene and Control cases.

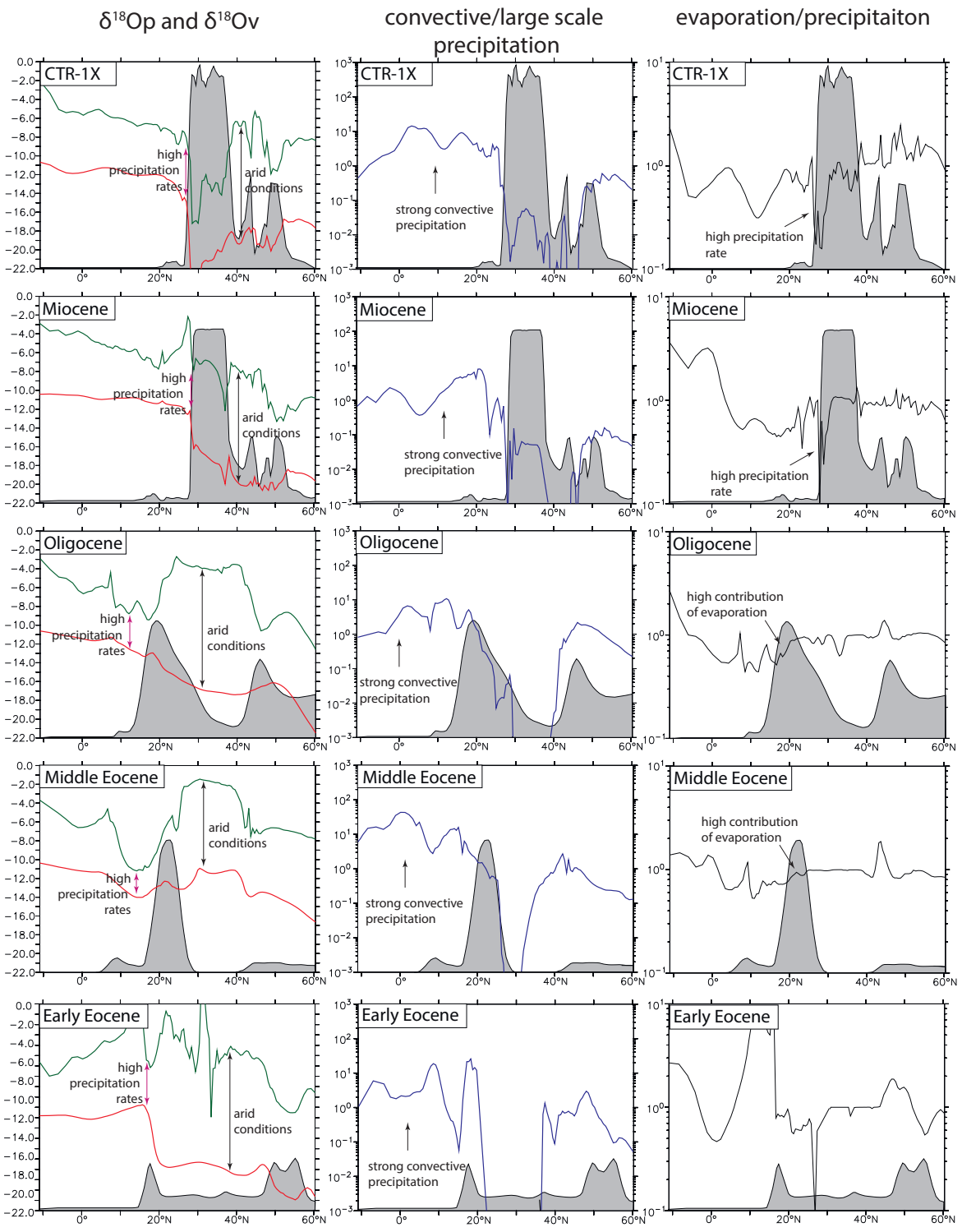

Figure 4.6 – South-North cross HTP sections for $\delta^{18}O_v$ (red line), $\delta^{18}O_p$ (green line), ratio between convective precipitation and large-scale precipitation (blue line) and the ratio between evaporation and precipitation (black line) for Middle Eocene, Oligocene, Miocene and Control cases. All variables are shown for MJJAS. Grey shade shows the topography for corresponding simulation.

4.3 Article in preparation for *EPSL*: Controls of the Eocene stable oxygen isotopes over Himalayas and Tibetan Plateau

Previously we have shown that simulated Eocene $\delta^{18}O_p$ over Asia appeared to be different from present-day distributions. Here we investigate in details simulated $\delta^{18}O_p$ patterns for the Eocene and their controlling factors. We present a paper in preparation for *EPSL*, with following main points:

- **Main point #1**. Less depleted $\delta^{18}O_p$ over Eocene Himalayas and Tibetan Plateau due to the increase in global and local temperatures and strong convection of enriched near-surface vapor;
- **Main point #2**. Weak impact of pCO_2 and topography variations for the Eocene due to the shift of the Himalayas and Tibetan Plateau into the convection zone;
- **Main point #3**. No Rayleigh distillation over the Himalayas for the Eocene case as a result of mixing of multiple air masses;
- **Main point #4**. No altitude-$\delta^{18}O_p$ relationship in the Eocene.

Controls of the Eocene stable oxygen isotopes over Himalayas and Tibetan Plateau

Svetlana Botsyun[1], Pierre Sepulchre[1], Camille Risi[2] and Yannick Donnadieu[1]

[1] Laboratoire des Sciences du Climat et de l'Environnement, CEA, CNRS, UVSQ, Gif-Sur-Yvette, France

[2] Laboratoire de Météorologie Dynamique, IPSL, UPMC, CNRS, Paris, France

Abstract

Stable oxygen isotopes paleoaltimetry has been widely used for reconstructing the altitude of the major orogens during the Cenozoic. The reconstruction of paleoelevation presumes the dependency of $\delta^{18}O$ in precipitation on the elevation. For the present-day case, the patterns of spatial $\delta^{18}O$ distribution are relatively well understood and $\delta^{18}O$-elevation relationship over the Himalayas is known to be mainly controlled by the Rayleigh distillation processes as a result of orographic ascend of a single air mass originated from southerly moisture source. However, during the Cenozoic ^{18}O distribution is not well constrained on account of lack of data from paleo carbonates and modeling results. Hence, the consistency of main controlling factors of $\delta^{18}O$ with those of present-day is uncertain and using present-day $\delta^{18}O$-elevation relationship might not be valid for paleo time periods. Here we provide high-resolution climate simulations using the isotope-equipped General Circulation Model LMDZ-iso with present-day and Eocene boundary conditions in order to test the impact of the paleogeography change and a variation of atmospheric pCO_2 on $\delta^{18}O_p$ over the Himalayas and the Tibetan Plateau. For the Eocene case $\delta^{18}O_p$ over the Himalayas and the Tibetan Plateau shows a significant increase compared to the present-day values following the increase in global temperature and a shift in its a latitudinal position towards large-scale convection zone, however the impact of pCO_2 on $\delta^{18}O$ in the Eocene configuration is weak. Wind trajectories back tracing applied to the model outputs allowed to compare the moisture feeding of the Himalayas and the Tibetan Plateau regions for the present-day and the Eocene cases and show that the Rayleigh distillation processes is not applicable for the Eocene Himalayas making paleoelevation reconstructions of the Eocene doubtful.

Introduction

Stable oxygen isotopes as tracer elements are widely used in geosciences, in particular for paleoelevation reconstructions. Multiple carbonate $\delta^{18}O$ measurements from the Eocene natural archives (e.g. lake or soil carbonates) are available due to a huge measurement afford of recent decades (studies of [*Rowley and Currie*, 2006; *Xu et al.*, 2013, 2015; *Ding et al.*, 2014; *Hoke et al.*, 2014; *Wei et al.*, 2016]) and a range of paleoaltimetry estimates for this time period have been providen: form comparable with present-day elevation for Eocene Tibet e.g [*Ding et al.*, 2014] to near-surface elevations [*Wei et al.*, 2016]. Classic stable oxygen isotopes-based approach relies on the knowledge about the relationship between low-elevation precipitation $\delta^{18}O$ ($\delta^{18}O_p$) and $\delta^{18}O_p$ at the point of interest. This relationship has been calibrated using present-day empirical [*Garzione et al.*, 2000; *Poage and Chamberlain*, 2001] and theoretical approaches that rely on basic thermodynamic principles, including Rayleigh distillation, that govern isotopic fractionation processes [*Rowley et al.*, 2001; *Rowley and Garzione*, 2007]. However, stationary of $\delta^{18}O_p$-elevation relationship through time is questionable [*Sturm et al.*, 2007].

Spatial distribution of $\delta^{18}O$ in modern precipitation and $\delta^{18}O$-elevation relationship is relatively well understood over Asia, based on data [e.g. *Rozanski et al.*, 1993; *Lee et al.*, 2012] and modeling both [*Li et al.*, 2016]. Non-homogeneity of the isotopic signal in precipitation and variations in $\delta^{18}O$-elevation relationship have been suggested, based on modern precipitation [*Tian et al.*, 2001a, 2007], modern ice-cores [*Tian*, 2003], and surface water samples [*Tian et al.*, 2001a; *Hren et al.*, 2009; *Quade et al.*, 2011; *Bershaw et al.*, 2012b]. In a series of studies, Tian et al. [*Tian et al.*, 2001b, 2007; *Tian*, 2003] isolate three distinct regions where stable water isotopes patterns appears to be different: (1) south of Himalayas, (2) southern TP, between Himalayas and Tanggula mountains and (3) TP north of Tanggula mountains. In these studies, moisture origin, vapor transport, as well as the "amount effect" of monsoon precipitation have been hypothesized to influence the final $\delta^{18}O$ signal of precipitation. Based on the isotopic composition of surface waters and soil carbonates, Quade et al. (2011) suggest a gradual increase in $\delta^{18}O$ values to the north of Himalayas crest and reduced isotope-elevation gradient in the northernmost TP that reflects the diminishing contribution of summer monsoon. In addition to the restricted influence of the Indian Ocean-derived moisture on the northern Plateau, Hren et al. [*Hren et al.*, 2009] showed an enriching impact of western-sourced air masses on moisture signature of the northern TP. Bershaw et al.

[*Bershaw et al.*, 2012b] used back-trajectories to estimate moisture sources contributing to the hydrological budget of Asia. The authors suggest that local moisture recycling has a crucial impact on the isotopic signature of precipitation regardless the origin of air mass. In regard to quite sparse distribution of observations, Atmospheric General Circulation Models (AGCM) also have been to simulate present-day distributions of $\delta^{18}O_p$ [*Yao et al.*, 2013] and the model results have been used to divide the HTP aria into three zones: (1) the monsoonal domain, controlled mainly by the monsoonal precipitation with very depleted $\delta^{18}O_p$, with a high role of the amount effect (2) the northern domain which hydrological budget is mainly controlled by the moisture transported with the westerlies, and (3) a transitional domain, which is controlled by either monsoonal or westerlies moisture depending on the season.

Reconstruction of spatial $\delta^{18}O_p$ distributions for pale time periods is more complicated, in a lack of paleo data and numerical simulations. In order to fill this gap and aiming to quantify how different aspects of climate changes influence $\delta^{18}O_p$ isotopes-equipped AGCMs have been used. Results highlight the sensitivity of $\delta^{18}O_p$ to climate change associated with variations in pCO_2 [*Poulsen et al.*, 2007; *Poulsen and Jeffery*, 2011], sea surface temperatures (SSTs) [*Sturm et al.*, 2007], sea level changes [*Poulsen et al.*, 2007], and uplifts of major orogens [*Ehlers and Poulsen*, 2009; *Poulsen et al.*, 2010; *Botsyun et al.*, 2016]. At the exception of [*Sewall and Fricke*, 2013] for the Cretaceous, these studies were based on sensitivity experiments using present-day continental positions and could not aim at simulating $\delta^{18}O$ for a particular period. In a very recent paper of [*Roe et al.*, 2016] an isotopes enabled GCM has been used for simulation using paleogeographies different from the present-day. However, these authors neither compare Eocene isotopic signal with present-day one nor explore the impact of Eocene topography variations on $\delta^{18}O_p$.

In this study we use isotope-enabled atmospheric general circulation model LMDZ-iso with realistic Eocene boundary conditions in order to study paleo $\delta^{18}O_p$ distributions over the Himalayas and the Tibetan Plateau and their controlling factors. Results of this study may perturb the elevation history of the Himalayas and the Tibetan Plateau as appeal directly to the paleoelevations reconstructions methodology.

2. Climate and Isotope modelling

We use LMDZ-iso, a derivative from the LMDz [*Hourdin et al.*, 2006] Atmospheric General Circulation model (GCM) developed at Laboratoire de Météorologie Dynamique, Paris, France, that is implemented with isotopes-tracking capabilities [*Risi et al.*, 2010]. This

model represents isotopic processes associated with all phase changes. Water in its vapour and condensed form is advected by the Van Leer advection scheme [*Van Leer*, 1977]. The ability of this model to simulate atmospheric dynamics and reproduce rainfall and $\delta^{18}O$ patterns over Asia has been shown in previous studies [*Yao et al.*, 2013; *Botsyun et al.*, 2016]. Here we use a model configuration with 144 grid points in longitude, 142 in latitude and 39 vertical layers. LMDZ-iso stretchable grid allows increasing regional spatial resolution and gives an averaged resolution of ~50 km over central Asia.

We provide experiments depicting both present-day-like and Eocene climate precipitation $\delta^{18}O$ patterns. As LMDZ-iso is an AGCM, we needed to prescribe sea-surface temperatures (SSTs) as boundary conditions. SSTs were obtained by using the fully coupled model FOAM (Fast Ocean–Atmosphere Model [*Jacob*, 1997] (ocean, 2.8° x 1.4° resolution with 24 vertical levels; atmosphere, 7.5° x 4.5° with 18 vertical levels) forced by present-day geography or Eocene paleogeography reconstruction [*Licht et al.*, 2014] respectively. Such a method using both models has been applied in recent studies on Cenozoic paleoclimates [*Ladant et al.*, 2014; *Licht et al.*, 2014]. For the Eocene case in order to obtain more realistic albedo and rugosity values, we used vegetation distribution simulated with biophysics vegetation model LPJ [*Sitch et al.*, 2003].

When compared to present-day, Eocene paleogeography includes a southward shift of the Asian continent, as well as the presence of a large Paratethys Sea covering the region between 30° N and 47° N in latitude and extending to 80°E. The HTP is also considerably shifted to the south (situated between 15° N and 27° N) **(Fig. 1)**. We also designed an additional experiment where the TP elevation was increased up to 5000 m, the elevations comparable with present-day ones. For revealing the effect of green house gases concentration combined with the paleogeographic one, atmospheric pCO_2 has been set to 280 ppm and 1120 ppm for present-day and Eocene configurations for the Eocene simulations, that lies within pre-industrial values approximations and the higher hand of Eocene estimates consequently [*Beerling and Royer*, 2011] **(Table 1)**.

FOAM simulation was integrated for 2,000 years without flux corrections or deep ocean acceleration. The last 50 model-years were used to build the SSTs climatology applied as input for LMDZ-iso. LMDz-iso experiments were run for 10 years, with 2 years used for spin-up.

In addition, we provide wind trajectories back tracing that allowed to compare the moisture feeding of the Himalayas and the Tibetan Plateau. Back-trajectories are calculated using daily LMDZ outputs for present-day and the Eocene cases. Simulated horizontal winds

at 100 hPa above the ground surface are used, neglecting vertical motions. Simulated winds are interpolated in time and space to each geographical position along the back-trajectory. The geographical positions along the back-trajectories are computed every 6 hours back to 6 days, so that each back-trajectory is characterized by 24 positions. One hundred and fifty trajectories are calculated for each climate setting: one for every day of MJJAS. To visualize the origin of air masses, spatial maps of probability density functions are computed using all the 24x150 back-trajectory geographical positions.

Table 1. List of experiments

Experiment	Configuration	pCO_2 (ppm)
CTR-1X	Present-day geography	280
CTR-4X	Present-day geography	1120
EOC-1X	Eocene paleogeography from Licht et al., 2014	280
EOC-4X	Eocene paleogeography from Licht et al., 2014	1120
EOC-XL	Eocene paleogeography with 150% of TP compared with EOC-4X	1120

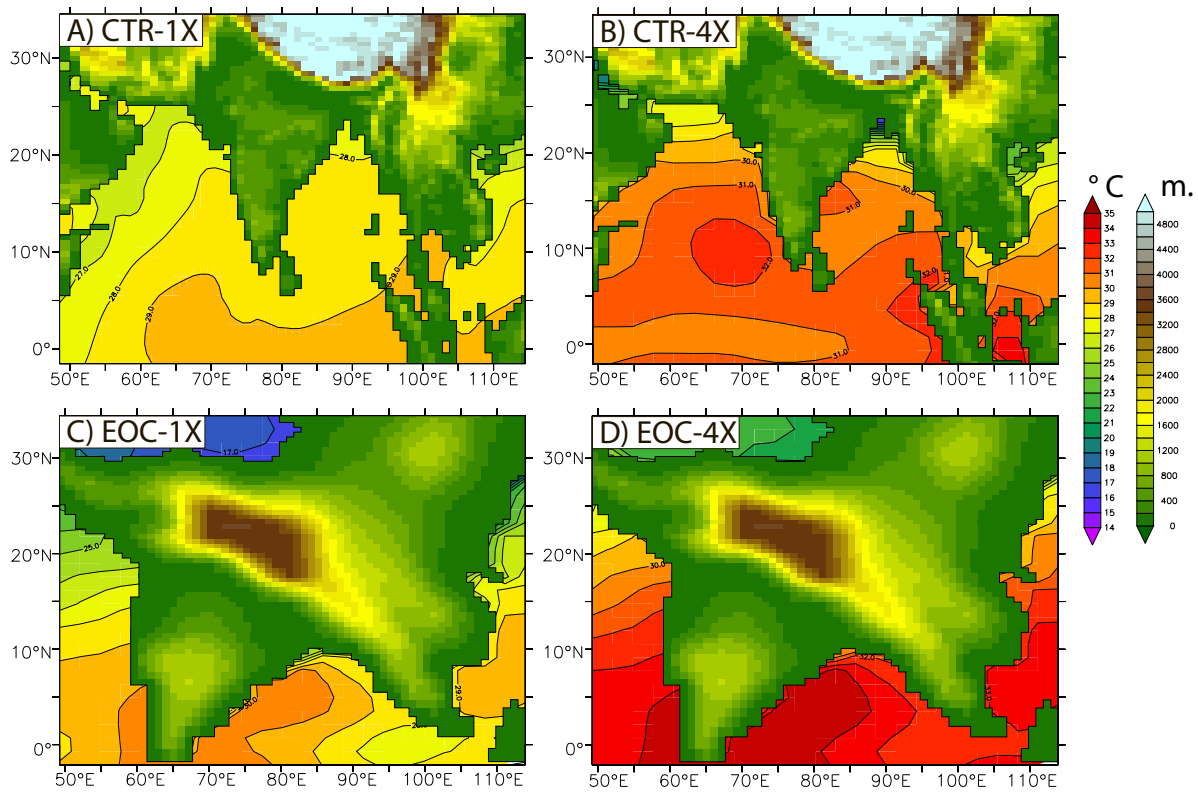

Figure 1. Geographical settings and FOAM-derived sea surface temperatures for A) CTR-1x B) CTR-4x, C) EOC-1x, D) EOC-4x

3. Model validation and effect of increased pCO_2 in a modern configuration

The ability of LMDZ-iso to simulate modern climate patterns and modern $\delta^{18}O_p$ have been shown in detail by [*Yao et al.*, 2013; *Botsyun et al.*, 2016]. Simulated with a model configuration used in this study, present-day $\delta^{18}O_p$ values over Asia are consistent with sparse observations from the International Atomic Energy Agency (IAEA) Global Network of Isotopes in Precipitation (GNIP) and show a sufficient agreement with modern precipitation and rivers $\delta^{18}O$ measurements [*Hren et al.*, 2009; *Quade et al.*, 2011; *Bershaw et al.*, 2012b; *Caves et al.*, 2015]. However, some model-data discrepancies over the northern and central part of the Plateau and over Mongolia could be probably explained by: i) correspondence of measured date to JJA $\delta^{18}O$ signal (season when rain events happen) that is much more positive that annual averaged one (not shown), ii) comparison with measurement of lake water $\delta^{18}O$, which is enriched in heavy isotopes due to evaporation processes, while currently used version of LMDZ-iso doesn't include lakes simulation.

The modern MJJAS (May to September average) isotopic distribution is characterized by a northward decrease in $\delta^{18}O_v$ from the Himalayas foothills (25° N) to the southern Tibet (with values down to -24‰) linked to Rayleigh distillation during rainout and ascent of air masses along the southern flanks of the HTP. This mechanism is consistent with what has been shown from data and 1-D models [*Rowley et al.*, 2001; *Rowley and Garzione*, 2007]. Not surprisingly, back-trajectories along South-North cross-Himalayas transect indicated mainly southern origin of air masses **(Fig. 2, points 1 and 2)**. Between 30°N and 40°N a shift to less negative values of $\delta^{18}O_v$ (ranging from -18 to -22 ‰) is simulated, that is linked to increased contribution of evaporation into the hydrological cycle **(Fig. 3 C).** This result is consistent with observations from several South-North transects across the Plateau [*Quade et al.*, 2007, 2011; *Bershaw et al.*, 2012b]. These studies inferred that this isotopic enrichment with latitude relied on the diminishing influence of ^{18}O-depleted monsoon rainfall, increasing of westerlies contribution [*Tian et al.*, 2001, 2007; *Yao et al.*, 2013] and the increasing fraction of enriched recycled surface water (including evaporation from soils and lakes) in the precipitation regime [*Bershaw et al.*, 2012b].

Compared to CTR-1X, $\delta^{18}O_p$ for the CTR-4X case show enriched values over the HTP region **(Fig. 4 A, B)** that is a direct consequence of warming associated with increased pCO_2. However, $\delta^{18}O_p$ becomes more enriched for the CTR-4X over the HTP (by up to 8‰, locally) than over low-elevation areas **(Fig. 5 A)**. This signal is consistent with a mechanism

previously described in [*Poulsen and Jeffery*, 2011]: increasing pCO_2 warms preferentially the upper troposphere, thereby in subsidence zones $\delta^{18}O_v$ is mechanically increased. The difference of $\delta^{18}O_v$ between CTR-1X and CTR-4X experiments clearly shows the increase in isotopic lapse rates for the CTR-4X case **(Fig. 5 H).** Moisture transport patterns as well as the hydrological cycle (relative contribution of convective and large-scale precipitation, the evaporation contribution) remains almost unchanged with the shift in CO_2 concentration for the CTR case **(Fig 3 A, C, E, H)**.

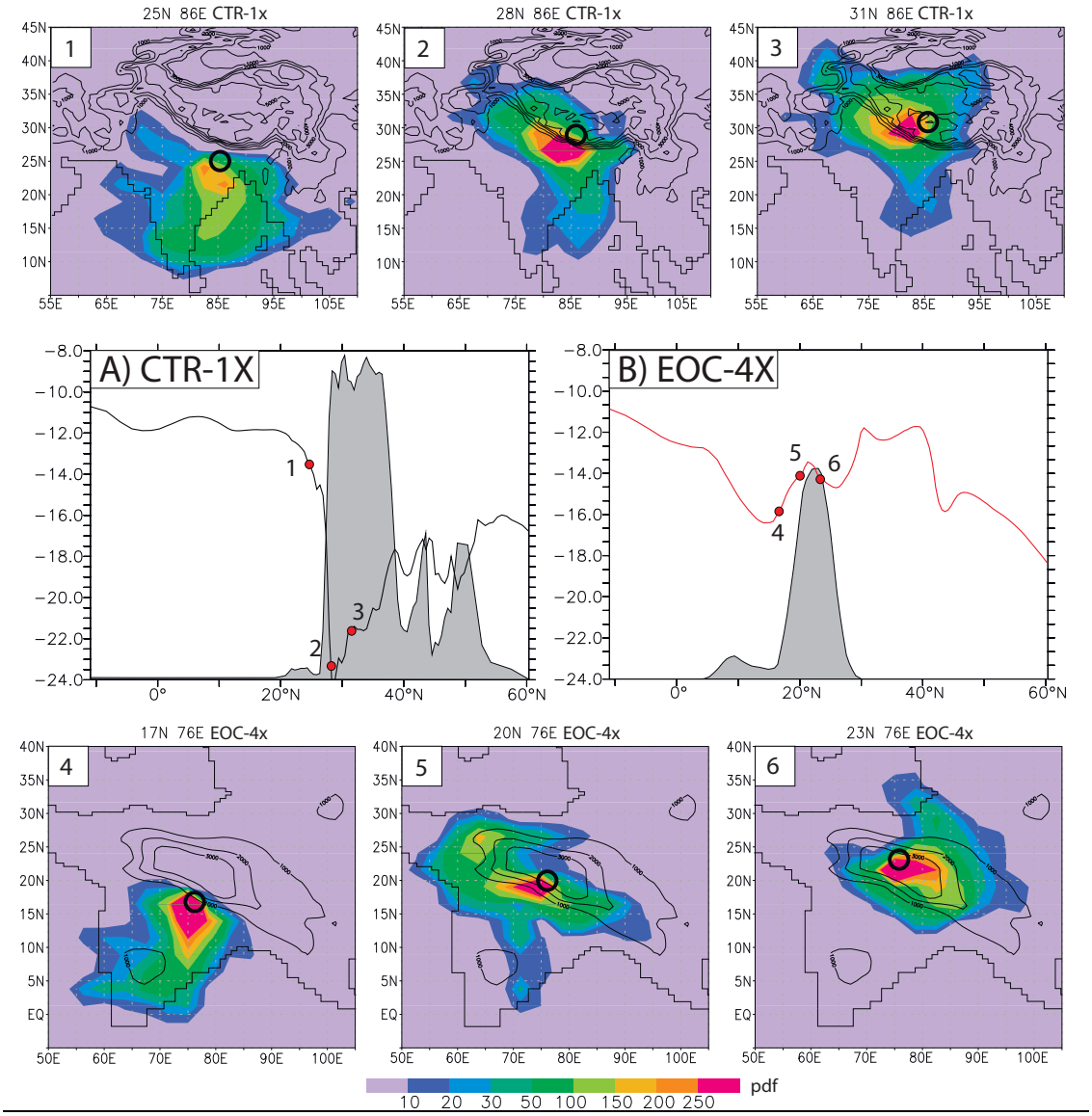

Figure 2. MJJJAS $\delta^{18}Op$ profiles from CTR-1x (A) and EOC-4x (B) experiments. Maps show the probability distribution of air masses along the back trajectories for each of the 6 points for CTR-1x (points 1-3) and EOC-4x (points 4-6). Back trajectories last 6 days and the distribution is calculated daily from May to September at 900hPa level.

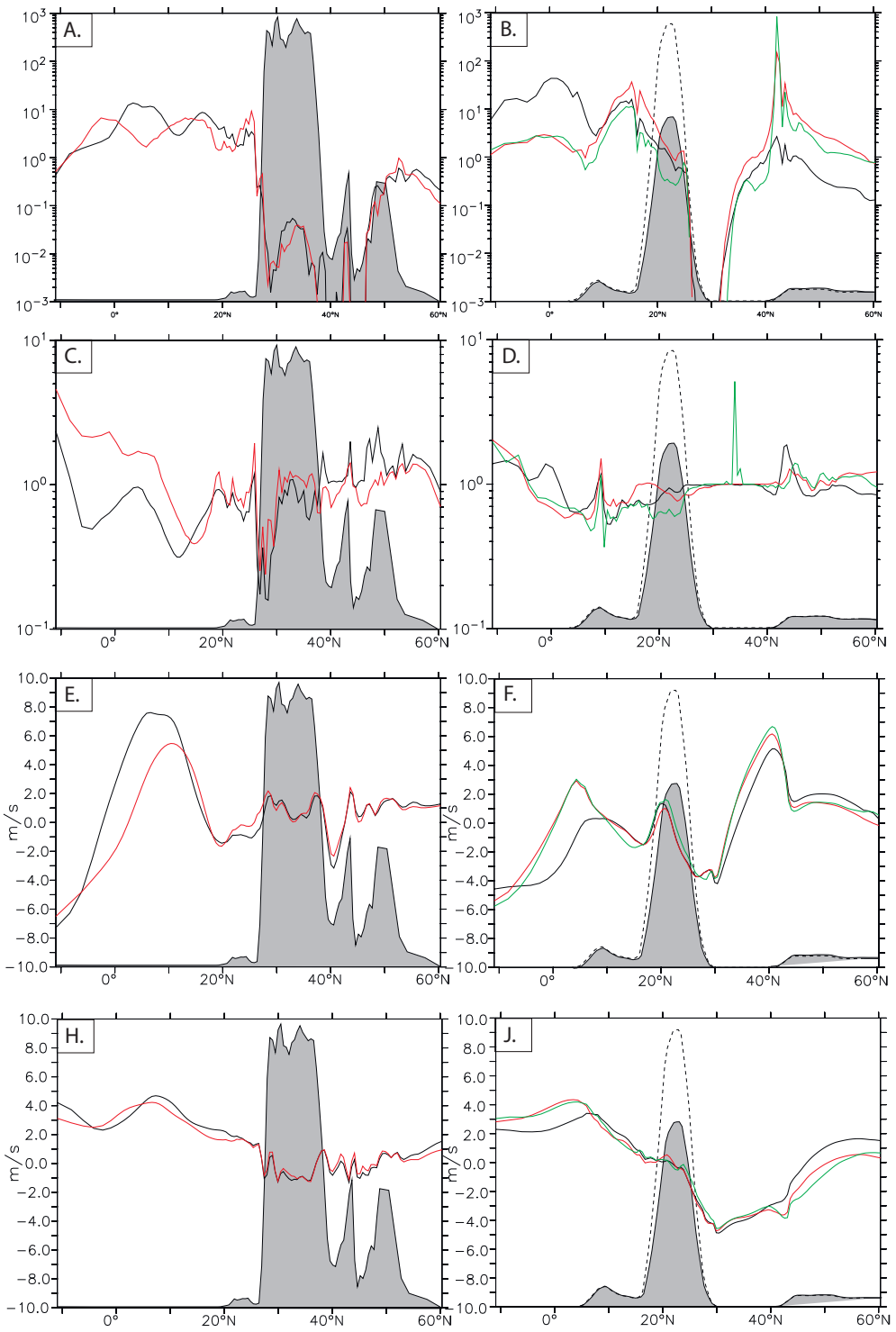

Figure 3. South-North cross HTP sections for A), B) the ratio between convective precipitation and large-scale precipitation C), D) the ratio between evaporation and precipitation, E), F) near surface zonal winds, H), J) near surface meridional winds for CTR (A, C, E, H) and Eocene cases (B, D, F, J). All variables are shown for MJJAS. Grey shade shows the topography for corresponding simulation. For the CTR case profiles are averaged between 85°E and 90° E, and between 73° E and 78° E for the Eocene cases.

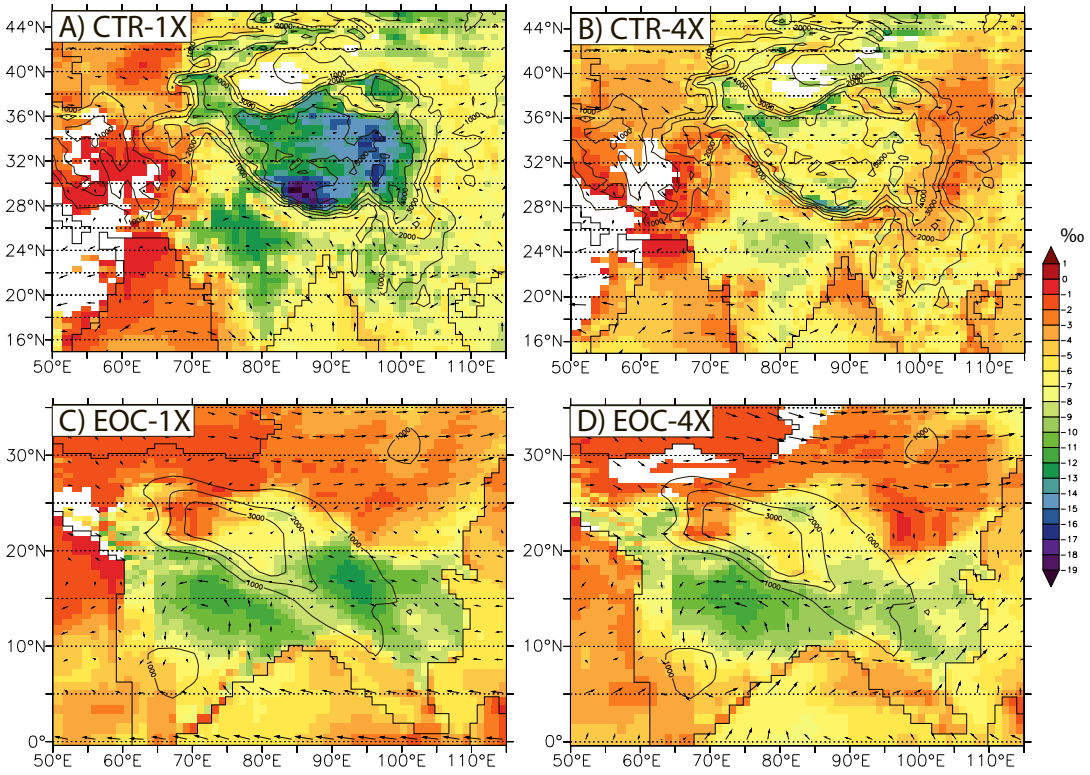

Figure 4. LMDZ-iso simulated mean MJJAS $\delta^{18}O_p$ (precipitation weighted) for: A) CTR-1X, B) CTR-4X, C) EOC-1X and D) EOC-4X cases. White shade corresponds to areas where precipitation is under 0.05 mm/month.

4. The Eocene world: Combining paleogeographic and pCO_2 effects

In general, for the EOC-1X the pattern of $\delta^{18}O_v$ over Asia depicts a strong latitudinal dipole associated with Eocene climate dynamics, with depleted values south of the HTP and highly enriched values to the North. Along a South-North transect **(Fig. 5 B)**, $\delta^{18}O_v$ gradually decreases through rainout from the Indian southern tip (ca. -4‰) to a minimum at the HTP foothills, at 12°N (-10‰), similarly to the patterns simulated south of the HTP in CTR-1X simulation. However, contrary to simulations with modern geography, EOC-1X experiment shows an absent of isotopic depletion over the southern slope of the HTP, with the $\delta^{18}O_v$ values increasing from 15°N to 22°N **(Fig. 4 B)**. Backtrajectories analyses shows that cite along S-N transect are feed by multiple disconnected air masses **(Fig. 3, point 4, 5, 6)**, while the Rayleigh distillation is valid for a single air mass only. For Himalayas foothills MJJAS wind trajectories are coming form the south *via* the Indian plain, further to the north, over the

Himalayas, they switch to preferably westerly source and, finally, at the top of the HTP wind trajectories are advected form the Pacific Ocean. A direct consequence of this air masses mixing over the Plateau is an absence of $\delta^{18}O_v$-elevation relationship predicted by the Rayleigh distillation and commonly used for paleoelevation reconstruction [*Rowley et al.*, 2001; *Rowley and Garzione*, 2007]. On the contrary, for the Eocene simulations, over the southern slope of Himalayas, $\delta^{18}O_p$ apparently increases with increasing elevation **(Fig. 6)**.

Compared to modern configuration, Eocene paleogeography makes the entire Asian continent being shifted ca. 13° southward. The first consequence is 3-to-5°C warmer continent, regardless prescribed pCO_2 **(Table 2)**. For the Eocene case, the HTP is located between ca. 10° N and 28° N and is surrounded by an almost equatorial Indian subcontinent to the south and a flat region including the eastern edge of Paratethys to the North of the HTP. This latter region lies under the subsidence branch of the Hadley cell, which latitudinal position is unaltered by varying pCO_2 **(Fig. 5 D F).** On the contrary, Eocene elevated topography is situated in a strong convection zone **(Fig. 5 D E),** which, together with high evaporation rates **(Fig. 3 D)** results in high $\delta^{18}O$ at the lifted condensation level over the HTP due to convective uplift of near-surface ^{18}O-enriched vapor. This shift of the Eocene HTP region into a convection zone results in low sensitivity of $\delta^{18}O_p$ over elevated topography to prescribed pCO_2 **(Fig. 5 J)**.

Table 2. LMDZ-iso simulated temperatures. Region temperatures are averaged from 10° N to 50°N and from 45° E and 120° E.

	CTR-1X	CTR-4X	EOC-1X	EOC-4X
Global annual averaged near surface temperatures	14.07	19.66	16.75	22.60
Regional annual averaged near surface temperatures	20.44	23.95	21.54	26.80

In addition to the processes described above, for the Eocene case large-scale subsidence between ca. 25 and 40°N contributes to extremely arid condition, thus increasing post-condensational isotopic enrichment in the very dry air column. Low relative humidity drives high rates of raindrop re-evaporation that occurs after initial condensation, leading to an isotopic enrichment of precipitation compared to water vapor [*Lee and Fung*, 2008].

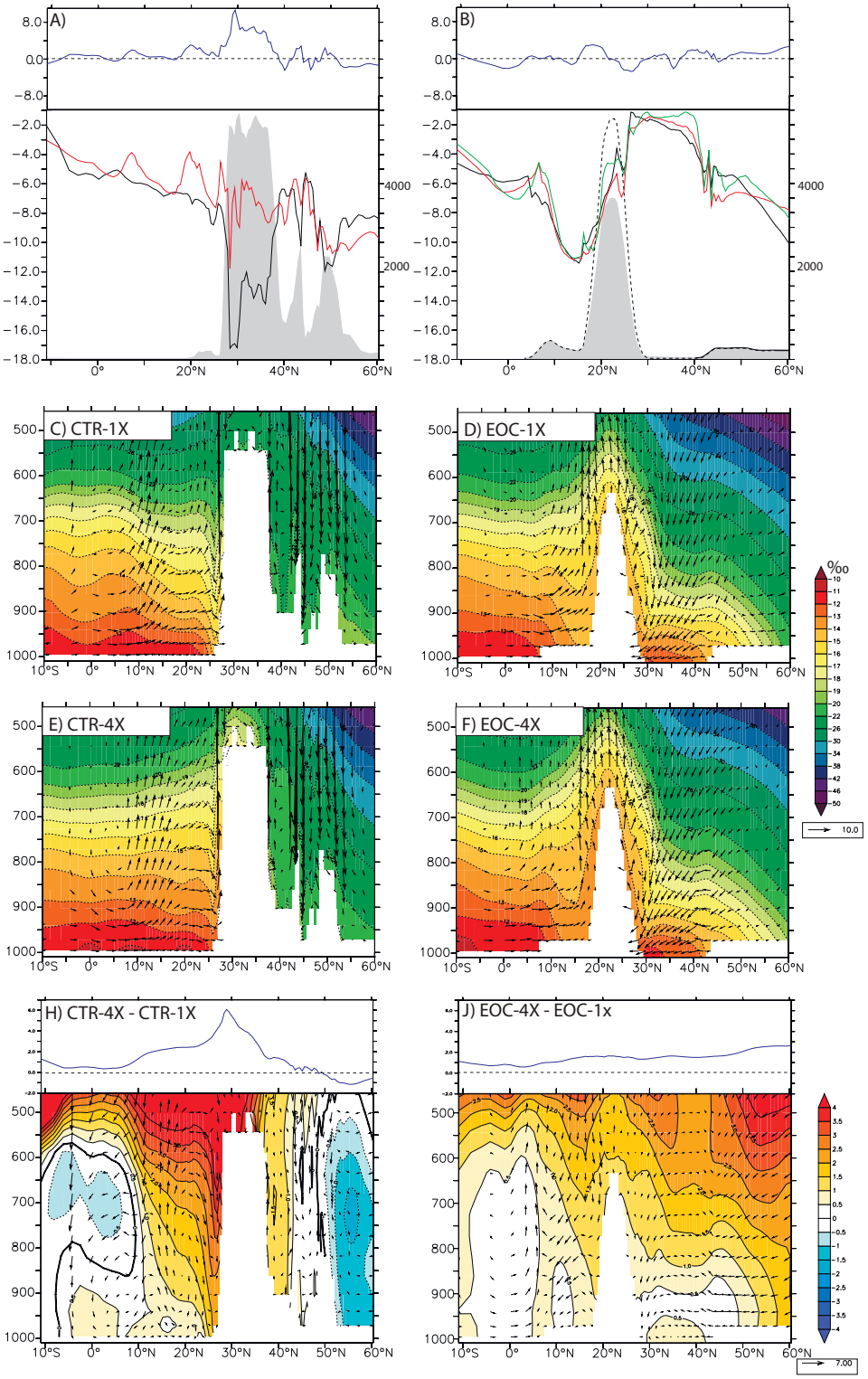

Figure 5. MJJJAS δ^{18}Op profiles from modern (A) and Eocene (B) experiments. Red line corresponds to CTR-4X and EOC-4X, black line to CTR-1X and EOC-1X cases and blue – to CTR-1X - CTR-4X and EOC-1X - EOC-4X respectively. MJJAS δ^{18}Ov and meridional-vertical wind velocities for C) CTR-1X, D) EOC-1X, E) CTR-4X, and F) EOC-4X experiments. Black line shows the lifted condensation level. MJJAS vertical profiles of the temperature and vertically integrated differences between CTR-1X and CTR-4X; EOC-1X and EOC-4X experiments. For the CTR case profiles are averaged between 85°E and 90° E, and between 73° E and

78° E for the Eocene cases.

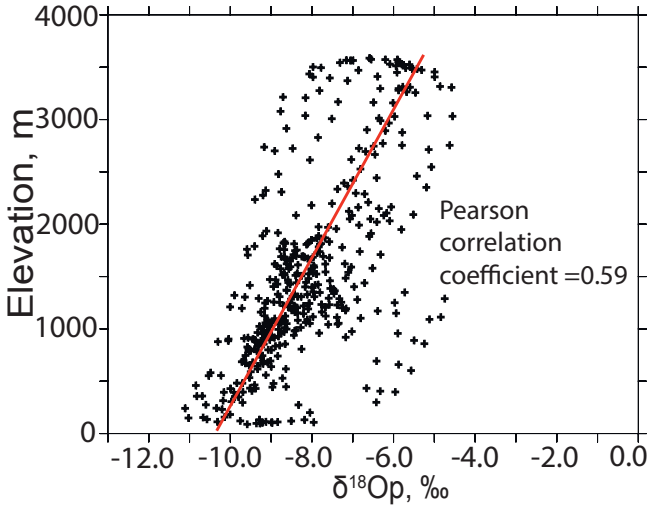

Figure 6. $\delta^{18}O_p$ – elevation relationship for the southern slope of the HTP for the EOC-4X experiment.

Conclusions

High surface temperatures linked to high CO2 concentrations and shift of the HTP to almost equatorial zone for the Eocene case, together with prevailing convective regime over the Eocene HTP shift $\delta^{18}O_p$ towards less negative values.

Our results suggest also suggest that the paleogeographycal changes are crucial for moisture feeding of the HTP region change dramatically $\delta^{18}O_p$ – elevation gradients. We show that the assumption about stationary of $\delta^{18}O$-elevation relationship through geological time [*Sturm et al.*, 2007] commonly used in paleoelevations studies is not valid. Thus, empirical paleoclimate reconstructions using oxygen stable isotopes are based on the assumption of stationary of $\delta^{18}O$-elevation relationship through geological time are likely no credible and the paleoelevation history of the HTP should be reviewed accounting for climatic processes that are recorded in the natural archives.

We suggest using high-resolution isotope-enabled GCM models with realistic boundary conditions in order to reconstruct paleoclimates and $\delta^{18}O$ both. Confronted against brut $\delta^{18}O$ from carbonate archives, results of such simulations my help in understanding the elevation history of major oregens.

Acknowledgments

This work is a part of iTECC (interaction Tectonics-Erosion-Climate-Coupling) project

funded by European Union. Computational resources were provided by IDRIS-GENCI (project 0292), France.

References cited

Abe, M., A. Kitoh, and T. Yasunari (2003), An Evolution of the Asian Summer Monsoon Associated with Mountain Uplift-Simulation with the MRI Atmosphere-Ocean Coupled GCM-, *J. Meteorol. Soc. Japan*, *81*(5), 909–933, doi:10.2151/jmsj.81.909.

Bershaw, J., S. M. Penny, and C. N. Garzione (2012), Stable isotopes of modern water across the Himalaya and eastern Tibetan Plateau: Implications for estimates of paleoelevation and paleoclimate, *J. Geophys. Res. Atmos.*, *117*(2), 1–18, doi:10.1029/2011JD016132.

Botsyun, S., P. Sepulchre, C. Risi, and Y. Donnadieu (2016), Impacts of Tibetan Plateau uplift on atmospheric dynamics and associated precipitation δ18O, *Clim. Past*, *12*(6), 1401–1420, doi:10.5194/cp-12-1401-2016.

Broccoli, A. J., and S. Manabe (1992), The Effects of Orography on Midlatitude Northern Hemisphere Dry Climates, *J. Clim.*, *5*(11), 1181–1201, doi:10.1175/1520-0442(1992)005<1181:teooom>2.0.co;2.

Ding, L., Q. Xu, Y. Yue, H. Wang, F. Cai, and S. Li (2014), The Andean-type Gangdese Mountains: Paleoelevation record from the Paleocene-Eocene Linzhou Basin, *Earth Planet. Sci. Lett.*, *392*, 250–264, doi:10.1016/j.epsl.2014.01.045.

Hahn, D. G., and S. Manabe (1975), The role of mountains in the south Asian monsoon circulation, *J. Atmos. Sci.*, *32*(8), 1515–1541.

Hoke, G. D., J. Liu-Zeng, M. T. Hren, G. K. Wissink, and C. N. Garzione (2014), Stable isotopes reveal high southeast Tibetan Plateau margin since the Paleogene, *Earth Planet. Sci. Lett.*, *394*, 270–278, doi:10.1016/j.epsl.2014.03.007.

Kitoh, A. (2004), Effects of Mountain Uplift on East Asian Summer Climate Investigated by a Coupled Atmosphere–Ocean GCM, *J. Clim.*, *17*(4), 783–802, doi:10.1175/1520-0442(2004)017<0783:EOMUOE>2.0.CO;2.

Kutzbach, J. E., P. J. Guetter, W. F. Ruddiman, and W. L. Prell (1989), Sensitivity of climate to late Cenozoic uplift in southern Asia and the American west: numerical experiments, *J. Geophys. Res. Atmos.*, *94*(D15), 18393–18407.

Lee, J. E., C. Risi, I. Fung, J. Worden, R. A. Scheepmaker, B. Lintner, and C. Frankenberg

(2012), Asian monsoon hydrometeorology from TES and SCIAMACHY water vapor isotope measurements and LMDZ simulations: Implications for speleothem climate record interpretation, *J. Geophys. Res. Atmos.*, *117*(15), 1–12, doi:10.1029/2011JD017133.

Li, J., T. A. Ehlers, S. G. Mutz, C. Steger, H. Paeth, M. Werner, C. J. Poulsen, and F. Ran (2016), Modern precipitaion d18O and trajectory analysis over the Himalaya-Tibet Orogen from ECHAM5-wiso simulations, *J. Geophys. Res. Atmos.*

Liu, X., and Z. Y. Yin (2002), Sensitivity of East Asian monsoon climate to the uplift of the Tibetan Plateau, *Palaeogeogr. Palaeoclimatol. Palaeoecol.*, *183*(3–4), 223–245, doi:10.1016/S0031-0182(01)00488-6.

Quade, J., C. Garzione, and J. Eiler (2007), Paleoelevation Reconstruction using Pedogenic Carbonates, *Rev. Mineral. Geochemistry*, *66*(1), 53–87, doi:10.2138/rmg.2007.66.3.

Quade, J., D. O. Breecker, M. Daëron, and J. Eiler (2011), The paleoaltimetry of Tibet: An isotopic perspective, *Am. J. Sci.*, *311*(2), 77–115, doi:10.2475/02.2011.01.

Rowley, D. B., and B. S. Currie (2006), Palaeo-altimetry of the late Eocene to Miocene Lunpola basin, central Tibet., *Nature*, *439*(7077), 677–681, doi:10.1038/nature04506.

Rowley, D. B., and C. N. Garzione (2007), Stable Isotope-Based Paleoaltimetry, *Annu. Rev. Earth Planet. Sci.*, *35*(1), 463–508, doi:10.1146/annurev.earth.35.031306.140155.

Rowley, D. B., R. T. Pierrehumbert, and B. S. Currie (2001), A new approach to stable isotope-based paleoaltimetry: Implications for paleoaltimetry and paleohypsometry of the High Himalaya since the late Miocene, *Earth Planet. Sci. Lett.*, *188*(1–2), 253–268, doi:10.1016/S0012-821X(01)00324-7.

Rozanski, K., L. Araguás-Araguás, and R. Gonfiantini (1993), Isotopic patterns in modern global precipitation, *Clim. Chang. Cont. Isot. Rec.*, 1–36.

Ruddiman, W. F., and J. E. Kutzbach (1989), Forcing of late Cenozoic northern hemisphere climate by plateau uplift in southern Asia and the American West, *J. Geophys. Res. Atmos.*, *94*(D15), 18409–18427.

Sturm, C., G. Hoffmann, and B. Langmann (2007), Simulation of the stable water isotopes in precipitation over South America: Comparing regional to global circulation models, *J. Clim.*, *20*, 3730–3750, doi:10.1175/JCLI4194.1.

Tian, L., V. Masson-Delmotte, M. Stievenard, T. Yao, and J. Jouzel (2001), Tibetan Plateau summer monsoon northward extent revealed by measurements of water stable isotopes, *J. Geophys. Res.*, *106*(D22), 28081, doi:10.1029/2001JD900186.

Tian, L., T. Yao, K. MacClune, J. W. C. White, A. Schilla, B. Vaughn, R. Vachon, and K. Ichiyanagi (2007), Stable isotopic variations in west China: A consideration of moisture sources, *J. Geophys. Res. Atmos.*, *112*(10), 1–12, doi:10.1029/2006JD007718.

Wei, Y., K. Zhang, C. N. Garzione, Y. Xu, B. Song, and J. Ji (2016), Low palaeoelevation of the northern Lhasa terrane during late Eocene: Fossil foraminifera and stable isotope evidence from the Gerze Basin, *Sci. Rep.*, *6*, 27508.

Xu, Q., L. Ding, L. Zhang, F. Cai, Q. Lai, D. Yang, and J. Liu-Zeng (2013), Paleogene high elevations in the Qiangtang Terrane, central Tibetan Plateau, *Earth Planet. Sci. Lett.*, *362*, 31–42, doi:10.1016/j.epsl.2012.11.058.

Xu, Q., L. Ding, R. Hetzel, Y. Yue, and E. F. Rades (2015), Low elevation of the northern Lhasa terrane in the Eocene: Implications for relief development in south Tibet, *Terra Nov.*, *27*(6), 458–466, doi:10.1111/ter.12180.

Yao, T. et al. (2013), A review of climatic controls on $\delta^{18}O$ in precipitation over the Tibetan Plateau: Observations and simulations, *Rev. Geophys.*, *51*(4), 525–548, doi:10.1002/rog.20023.

4.4 Additional Eocene experiments

In the article in preparation shown in the previous section, two Eocene simulations were used, a reference one, with the paleogeography from the publication of Licht et al. (2014) and a pre-industrial values for the pCO_2, and another one, with the same paleogeography, but 4 times increased pCO_2. However, during my PhD thesis, I have performed additional simulations for the Eocene period. The impact of the surface albedo, SSTs, orbital parameters and the Paratethys Sea retreat has been tested (Figure 4.15). These simulations are complementary to those described in the article in preparation and enlarge the potential vision of the isotopic oxygen spatial variability over Asia and during the Eocene we may get from our modeling perspective. These simulations are briefly described below to tentatively show that main features described in the article hold against potential changes in boundary conditions.

4.4.1 The impact of orbital forcings

Orbital forcing is the effect on climate of changes in the tilt of the Earth's axis and in the shape of the orbit. In modern studies, it has been shown that such variations may have a significant impact on the hydrological cycle over Asia (Licht et al., 2014). In our previous experiments, the orbital parameters were kept unchanged to their modern values (see Section 2.4). Here we test two extreme orbital configurations for the Eocene case in order to produce either a warm austral summer ("warm austral" orbit (or "cold boreal" orbit), with eccentricity 0.05, obliquity 24.5 and with Earth at perihelion in January) or a cold austral summer (and thus a "warm boreal" summer, with eccentricity 0.05, obliquity 22.5 and with Earth at perihelion in July) (Figure 4.13).

Results of these simulations show that when "warm boreal" scenario is applied, the summer (MJJAS averaged) precipitation rate increases over Asia (Figure 4.14, panels A, B). In addition, the seasonality of rainfall is much stronger than for the simulation with present-day like orbital forcing (Figure 4.14, panels D, E). On the contrary, for the case with "cold boreal" scenario, mean summer precipitation amount is smaller and seasonality is less pronounced (Figure 4.14, panels C, A).

$\delta^{18}O_p$ summer (MJJAS) patterns appear to be fairly similar for the three forcings tested here (Figure 4.15). For all cases more negative values of $\delta^{18}O_p$ are simulated over India and southern slopes of the HTP, while over Asia (between 20° N and 40° N) much more positive values of $\delta^{18}O_p$ are simulated. This gradient is stronger for the "warm boreal" scenario case. This is consistent with the stronger precipitation simulated in this scenario over India which in turn induce a larger amount effect and more negative isotopic values and with desert conditions (shift towards less negative $\delta^{18}O_p$ *via* droplet evaporation) behind the Plateau.

4.4.2 Paratethys retreat

In previous studies with numerical experiments, it has been shown that the change in land-sea distribution over Asia and the Paratethys shrinkage in particular has an impor-

tant impact on the hydrologycal cycle (e.g. Ramstein et al., 1997). It was also hypothesized that the change in land-sea distribution since the Eocene could cause the source of water vapor to shift from local (Paratethys) to more distal areas (proto-Atlantic and/or Indian Ocean), resulting in a decrease in the $\delta^{18}O_p$ value over the HTP (Bershaw et al., 2012).

Here we test the impact of the Paratethys retreat on $\delta^{18}O_p$ for the Eocene case. For this purpose, we have changed the land-sea mask (Figure 4.15). The most dramatic changes occur during winter months when the simulation with the Paratethys retreat appears to be dryer then the control Eocene case (compare white area over Asia between the first and last column of the Figure 4.15). Ramstein et al. (1997) have reached similar conclusions about the increased continentality. Conversely, both summer and annual mean precipitation $\delta^{18}O$ over elevated parts of the HTP appears to be not very different from the values simulated in control Eocene experiment.

We conclude that the Paratethys retreat has a small impact on the precipitation $\delta^{18}O$, at least for the Eocene case. However, for further investigations addition experiment with bigger portion of land to the north-west of the HTP should be set.

4.4.3 Surface albedo variation

The effect of surface albedo changes linked to the vegetation variations on climate has been shown using numerical modeling tools since more then 30 years ago (Henderson-Sellers and Wilson, 1983). However, the impact of the surface albedo on $\delta^{18}O$ has barely been explored, especially for the paleo case.

In our Cenozoic simulations, biophysical characteristics setting values of surface albedo, roughness and evapotranspiration capability have been obtained using the LPJ vegetation model (see more on the method used in Section 2.3.5). In order to evaluate the magnitude of isotopic changes linked to the biophysical characteristics, we have designed an additional idealistic simulation in which mean values of biophysical characteristics have been uniformly applied to each continental pixel of the model.

Preliminary results show that $\delta^{18}O_p$ over Asia for the Eocene are sensitive to these changes in order of magnitude of ~3 ‰. These changes are not homogeneous: the maximal effect is simulated between 20° N and 40° N, where high surface albedo (that corresponds to a desert) for control Eocene case has been replaced by a modest (Figure 4.15, 1st and 3rd columns).

4.4.4 SSTs changes

Paleo sea surface temperatures are controlled by greenhouse and paleogeographic forcing both. For more realist paleo experiments we force LMDZ-iso with FOAM sea surface temperatures (for more details on this method see Chapter 2 and Section 2.3.5 in particular). For the Eocene case we have tested the impact of sea surface temperatures on $\delta^{18}O$ over Asia. For this purpose we designed LMDZ-iso experiment with Eocene paleogeography, 4x CO_2 concentration, but present-day sea surface temperatures and compare the results of this experiment with Eocene control experiment.

Results of our experiments (Figure 4.15, column 2) show that $\delta^{18}O_p$ over the Asian

region is sensitive to the SST forcing, as a direct consequence of atmospheric dynamics changes: for the case with present-day SSTs, moisture over the HTP is advected preferably from the Pacific ocean with minimum in $\delta^{18}O_p$ over the eastern flank of the HTP, which is also consistent with summer precipitation maximum (not shown). In average $\delta^{18}O_p$ over the region are ~ 5 ‰ more depleted that for the control Eocene case (compare Figure 4.15, column 1 and 2) due to cooler SSTs. However, we aware that configuration with present-day SSTs and Eocene paleogeography is impossible in nature, as a paleogeography has direct effect on SSTs.

4.4.5 Himalayas and Tibetan Plateau uplift

In order to investigate the impact of the HTP uplift on Eocene $\delta^{18}O_p$ we set a group of experiments with various elevation of the mountains over the region. Surprisingly, $\delta^{18}O_p$ appeared to be insensitive to the topography changes (Figure 4.16). We provide deeper analysis of these simulations together with model-data comparison in Chapter 5.

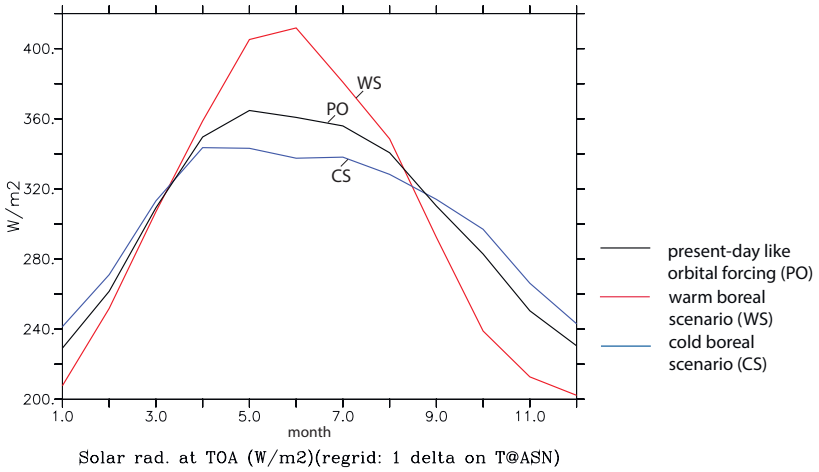

Figure 4.13 – Solar radiation at top of the atmosphere during a seasonal cycle, averaged over a domain from 40° E to 120° E and from 5° S to 45° N for 3 Eocene simulations: 1) with present-day orbital parameters (black line), 2) with eccentricity 0.05, obliquity 24.5 and with Earth at perihelion in January, that corresponds to "cold boreal" scenario (blue line), 3) "warm boreal" scenario with eccentricity 0.05, obliquity 22.5 and with Earth at perihelion in July (red line). When "warm boreal" scenario is applied, the Asian region receives much more solar energy during the boreal summer and less solar energy during boreal winter (more contrast seasonal cycle.), then when "cold boreal" scenario is applied.

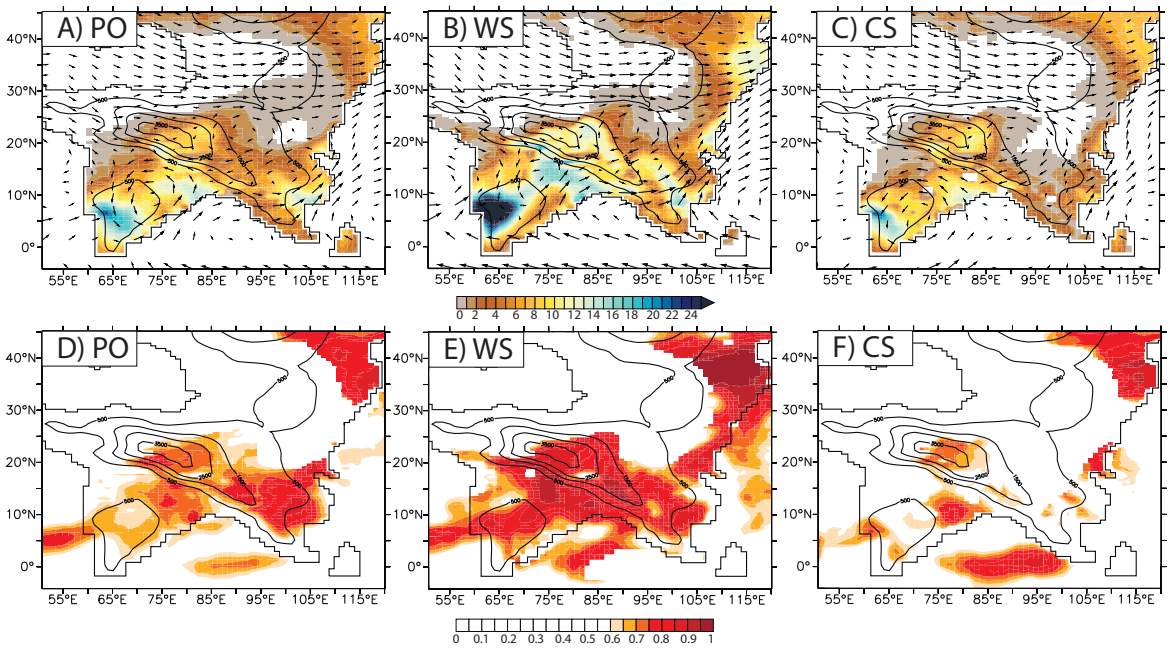

Figure 4.14 – A,B,C) MJJAS precipitation and vertically integrated moisture transport, and D,E,F) precipitation seasonality index (ratio of rainfall from May to September versus annual rainfall) for A,D) Present-day like orbital forcing (PO), B,E) Warm boreal scenario (WS), C,F) Cold boreal scenario (CS). The simulation with the warn boreal scenario is characterized by the highest summer precipitation rate and the strongest seasonality, while the simulation with the cold boreal scenario shows contrasting results with the lowest summer precipitation rates and seasonality.

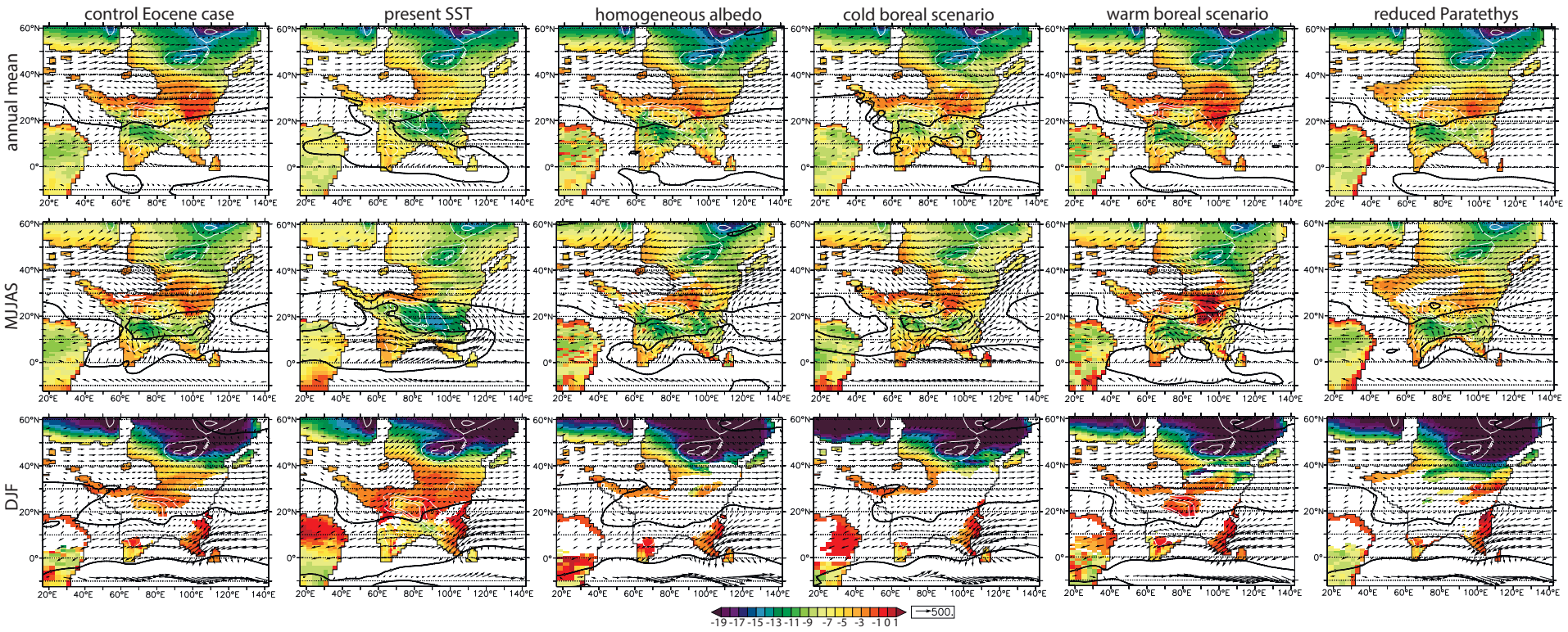

Figure 4.15 – LMDZ-iso simulated stable oxygen isotopes in precipitation for the Eocene period, under different forcings. Upper line - mean annual $\delta^{18}O_p$, middle line - MJJAS $\delta^{18}O_p$, bottom line - DJF $\delta^{18}O_p$. Arrows show moisture transport directions.

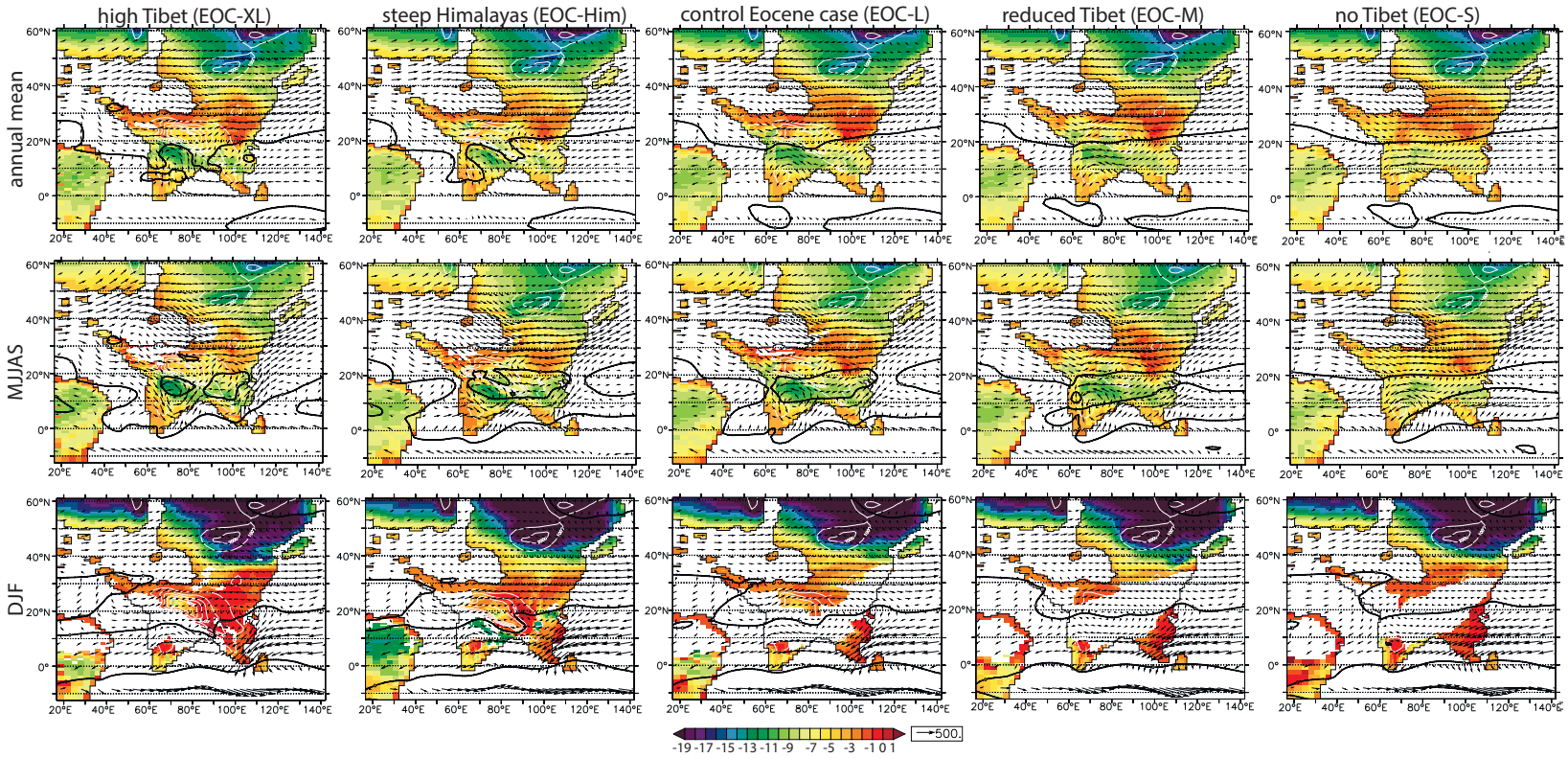

Figure 4.16 – LMDZ-iso simulated stable oxygen isotopes in precipitation for the Eocene period, with varied elevation and geometry of the HTP. Upper line - mean annual $\delta^{18}O_p$, middle line - MJJAS $\delta^{18}O_p$, bottom line - DJF $\delta^{18}O_p$

4.5 Summary and conclusions

In this chapter we study Cenozoic $\delta^{18}O_p$ over Asia, using numerical tools. We show to what extant $\delta^{18}O_p$ over Asia may vary through the Cenozoic using realistic boundary conditions for Early Eocene, Middle Eocene, Oligocene and Miocene periods. In general, for all Cenozoic experiments $\delta^{18}O_p$ over the HTP region are at least 9 ‰ less negative that for the control (present-day) case. For the Miocene experiment a shift towards less depleted $\delta^{18}O$ over elevated topography is consistent with the mechanism suggested by Poulsen and Jeffery (2011) based on sensitivity experiments with increased pCO_2: heating of the upper troposphere results in steeper temperature lapse rates and relatively enriched $\delta^{18}O_v$ that are transported downwards over subsidence areas.

For earlier time periods, such as the Eocene and the Oligocene, paleo HTP is situated more then 10° to the south. This southward shift together with high pCO_2 concentration results in 1) shift in $\delta^{18}O_v$ towards less depleted values following higher temperatures, 2) less depleted $\delta^{18}O_p$ over the HTP due to larger hydrological recycling component including more enriched air water masses and a convection of enriched near-surface air. More comprehensive analysis with backward wind trajectories tracing for the Eocene allow to conclude that over the southern slope of the Himalayas the Rayleigh distillation processes is not valid for the Eocene case because the moisture coming from the southerly source (the monsoon) precipitates before the Himalayas foothill and $\delta^{18}O_v$ over the HTP is controlled by air mixing process between westerly and easterly moisture sources.

Sensitivity experiments for the Eocene case, show that variations in orbital forcings, the partial retreat of the Paratethys Sea, continental biophysical characteristics, topography variations, pCO_2 forcing have less important effect on the Eocene $\delta^{18}O$ over the HTP that the change of paleogeography. Simulated insensitivity of Eocene $\delta^{18}O$ to the topographic changes have important consequences for paleoaltimetry studies (see Chapter 5).

One of the major uncertainty here remains linked to the uncertainty we have on paleogeography constraints. While we can hope that our constraints on continental configurations for the Cenozoic will become far better in the near future, additional sensitivity experiments with artificially changed position of the India continent and the HTP are planed in the next months.

Chapter 5

Forward proxy modeling for the Eocene

In this Chapter (Sections 5.2) we present a draft paper "Eocene stable oxygen isotopes in the Himalayas and Tibetan Plateau: A record of elevation or of climate change?", ready for submission to *Nature Communications*. We use so-called “forward proxy modeling” that relies on a direct comparison of stable water isotopes-enabled GCM outputs with measured isotopic data from natural archives. Here we confront the results of our Eocene simulations using LMDZ-iso against published data of $\delta^{18}O$ from soil and lacustrine carbonate sampled over the HTP.

Contents

5.1 Introduction

Simulated climate patterns and associated isotopic signals can provide a "transfer function" between the isotopic signal and climate variables. This technique of direct comparison of data with the results of numerical simulations (commonly GCMs runs) is called "forward proxy modeling" (Evans, 2007; Schmidt, 1999; Sturm et al., 2010). The advantages of such an approach are: 1) modeling allows not only to simulate physical variable ($\delta^{18}O$ for our case), but also the processes that influence the recorded signal, 2) using models with different boundary condition allows to chose the best-fit model. Joined efforts of measurements and climate modeling could reduce the uncertainty associated with the interpretation of a proxy signal. Principles, benefits and caveats of using water isotopes embedded GCMs for supporting the interpretation of isotopic records from natural archives are reviewed in Sturm et al. (2010).

We have chosen the Eocene period for a detailed investigation because the early elevation evolution of the region is particularly controversial, but may provide particularly important information for geodynamical and climatic reconstructions in the Early Cenozoic.

In Section 1.3.3 we summarize basic principles of the paleoaltimetry approach based on stable oxygen isotopes. As it has been shown, ones $\delta^{18}O_c$ from the mineral material have been measured, paleoprecipitation $\delta^{18}O$ ($\delta^{18}O_{pp}$) can be restored using the calcite-water fractionation coefficients (see the Equation 1.8) and assuming the knowledge about carbonate formation temperature. In paleoaltimetry studies based on a classic approach this last parameter is more often unknown and the range of estimations depends on the assumptions made. For example, (Bershaw et al., 2012) used temperature of 19 °C for their recalculations for the Eocene period, which is the average present-day temperature for relatively dry months in their study area (Kashgar); (Caves et al., 2014) use the temperature of 25 °C; (Rowley and Currie, 2006) - the temperature of 10 °C. The choice of this temperature is subjective, based on assumptions about the elevation and global temperature change due to pCO_2 variations.

Second major assumption of stable oxygen isotopes-based paleoaltimetry is the presumed stationary of $\delta^{18}O_p$ - elevation relations through time. Ones $\delta^{18}O_{pp}$ is recalculated from $\delta^{18}O_c$ data, it is related to the low-elevated reference values. For this purpose most modern studies use the 1-D model suggested by Rowley et al. (2001), which is based on the Rayleigh distillation process. Here we use LMDZ-iso GCM in order improve the classic paleoaltimetry approach for the Eocene case and to provide the forward proxy modeling over the Himalayas and Tibetan Plateau for this time period.

5.2 Article in preparation for *Nature Communications*: Eocene stable oxygen isotopes in the Himalayas and Tibetan Plateau: A record of elevation or of climate change?

In this Section we present our manuscript ready for a submission to *Nature Communications* journal. The main points of the paper:

- **Main point #1**. Consistent S-N gradient in water $\delta^{18}O$ in the Eocene linked to atmospheric dynamics patterns, i.e. convective precipitation to the south, aridity to the north;
- **Main point #2**. Low sensitivity of Eocene water $\delta^{18}O$ to the topography change;
- **Main point #3**. High sensitivity of carbonate $\delta^{18}O$ ($\delta^{18}O_c$) to the local temperature changes, that makes possible to use measured $\delta^{18}O_c$ to paleoelevation studies;
- **Main point #4**. Eocene HTP did not reach present-day (3000+ m) elevations during the Eocene;

Eocene stable oxygen isotopes in the Himalayas and Tibetan Plateau: A record of elevation or of climate change?

Svetlana Botsyun[1], Pierre Sepulchre[1], Yannick Donnadieu[1], Camille Risi[2], Alexis Licht[3], and Jeremy K. Caves[4]

[1] Laboratoire des Sciences du Climat et de l'Environnement, LSCE/IPSL, CEA-CNRS-UVSQ, Université Paris-Saclay, Gif-sur-Yvette, France

[2] Laboratoire de Météorologie Dynamique, IPSL, UPMC, CNRS, Paris, France

[3] Department of Earth and Space Sciences, University of Washington, Seattle WA USA

[4] Department of Earth System Science, Stanford University, Stanford, CA, USA

Correspondence to: S. Botsyun (svetlana.botsyun@lsce.ipsl.fr)

Abstract

Oxygen isotope paleoaltimetry is frequently used to reconstruct the Cenozoic elevation history of mountains, including the Himalayas and Tibetan Plateau (HTP). This technique is based on the isotopic equilibrium fractionation between calcite and water $\delta^{18}O$. However, the temperature uncertainty of carbonate formation makes such reconstructions challenging. During the Cenozoic there have been major changes in global temperature linked to changes in paleogeography and atmospheric CO_2 concentrations as well as local temperature variations associated with the topography. Here we use the isotope-equipped General Circulation Model (GCM) LMDZ-iso in a high-resolution configuration with present-day and Eocene boundary conditions. For the Eocene simulations, we vary the altitude and geometry of the HTP to test the sensitivity of water $\delta^{18}O$ ($\delta^{18}O_w$) to different topographies and

geometries. For the purpose of the model-data comparison, we derive carbonate $\delta^{18}O$ ($\delta^{18}O_c$) using model simulated $\delta^{18}O_w$ and surface temperatures and compare it with published $\delta^{18}O_c$. Our results suggest that the spatial distribution of $\delta^{18}O_w$ for the Eocene is almost insensitive to topographic height in Asia. For all topography configurations, we simulate a south-north positive $\delta^{18}O_w$ gradient, with more depleted values over the Indian subcontinent and more enriched values over the northern part of the Plateau. Over the Himalayan foothills, this gradient is associated with the amount effect, while over the northern HTP, it is caused by low precipitation rates, associated with wide-spread aridity driven by large-scale subsidence. However, $\delta^{18}O_c$ still records paleo-elevation because the fractionation between calcite and water is sensitive to temperature, which depends on altitude. The models where HTP elevation is 1500 and 3000 m show the best agreement with $\delta^{18}O_c$. We conclude that the Himalayas and the Tibetan Plateau did not reach present-day (3000+ m) elevations during the Eocene.

Introduction

It is pivotal to constrain the timing of uplift of the HTP to understand the mechanics of continental deformation (e.g. [*Tapponnier et al.*, 2001; *Royden et al.*, 2008]) and regional to global climatic changes during the Cenozoic (e.g. [*Raymo and Ruddiman*, 1992; *Molnar et al.*, 2010]). The present-day geography of Asia results from both the ongoing collision between the Indian and Eurasian plates that began ~55 Ma [*Le Pichon and Heirtzler*, 1968] and the buoyancy of continental crust [*Molnar et al.*, 2010]. Though the latitudinal positions of India and Asia over this period are well constrained by paleomagnetism [*Lippert et al.*, 2014], the altitude of HTP through time remains disputed [*Wang et al.*, 2014]. Recent studies have proposed numerous uplift scenarios for the HTP, from a pre-collision, highly elevated Plateau (e.g. ~100 Ma ago) [*Murphy et al.*, 1997] to stepwise uplift since collision ~55 Ma

ago (e.g. Tapponnier et al., 2001) to more recent rapid uplift, particularly of the northern HTP (<7 Ma ago) [*Sun and Liu*, 2000]. In particular, the early uplift history of the HTP remains controversial [*Wang et al.*, 2008], with estimates spanning from a near sea-surface Plateau [*Wei et al.*, 2016] to high Eocene elevations [*Ding et al.*, 2014].

Stable isotope paleoaltimetry has been widely used to reconstruct the Cenozoic elevation history of the HTP (see data compilation in Extended Data Table 1). Stable isotope paleoaltimetry is based on the decrease of $\delta^{18}O_w$ (expressed in ‰ relative to the V-PDB standard) with increasing elevation across mountain ranges [*Poage and Chamberlain*, 2001; *Rowley et al.*, 2001]. In the Himalayas and southern Tibet, the isotopic lapse rate is approximately -2.8 ‰/km [*Quade et al.*, 2011], in agreement with distillation models that predict decreasing $\delta^{18}O_w$ in response to decreasing atmospheric relative humidity and temperature during orographic ascent [*Rowley et al.*, 2001]. This altitude effect is archived in continental carbonates ($\delta^{18}O$ for carbonates, $\delta^{18}O_c$, expressed in ‰ relative to the V-PDB standard), with a fractionation factor that depends on carbonate growth temperature.

However, stable isotope paleoaltimetry relies on the key assumption that the main atmospheric factors that control atmospheric distillation and air mass $\delta^{18}O$ values have remained constant over millions of years. The impact of past changes in climate on $\delta^{18}O_w$ is uncertain but has been hypothesized to significantly effect $\delta^{18}O_w$ [*Botsyun et al.*, 2016]. Changes in lapse rates [*Poulsen and Jeffery*, 2011], sources of precipitation e.g. [*Hren et al.*, 2009; *Xu et al.*, 2013], and changes in monsoonal regime [*Quade et al.*, 1989] are all possible sources of isotopic variation in the HTP. In addition, knowledge regarding the temperature of carbonate formation is necessary for adequate reconstruction of paleo $\delta^{18}O_w$, that is a direct consequence of the equilibrium between calcite and water $\delta^{18}O$ [*Kim and O'Neil*, 1997].

Here, we test the impact of Eocene paleogeography and topography variations on water vapor and precipitation $\delta^{18}O$ with climate simulations, and compare simulated $\delta^{18}O_c$

values with previously published data. Our climate simulations take into account changes in the HTP latitude, roughness length, albedo, and SST, that have been suggested to change the relative contribution of different air masses within the HTP and hypothesized to have caused significant shifts in $\delta^{18}O_w$ [*Kutzbach et al.*, 1989; *Broccoli and Manabe*, 1992; *Liu and Yin*, 2002; *Abe et al.*, 2003; *Kitoh*, 2004]. We provide a data-model comparison for understanding the role of topography and climate on $\delta^{18}O_c$ as well as estimating the validity of $\delta^{18}O$-based paleoaltimetry in deep time.

Methods

We use the LMDZ-iso Atmospheric General Circulation Model (GCM) [*Risi et al.*, 2010], which has been shown to properly simulate atmospheric dynamics and reproduce rainfall and $\delta^{18}O_w$ patterns consistent with data over Asia [*Botsyun et al.*, 2016]. A stretchable grid allows for increased averaged spatial resolution up to ~50 km over central Asia. Simulated present-day $\delta^{18}O_w$ values over Asia are consistent with sparse observations from the Global Network of Isotopes in Precipitation [*GNIP*, 2016] and show agreement with modern precipitation and river $\delta^{18}O$ (Extended Data Fig. 1).

We provide experiments depicting both present-day and Eocene climate. For the Eocene experiments, we use the Eocene paleogeography reconstruction of Licht et al. 2014 [*Licht et al.*, 2014], which includes a southward shift of the Himalayan front, and a large Paratethys Sea to the north of HTP (Fig. 1). To understand the role of topography on Eocene climate and the distribution of $\delta^{18}O_c$, we perform a series of experiments by varying the elevation of the HTP. The Eocene HTP reaches up to 3500 m in the initial reconstruction [*Licht et al.*, 2014] (EOC-L simulation, Extended Data Fig. 2A) and is increased to 5000 m in the EOC-XL simulation (Extended Data Fig. 2B), reduced to 1750 m in the EOC-M simulation (Extended Data Fig. 2C) and lowered to 200 m in the EOC-S simulation (Extended

Data Fig. 2D**)**. Also, we modify the HTP geometry to obtain steep, narrow mountains analogous to the present-day Himalayas over the southern flank of the elevated topography in the EOC-Him experiment (Extended Data Fig. 2E). For all Eocene simulations, we use pCO_2 of 1120 ppm, which lies within published estimates [*Beerling and Royer*, 2011], and identical sea-surface temperatures (SSTs) to isolate the effect of topography on atmospheric dynamics and $\delta^{18}O_w$.

We compare Eocene precipitation-weighted $\delta^{18}O_c$ derived from our simulations with published Eocene $\delta^{18}O_c$ data (Extended Data Table 1). Pedogenic carbonates in the HTP commonly form during the summer season [*Quade et al.*, 2013]. Thus, to derive $\delta^{18}O_c$ from our simulated $\delta^{18}O_w$ values, we use May-September mean surface temperatures and use the standard fractionation factors from [*Kim and O'Neil*, 1997].

Results

The Eocene paleogeography together with globally higher temperatures result in systematically higher $\delta^{18}O_w$ for all Eocene simulations compared to the present-day (CTR). Simulated $\delta^{18}O_w$ gradually decreases from the southern tip of India (ca. -4‰) to a minimum in the Indian Foreland, at 10°S (from -8 to -11‰ for different simulations), and then, over the northern HTP, increases up to -2 ‰ (Extended Data Fig. 3).

Although a detailed comparison of present-day and Eocene climates is beyond the scope of this study, the shift of the Eocene HTP to the zone of strong convection, where near surface enriched vapor in transported towards the lifted condensation level, that results in less depleted vapor over the HTP (Botsyun et al., 2017, in prep.). The results of our simulations show a low sensitivity of vapor $\delta^{18}O$ ($\delta^{18}O_v$) at the lifted condensation level to the HTP topography change, due to similarity in convection/subsidence patterns (Extended Data Fig. 4). Simulated depleted $\delta^{18}O_p$ over the India, south China and south HTP are consistent with

high precipitation rates (the amount effect), while $^{8}O_p$-rich values over the inner Asia coexists with extremely arid environments, driven by the descending branch of Hadley circulation (Extended Data Fig. 5). These processes result in a marked latitudinal $\delta^{18}O_c$ dipole over the Eocene Asian continent, with depleted values south of the HTP and enriched values to the north (Fig. 2), that follows simulated $\delta^{18}O_w$ (Extended Data Fig. 3). The HTP uplift results in higher summer precipitation rates (Extended Data Fig. 5) over the India and south Asia following the monsoon intensification, that results in more depleted $\delta^{18}O_p$ through the amount effect and, consequently, much pronounced S-N $\delta^{18}O_c$ gradient for simulations with higher HTP (Fig. 2). Decomposition of total $\delta^{18}O_c$ signal variations associated with the HTP uplift shows total $\delta^{18}O_c$ signal evenly dependents on $\delta^{18}O_p$ and temperature changes. However, $\delta^{18}O_w$ changes contribute to the $\delta^{18}O_c$ not only over the HTP, but also over India and inner Asia, that is consistent with the increase of S-N isotopic gradient in $\delta^{18}O_w$ with the HTP uplift. Local temperature variations have the most important impact over the HTP and their contribution becomes more important for bigger portion of the uplift (Extended Data Fig. 6).

Measured $\delta^{18}O_c$ from previous publications show good agreement with the simulated S-N isotopic gradient in $\delta^{18}O_c$ for all experiments (Fig. 2D,F,J,L,N). However, for the simulations with high Asian topography (EOC-Him, EOC-XL), measured $\delta^{18}O_c$ is systematically more negative than simulated $\delta^{18}O_c$ (Fig. 2H,J,K,L), while for simulations with relatively low Asian topography (EOC-S, EOC-M, EOC-L) measured $\delta^{18}O_c$ show a good agreement with simulated $\delta^{18}O_c$. According to a Kolmogorov-Smirnov (K-S) test, $\delta^{18}O_c$ distributions in EOC-Him and EOC-XL simulations are different from measured data within 95% confidence interval **(**Extended Data Table 2). Simulations with low and modest elevations of the HTP (EOC-S, EOC-M and EOC-L) show the best fit to the recalculated data **(Fig. 2C,D,K,L,M,N) (**Extended Data Table 2).

Discussion and Conclusions

Our Eocene simulations suggest a consistency between Eocene and present-day atmospheric processes that govern the spatial distribution of $\delta^{18}O_w$ over Asia. Persistency of large-scale atmospheric circulation (*i.e.*, the monsoon in the south and westerlies in the north of the HTP) throughout the Cenozoic and the permanence of a latitudinal $\delta^{18}O_p$ dipole are consistent with conclusions from recent studies [*Caves et al.*, 2015; *Licht et al.*, 2016].

However, the rainfall isotope system is different for the Eocene case as a result of southward shift of the HTP into the convection zone. Rainfall isotope patterns might have changes to become the present-day system only for recent time periods when the HTP achieved its near-modern position.

None of our simulations can replicate the exceptionally low $\delta^{18}O_c$ values reported in the southern Plateau by Ding et al. (2014) and Rowley and Currie (2006) (Fig. 2). The data-model disagreement is even more pronounced when using the most negative $\delta^{18}O_c$ value as a proxy for meteoric $\delta^{18}O$ (Extended Data Fig. 3) so as to account for evaporitic effects (Rowley and Currie 2006). That even our highest HTP simulation (EOC-XL) cannot replicate these low values suggests that these $\delta^{18}O_c$ data may not be reliable recorders of paleoaltimetry; rather, they may have experienced post-deposition resetting of $\delta^{18}O_c$, perhaps through deep burial of these basins (Carrapa et al. 2014). The exceptionally low $\delta^{18}O_w$ that is currently observed in the southern HTP appears to require both further uplift and, importantly, the cooler climate of the late Cenozoic.

The relative constancy of the spatial $\delta^{18}O_w$ pattern suggests that topography itself has a minor impact on HTP $\delta^{18}O_w$. Thus, $\delta^{18}O_c$ primarily records a combination of large-scale atmospheric circulation and local temperature. Our simulations highlight the limit of standard atmospheric distillation models; the Eocene hydrological system is too complex to allow precise paleoelevation estimates based on standard paleoaltimetry methods. Modest Eocene

elevations (not higher than 3000 m), as suggested by our simulations, are consistent with the hypothesis that uplift of at least some parts of the HTP followed two pulses of tectonic activity in the Oligocene (around 30-25 Ma) [*Wang et al.*, 2012] and Miocene (10-15 Ma) [*Blisniuk et al.*, 2001; *Harris*, 2006], reflecting distinct mechanisms of crustal thickening [*Wang et al.*, 2012] and the convective removal of the lower portion of the thickened Asian lithosphere [*Molnar et al.*, 1993]. Eocene elevations of about 3000 m are also reported by [*Song et al.*, 2010] based on fossil pollen records. However, these elevations are significantly lower than those predicted by δ^{18}O-paleoaltimetry e.g. [*Rowley and Currie*, 2006; *Ding et al.*, 2014]. We demonstrate that, while the spatial distribution of $\delta^{18}O_w$ is relatively insensitive to topography, the strong dependency of $\delta^{18}O_c$ on local surface temperatures, which in turn depends on the elevation, makes the choice of carbonate formation temperature crucial [*Kim and O'Neil*, 1997].

Acknowledgments

This work is a part of iTECC (interaction Tectonics-Erosion-Climate-Coupling) project funded by European Union. Computational resources were provided by IDRIS-GENCI (project 0292), France.

References cited

Abe, M., A. Kitoh, and T. Yasunari (2003), An Evolution of the Asian Summer Monsoon Associated with Mountain Uplift-Simulation with the MRI Atmosphere-Ocean Coupled GCM-, *J. Meteorol. Soc. Japan*, *81*(5), 909–933, doi:10.2151/jmsj.81.909.

Beerling, D. J., and D. L. Royer (2011), Convergent Cenozoic CO2 history, *Nat. Geosci.*, *4*(7), 418–420, doi:10.1038/ngeo1186.

Blisniuk, P. M., B. R. Hacker, J. Glodny, L. Ratschbacher, S. Bi, Z. Wu, M. O. McWilliams,

and a Calvert (2001), Normal faulting in central Tibet since at least 13.5 Myr ago., *Nature*, *412*(6847), 628–632, doi:10.1038/35088045.

Botsyun, S., P. Sepulchre, C. Risi, and Y. Donnadieu (2016), Impacts of Tibetan Plateau uplift on atmospheric dynamics and associated precipitation δ18O, *Clim. Past*, *12*(6), 1401–1420, doi:10.5194/cp-12-1401-2016.

Broccoli, A. J., and S. Manabe (1992), The Effects of Orography on Midlatitude Northern Hemisphere Dry Climates, *J. Clim.*, *5*(11), 1181–1201, doi:10.1175/1520-0442(1992)005<1181:teooom>2.0.co;2.

Caves, J. K., M. J. Winnick, S. A. Graham, D. J. Sjostrom, A. Mulch, and C. P. Chamberlain (2015), Role of the westerlies in Central Asia climate over the Cenozoic, *Earth Planet. Sci. Lett.*, *428*, 33–43.

Ding, L., Q. Xu, Y. Yue, H. Wang, F. Cai, and S. Li (2014), The Andean-type Gangdese Mountains: Paleoelevation record from the Paleocene-Eocene Linzhou Basin, *Earth Planet. Sci. Lett.*, *392*, 250–264, doi:10.1016/j.epsl.2014.01.045.

Eiler, J. M. (2011), Paleoclimate reconstruction using carbonate clumped isotope thermometry, *Quat. Sci. Rev.*, *30*(25–26), 3575–3588, doi:10.1016/j.quascirev.2011.09.001.

GNIP (2016), IAEA/WMO, Global Network of Isotopes in Precipitation: The GNIP Database. Accessible at: http://www.iaea.org/water.,

Harris, N. (2006), The elevation history of the Tibetan Plateau and its implications for the Asian monsoon, *Palaeogeogr. Palaeoclimatol. Palaeoecol.*, *241*(1), 4–15, doi:10.1016/j.palaeo.2006.07.009.

Hren, M. T., B. Bookhagen, P. M. Blisniuk, A. L. Booth, and C. P. Chamberlain (2009), δ18O and δD of streamwaters across the Himalaya and Tibetan Plateau: Implications for moisture sources and paleoelevation reconstructions, *Earth Planet. Sci. Lett.*, *288*(1–2),

20–32, doi:10.1016/j.epsl.2009.08.041.

Kim, S. T., and J. R. O'Neil (1997), Equilibrium and nonequilibrium oxygen isotope effects in synthetic carbonates, *Geochim. Cosmochim. Acta*, *61*(16), 3461–3475, doi:10.1016/S0016-7037(97)00169-5.

Kitoh, A. (2004), Effects of Mountain Uplift on East Asian Summer Climate Investigated by a Coupled Atmosphere–Ocean GCM, *J. Clim.*, *17*(4), 783–802, doi:10.1175/1520-0442(2004)017<0783:EOMUOE>2.0.CO;2.

Kutzbach, J. E., P. J. Guetter, W. F. Ruddiman, and W. L. Prell (1989), Sensitivity of climate to late Cenozoic uplift in southern Asia and the American west: numerical experiments, *J. Geophys. Res. Atmos.*, *94*(D15), 18393–18407.

Licht, A. et al. (2014), Asian monsoons in a late Eocene greenhouse world, *Nature*, *513*(7519), 501–506, doi:10.1038/nature13704.

Licht, A., G. Dupont-Nivet, A. Pullen, P. Kapp, H. A. Abels, Z. Lai, Z. Guo, J. Abell, and D. Giesler (2016), Resilience of the Asian atmospheric circulation shown by Paleogene dust provenance, *Nat. Commun.*, *7*.

Lippert, P. C., D. J. J. van Hinsbergen, and G. Dupont-Nivet (2014), Early Cretaceous to present latitude of the central proto-Tibetan Plateau: A paleomagnetic synthesis with implications for Cenozoic tectonics, paleogeography, and climate of Asia, *Geol. Soc. Am. Spec. Pap.*, *2507*(1), 1–21, doi:10.1130/2014.2507(01).

Liu, X., and Z. Y. Yin (2002), Sensitivity of East Asian monsoon climate to the uplift of the Tibetan Plateau, *Palaeogeogr. Palaeoclimatol. Palaeoecol.*, *183*(3–4), 223–245, doi:10.1016/S0031-0182(01)00488-6.

Molnar, P., P. England, and J. Martinod (1993), Mantle dynamics, uplift of the Tibetan Plateau, and the Indian monsoon, *Rev. Geophys.*, *31*(4), 357–396.

Molnar, P., W. R. Boos, and D. S. Battisti (2010), Orographic Controls on Climate and

Paleoclimate of Asia: Thermal and Mechanical Roles for the Tibetan Plateau, *Annu. Rev. Earth Planet. Sci.*, *38*(1), 77–102, doi:10.1146/annurev-earth-040809-152456.

Murphy, M. A., A. Yin, T. M. Harrison, S. B. Dürr, Z. Chen, F. J. Ryerson, W. S. F. Kidd, X. Wang, and X. Zhou (1997), Did the Indo-Asian collision alone create the Tibetan plateau?, *Geology*, *25*(8), 719–722.

Le Pichon, X., and J. Heirtzler (1968), Magnetic anomalies in the Indian Ocean and seafloor spreading, *J. Geophys. Res.*, *73*(6), 2101–2117.

Poage, M. A., and C. P. Chamberlain (2001), Empirical relationships between elevation and the stable isotope composition of precipitation and surface waters: Considerations for studies of paleoelevation change, *Am. J. Sci.*, *301*(1), 1–15, doi:10.2475/ajs.301.1.1.

Poulsen, C. J., and M. L. Jeffery (2011), Climate change imprinting on stable isotopic compositions of high-elevation meteoric water cloaks past surface elevations of major orogens, *Geology*, *39*(6), 595–598, doi:10.1130/G32052.1.

Quade, J., T. E. Cerling, and J. R. Bowman (1989), Systematic variations in the carbon and oxygen isotopic composition of pedogenetic carbonate along elevation transects in the suthern Grat Basin, United Satates., *Bull. Geol. Soc. Am.*, *101*(April), 464–475.

Quade, J., D. O. Breecker, M. Daëron, and J. Eiler (2011), The paleoaltimetry of Tibet: An isotopic perspective, *Am. J. Sci.*, *311*(2), 77–115, doi:10.2475/02.2011.01.

Quade, J., J. Eiler, M. Daeron, and H. Achyuthan (2013), The clumped isotope geothermometer in soil and paleosol carbonate, *Geochim. Cosmochim. Acta*, *105*, 92–107.

Raymo, M. E., and W. F. Ruddiman (1992), Tectonic forcing of late Cenozoic climate, *Nature*, *359*(6391), 117–122.

Risi, C., S. Bony, F. Vimeux, and J. Jouzel (2010), Water-stable isotopes in the LMDZ4 general circulation model: Model evaluation for present-day and past climates and

applications to climatic interpretations of tropical isotopic records, *J. Geophys. Res. Atmos.*, *115*(12), 1–27, doi:10.1029/2009JD013255.

Rowley, D. B., and B. S. Currie (2006), Palaeo-altimetry of the late Eocene to Miocene Lunpola basin, central Tibet., *Nature*, *439*(7077), 677–681, doi:10.1038/nature04506.

Rowley, D. B., R. T. Pierrehumbert, and B. S. Currie (2001), A new approach to stable isotope-based paleoaltimetry: Implications for paleoaltimetry and paleohypsometry of the High Himalaya since the late Miocene, *Earth Planet. Sci. Lett.*, *188*(1–2), 253–268, doi:10.1016/S0012-821X(01)00324-7.

Royden, L. H., B. C. Burchfiel, and R. D. Van Der Hilst (2008), The Geological Evolution of the Tibetan Plateau, *Science (80-.).*, *321*(August), 1054–1058.

Song, X. Y., R. a. Spicer, J. Yang, Y. F. Yao, and C. Sen Li (2010), Pollen evidence for an Eocene to Miocene elevation of central southern Tibet predating the rise of the High Himalaya, *Palaeogeogr. Palaeoclimatol. Palaeoecol.*, *297*(1), 159–168, doi:10.1016/j.palaeo.2010.07.025.

Sun, J., and T. Liu (2000), Stratigraphic Evidence for the Uplift of the Tibetan Plateau between ~1.1 and ~0.9 myr Ago, *Quat. Res.*, *54*(3), 309–320, doi:10.1006/qres.2000.2170.

Tapponnier, P., X. Zhiqin, F. Roger, B. Meyer, N. Arnaud, G. Wittlinger, and Y. Jingsui (2001), Oblique stepwise rise and growth of the Tibet plateau., *Science*, *294*(5547), 1671–1677, doi:10.1126/science.105978.

Wang, C., X. Zhao, Z. Liu, P. C. Lippert, S. a Graham, R. S. Coe, H. Yi, L. Zhu, S. Liu, and Y. Li (2008), Constraints on the early uplift history of the Tibetan Plateau., *Proc. Natl. Acad. Sci. U. S. A.*, *105*(13), 4987–4992, doi:10.1073/pnas.0703595105.

Wang, C., J. Dai, X. Zhao, Y. Li, S. a Graham, D. He, B. Ran, and J. Meng (2014), Outward-growth of the Tibetan Plateau during the Cenozoic: A review, *Tectonophysics*, *621*, 1–

43, doi:10.1016/j.tecto.2014.01.036.

Wang, E., E. Kirby, K. P. Furlong, M. van Soest, G. Xu, X. Shi, P. J. J. Kamp, and K. V. Hodges (2012), Two-phase growth of high topography in eastern Tibet during the Cenozoic, *Nat. Geosci.*, *5*(9), 640–645, doi:10.1038/ngeo1538.

Wei, Y., K. Zhang, C. N. Garzione, Y. Xu, B. Song, and J. Ji (2016), Low palaeoelevation of the northern Lhasa terrane during late Eocene: Fossil foraminifera and stable isotope evidence from the Gerze Basin, *Sci. Rep.*, *6*, 27508.

Xu, Q., L. Ding, L. Zhang, F. Cai, Q. Lai, D. Yang, and J. Liu-Zeng (2013), Paleogene high elevations in the Qiangtang Terrane, central Tibetan Plateau, *Earth Planet. Sci. Lett.*, *362*, 31–42, doi:10.1016/j.epsl.2012.11.058.

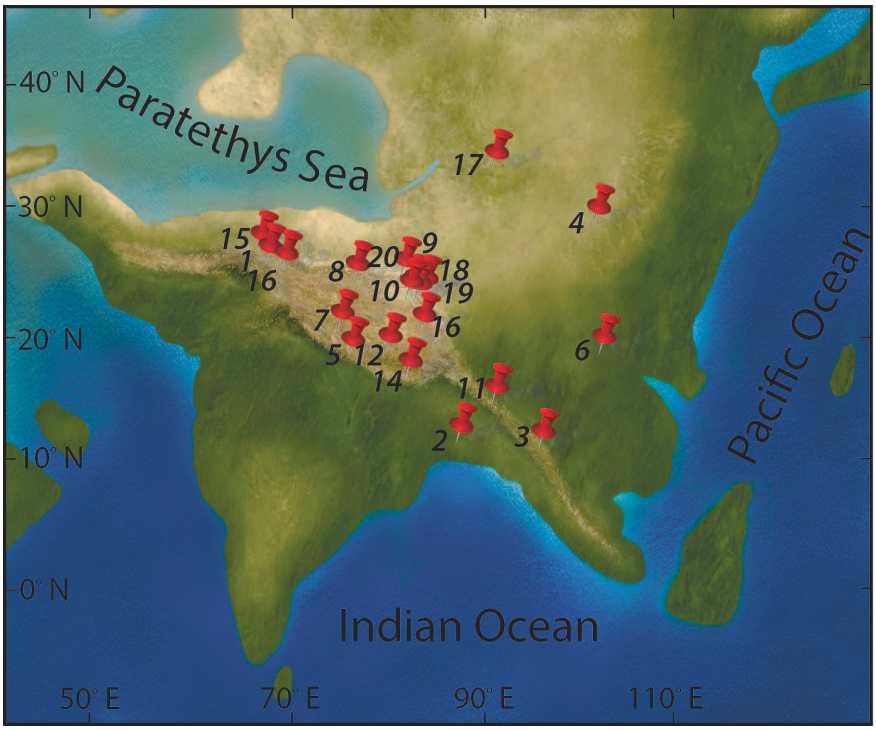

Figure 1. Palaeogeographic reconstruction [*Licht et al.*, 2014] used in this study for the late Eocene (42 Myr ago) climate simulations with the Tibetan Plateau maximum height set to 3,500 m and Sino-Burman Ranges to 1,500 m and localities of paleoaltimetry sites used in this study (numbers corresponds to those in the Extended Data Table 1). More detailed topography is given in Extended Data Fig. 1.

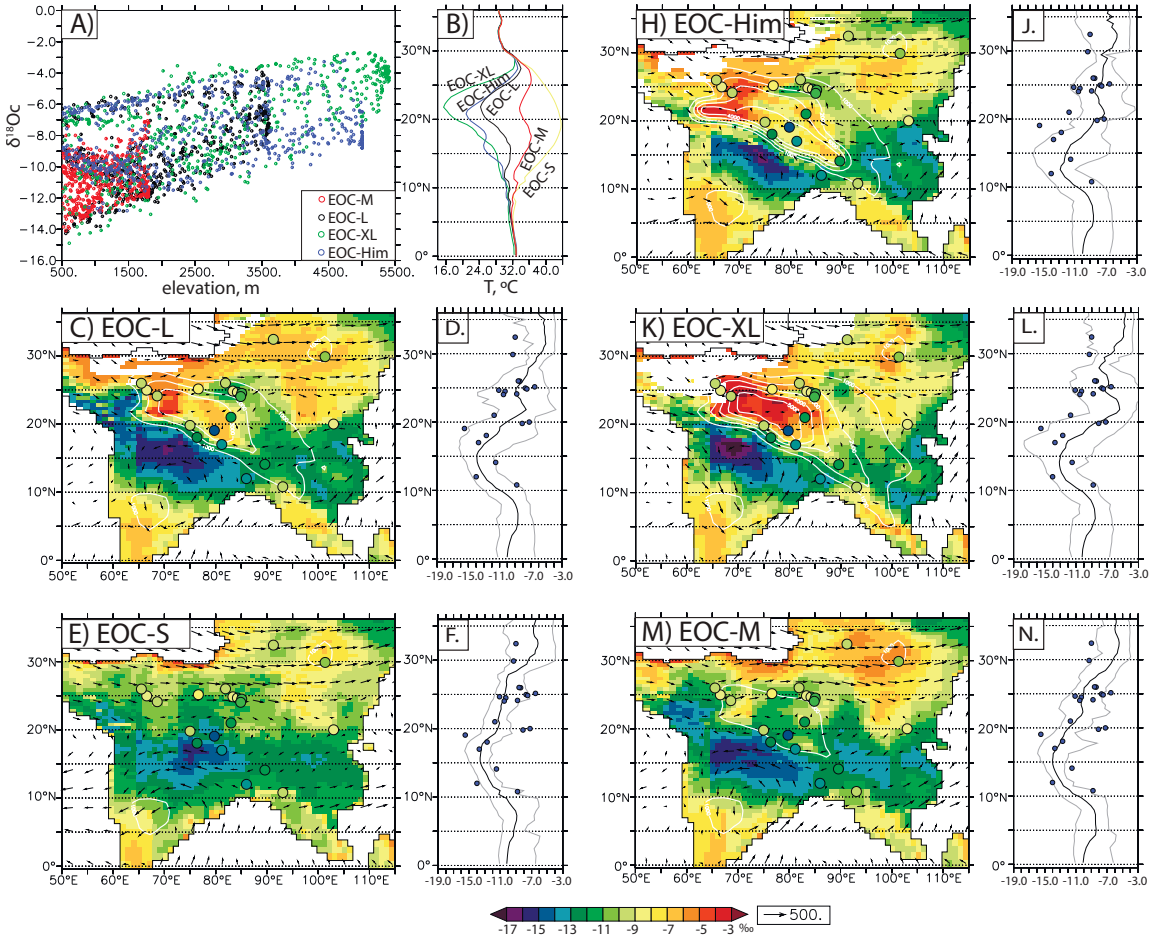

Figure 2. Maps and S-N profiles of $\delta^{18}O_c$ calculated from model simulated MJJAS precipitation-weighted $\delta^{18}O_w$ and model MJJAS mean temperatures for Eocene cases: C), D) EOC-L, E), F) EOC-S, H), J) EOC-Him, K), L) EOC-XL and M), N) EOC-M. The $\delta^{18}O$ profiles are averaged between 70º E and 90º E. Grey lines show minimum and maximum values for the selected range of longitudes. For all Eocene maps and profiles points show measures $\delta^{18}O_c$ from published data sets, the most negative values for lacustrine/biotic carbonates and average values for paleosols (see Extended Data Table 1). The subplot A) shows $\delta^{18}O_c$ – elevation relationships for Eocene simulations, B) simulated MJJAS temperature averaged between 70º E and 90º E for the Eocene simulations.

Extended Data Materials

Modeling approach

In order to assess spatial and temporal variations of climatic parameters and the isotopic composition of vapour and precipitation, we use the LMDZ-iso Atmospheric General Circulation model (GCM) [*Risi et al.*, 2010], a derivative of LMDZ [*Hourdin et al.*, 2006]. This model represents isotopic processes associated with all phase changes. Water in its vapour and condensed form is advected by the Van Leer advection scheme [*Van Leer*, 1977] Here we use a model configuration with 144 grid points in longitude, 142 in latitude and 39 vertical layers and a stretchable grid that permits increasing regional spatial resolution and gives an averaged resolution of ~50 km over central Asia. We force LMDZ-iso with realistic sea-surface temperatures (SSTs) simulated by FOAM and by realistic albedo and rugosity values, obtained with the vegetation distribution simulated with biophysics vegetation model LPJ [*Sitch et al.*, 2003].

Uncertainties and limits of our modeling approach

The major uncertainty in this study is related to the reconstruction of the geographical position of each site during Eocene. Based on paleomagnetic data for the Hoh Xil Basin (modern coordinates: 34.60º N, 93º E), [*Liu et al.*, 2003] reconstruct its Eocene paleolatitude as approximately 21º N (as a result of northward convergence of the Hoh Xil Basin with respect to Eurasia (Siberia) since Early Eocene–Late Oligocene time). Thus, we use a constant correction of 13º for positioning all of the geologic $\delta^{18}O$ sampling sites over our Eocene paleogeography. Such paleoaltitude estimates and corrections of about 13 ± 5º are in general consistent with the palaeolatitudes derived from a large number of high-quality palaeomagnetic studies from eastern China to Kyrgyzstan [*Lippert et al.*, 2014].

Though GCMs produce realistic Eocene temperatures over Asia and simulate the associated response of $\delta^{18}O_w$, numerical modeling with GCMs involves several uncertainties, including the

assumption of constant seawater $\delta^{18}O$ and the accuracy of the paleogeographic reconstruction. The Eocene latitudinal position of the Indian subcontinent and the height of other orogens in Asia, as well as their spatial extent remain a point of contention [*Najman et al.*, 2010; *Lippert et al.*, 2014] and may impact the results of our experiments. To address this limitation, additional paleogeographic scenarios should be tested in future work. Other potential limitations of using isotope-enabled GCMs include complexity associated with realistic representation of soils, evapotranspiration schemes, geochemistry, and vegetation. However, results of our current study permit a first-order estimate of Eocene $\delta^{18}O_w$ and its low sensitivity to topographic change.

Decomposing $\delta^{18}O_c$ differences

Our goal is to understand to what extent $\delta^{18}O_w$ changes explain the $\delta^{18}O_c$ signal over the Eocene HTP and what part of this signal depends on the temperature of the carbonate formation.

First, based on an assumption of equilibrium between water and calcite, $\delta^{18}O_c$ is related to $\delta^{18}O_w$ using Kim and O'Neil relationship [*Kim and O'Neil*, 1997]:

$$R_c = R_w/1.0309 - 29.98 + 17.49*1000/T - 31.45, \quad (1)$$

where T is the temperature of carbonate formation, R_c – isotopic ratios in carbonate and R_w – isotopic ratios in paleo surface water,

or in a simpler form:

$$R_c = R_c\,(R_w, T) \quad (2)$$

In order to understand why R_w varies from one climatic state to another, we decompose $\Delta R_c = R_{c2} - R_{c1}$ into contribution from dR_w and dT terms, referring to the climatic states using subscript 1 and 2 and to their difference using the Δ notation:

$$\Delta R_c = \Delta R_{c,dRw} + \Delta R_{c,dT} + N \quad (3)$$

where $\Delta R_{c,dRw}$ and $\Delta R_{c,dT}$ are the contributions of the part of the R_c signal related to the change of R_w and temperature accordingly. Non-linear terms of decomposition are gathered into the residual term

N.

Similarly to the isotopic signal decomposition suggested in [*Botsyun et al.*, 2016], contributions could be estimated as:

$\Delta R_{c,dRw} = R_c (R_{w2}, dT') - R_c (R_{w1}, dT')$, (4)

and

$\Delta R_{c,dT} = R_c (dR_w', T_2) - R_c (dR_w', T_1)$, (5)

where R_{w2}, R_{w1}, T_2, T_1 are $\delta^{18}O_w$ and temperature from two climatic states respectively and dR_w', dT' are centred differences:

$dR_w' = (R_{w1} + R_{w2}) / 2$, (6)

$dT' = (T_1 + T_2) / 2$, (7)

From the Eq. 1 and Eq. and 5 we have:

$\Delta R_{c,dRw} = (R_{w2} - R_{w1}) / 1.0309$, (8)

$\Delta R_{c,dT} = 17.49 * (1000 / T_2 - 1000 / T_1)$, (9)

$N = \Delta R_c - (\Delta R_{c,dRw} + \Delta R_{c,dT})$ (10)

Extended Data Table 1. Compilation of measured Eocene $\delta^{18}O_c$ from published materials (data from [*Ting et al.*, 2003; *Bowen et al.*, 2005; *Cyr et al.*, 2005; *Rowley and Currie*, 2006; *Kent-Corson et al.*, 2009; *Bershaw et al.*, 2012a; *Bougeois et al.*, 2014; *Ding et al.*, 2014; *Hoke et al.*, 2014; *Licht et al.*, 2014; *Xu et al.*, 2015; *Caves et al.*, 2015; *Wei et al.*, 2016]). $\delta^{18}O_c$ are reported relative to PDB. Each time we report the minimum measured values for lacustrine/biotic data and minimum and averaged values for paleosoils.

	Locality	Age	Carbonate nature	$\delta^{18}O_c$ (PDB) (‰), min values (average values for paleosols)	Chosen $\delta^{18}O_c$	Temperature used in the original study (º C)	Ref isotopic data
1.	Aertashi	40-34,3 Ma	Undifferentiated (Pedogenic nodule or sediment matrix)	-7,7	Min	-	[*Kent-Corson et al.*, 2009]
2.	Central Myanmar	Eo	Gastropods	-14	Min	34 ± 5	[*Licht et al.*, 2014]
3.	Chake Basin	Eo	Pedogenic nodules	-10.4 (-8,8)	Min and average	27	[*Hoke et al.*, 2014]
4.	Erlian Basin	PETM	paleosol	-12,6 (-9,3)	Min and average	-	[*Bowen et al.*, 2005]
5.	Gerze Basin	34-42 Ma	Lacustrine carbonate	-8,1	Min	25 ± 10	[*Wei et al.*, 2016]
6.	Hengyang Basin	Eo	paleosol	-9.9 (-7,2)	Min and average	-	[*Ting et al.*, 2003]
7.	Hoh Xil Basin	37.5 Ma	Lacustrine carbonates	-11,7	Min and average	15 - 30	[*Cyr et al.*, 2005]
8.	Janggalsay	34 Ma	Undifferentiated (Pedogenic nodule or sediment matrix)	-6,5	Min	-	[*Kent-Corson et al.*, 2009]
9.	Lake Mahai	50-34 Ma	Undifferentiated (Pedogenic nodule or sediment matrix)	-11,1	Min	-	[*Kent-Corson et al.*, 2009]
10.	Lenghu	Eo	Undifferentiated (Pedogenic nodule or sediment matrix)	-7,5	Min	-	[*Kent-Corson et al.*, 2009]
11.	Liming	Eo	Pedogenic nodules	-14.4 (-11,5)	Min and average	26 and 21	[*Hoke et al.*, 2014]

12.	Linzhou Basin, Pana Formation	51-48 Ma	Pedogenic nodules	-16.2 (-13,7)	Min and average	13.8 ± 8	[*Ding et al.*, 2014]
13.	Lulehe	Eo	Undifferentiated (Pedogenic nodule or sediment matrix)	-10,3	Min	-	[*Kent-Corson et al.*, 2009]
14.	Lunpola Basin, Middle Niubao and Upper Niubao	55-37.5 Ma	Lacustrine and pedogenic nodules	-15,5	Min and average	10 ±10	[*Rowley and Currie*, 2006]
15.	Oytag	Eo	Mudstone	-8,4	Min	19	[*Bershaw et al.*, 2012]
16.	Puska	Eo	Undifferentiated (Pedogenic nodule or sediment matrix)	-8,8	Min	-	[*Kent-Corson et al.*, 2009]
17.	Taatsin Gol	36-34 Ma	paleosol	-9,6 (-9)	Min and average	25	[*Caves et al.*, 2014]
18.	Tangra Yum Co	~46 Ma	paleosol	-18.3 (-12,7)	Min and average	15 ± 8	[*Xu et al.*, 2015]
19.	Xiao Qaidam	Eo	Undifferentiated (Pedogenic nodule or sediment matrix)	-10,5	Min	-	[*Kent-Corson et al.*, 2009]
20.	Xorkol	Eo	Undifferentiated (Pedogenic nodule or sediment matrix)	-8,6	Min	-	[*Kent-Corson et al.*, 2009]

Extended Data References:

Bershaw, J., C. N. Garzione, L. Schoenbohm, G. Gehrels, and L. Tao (2012a), Cenozoic evolution of the Pamir plateau based on stratigraphy, zircon provenance, and stable isotopes of foreland basin sediments at Oytag (Wuyitake) in the Tarim Basin (west China), *J. Asian Earth Sci.*, *44*, 136–148, doi:10.1016/j.jseaes.2011.04.020.

Bershaw, J., S. M. Penny, and C. N. Garzione (2012b), Stable isotopes of modern water across the Himalaya and eastern Tibetan Plateau: Implications for estimates of paleoelevation and paleoclimate, *J. Geophys. Res. Atmos.*, *117*(2), 1–18, doi:10.1029/2011JD016132.

Botsyun, S., P. Sepulchre, C. Risi, and Y. Donnadieu (2016), Impacts of Tibetan Plateau uplift on atmospheric dynamics and associated precipitation δ18O, *Clim. Past*, *12*(6), 1401–1420, doi:10.5194/cp-12-1401-2016.

Bougeois, L., M. de Rafélis, G. J. Reichart, L. J. de Nooijer, F. Nicollin, and G. Dupont-Nivet (2014), A high resolution study of trace elements and stable isotopes in oyster shells to estimate central asian middle eocene seasonality, *Chem. Geol.*, *363*, 200–212, doi:10.1016/j.chemgeo.2013.10.037.

Bowen, G. J., P. L. Koch, J. Meng, J. Ye, and S. Ting (2005), Age and Correlation of Fossiliferous Late Paleocene–Early Eocene Strata of the Erlian Basin, Inner Mongolia, China, *Am. Museum Novit.*, *3474*(1), 1, doi:10.1206/0003-0082(2005)474[0001:AACOFL]2.0.CO;2.

Caves, J. K., M. J. Winnick, S. A. Graham, D. J. Sjostrom, A. Mulch, and C. P. Chamberlain (2015), Role of the westerlies in Central Asia climate over the Cenozoic, *Earth Planet. Sci. Lett.*, *428*, 33–43.

Cyr, A. J., B. S. Currie, and D. B. Rowley (2005), Geochemical Evaluation of Fenghuoshan Group Lacustrine Carbonates, North-Central Tibet: Implications for the Paleoaltimetry of the Eocene Tibetan Plateau, *J. Geol.*, *113*(5), 517–533, doi:10.1086/431907.

Ding, L., Q. Xu, Y. Yue, H. Wang, F. Cai, and S. Li (2014), The Andean-type Gangdese Mountains: Paleoelevation record from the Paleocene-Eocene Linzhou Basin, *Earth Planet. Sci. Lett.*, *392*, 250–264, doi:10.1016/j.epsl.2014.01.045.

Hoke, G. D., J. Liu-Zeng, M. T. Hren, G. K. Wissink, and C. N. Garzione (2014), Stable isotopes reveal high southeast Tibetan Plateau margin since the Paleogene, *Earth Planet. Sci. Lett.*, *394*, 270–278, doi:10.1016/j.epsl.2014.03.007.

Hourdin, F. et al. (2006), The LMDZ4 general circulation model: Climate performance and sensitivity to parametrized physics with emphasis on tropical convection, *Clim. Dyn.*, *27*(7–8), 787–813, doi:10.1007/s00382-006-0158-0.

Hren, M. T., B. Bookhagen, P. M. Blisniuk, A. L. Booth, and C. P. Chamberlain (2009), δ18O and δD of streamwaters across the Himalaya and Tibetan Plateau: Implications for moisture sources and paleoelevation reconstructions, *Earth Planet. Sci. Lett.*, *288*(1–2), 20–32, doi:10.1016/j.epsl.2009.08.041.

Kent-Corson, M. L., B. D. Ritts, G. Zhuang, P. M. Bovet, S. a. Graham, and C. Page Chamberlain (2009), Stable isotopic constraints on the tectonic, topographic, and climatic evolution of the northern margin of the Tibetan Plateau, *Earth Planet. Sci. Lett.*, *282*(1–4), 158–166, doi:10.1016/j.epsl.2009.03.011.

Kim, S. T., and J. R. O'Neil (1997), Equilibrium and nonequilibrium oxygen isotope effects in synthetic carbonates, *Geochim. Cosmochim. Acta*, *61*(16), 3461–3475, doi:10.1016/S0016-7037(97)00169-5.

Van Leer, B. (1977), Towards the ultimate conservative difference scheme. IV. A new approach to numerical convection, *J. Comput. Phys.*, *23*(3), 276–299, doi:http://dx.doi.org/10.1016/0021-9991(77)90095-X.

Licht, A. et al. (2014), Asian monsoons in a late Eocene greenhouse world, *Nature*, *513*(7519), 501–506, doi:10.1038/nature13704.

Lippert, P. C., D. J. J. van Hinsbergen, and G. Dupont-Nivet (2014), Early Cretaceous to present latitude of the central proto-Tibetan Plateau: A paleomagnetic synthesis with implications for Cenozoic tectonics, paleogeography, and climate of Asia, *Geol. Soc. Am. Spec. Pap.*, *2507*(1), 1–21, doi:10.1130/2014.2507(01).

Liu, Z., X. Zhao, C. Wang, S. Liu, and H. Yi (2003), Magnetostratigraphy of Tertiary sediments from the Hoh Xil Basin: implications for the Cenozoic tectonic history of the Tibetan Plateau, *Geophys. J. Int.*, *154*(2), 233–252.

Najman, Y. et al. (2010), Timing of India-Asia collision: Geological, biostratigraphic, and palaeomagnetic constraints, *J. Geophys. Res. Solid Earth*, *115*(12), 1–18, doi:10.1029/2010JB007673.

Quade, J., D. O. Breecker, M. Daëron, and J. Eiler (2011), The paleoaltimetry of Tibet: An isotopic perspective, *Am. J. Sci.*, *311*(2), 77–115, doi:10.2475/02.2011.01.

Risi, C., S. Bony, F. Vimeux, and J. Jouzel (2010), Water-stable isotopes in the LMDZ4 general circulation model: Model evaluation for present-day and past climates and applications to climatic interpretations of tropical isotopic records, *J. Geophys. Res. Atmos.*, *115*(12), 1–27, doi:10.1029/2009JD013255.

Rowley, D. B., and B. S. Currie (2006), Palaeo-altimetry of the late Eocene to Miocene Lunpola

basin, central Tibet., *Nature*, *439*(7077), 677–681, doi:10.1038/nature04506.

Sitch, S. et al. (2003), Evaluation of ecosystem dynamics, plant geography and terrestrial carbon cycling in the LPJ dynamic global vegetation model, *Glob. Chang. Biol.*, *9*, 161–185, doi:10.1046/j.1365-2486.2003.00569.x.

Ting, S., G. J. Bowen, P. L. Koch, W. C. Clyde, Y. Wang, Y. Wang, and M. C. Mckenna (2003), Biostratigraphic, chemostratigraphic, and magnetostratigraphic study across the Paleocene-Eocene boundary in the Hengyang Basin, Hunan, China, *Geol. Soc. Am.*, *Spacial Pa*, 521–535, doi:10.1130/0-8137-2369-8.521.

Wei, Y., K. Zhang, C. N. Garzione, Y. Xu, B. Song, and J. Ji (2016), Low palaeoelevation of the northern Lhasa terrane during late Eocene: Fossil foraminifera and stable isotope evidence from the Gerze Basin, *Sci. Rep.*, *6*, 27508.

Xu, Q., L. Ding, R. Hetzel, Y. Yue, and E. F. Rades (2015), Low elevation of the northern Lhasa terrane in the Eocene: Implications for relief development in south Tibet, *Terra Nov.*, *27*(6), 458–466, doi:10.1111/ter.12180.

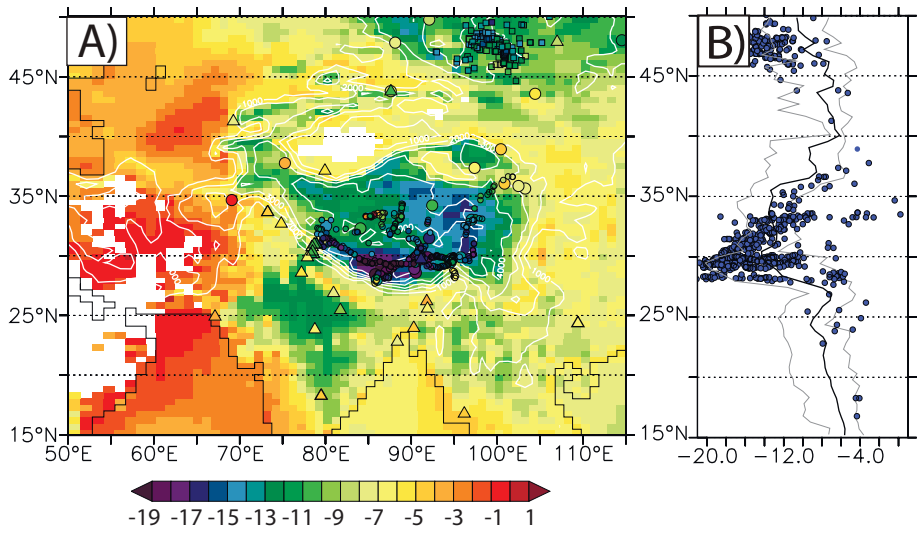

Extended Data Fig. 1. Maps and S-N profiles of model simulated MJJAS precipitation-weighted $\delta^{18}O_w$ for CTR case. Triangles show $\delta^{18}O_w$ from GNIP stations, big circles – $\delta^{18}O_w$ from Caves et al. (2015) compilation, small circles represent $\delta^{18}O$ in streams, lakes and springs compiled from [*Hren et al.*, 2009; *Quade et al.*, 2011; *Bershaw et al.*, 2012b]. The $\delta^{18}O$ profiles are averaged between 70º E and 90º E. Grey lines show minimum and maximum values for the selected range of longitudes.

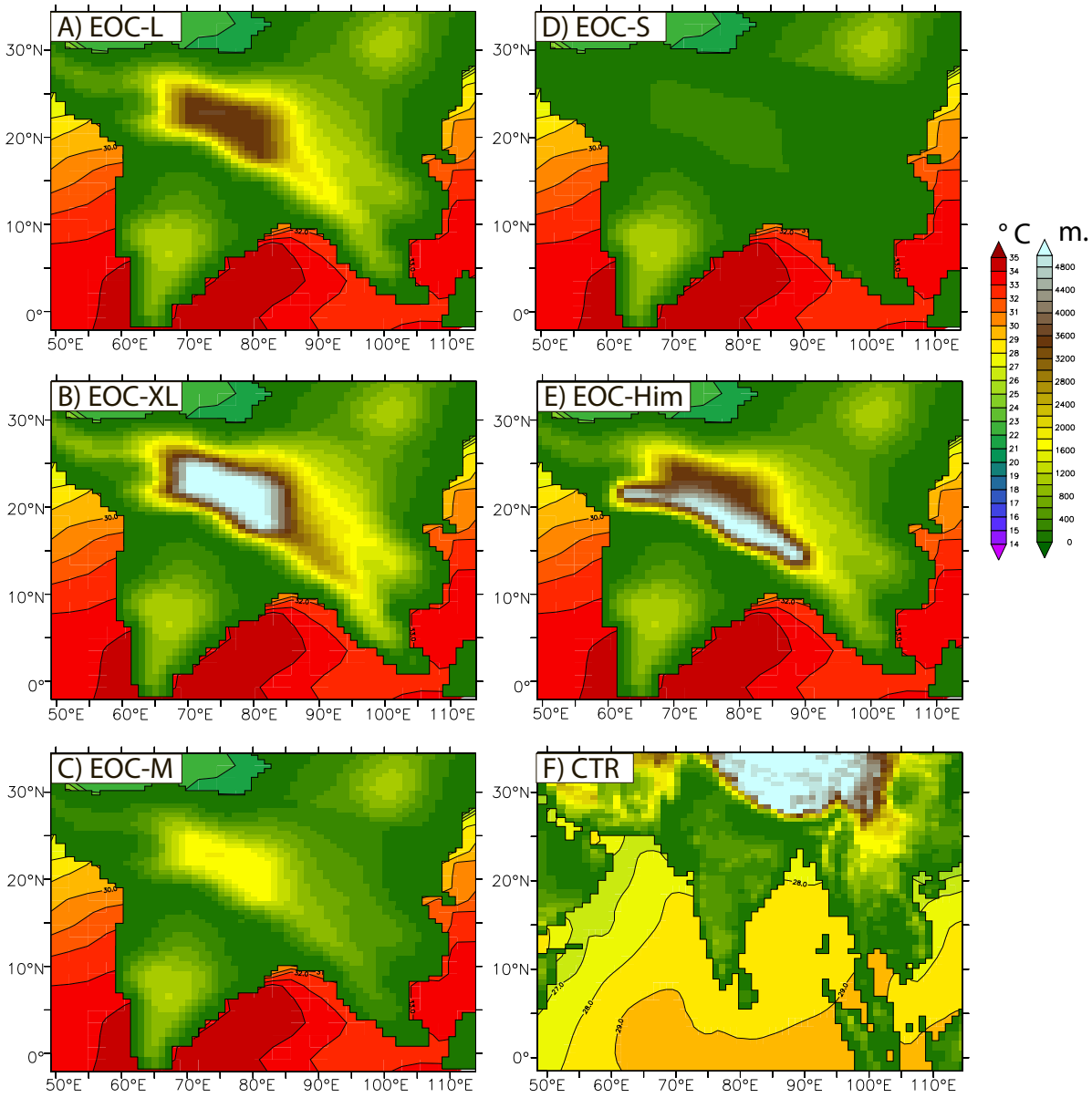

Extended Data Fig. 2. Geography, topography and FOAM-derived sea surface temperatures for A) CTR, B) EOC-L, C) EOC-XL, D) EOC-Him, E) EOC-M, and F) EOC-S experiments in a resolution of LMDZ-iso.

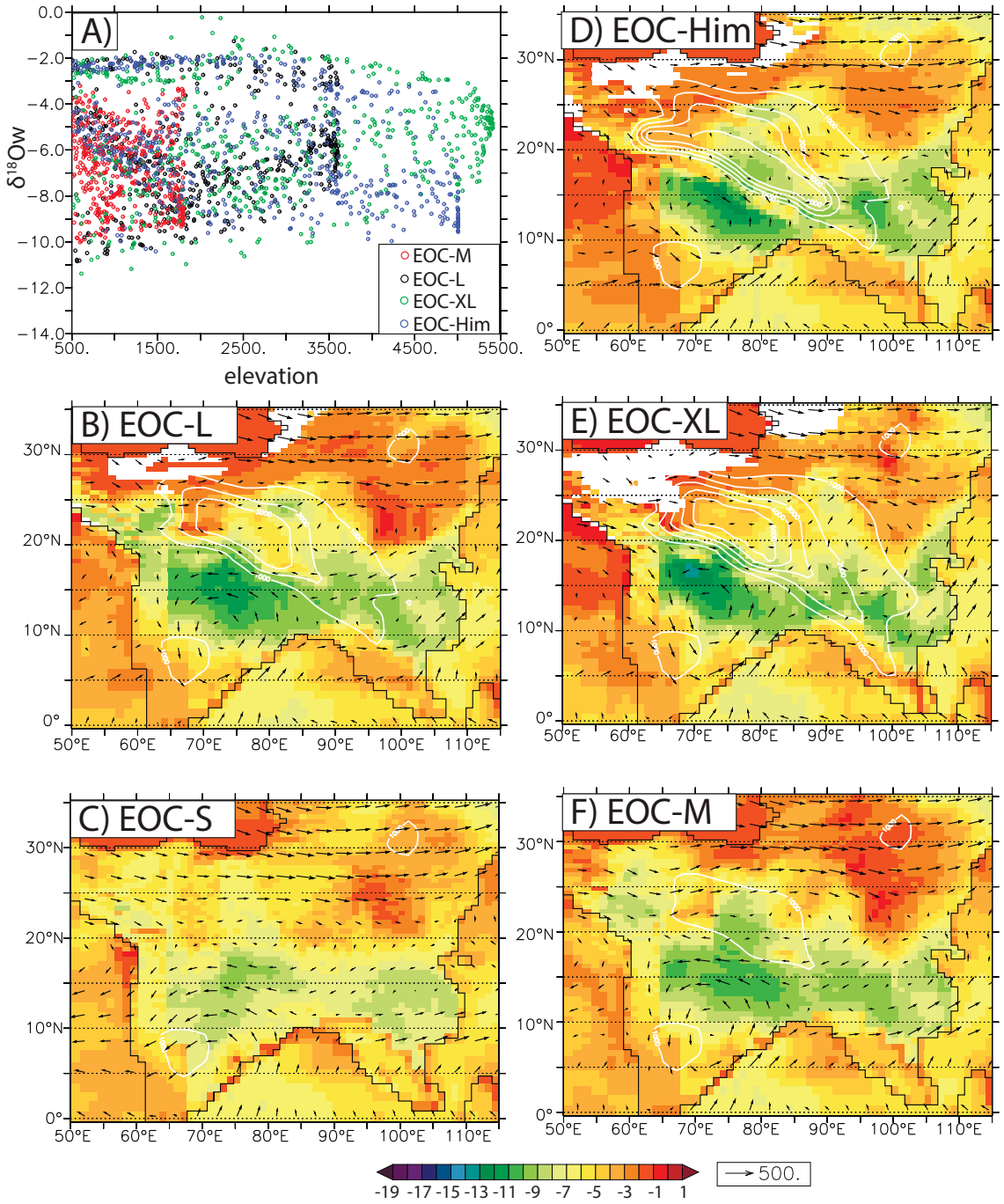

Extended Data Fig. 3. Relationships between model elevations and simulated precipitation weighted MJJAS $\delta^{18}O_w$ for Eocene cases (A) and maps of model simulated precipitation weighted MJJAS $\delta^{18}O_w$ for Eocene cases: B) EOC-L, C) EOC-S, D) EOC-Him, E) EOC-XL and F) EOC-M. Vectors show MJJAS vertically integrated moisture transport (kg m^{-1} s^{-1}).

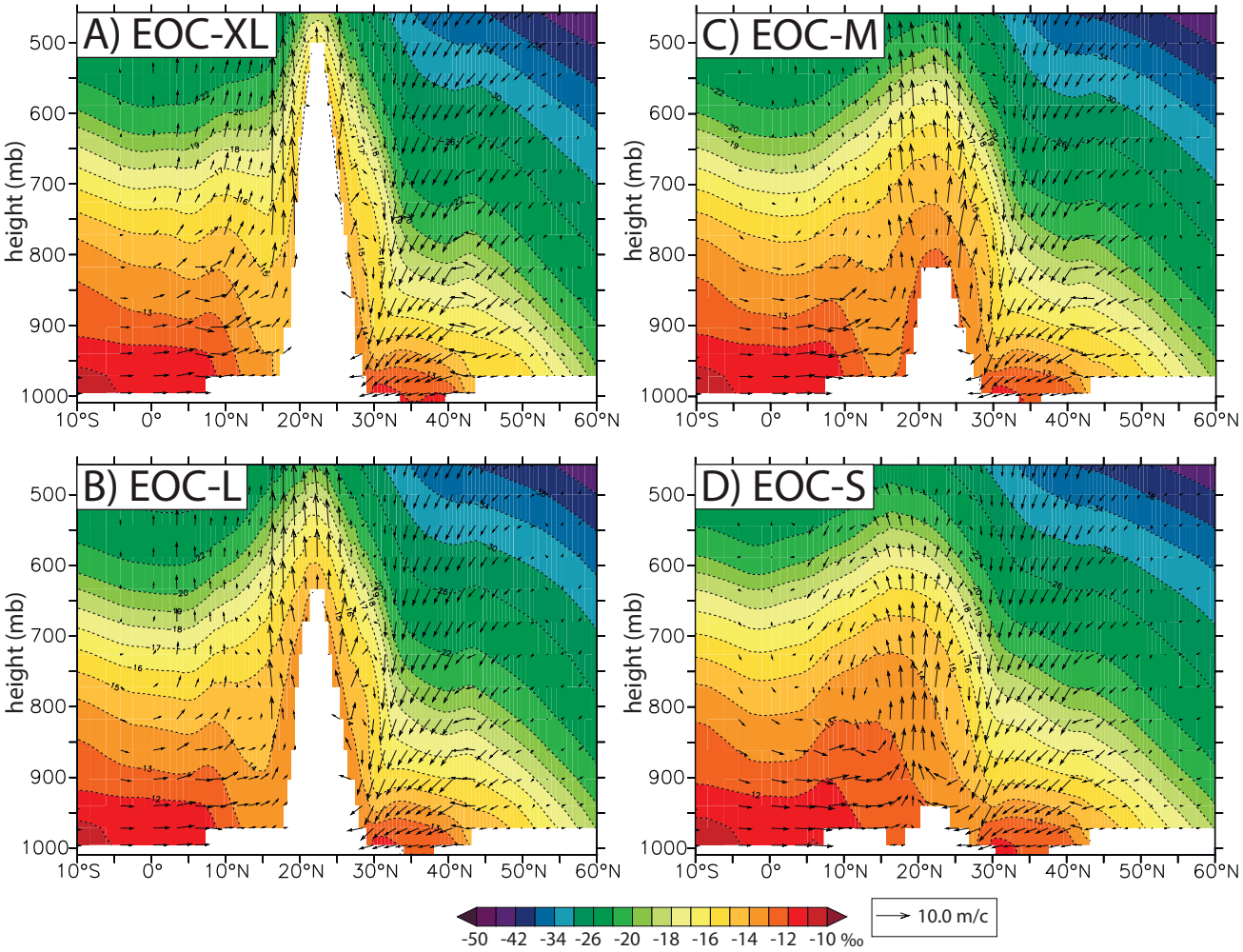

Extended Data Fig. 4. MJJAS $\delta^{18}O_v$ and meridional-vertical wind velocities (m/c) for A) EOC-XL, B) EOC-L, C) EOC-M, and D) EOC-S simulations. Profiles are averaged between 72º E and 78º E for all Eocene simulations.

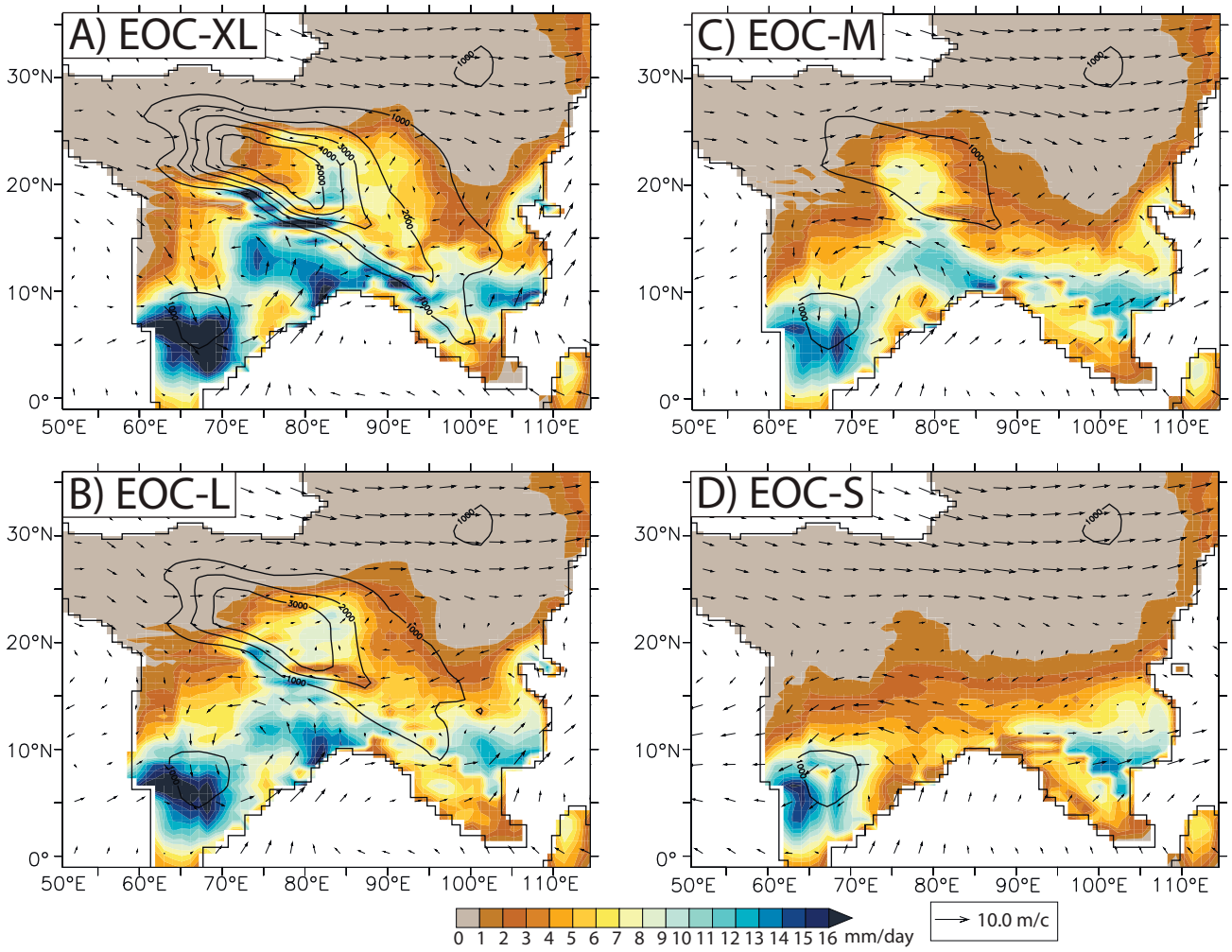

Extended Data Fig. 5. MJJAS mean rainfall (mm/day) and surface winds for for A) EOC-XL, B) EOC-L, C) EOC-M, and D) EOC-S simulations.

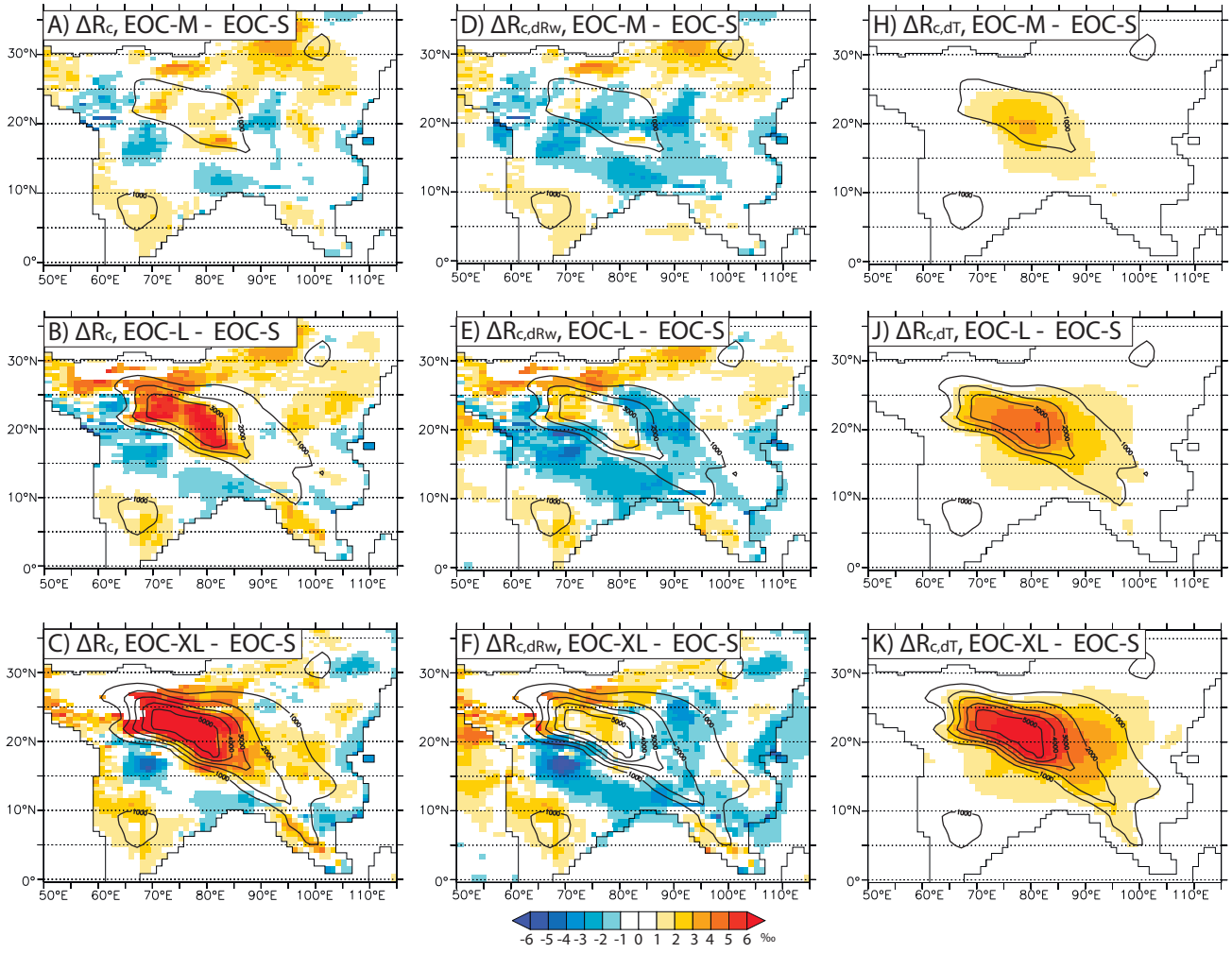

Extended Data Fig. 6. Total isotopic difference (ΔR_c) between A) EOC-M and EOC-S, B) EOC-L and EOC-S, C) EOC-XL and EOC-S experiments and spatial isotopic variations related to the variations in $\delta^{18}O_w$ ($\Delta R_{c,dRw}$) and temperature variations ($\Delta R_{c,dT}$). See the Section Decomposing $\delta^{18}O_c$ differences in the Extended data.

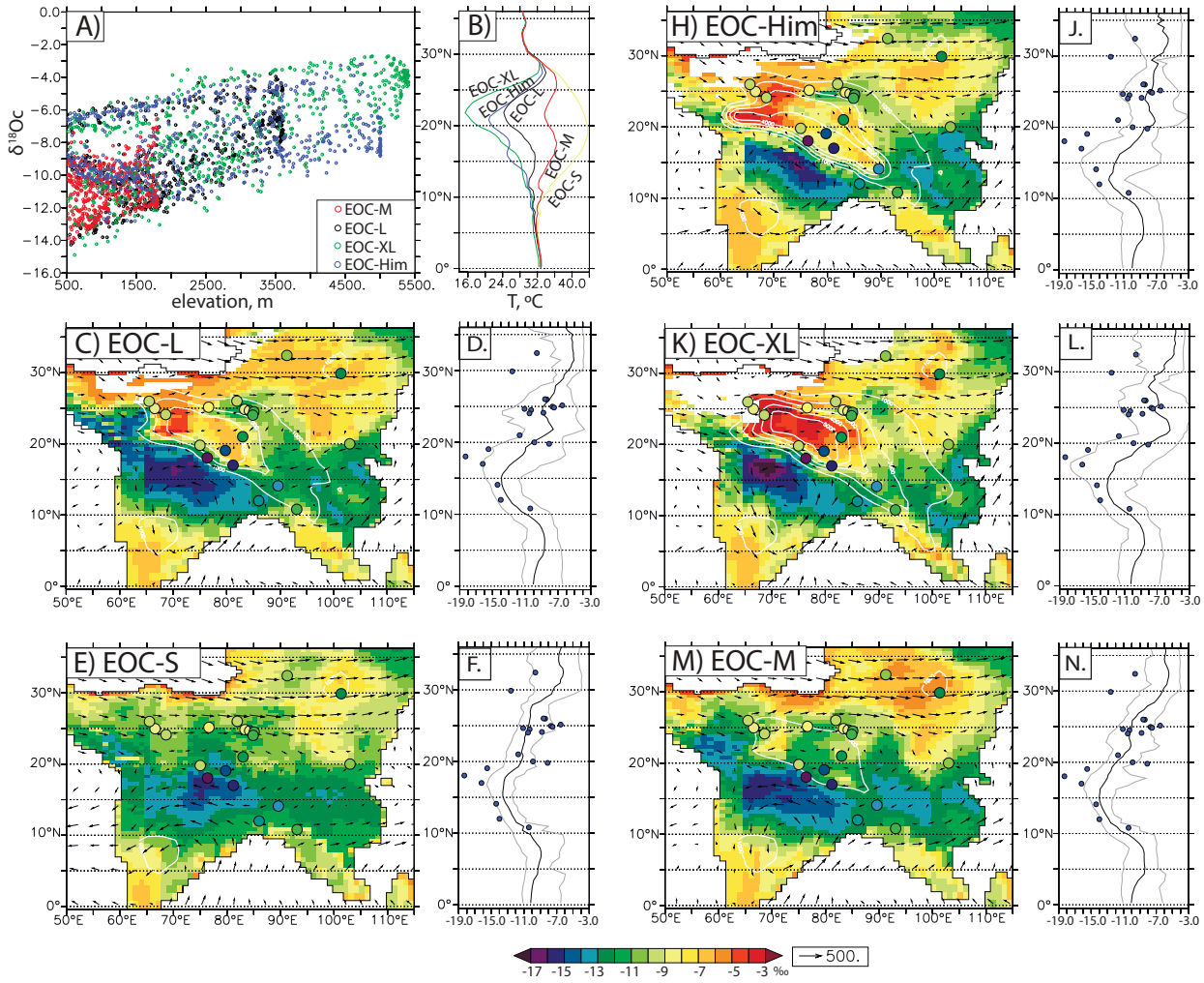

Extended Data Fig. 7. Maps and S-N profiles of $\delta^{18}O_c$ calculated from model simulated MJJAS precipitation-weighted $\delta^{18}O_w$ and model MJJAS mean temperatures for Eocene cases: C), D) EOC-L, E), F) EOC-S, H), J) EOC-Him, K), L) EOC-XL and M), N) EOC-M. The $\delta^{18}O$ profiles are averaged between 70º E and 90º E. Grey lines show minimum and maximum values for the selected range of longitudes. For all Eocene maps and profiles, points are the most-negative measured $\delta^{18}O_c$ for each site from published data sets (see Extended Data Table 1). The subplot A) shows $\delta^{18}O_c$ – elevation relationships for Eocene simulations, B) simulated MJJAS temperature averaged between 70º E and 90º E for the Eocene simulations.

Extended Data Table 2. Kolmogorov-Smirnov test with two-side alternative hypothesis applied for measured $\delta^{18}O_c$ and $\delta^{18}O_c$ calculated using LMDZ-iso simulated MJJAS mean temperature and $\delta^{18}O_w$ values (for a S-N profile (from 10º N to 36º N) averaged between 70º E to 90º E over the continent). N=21. Results show that when the minimum $\delta^{18}O_c$ values are taken for all carbonate data, EOC-Him and EOC-XL modeled $\delta^{18}O_c$ distribution is different from measured data within 95% confidence interval, while for EOC-M, EOC-L, and EOC-S experiment the hypothesis that these distributions are similar could not be refuted with 5% significance level. When the minimum $\delta^{18}O_c$ values are taken for lacustrine/biotic data and averaged values for paleosoils data, EOC-XL modeled $\delta^{18}O_c$ distribution is different from measured data within 95% confidence interval, while for EOC-Him, EOC-M, EOC-L, and EOC-S experiment the hypothesis that these distributions are similar could not be refuted with 5% significance level.

	Min-ave		Min	
Simulation	p-value	D-statistic	p-value	D-statistic
EOC-L	0.3507	0.2408	0.1806	0.2884
EOC-S	0.2491	0.2637	0.3646	0.2381
EOC-Him	0.2184	0.272	0.05141	0.3498
EOC-XL	0.01812	0.3965	0.00547	0.4441
EOC-M	0.4546	0.2216	0.3646	0.2381

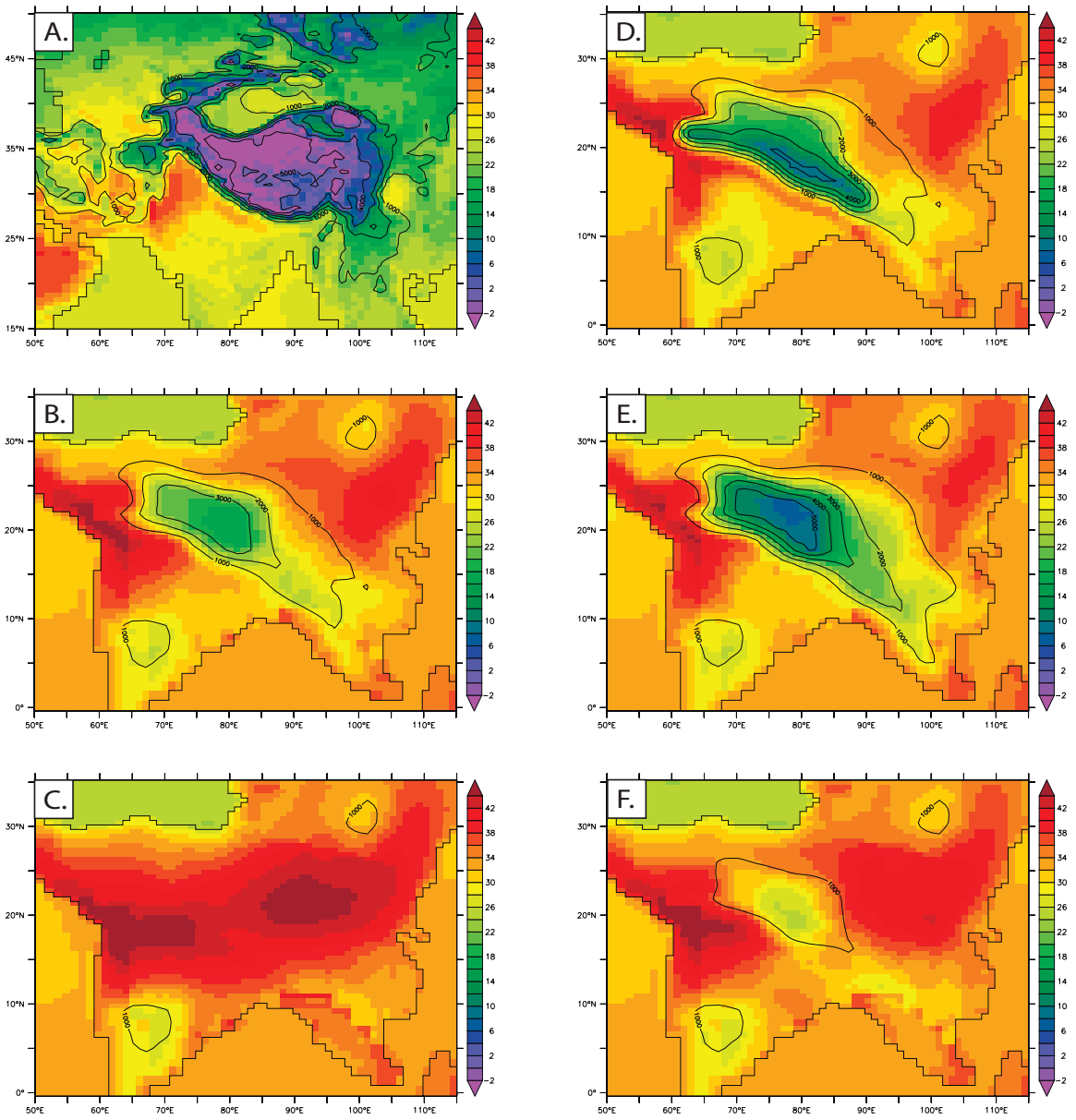

Extended Data Fig. 8. LMDZ-iso simulated MJJAS temperatures at 2 meters for A) CTR, B) EOC-L, C) EOC-S, D) EOC-Him, E) EOC-XL, and F) EOC-M experiments.

5.3 Summary and conclusions

In this Chapter, in order to provide "forward proxy modeling", we compare directly LMDZ-iso output with the measured isotopic data from natural archives for the Eocene case (42 Ma). We show that classic paleoaltimetry approach based on stable oxygen isotopes is not valid for ancient time periods such as the Eocene, because 1) Eocene $\delta^{18}O_w$ patterns over the HTP are different from the present-day due to the displacement of the whole Asian continent to the south, and 2) local temperature significantly contributes to the total $\delta^{18}O_c$ signal. We urge using GCM model simulations as an efficient method that give an access to paleoclimate and $\delta^{18}O$ both. In particular, reconstruction of soil temperature of carbonate formation and $\delta^{18}O_w$ both is a robust method to reconstruct predicted $\delta^{18}O_c$.

Chapter 6

Climate evolution over Asia during the Cenozoic

A lot of recent modeling efforts have been undertaken in order to clarify the impact of the HTP uplift on the monsoonal circulation and aridification over the Asian region. However, most of the studies use near-modern boundary conditions to test the role of tectonics on monsoon, including present-day continental configuration and pCO_2 concentration. Thus, the relative contributions of tectonics and greenhouse gasses forcings on Cenozoic monsoon intensification and onset of deserts over Asia are barely understood. On the other hand, acquirement of new geological data requires physical bases for their interpretation. In this chapter, using the general circulation model (LMDZ) we test the sensitivity of Cenozoic climate over Asia to the surface elevation uplift and pCO_2 concentrations changes together with Early Eocene (55 Ma), Middle Eocene (42 Ma), Oligocene (30 Ma) and Miocene (15 Ma) continental configurations. Such a technique allows us to evaluate the relative importance of each of these factors for the spatial patterns of summertime climate fields. For more realistic experiments, LMDZ was forced with sea surface temperatures calculated using the fully coupled model FOAM and with albedos obtained from LPJ vegetation simulations. Preliminary results of our numerical modeling show a significant influence of topography changes on the Asian climate for all Cenozoic periods except for the Early Eocene. Our results have possible implications for the interpretation of single-site paleo proxy records as provide first-order information on the precipitation amount and seasonality.

Contents

6.1 Introduction

Reconstruction of climate change through geological time can help to interpret regional geodynamical evolution (Molnar et al., 2010) on one hand and to estimate the scale of surface processes on the other (Clift et al., 2010; Peizhen et al., 2001). Over the past several decades, the Himalayas and the Tibetan Plateau have been the focus of numerous studies examining different aspects of tectonic-climate interactions at a broad range of spatial and temporal scales (Clift et al., 2008; Grujic et al., 2006; Kutzbach et al., 1993; Molnar and England, 1990; Ruddiman and Kutzbach, 1989). The impact of tectonic evolution of Indo-Asia collision zone on the monsoonal circulation is a classical example of such interactions (Huber and Goldner, 2012; Molnar et al., 1993; Roe et al., 2016) (for more details see Section 1.1.4).

Today, Asian climate is characterized not only by highly seasonal precipitation and seasonal reversal of prevailing surface wind (i.e the monsoon circulation (Wang et al., 2012b)), but also by extremely arid regions in its inner part, with cumulative annual precipitation bellow 200 mm/year. Cenozoic environments have been reconstructed based on geological evidences (records from loesses, lakes, deserts, organisms and marine sediments) and climate simulations both. However, the reconstructions of the timing of the monsoon-arid environment evolution remains controversial. For example, no consensus exists for the timing of initial Indo-Asian monsoon (IAM) onset or its intensification. Proposed ages cluster in the early Miocene (~22–20 Ma; e.g. Guo et al. (2002)), the middle Miocene (16–11 Ma; e.g Clift et al. (2004)) and the late Miocene (11–8 Ma; e.g. Chen et al. (2003)), or even in the Eocene period (55-34 Myr ago; e.g Licht et al. (2014)). Spatial distribution of desert regions through the Cenozoic is also uncertain, partly because desert sediments are usually scattered, discontinuous and difficult to date (Guo et al., 2002).

In order to obtain better estimates of the timing, driving forces should be evaluated first. Based on magnetostratigraphycal and cyclostratigraphycal evidences, Dupont-Nivet et al. (2007) have hypothesized the main driving forces of the IAM and aridity variations over Asia: 1) the uplift of the Tibetan Plateau and adjacent areas, 2) land–sea redistribution associated with the continental collision of India and Asia, and 3) global cooling at the Eocene-Oligocene, associated with the drop in CO_2 concentration trough the early Cenozoic and the onset of Antarctic ice sheet formation at 34 Ma (DeConto and Pollard, 2003). In opposite to geological methods based on proxy data, climate modeling allows to study the mechanisms that drive the environmental changes through the Cenozoic, which is crustal for understanding the climate evolution through time.

The impact of the HTP uplift on the IAM has become a focus of climate modeling studies since a quarter of a century. However, Asian topography during the Cenozoic is highly debated nonetheless big amount of paleoelevation estimates based on various methods (Currie et al., 2016; Rowley et al., 2001; Wei et al., 2016). Climate modeling technique allows to test the impact of various uplift scenarios on environment evolution for various time periods. In previous studies the impact of the atmospheric circulation was studied applying different uplift scenarios, including bulk plateau uplift (Zhang et al., 2015, 2012) or plateau regional uplift (in which each sub-regional uplift is considered separately and its influence on the climatic subsystems in different regions is investigated) (e.g Tang

et al., 2013). However, still the physical basics of Asian topography and monsoon circulation are disputed. For example, many heated discussions have been carried on the impact of Asian mountain ranges on atmosphere circulation through mechanical and thermodynamic effects (e.g. Boos and Kuang, 2010; Wu et al., 2015, 2012) (see more details in Section 1.1.4) and change of such effects with the growth of mountains buildings (Tang et al., 2013). Yanai and Wu (2006) and more recently Wu et al. (2015) gave a thorough review on the effects of the HTP and now it is commonly excepted that the topography has thermal and mechanical effects on the monsoon both (Wu et al., 2015) (see Section 1.1.4). In addition, climate models are frequently used to investigate the impact of topography uplift on aridity through a simple rain-shadow effect or stationary waves (Broccoli and Manabe, 1992; Lunt et al., 2010).

Second, the land–sea redistribution associated with the continental collision of India and Asia may reach considerable scale, since during the collision, India was rapidly shifted from south to north with a convergent rate ranging from ~15-25 cm/yr to ~13-18 cm/yr at the beginning of the Cenozoic with following slowing of the convergence (Achache et al., 1984). Paleomagnetic data (see data compilation in Molnar et al., 2010) indicates that during the Eocene and the Oligocene the Indian subcontinent was likely situated in the equatorial zone (see Section 1.2.3). However, only few climate modeling studies take into account the latitudinal shift of the HTP during the collision. For example, Roe et al. (2016) use a climate modeling approach together with stylized Indian geometry (with the Indian subcontinent artificially shifted to the south, that barely corresponds to 50 Ma configuration). These authors show that for the configuration with the India shifted to the south, summertime temperatures peaking at 45 °C concomitant with extremely low precipitation contributes to extremely desert conditions over the region currently occupied by the Tibetan plateau, central India, and the Bay of Bengal. They conclude that such a climate results from the combination of intense solar heating at subtropical latitudes together with the region's extreme isolation from moisture sources that would otherwise provide the twin buffering effect of reflective clouds and surface evaporation.

During the Cenozoic, except for the latitudinal shift, paleogeography had other major changes, for example the retreat of the epicontinental Parathetys Sea. Ramstein et al. (1997) first provided numerical experiments which highlight the importance of the configuration of the continents in the implementation of the monsoon and suggested that the closure of the Paratethys has made possible the monsoon through the establishment of a more continental climate in Eurasia. Similarly, Roe et al. (2016) show that the presence of a Paratethys Sea acts to enhance extremely desert conditions in the central Asia. The studies of Zhang et al. (2007a,b) show that the Paratethys retreat strengthens the East-Asia monsoon.

Although studies listed here have been focused on the role of land-sea distribution and orography, in the Asian monsoon system there no general consensus on which forcing is more fundamental: the orography or land-sea distribution. Some studies suggested that the land-sea distribution is crucial in formation of the Asian monsoon (e.g. Kuo and Qian, 1982; Webster et al., 1998); some emphasized the importance of the Tibetan Plateau (e.g. Kutzbach et al., 1993; Wu et al., 2007a). Chao and Chen (2001) suggested that land-sea distribution and orography are not necessary for the Asian and Australian monsoon

because most features of the Asian and Australian summer monsoon circulation can be reproduced even without Asia, maritime continents, and Australia in the numerical experiment. Xu et al. (2009) using numerical experimentation attempted to estimate the relative contribution of the role of land-sea distribution and orography on Asian climate. In this study authors concluded that the tropical subcontinental-scale zonal land-sea distribution and the Asian mountains almost equally contribute to the increase in monsoon and play a more important role than the large-scale meridional land-sea distribution between the Eurasian continent and the Indian Ocean.

The third hypothesized potential effect on Asian climate, the global cooling, has been also extensively studied. It has been shown that the monsoonal circulations are sensitive to greenhouse gas forcing because of non-linear impacts of increased temperatures (Washington and Meehl, 1983). In a more recent study, Cherchi et al. (2011) examined the role of increased CO_2 concentration on monsoons and have shown that, despite a common response in terms of atmospheric water vapor increase to the atmospheric warming, most studied monsoons simulate less or equal summer mean precipitation, but a huge increase of atmospheric vertically integrated specific humidity. However, studies that use realistic paleogeography and CO_2 concentrations are lacking.

Although the driving forces of the monsoon onset and aridification of the Inner Asia have been hypothesized, the relative contribution of tectonic and greenhouse forcing are unknown and the temporal and spatial distributions of wet and arid climates over Asia through the Cenozoic is poorly reconstructed. In addition, most modeling studies are using near-present-day boundary conditions (SSTs, greengases, paleogeographyes), thus the link between the tectonics, greenhouse forcing and Asian climate and their relative contributions to the climate change through the Cenozoic is still uncertain. Here for the first time we evaluate the 1) Sensitivity of IAM to continents position configuration 2) Sensitivity of IAM to topography change and 3) Sensitivity of IAM to CO_2 change using realistic paleogeographies with varying topography and CO_2 concentration.

6.2 Methods

6.2.1 Modeling methods and experimental design

For the modeling experiments we use atmosphere general circulation model (AGCM) LMDZ (Hourdin et al., 2006) developed at the Laboratoire de Météorologie Dynamique, Paris, France. The ability of this model to simulate atmospheric dynamics and reproduce rainfall patterns over Asia was shown in numerous studies (Day et al., 2015; Krishnan et al., 2015; Ladant et al., 2014; Lee et al., 2012; Licht et al., 2014; Zhou and Li, 2002). Here we use a model configuration with 96 grid points in longitude, 95 in latitude and 19 vertical layers.

Our experiments cover the whole Cenozoic from the Paleocene to Miocene: we use paleogeographies for 55 Ma (Herold et al., 2014), 42 Ma (Licht et al., 2014), 30 Ma (Zhang et al., 2014) and 15 Ma (Herold et al., 2008). Over the Asian region, the early Eocene paleogeography (Herold et al., 2014) is characterized by presence of a sea (probably epicontinental) separating India from Asia (see Section 2.4.1, Figure 2.6, panel A). The topography

in the original paleoreconstructions is rather low over Indian and Asian part both. The reconstruction that corresponds to middle Eocene (Licht et al., 2014) includes a southward shift of the Asian continent, as well as the presence of a large Paratethys Sea covering the region between 30° N and 47° N in latitude and extending to 80° E (Fig. 2.6, panel B). In the middle Eocene case, the HTP is considerably shifted to the south (situated between 15° N and 27° N) when compared to the present-day geography and its altitude reaches up to 3500 m (Figure 2.6). Compared with the middle Eocene paleogeography, the Oligocene one (Zhang et al., 2014) depicts a restricted Paratethys Sea and a larger part of Asia that is not covered by water (Figure 2.6, panel C). The Miocene paleogeography Herold et al. (2008) is quite similar to the present-day, with some exceptions, including the latitudinal position of the Indian subcontinent (Fig. 2.6, panel D). Compared to the present-day, the Miocene paleogeography has lower topography globally.

We have designed three groups of experiments (Table 6.1). The first group was based on paleogeographies with original topography (from the original publication). Atmospheric pCO_2 concentration for all experiments in this group has been set to 280 ppm (pre-industrial values). The second group includes experiments with the same continental configurations and topography, but with atmospheric pCO_2 increased up to 1120 ppm, that is consistent with early Cenozoic pCO_2 estimates (Beerling and Royer, 2011). Finally, for the third group of experiments we used the land-sea distribution from original paleogeographies, but the topography was reduced to 200 meters worldwide. For all experiments in this group we also used pre-industrial atmospheric pCO_2.

As LMDZ is an AGCM, we needed to prescribe the sea surface temperature (SST) as boundary conditions. We obtained SSTs by using the fully coupled model FOAM (Jacob, 1997) (ocean, 2.8° x 1.4° resolution with 24 vertical levels; atmosphere, 7.5° x 4.5° with 18 vertical levels) forced by corresponding paleogeography. Such a method using both models has been applied in recent studies on Cenozoic paleoclimates Ladant et al. (2014); Licht et al. (2014).

For all experiments the solar constant and orbital parameters were set to pre-industrial. The vegetation on land was prescribed. FOAM simulation was integrated for 2,000 years without flux corrections or deep ocean acceleration. The last 50 model-years were used to build the SSTs climatology used as input for LMDz. LMDz experiments were run for 20 years, with 4 years used for spin-up.

6.2.2 Model-data comparison

We compared simulated precipitation patterns with published data on spatial distribution of rocks markers of environment: evaporites (e.g., halite, gypsum, anhydride) as indicators of more arid condition and coals and peats, which preferably forms in humid environments (Parrish et al., 1982; Ziegler et al., 2003). Such comparison allows to provide qualitative estimation of precipitation amount in different simulations.

Table 6.1 – Summary of LMDZ experiments

Age	Simulation name	Paleogeography	Topography	pCO_2 (in ppm)
0 Ma	RT0Ma1x	Actual	Actual	280
15 Ma	RT15Ma1x	Herold et al. (2008)	Herold et al. (2008)	280
30 Ma	RT30Ma1x	Zhang et al. (2014)	Zhang et al. (2014)	280
42 Ma	RT42Ma1x	Licht et al. (2014)	Licht et al. (2014)	280
55 Ma	RT55Ma1x	Herold et al. (2014)	Herold et al. (2014)	280
0 Ma	RT0Ma4x	Actual	Actual	1120
15 Ma	RT15Ma4x	Herold et al. (2008)	Herold et al. (2008)	1120
30 Ma	RT30Ma4x	Zhang et al. (2014)	Zhang et al. (2014)	1120
42 Ma	RT42Ma4x	Licht et al. (2014)	Licht et al. (2014)	1120
55 Ma	RT55Ma4x	Herold et al. (2014)	Herold et al. (2014)	1120
0Ma	FE0Ma1x	Actual	≤ 200 m worldwide	280
15Ma	FE15Ma1x	Herold et al. (2008)	≤ 200 m worldwide	280
30Ma	FE30Ma1x	Zhang et al. (2014)	≤ 200 m worldwide	280
42Ma	FE42Ma1x	Licht et al. (2014)	≤ 200 m worldwide	280
55Ma	FE55Ma1x	Herold et al. (2014)	≤ 200 m worldwide	280

6.2.3 Monsoon indices

In order to facilitate monitoring and prediction of regional monsoon variability, various precipitation and circulation indices have been used (e.g., Fasullo and Webster, 2003; Gan et al., 2005; Yim et al., 2013). Here we use some of these monsoon indices for studying the monsoon variability during the Cenozoic. We have estimated 1) the spatial distribution of regions affected by the monsoons over Asia 2) the time of the monsoon onset and withdrawal 3) the strength of the monsoon as main characteristics of the monsoon.

First, for estimating the regions affected by the Indo-Asia monsoon system we calculated the relative contribution of the summer precipitation to the total annual precipitation. For estimating the time of offset and withdrawal of the monsoon for simulations with different boundary conditions we use precipitation, wind directions and moisture transport-based monsoon indices. Precipitation seasonality index (SI) shows the ration of wet season precipitation (MJJAS) to the annual cumulative precipitation, and thus obviously allows tracing regions with high seasonality of precipitation.

We also use indices based on wind components, because GCMs are known to better simulate the wind directions than the precipitation (Gan et al., 2005). We use the 850-hPa zonal wind index (850ZWI) indices (Gan et al., 2005), that is defined as 850-hPa zonal

wind component averaged between 60° E - 100° E and 10° N - 20° N, and gives access to the onset and demise dates. To examine the influence of the moisture transport by the lower level jet, we used 850-hPa zonal and meridional wind index (UVI) (Gan et al., 2005). It is defined as the sum of 850-hPa zonal wind averaged in the 60° E - 100° E and 850-hPa meridinal wind averaged in the 10° N - 20° N. Also we have used a hydrological onset and withdrawal index (HOWI), that was shown to be robust for the India region (Fasullo and Webster, 2003). This index is based on vertically integrated moisture transport, which is, in contrast to rainfall, is represented by GCM well.

The monsoon strength was estimated using the Webster-Yang monsoon index (WYI) (Webster and Yang, 1992), calculated as the difference between the zonal wind at 850 hPa and 200 hPa, averaged over a box from 40° to 110° E and from 0° to 20° N. We have also calculated the monsoon intensity index (MSW) based on the winter and summer average surface wind direction and velocity (Liu and Yin, 2002). This last index suggests that monsoons only exist when the differences between winter and summer mean wind directions are greater than 90° and less than 270°. Also, the higher the average wind velocities and the closer to 180° for the difference between the average wind directions in winter and summer, the greater the monsoon intensity (Liu and Yin, 2002).

6.3 Results

6.3.1 Summer precipitation and winds patterns over Asia during the Cenozoic

In general, for all time periods, a **bipolar distribution** of precipitation is simulated over Asia with high MJJAS precipitation rates over the southern part, and low rates over the northern part of the selected domain (Figure 6.1). However, the latitudinal extend of regions with high and low precipitation rates depends on the boundary conditions used. For example, for all simulations without topography (Figure 6.1 A, B, C, D, E) zone with extremely **low** summer **precipitation rate** (below 1 mm/month) has similar location (between 20 and 40 ° N). This arid zone is restricted more to the north-west by a presence of the HTP (compare Figure 6.1 A and F, B and G, C and H, D and J). This tendency is valid for all paleogeographies used except for the Early Eocene one, where the the northward shift is not simulated, because of the elevated topography has too southern position on the initial paleogeography. Increase in atmospheric CO_2 concentration results in small spatial restriction of hyper arid zone for present-day, Miocene and Oligocene case (compare Figure 6.1 F and L, G and M, H and N). For the Eocene simulations (Early Eocene and Middle Eocene cases both) CO_2 increase has smaller effect on arid zones spatial extend during the MJJAS.

Areas with very **high** summer **precipitation rate** (over 10 mm/day) are located over the Indian subcontinent and South-East Asia for most simulations. The southward shift of India for ancient time periods promotes the increase in summer precipitation rates over this region (e.g Figure 6.1 F, G, H, J, K), while for the simulations with high HTP, areas with high precipitation rates is shifted northward, up to the Himalayas foothills (compare

Figure 6.1 A and F, B and G, C and H, D and J). Again, this tendency is valid for all time periods except for the Early Eocene, where India is separated from the Asia by oceanic passage and the elevations on the original paleogeography are not very high.

Present-day Asian summer monsoon climate is characterized by strong low-level westerly **winds** over the Arabian Sea and India, and southerly wind over East Asia, which bring abundant rainfall far into the continent (Figure 6.1 F). The removal of orography greatly suppresses such summer monsoon flows and associated precipitation (Figure 6.1 A). To the first order, wind patterns for the RT15Ma1x experiment are similar to those of RT0Ma1x, except for the southerly wind over East Asia which is stronger for the RT0Ma1x experiment (Figure 6.1 F, G). Once India is shifted to the south like in RT30Ma1x and RT42Ma1x experiments, westerly flow over the Arabian Sea is remarkably reduced, while the winds over the Bengal Sea reverse their directions to easterly. Thus, for the Oligocene and Middle Eocene continents configuration, the India subcontinent is mainly fed by the easterly moisture. For the RT55Ma1x experiment, a particularly interesting wind system is formed: India, that occupies an equatorial position, prevailing by the easterly flow (ITCZ), while the South-East Asia is fed by the westerlies winds that reverse their direction over the Bay of Bengal.

For the simulations without topography, the westerly flow is stronger and the main jet axis is shifted to the south comparable to the simulations with high HTP (compare Figure 6.1 A and F, B and G, C and H, D and J, E and K). Simultaneously, westerly low-level jet over the Arabian Sea is weaker for the FE0Ma1x, and is completely disturbed for all paleo cases (compare Figure 6.1 A, B, C, D, E). Wind patterns for simulations with various CO_2 concentrations are similar between the simulations with the same paleogeography (Figure 6.1 F and L, G and M, H and N, J and O, K and P).

6.3.2 Cenozoic Indo-Asian monsoons

Precipitation seasonality

Calculated based on our models outputs, SI shows the presence of areas with high seasonality over Asia for all used boundary conditions (Figure 6.2). However, spatial variability depends on paleogeography, topography and CO_2 concentration applied.

Maximum of precipitation for CTR simulation is August - September - October that is in a good agreement with rainfall data from the Climate Research Unit (CRU) (New et al., 2002) (Figure 6.3 A). For most other simulations the maximum of precipitation is also simulated during August - September - October. The precipitation seasonally over the India and South-East Asia is strong for all simulations with an exception of FE15Ma1x experiment, where even summer precipitation is very low, and RT0Ma4x experiment, where precipitation is extremely strong all the year round (Figure 6.3 A).

Wind reversal

The strongest zonal winds reversal is simulated for RT0Ma1x and RT15Ma1x simulations (Figure 6.3 B). For RT0Ma4x and RT15Ma4x the seasonal wind reversal is less pronounced, but still strong. On the contrary, RT30Ma1x, RT42Ma1x, RT55Ma1x, RT30Ma4x,

Table 6.2 – Monsoon indices

Age	Simulation name	Monsoon SI	Monsoon SI (masked over the continent)	MSW
0Ma	RT0Ma1x	33.68	78.85	6.155
15Ma	RT15Ma1x	28.20	61.33	6.545
30Ma	RT30Ma1x	25.46	57.26	4.760
42Ma	RT42Ma1x	28.37	75.20	1.651
55Ma	RT55Ma1x	20.09	49.89	2.242
0Ma	RT0Ma4x	18.16	67.61	4.558
15Ma	RT15Ma4x	34.98	68.05	2.918
30Ma	RT30Ma4x	35.38	81.33	4.545
42Ma	RT42Ma4x	33.63	83.93	2.281
55Ma	RT55Ma4x	20.03	65.08	2.754
0Ma	FE0Ma1x	40.5	70.50	1.856
15Ma	FE15Ma1x	21.24	21.65	1.416
30Ma	FE30Ma1x	27.88	61.11	0.011
42Ma	FE42Ma1x	33.34	76.85	0.043
55Ma	FE55Ma1x	15.88	57.26	1.258

RT42Ma4x, RT55Ma4x show the lowest seasonality in zonal winds directions (Figure 6.3 B).

Monsoon strength

WYI indices indicate the strongest monsoon for RT0Ma1x, RT15Ma1x and RT30Ma1x simulations, while for RT42Ma1x and RT55Ma1x this parameter shows the lowest variability (Figure 6.3 D). MSW is also the highest for the RT0Ma1x, RT15Ma1x simulations (Table 6.2). For RT30Ma1x, RT0Ma4x and RT30Ma4x the monsoon strength estimated with this index is also high, while it is the smallest for FE30Ma1x and FE42Ma1x simulations (Table 6.2).

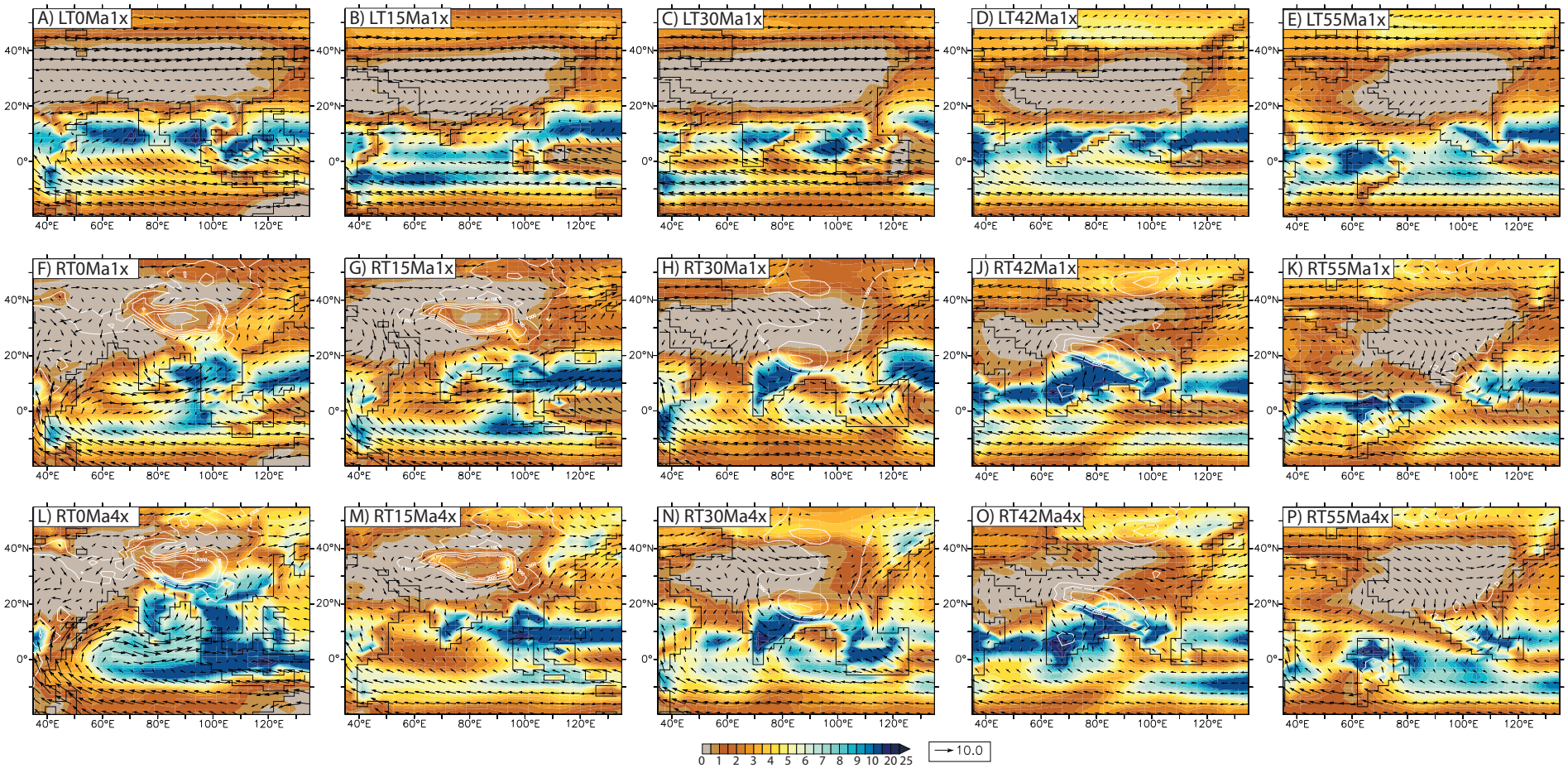

Figure 6.1 – MJJAS averaged precipitation amount and 850 hPa winds for 3 groups of experiments: A,B,C,D,E) with reduced topography, F,G,H,J,K) 1x, L,M,N,O,P) 4x and for time periods corresponding to A,F,L) 0 Ma B,G,M) 15Ma, C,H,N) 30Ma, D,J,O) 42Ma, and E,K,P) 55Ma (see the Table 6.1)

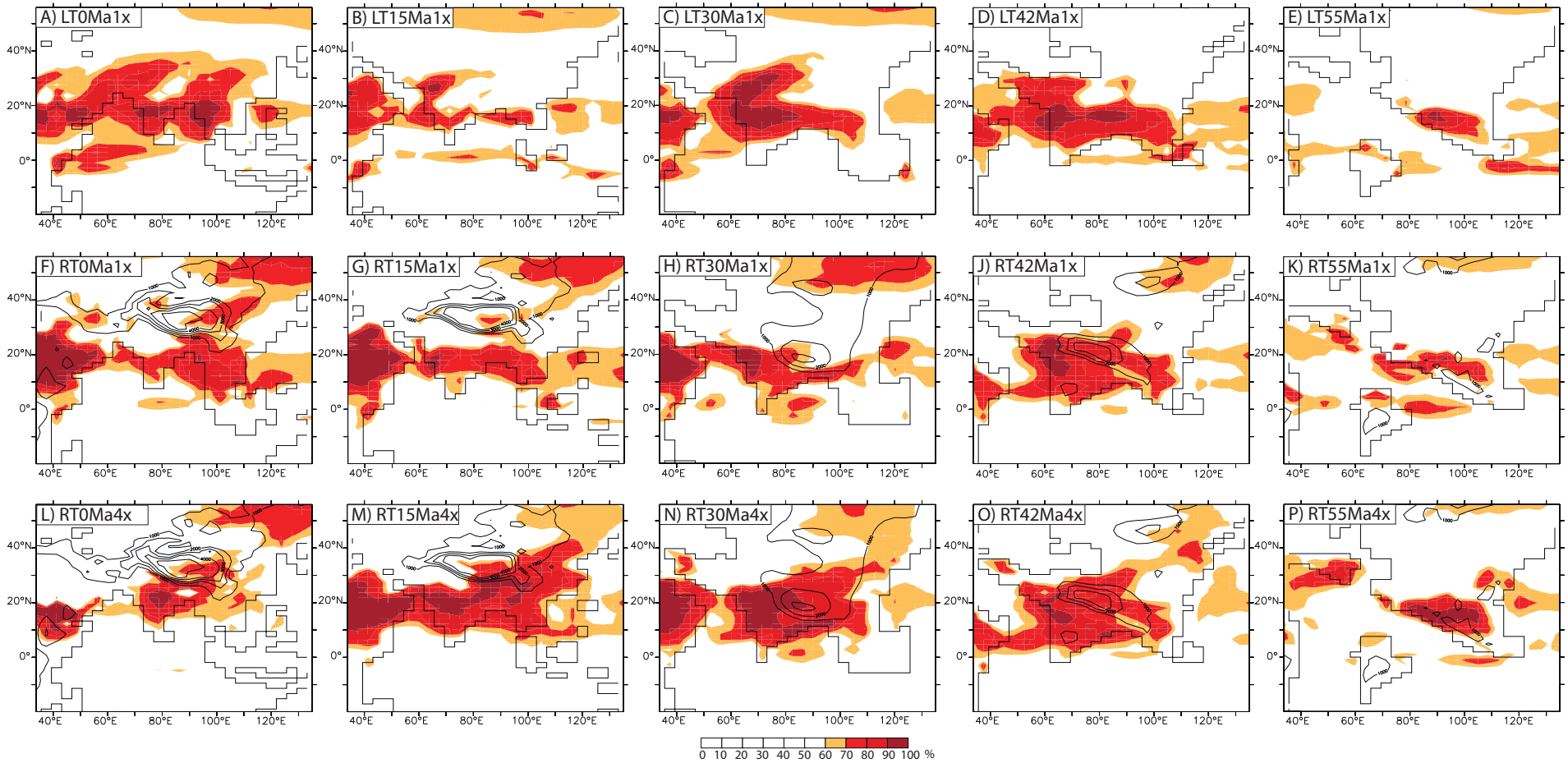

Figure 6.2 – Precipitation seasonality index (SI), which is the percentage of mean annual precipitation falling in the extended summer season (MJJAS) for 3 groups of experiments: A,B,C,D,E) with reduced topography, F,G,H,J,K) 1x, L,M,N,O,P) 4x and for time periods corresponding to A,F,L) 0 Ma B,G,M) 15Ma, C,H,N) 30Ma, D,J,O) 42Ma, and E,K,P) 55Ma (see the Table 6.1). Areas, where the SI is higher than 60% are considered as "monsoon areas".

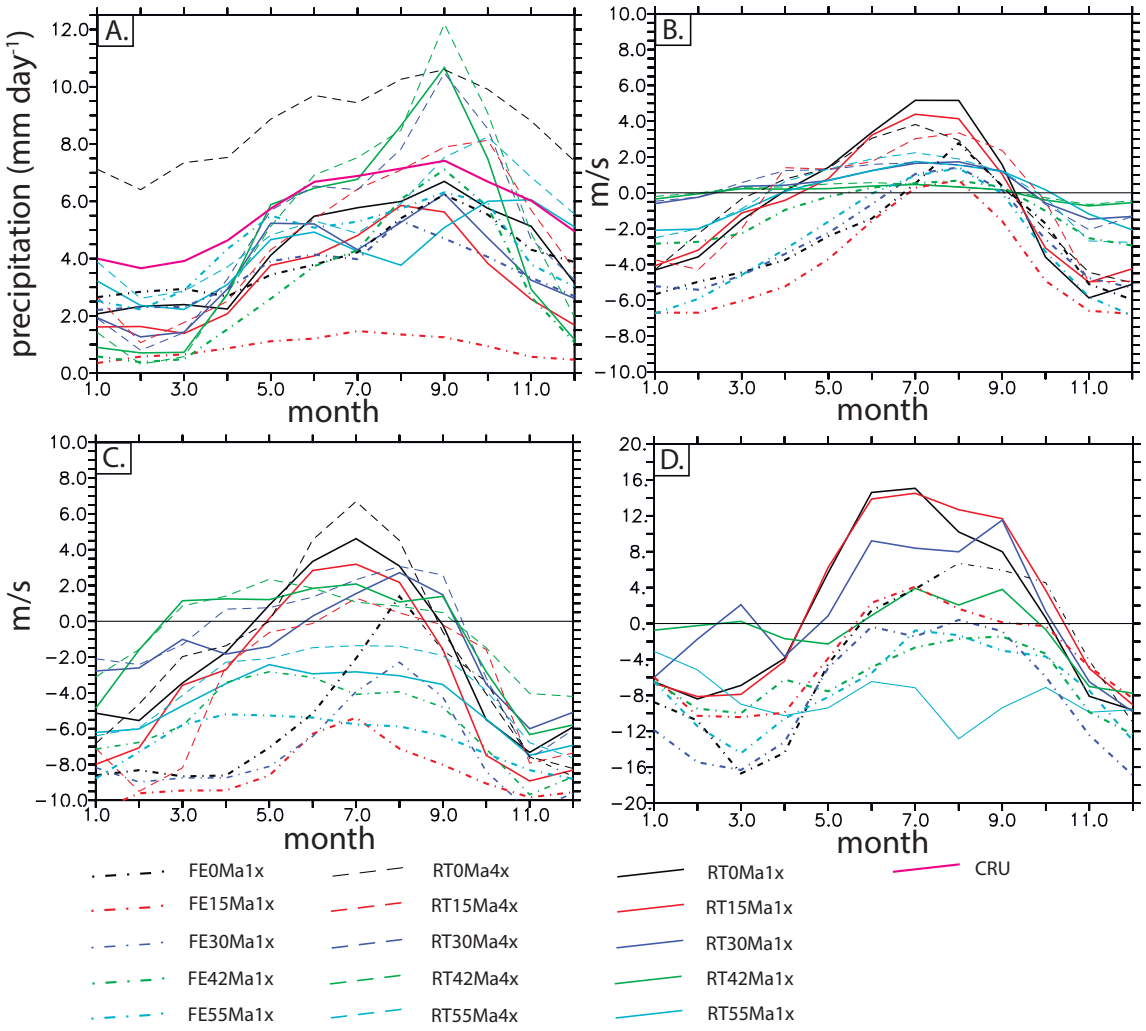

Figure 6.3 – A) Seasonal cycle of precipitation B) seasonal cycle of zonal winds directions C) 850ZWI averaged over a box from 60° to 110° E and from 10° to 20° N, and D) Webster-Yang monsoon index (WYI), averaged over a box from 40° to 110° E and from 0° to 20° N for 3 groups of experiments.

6.4 Discussion

Our results are consistent with recent modeling studies for the Eocene period and new paleoclimate data (Huber and Goldner, 2012; Licht et al., 2014; Roe et al., 2016) in which a monsoon-like circulation over Asian back to ~40 Ma have been found. However, our modeling results show that these early Asian monsoons where much weaker that present-day ones. Our results are also consistent with well-known hypotheses (e.g. Boos and Kuang, 2010; Wu et al., 2015, 2012) that the monsoon circulation over Asia intensifies with the HTP uplift. Here we argue that the monsoon intensification through the Cenozoic is linked not only to the HTP uplift, but also to the northward shift of the Indian subcontinent.

We compare annual precipitation simulated with our numerical experiments with precipitation-seasonality-sensitive sedimentological indicators previously compiled by Parrish et al. (1982) and Ziegler et al. (2003), following a similar comparison provided for the Eocene case by Huber and Goldner (2012). Coal deposits are preferably formed in "ever-wet" conditions, whereas evaporites are closely associated with arid, or seasonally arid conditions (Ziegler et al., 2003). Confrontation of data against the model provides a possibility of qualitative comparison only, because the error bars on proxy estimates of precipitation are large enough and the precipitation biases in models leave much to be desired (Huber and Goldner, 2012).

In general, our model results and reconstructed patterns of precipitation are an about to match for all time periods (Figure 6.5). For the Miocene case, simulated spatial patterns of precipitation show the agreement with the data for RT15Ma1x and RT15Ma4x experiments. For the Miocene experiment with reduced topography, arid conditions are simulated over the northern India, while coals formation over this region for this period of time indicates wet conditions. In addition, for the FT15Ma1x experiment, cumulative precipitation is high at about 40° N, while multiple sites with evaporites are recorded in this region in the Miocene. However, a northward shift of desert regions over the Central Asia, associated with the HTP uplift (in tern, associated with the northward shift of a subsidence zone), is in good agreement with the data (Figure 6.5 B, G, M). This model-data comparison for the Eocene case could be an addition argument to already high Miocene HTP elevations. For all Oligocene and Eocene simulations, cumulative annual precipitation patterns are in a good agreement with the data (Figure 6.5 C, D, E, H, J, K, N, O, P).

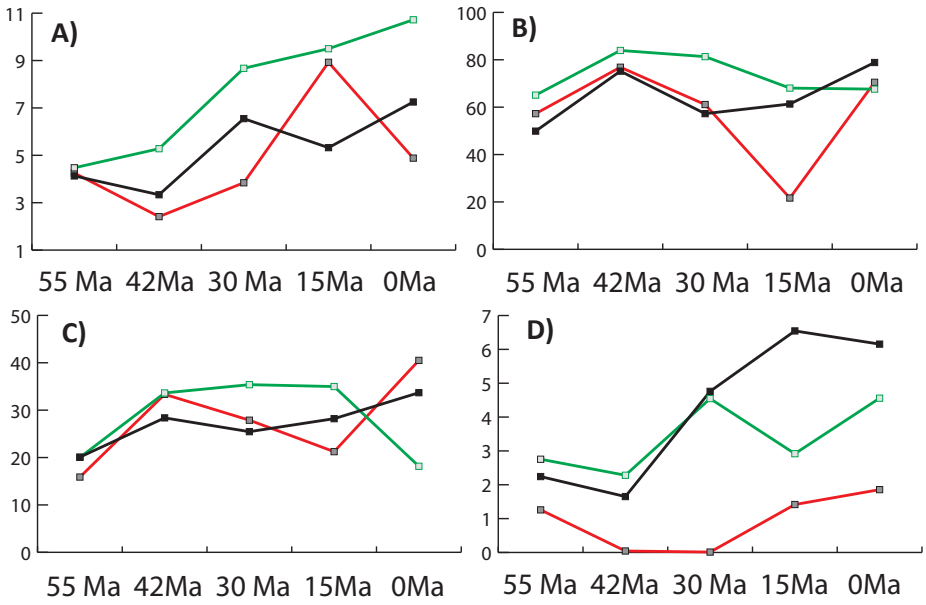

Figure 6.4 – Evolution of IAM in time for 3 groups of experiments: RT1x (green), RT4x (black) and LT1x (red) defined from A) regional ocean-continent temperature gradient, B) percentage of region covered with monsoon (region with the ratio of MJJAS precipitation to annual mean precipitation is greater than 60%), C) percentage of the surface of the region where precipitation is greater then evaporation D) monsoon intensity index (MSW)

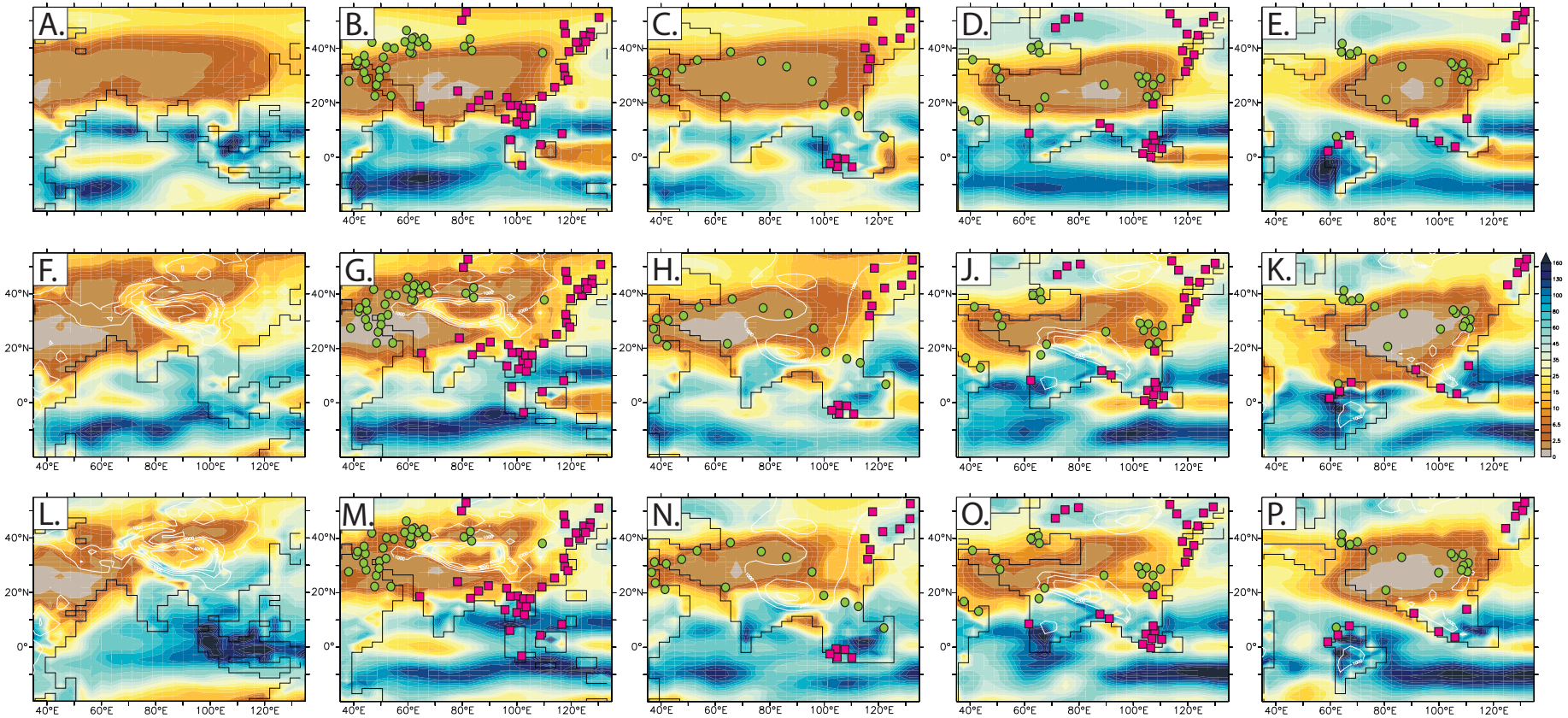

Figure 6.5 – Cumulative annual precipitation for 3 groups of experiments: A,B,C,D,E) with reduced topography, F,G,H,J,K) 1x, L,M,N,O,P) 4x and for time periods corresponding to A,F,L) 0 Ma B,G,M) 15Ma, C,H,N) 30Ma, D,J,O) 42Ma, and E,K,P) 55Ma. Rectangles and circles correspond to distribution of evaporites (green circles), coals and peats (pink circles) from Parrish et al. (1982); Ziegler et al. (2003). Star show palinological data site from (Tang et al., 2011).

6.5 Summary

- Monsoon-like patterns and wide-spread arid conditions are simulated for all paleogergaphies uses, all elevation scenarios and both high and low pCO_2 concentrations;
- There are highly seasonal precipitation patterns over Asia for all experiments. On the contrary, the spatial position of such patterns changes depending on the boundary conditions used;
- The seasonal circle is strong for almost all simulation with an exception of LT15Ma1x experiment, where even summer precipitation is very low, and RT0Ma4x experiment, where precipitation is extremely strong all the year round;
- Maximum of precipitation for most simulations is August-September-October that is in a good agreement with CRU dataset. Seasonality weaker for all paleogeographies when the topography is reduced, but it does not disappear completely;
- For 0 Ma and 15 Ma monsoonal area are the most sensitive to the change of all parameters tested;
- In general, simulations show a good agreement with distribution of climate-sensitive sediments

Chapter 7

General conclusions and perspectives

In this final chapter we synthesize the results of 3 years of our work on the project. In summary form we present our main conclusions and discuss them in wider context. We also review uncertainties, limits and caveats of this study that are mainly associated with the physical processes represented in the numerical models used and with the boundary conditions applied for the numerical simulations (Section 7.1). Advances in our research allow us to suggest directions for further investigations and possible ways for application of our results in future studies (Section 7.2).

Contents

7.1 Conclusions

In this study, first of all, we show that the $\delta^{18}O_p$-elevation relationship is spatially inhomogeneous. We highlight the importance of using different isotopic lapse rates for various regions of the Tibetan Plateau and Himalayas. Water tagging capabilities help to quantify the contribution of different evaporation sources to the hydrological budget on the Himalayas and Tibetan Plateau and thus to determine the initial condition for the Rayleigh distillation. Comparison of our results with published data reveals possible underestimation of Eocene elevation of the Tibetan Plateau up to 1200 meters that could be a significant argument in the debate around the early Cenozoic "high" Tibetan Plateau.

Further, deeper investigations show that the isotopic composition of precipitation is very sensitive to climate changes related to the growth of the Himalayas and Tibetan Plateau. Topography is shown to be not an exclusive controlling $\delta^{18}O_p$ factor. The relative contribution of other-than-topography controlling factors and their magnitude differs depending on the uplift stage and the region considered. Notably, we show that changes in relative humidity, precipitation amount and post-condensation processes over Asia has considerable impact of $\delta^{18}O_p$, however such an influence greatly depends on the stage of uplift of the HTP. We highlight that future paleoaltimetry studies should take into account constraints on climatic factors to avoid misestimating ancient altitudes.

When more realistic experiments (with varied paleogepgraphy and pCO_2) have been established, our modeling results show a significant influence of paleogeography changes on the Asian climate and $\delta^{18}O_p$. Our simulations with Eocene boundary conditions suggest that topography change has a minor impact on HTP $\delta^{18}O_p$. On the contrary, Eocene $\delta^{18}O_p$ is primarily controlled by the atmosphere circulation and global temperature changes. Based on our numerical experiments, we show that despite persistence of large-scale atmospheric flows such as the monsoons and westerlies, Eocene $\delta^{18}O_p$ over the HTP region is different from those of the present-day due to global higher temperatures, southward shift to a zone of strong convection and increased role of westerlies moisture source. We show that the Rayleigh distillation is not applicable for the Eocene Himalayas and conclude that the assumption about the stationarity of $\delta^{18}O$-elevation relationship through geological time is inaccurate and misleading paleoelevation estimates.

A strong dependency of $\delta^{18}O_p$ on local surface temperatures, which, in turn, depends on the elevation, makes the choice of carbonate formation temperature crucial. Our Eocene modeling demonstrates that temperatures used in Eocene paleoelevation studies are likely underestimated, resulting in a prediction of high Eocene elevation of the HTP. We deduce that carbonates $\delta^{18}O_p$ are primarily recording large-scale atmospheric circulation and local temperature. Our simulations highlight the limit of standard atmospheric distillation models when they are applied to deep paleo.

Our climate simulations show that the retreat of the Paratethys ocean, the changes in latitudinal position of India, and the height of the Tibetan Plateau control precipitation patterns over Asia and cause the monsoon variability over Asia. Aridity patterns persist through all the Cenozoic, however, lateral extent of deserts is controlled by topography, paleogeography and CO_2 concentration.

The results of our study allow us to provide some suggestions for improving paleoal-

timetry estimates of the HTP. First, we conclude that present-day $\delta^{18}O$-elevation gradient established for the Himalayas is not valid for other regions of the HTP. We suggest using GCMs in addition to measurement of the surface waters $\delta^{18}O$ in order to access spatial variability of the isotopic lapse rates. More importantly, we show that present-day isotopic lapse rates are not valid for the early times of the HTP. Isotopes-enabled GCMs provides a unique opportunity to obtain an idea on paleo $\delta^{18}O_p$ distribution for specified boundary conditions for deep paleo. On the other hand, acquirement of new data on paleo $\delta^{18}O_c$ requires physical bases for their interpretation. For this purpose we insist using modeling approach in order to avoid considerable errors in data interpretation. However, climate modeling method that is used in this study has its own limitation that we discuss in the next section.

Our results allude to the necessity of reinterpretation of $\delta^{18}O$ available from multiple published sources given the results of numerical simulations enabled with the isotopes. Such reinterpretation may have consequences for understanding climate and geodynamical evolution of the HTP both. Summing up, our research appeals to a broad community of geochemists, climatologists, but also to geologists and geophysicists interesting in elevation history of mountains belts as well as geodynamical evolution of the Himalayan collision.

7.1.1 Uncertainties, limits and caveats of this study

In this study we use climate modeling approach and comparison of models results with the proxy data. We are aware that this technique has its limitations and should be applied with caution on those restrictions. Modeling uncertainties arise from fundamental choices made when a GCM is build - physical processes parameterization, grid resolution, and from further choice of initial and boundary conditions. In addition, data used in our study for model-data comparison brings its own uncertainty.

Uncertainties linked with the processes representation in the model

In this study we use the AGCMs, in other words, the oceanic circulation is not presented in these models. A method of the model forcing with the SSTs (for more details see the Section 2.3.5) allows us to save some computation time, but brings an additional uncertainty to the choice of the SSTs. Besides this, first order uncertainties of our modeling approach are associated with the physical parametrization of climatic and isotopic processes represented in the models used. Key uncertainties are linked to the clouds parametrization, atmospheric convection, terrestrial surface processes representation and the isotopic exchange between the vapor and the rain.

In our work we show that the clouds cover may impact the $\delta^{18}O$ in order of magnitude of 2 ‰, through the modification of the radiative and water budgets. However, clouds parameterization is known to be complex in GCMs (Rio and Hourdin, 2015). In our study we use a default version of the clouds scheme (the Emanuel's scheme) (Hourdin et al., 2006) and we are aware that the improvements in the clouds representation may impact modeled isotopic distribution. For example, using of thermal plume model for the con-

vective boundary layer (Rio and Hourdin, 2015) may improve the boundary layer representation, particularly its progressive deepening during the day and the associated near-surface drying. Alternatively, using "super-parameterized" GCMs (e.g. Li et al., 2012) may allow to better reproduce the convection and clouds. The approach involves applying a two-dimensional cloud-resolving model in each column of a three-dimensional large-scale model, that constantly interact with the large-scale dynamics (Grabowski, 2001). However, this technique requires increased computation capabilities.

In the tropics, the convective process is known to have a significant imprint on the stable oxygen isotopes composition of precipitation (for example, through the amount effect) (Risi et al., 2008). However, the convective processes in a GCM depends on the parameterization applied. The LMDZ version 4 uses the Emanuel's convection scheme that was shown to be reasonable in terms of representation of modern convective processes (Hourdin et al., 2006). However, the known issue of this parameterization is an overestimated precipitation amount over the elevated topography (topography picks) and underestimated precipitation on the topography foothills (Francis Codron and Camille Risi, personal communication). This issue is translated in the precipitation field simulated in our experiments at least for the pre-industrial simulation (for example, see Figure 3.6 A, B) In order to avoid this limitation, we suggest using multi-models approach (models intercomparison) or tuning the orographic precipitation in LMDZ.

The surface processes representation in the model brings an addition source of uncertainties. We run the model version where the soil moisture is represented as a single reservoir (called "bucket" scheme). This simplified version of the surface hydrology does not allow the distinction between evaporation and transpiration. An absence of realistic multi-level soil moisture schemes has an evident impact on representation of the continental moisture recycling and, thus, on the water stable isotopes in the hydrological cycle.

In addition, in the model version we use, the vegetation evolution is not solved explicitly, instead we use the vegetation distribution as a boundary condition (see Section 2.3.5). However, terrestrial vegetation cover has a potential impact on stable oxygen isotopes through modifying the surface albedo and thus the energy balance from one hand and through the evapotranspiration variations from the other. In order to reduce the uncertainty linked with the simplified representation of the surface processes and in order to estimate the order of magnitude of this uncertainty LMDZ-iso should be coupled to the ORCHIDEE land Surface Model of IPSL. However, this coupling increases exponentially the computation time and was not possible in the framework of this thesis.

A large uncertainty in the representation of water stable isotopes in GCMs and in LMDZ-iso in particular, is linked to the parametrization of the isotopic exchanges between vapor and rain droplets during their way to the surface and their partial reevaporation (Lee and Fung, 2008; Risi et al., 2010). In LMDZ-iso, the relative effect of raindrop evaporation rely on a tunable parameter ϕ, controlling the relative humidity at the droplet contact (RH_c), and thus the intensity of kinetic effects (Risi et al., 2010): $RH_c = \phi + (1-\phi)\cdot h$, where h is the relative humidity of the vapor reservoir in which droplets reevaporate.

Risi et al. (2010) show that the modeling results are very sensitive to this parameter, especially in dry regions where the reevaporation is strong. In LMDZ-iso ϕ is set to 0.9 Bony et al. (2008). Risi et al. (2010) also indicate that if the coefficient ϕ is set to 0, the

amount effect becomes stronger and the raindrop evaporation lower. In addition, the isotopic equilibration time of raindrops is drop-size dependent, with smaller equilibration time for small raindrops (Lee and Fung, 2008), but, in the current version of LMDZ-iso the raindrops size is not taken into account, that may results in underestimation of equilibration time for heavy rains with big raindrops. In further versions of LMDZ-iso the parametrization of rain drop size should be added and modern and paleo climate experiments should be set for testing the sensitivity of $\delta^{18}O$ distribution (especially in arid condition) to the variations of rain drop size.

Uncertainties linked with the model resolution

In this study we use LMDZ in different resolutions (see Section 2.3.3), with a minimum size of cell obtained with a zoomed grid of ~50 km. This resolution obtained for the Asian region can be considered as very high, given modern computation resources and use of a GCM and not a regional model. However, relief peculiarities such as narrow valleys or high mountain pick could not be presented in this grid configuration but have possible impact on the hydrological cycle through exchanging the air masses trajectories. In addition, model-data comparison should be applied with caution, because in this case we compare data in a point with simulated variable *de facto* averaged on a 50 x 50 km area. In order to avoid this limitation, statistic downscaling methods should be applied to the model outputs.

Uncertainties linked with the boundary condition used

Another group of uncertainties is associated with the boundary condition we use for our paleo experiments (see Section 2.4). Except for the uncertainty linked to the choice of the SSTs that we discussed earlier, important limitations of paleomodeling approach are linked to the paleogepgraphies reconstructions used. Unfortunately, today consistent paleogeographies for the Cenozoic that could be used for climate modeling are lacking. For example, for paleogeographies used in this thesis, a large uncertainty is linked not only to the mountains elevations, but also to the land-sea distribution (uncertainty in the sea-lave), continental shelf extensions, ocean floor bathymetry (especially over areas where simple time-depth relationship is not applicable) and even to the latitudinal position of continents (e.g. India) which is associated to recent improvements in paleomagnetic data. Further scientific efforts should be concentrated on creation of paleogeographical global maps sets that covers the whole Phanerozoic and where the latest paleomagnetic, sedimentological and paleoaltimetry data are incorporated.

Some projects are working on the improvement of present-day lack of consistent paleogeographical sets, for example, PALEOMAP project of Christoper Scotese (see http://www.scotese.com) or Deep Time Maps™ Paleogeography (paleogeographic maps produced by Colorado Plateau Geosystems, Inc.) (see https://deeptimemaps.com). However, these paleogeographies, besides some questionable decisions (e.g. elevation of major orogens, sea-surface level that is linked with sea-land distribution, accretion timing of the volcanic arcs in the Tethyan belt and so on), brings some technical difficulties associated with adaptation of these kind of maps for numerical simulation. A new technical

approach has been proposed recently for paleogeographies reconstructions by Baatsen et al. (2016), that is based on the use of depth-age relationships for oceanic crust together with adjusted present-day topography and allows to create Cenozoic paleogeographies suitable for climate simulations. Authors indicate that this approach gives a first estimate of the global geography at a chosen time frame. However, the resulting maps need to be editing manually taking into account the geological data.

Uncertainties linked with the data used for the comparison

In a conclusion we want to stress that not only the modeling approach brings different uncertainties to the results of our study, but also the data from the natural archives should be considered with a caution. First of all, a large uncertainty is linked to the dating of paleocarbonate samples. Second, alteration processes may completely overprint the initial isotopic record. In the case of visible evidences of alteration, the data should not be used for isotopic studies. However, altered samples sometimes have been used by some authors (e.g. Kent-Corson et al., 2009) under the pretext of climate changes tracing. The results of these measurements should be considered with additional caution.

For the precipitation data that are used for the model validation a caution should be also applied, because the samples were not collected every day and might thus not be representative of monthly averages, given the significant variability observed in the vapor at the daily time scale.

Finally, we want to discuss the uncertainty linked with the choice of carbonate formation temperatures. It is commonly assumed that pedogenic carbonates are forming during the summer period (Quade et al., 2013), however few works are available on this subject. Some questions are arising: is the carbonates formation period the same for warmer (e.g. Eocene) climates? Is there a kind of "closing" temperature above/below which the carbonates are not forming? In this case, what is the threshold? Answering these questions is crucial for relevant reconstruction of $\delta^{18}O_p$ $\delta^{18}O_c$ and thus paleoelevation estimates.

7.2 Perspectives

7.2.1 Short-term perspectives

Review of the recent progress in the surface elevation reconstruction of the HTP through the Cenozoic and its reinterpretation taking into account our modeling results

In the introductory chapter we provide a compilation of available paleoaltimetry studies for the HTP which are based on different proxies including stable oxygen isotopes evidences, paleobotanical data, biomarkers and others (see Section 1.3.6). To our knowledge, today there are no published works that summarize the elevation history of the HTP using all available data. For example, in the work of Rowley and Garzione (2007) the Cenozoic elevation scenario of the HTP has been suggested using only 6 published quantitative estimates. Jiang et al. (2015) provide a summary of 23 studies in a form of a table, but the

discussion is lacking. Form the other hand, the results of our study shows that the $\delta^{18}O_c$ measure from the natural archives is not only a record of the surface elevation, like it was hypothesized before, thus this measurements should be reinterpreted taking into account the climatic imprint on $\delta^{18}O_c$. A comprehensive review of the elevation history of the HTP may become a logic accomplishment of this thesis.

Study of the contribution of the Paratethys See retreat to the isotopic composition of the HTP

In this study we have used paleogeographies where a large Paratethys Sea is presented. In this manuscript we discuss several times the role of the Paratethys Sea retreat of Asian climate. Despite the Eocene experiment with "closed" Paratethys (Section 4.4.2), the contribution of moisture that evaporates over the Paratethys to the hydrological budget of the HTP is still barely estimated. In order to estimate this contribution, additional experiments should be set. We suggest following experiment design: sea water $\delta^{18}O$ should be increased locally over the Paratethys Sea. A comparison of simulated $\delta^{18}O$ over the HTP of such an experiment with control experiment outputs may show if Paratethys moisture contributes to the isotopic shift over Asia or not.

Study of the impact of the latitudinal position of India to the isotopic composition of precipitation

One of the main conclusions of the Chapter 4 is that the southward position of the HTP for the Early Cenozoic brings the region of interest to the convection zone that results in more enriched $\delta^{18}O$. However, available paleogeography reconstructions do not allow follow the impact of gradual shift of the India and the HTP northward during the collision between India and Asia. A discussion of the results of our experiments with Christopher Poulsen, encouraged us to provide additional sensitivity experiments with artificially changed position of the India continent and the HTP. These experiments could become a nice illustration of the impact of convection/subsidence zones position to the isotopic composition over elevated topography.

Vegetation reconstructions through the Cenozoic and implications for biodiversification

Major biodiversification events, hot spots generation and evolutionary transitions (e.g. C3/C4 transition) that took place during the Cenozoic over Asia are reconstructed using different evidences (Favre et al., 2014; Wen et al., 2014). However, their causes are poorly understood. Some hypotheses indicate that besides global temperature changes (associated with CO_2 drop), the uplift of major orogens (including the HTP) through the Cenozoic as well as continents movements may have contributed to this biodiversification (Favre et al., 2014). Multiple paleo-archives allowed to reconstruct paleo-vegetation changes through the Cenozoic, however a consistent history is lacking. Monsoon changes are also extremely important (Favre et al., 2014), since the changes of the hydrological cycle, in particular, the precipitation seasonality variations have direct impact on plants.

Implication of climate models with interactive vegetation modules may also allow to infer the vegetation changes at various time scale consistent with the simulated climate variations. A modeling approach may help to provide a new global database of the potential vegetation and to entail many prospects in paleoclimatology.

During this thesis we have run LPJ vegetation model in order to create realistic boundary conditions for our paleo experiments. However, these results have never been analyzed as an independent topic. A first step forward has been undertaken by Inès Mangolte during her internship at LSCE. Based on our FOAM and LMDZ simulation presented in Chapter 6, she has studied the linkage between the monsoon onset during the Cenozoic and associated vegetation response.

Apart from this, based on our Cenozoic climate simulations we have built vegetation maps using Köppen-Geiger climate classification (Peel et al., 2007) (Figure 7.1). Southward shift of the Tibetan Plateau in the early Cenozoic together with higher CO_2 concentrations results in predominance of temperate and savannah vegetation over the Tibet. Highly seasonal precipitation is simulated for all studied time periods over the southern Asia and India that results in wide distribution of monsoon and rainforest vegetation. However, a deep analysis of this paleovegetation distribution is out of scope of this present study and may be a subject of future research. In addition we may suggest providing independent simulation with the interactive vegetation simulations using the same boundary conditions as in this study in order to compare the results of the both techniques.

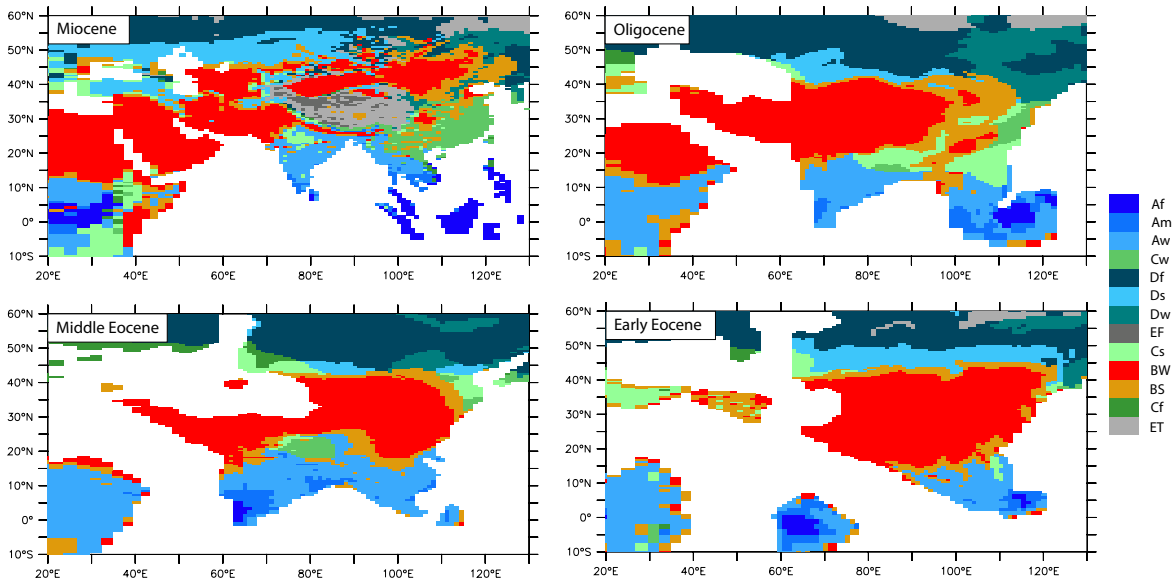

Figure 7.1 – Preliminary results of paleovegatation modeling (of-line, based on LMDZ-iso outputs) using Köppen-Geiger climate classification (Peel et al., 2007). Climate symbols used in the legend: ET - tundra; Cf - Temparate without dry season; BS - steppe; BW - Desert; Cs - temperate with dry summer; EF - frost; Dw - cold with dry winter; Ds - cold with dry summer; Df - cold without dry season; Cw - cold with dry winter; Aw - savannah; Am - monsoon; Af - rainforest. For detail description of Köppen climate definition criteria see Peel et al. (2007).

Modeling of climate and stable oxygen isotopes in Miocene

In this thesis we have presented climate model experiments with boundary conditions for whole Cenozoic period. However, a detailed analysis and full model-data comparison has been applied for the Eocene period only.

Miocene is the period in Cenozoic that started ~ 23 Myr and finished ~ 5 Myr. Number of preserved evidences of paleoelevations increases for more recent time periods and a lot of (about 30 measurements from different publications) Miocene paleoelevations estimates from geological, paleontological, and of course, from carbonate $\delta^{18}O$ are available. However, despite high abundance of paleoelevations evidences, consistent history of HTP uplift in the Miocene is lacking and paleoelevation estimates ranging from 1000 - 1500 m (Chen et al., 2002; Hoke et al., 2014; Murphy et al., 2009) to > 5000 m (e.g. Currie et al., 2016) (see Section 1.3.6).

In current study we reconstruct Miocene climates and stable isotopes in precipitation using only one paleogeography reconstruction. Results of additional simulations (with multiple paleogeographical and topographical scenarios) confronted against available carbonate archives may help to quantitatively reconstruct the Miocene HTP topography elevation and, consequently may have implications for reinterpretation of climatic and geodynamical evolution over the region.

7.2.2 Long-term perspectives

Paleogeographical maps building

In this work we have used the paleogeography maps for several time periods through the Cenozoic, that comes from different authors and, thus, does not provide consistent evolution of the continents configuration and topography elevation (see Section 7.1.1). In addition, the time step between the paleogeographies used is too big. Today few sets of paleogeographical maps are open for scientific non-commercial use and even fewer are adopted for climate modeling needs. However, paleomodeling community needs modern reconstructions that incorporates geological data acquired during the last years, since the paleogeography appears to be a crucial factor controlling paleoclimate.

The impact of HTP uplift on oceanic circulation and ocean - atmosphere feedback

Uplift of major orogens, such as the Andes, has been shown to impact oceanic circulation (e.g. Sepulchre et al., 2009a). However, with few exceptions (e.g. studies of Abe et al., 2003; Kitoh, 2004), the influence of HTP uplift on oceanic circulation, sea surface temperature and ocean-atmosphere feedback is unknown. Recently, a modeling effort has been undertaken by our colleagues (Baohuang et al. in prep.) from Key Laboratory of Cenozoic Geology and Environment (China) to investigate the linkage between HTP uplift and meridional overturning circulation (MOC) in the North Atlantic and North Pacific oceans. For this purpose these authors use ocean-atmosphere GCM (the work is in preparation for a publication). However, in this study present-day geography with varied HTP topography has been used. Here we stress a necessity of realistic paleogeographies in such kind of

works in order to better constrain oceanic circulation through the past, that may become a subject of our further investigations. Moreover, in order to avoid model-dependent estimates, models intercomparison approaches should be applied.

Paleo-monsoon reconstructions using multiple high-resolution models

Modeling of the monsoons systems is known to be dependent on representation of the atmospheric dynamics and the hydrological cycle in a particular model (Kripalani et al., 2007). Our current research may be completed by intercomparison of outputs of different models. In these models high-resolution (at least over Asia) may allow more representative comparison with different geological records on the monsoonal signal.

Modeling of hydrogen isotopes in precipitation and deuterium excess

The deuterium excess (or d-excess), defined by d(‰) ≡ δ^2H - 8 · δ^{18}O (Dansgaard, 1964), where δ^2H and δ^{18}O are deuterium and oxygen-18 composition of water. The climatological significance of the deuterium excess parameter for tracing precipitation processes is very high as it reflects the prevailing conditions during evolution and mixing of air masses *en route* to the precipitation site (Benetti et al., 2014; Froehlich et al., 2001). d-excess of paleo precipitation can be inferred from leaf wax, which persists in sediments over geological timescales and has been measured in modern studies over Asian region (e.g. van der Veen et al., 2015; Zhuang et al., 2014). LMDZ-iso allows tracing the stable hydrogen isotopes in a hydrological cycle and to investigate the physical basics for the controlling factors of hydrogen isotopes in paleoprecipitation. We do not trace δD in our simulations in order to reduce the computation time, however, such simulations together with model-data comparison approach may be promising as may provide additional instrument to infer the moisture source conditions (Benetti et al., 2014; Pfahl and Sodemann, 2014) and the continental recycling rate (Liu et al., 2008).

Cenozoic erosion rate modeling using GCM-generated precipitation patterns and creation of "Fully Coupled Earth System Models"

Erosion is a crucial link between internal geodynamics and climate. However, long term (> 1 Ma) erosion rates remain poorly constrained (e.g. Charreau et al., 2011; Molnar, 2004). Climate (e.g. precipitation rate) is an important element for understanding paleo erosion rate and thus, paleoclimate reconstructions are indispensable for erosion modeling. In this thesis we have shown how the uplift of vast mountain belts like the HTP as well as changes in paleogeography and atmospheric CO_2 concentration have an impact on atmospheric dynamics and precipitation patters. Precipitation rates over the Asian region have been significantly changed through the Cenozoic. We may suggest two possible solutions for relating paleoprecipitation rates and the erosion rates through the Cenozoic, that may shade some light to the uplift rates of major orogens consistent to the climate evolution:

- Using of precipitation rate patterns generated with high resolution global climate models as external forcings for erosion models in order to reproduce realistic ero-

sion through time. For this purpose the simulation that we have already done may be used as well as additional simulations with various boundary conditions;

- Creation of "Fully Coupled Earth System Models" - a new types of models, that couple solid Earth dynamics model (e.g. visco-elasto-plastic code of Taras Gerya (Gerya, 2010)), landscape models (exhumation and erosion rate model of Jean Braun (Braun, 2003)) and a climate model (probably a simplified version). Such models should become a powerful instrument for studding the interactions between the solid Earth and the climate. However, several caveats of such approach are evident. First, different time scales of acting of geological and climatic processes may have result in either increase in computation time or simplification of several components (it depends on what component the focus will be done). Second, the vertical scale of the Earth interior is several times larger than the vertical scale of the atmosphere. Finally, such models may be very expensive in terms of computation time.

General perspectives

Methodology developed in this study with an example of the HTP, may be applied for other major orogens all over the world. For example, it can be used for revealing the main controls of $\delta^{18}O$ over Andes, Cordillera Mountains, Caucasus, etc. and together with model-data approach may significantly contribute to understanding of the vertical movements of the Earth surface. Finally, paleoclimate simulation presented in this thesis are global and may be used for studying the global monsoon as well as other regional monsoon systems.

List of Acronyms

850ZWI 850-hPa zonal wind index. 195, 201

AGCM atmosphere general circulation model. 57, 58, 60, 61, 62, 65, 71, 83, 121, 193, 194, 209, 227

ANL Argonne National Laboratory. 62

BNS Bangong-Nujiang Suture. 19, 20

CAM Community Atmosphere Model. 60, 61, 121

CCM2 Community Climate Model version 2. 62

CCM3 Community Climate Model version 3. 62

CESM Community Earth System model. 62

CGCM couple general circulation model. 57

CMIP Coupled Model Intercomparison Project. 63

CRU Climate Research Unit. 197

CSIM2.2.6 Community Sea Ice Model version 2.2.6. 62

EBM Energy balance model. 56

ECHAM European Centre Hamburg Model. 60, 61

EMIC Earth system Models of Intermediate Complexity. 57, 60

FOAM Fast Ocean Atmosphere Model. xii, xiv, 12, 62, 63, 65, 66, 71, 122, 147, 189, 194, 214

GCM general circulation model. 5, 7, 9, 12, 14, 29, 49, 55, 56, 57, 58, 60, 61, 62, 63, 64, 78, 80, 81, 115, 121, 122, 124, 153, 154, 188, 189, 195, 208, 209, 210, 211, 215, 223

GENESIS Global Environmental and Ecological Simulation of Interactive Systems. 60, 61, 121

GFDL Geophysical Fluid Dynamics Laboratory. 62

GISS Goddard Institute for space studies. 60, 61

GNIP Global Network of Isotopes in Precipitation. 31, 32, 81, 122, 123, 223

GSM Global Spectral Model. 60, 61

HadCM3 Hadley Centre Coupled Climate Model, version 3. 60, 61

HKT Himalaya-Karakoram-Tibetan. iii

HOWI hydrological onset and withdrawal index. 195

HPT l'Himalaya et le plateau tibétain. xi, xii, xiii

HTP Himalayas and Tibetan Plateau. ix, 1, 2, 3, 5, 8, 9, 10, 14, 15, 16, 17, 20, 36, 37, 38, 39, 40, 37, 46, 47, 64, 65, 66, 69, 70, 75, 76, 78, 79, 80, 81, 82, 83, 85, 116, 117, 119, 122, 124, 125, 126, 129, 130, 146, 147, 148, 151, 152, 153, 154, 155, 188, 189, 191, 192, 193, 196, 197, 202, 208, 209, 212, 213, 215, 216, 217, 223, 224, 227

IAEA International Atomic Energy Agency. 31, 81, 122

IAM Indo-Asian monsoon. 191, 193, 202, 226

IPCC Intergovernmental Panel on Climate Change. 51

IPSL Institute Pierre Simon Laplace. 63, 210

ITCZ Intertropical Convergence Zone. 197

iTECC Investigating Tectonism Erosion Climate Couplings. iii

ITS Indus-Tsangpo Suture. 19

JS Jinshajiang Suture. 19

LGM Last Glacial Maximum. 61, 65

LIPs Large Igneous Provinces. 13

LMD Laboratoire de Météorologie Dynamique. 60, 61, 63, 193, 194

LMDZ Laboratoire de Météorologie Dynamique, zoomed. vi, xii, xiv, 49, 60, 63, 64, 65, 66, 71, 189, 193, 194, 210, 211, 214, 227

LMDZ-iso Laboratoire de Météorologie Dynamique, zoomed, isotopic version. ix, xii, xiii, 58, 61, 64, 65, 71, 83, 115, 117, 122, 123, 124, 147, 150, 151, 153, 154, 188, 210, 214, 216, 224

LPJ Lund-Potsdam-Jena dynamic global vegetation model. xii, xiv, 63, 65, 66, 71, 147, 189, 214

LSCE Laboratoire des Sciences du Climat et de l'Environnement. iii, 214

MAT mean annual temperature. 28, 34

MBT Main Boundary Thrust. 18, 19

MCT Main Central Thrust. 18, 19

MIROC 3.2 Model for Interdisciplanery Research on Climate, version 3.2. 61

MJJAS May-June-July-August-September. 122, 123, 124, 126, 128, 129, 146, 150, 151, 195, 196, 199, 200, 202, 224, 225

MOC meridional overturning circulation. 9, 215

MOM Modular Ocean Model. 62

MSW monsoon intensity index. 196, 198, 202

MUGCM Melbourne University General Circulation Model. 60, 61

NCAR National Center for Atmospheric Research. 60, 62

OGCM ocean general circulation model. 57

ORNL Oak Ridge National Laboratory. 62

PCCM2 Parallel Community Climate Model version 2. 62

PCCM3-UW Parallel Community Climate Model version 3 - University of Wisconsin. 62

PDB Pee Dee Belemnite. 29

PFT plant functional type. 63, 66

POP Parallel Ocean Program. 62

RCM Radiative-convective model. 56, 57

REMO-iso Regional Model, isotopic version. 60, 121

RH relative humidity. 79

SI seasonality index. 195, 197, 198, 200, 226

SMOW Standard Mean Ocean Water. 29

SST sea surface temperature. vii, xiv, 9, 12, 15, 62, 65, 80, 83, 119, 121, 146, 147, 193, 194, 209, 211

STDS South Tibetan Detachment System. 18, 19

SWI stable water isotopes. 3, 29, 49, 58, 60, 61, 71, 121, 153

TES Tropospheric Emission Spectrometer. 32

TP Tibetan Plateau. 6, 7, 15, 21, 20, 27, 36, 38, 39, 40, 70, 75, 77, 78, 79, 81, 82, 115, 122, 126

UVI 850-hPa zonal and meridional wind index. 195

WMO World Meteorological Organization. 31, 51

WYI Webster-Yang monsoon index. 196, 198, 201

List of Figures

List of Tables

Publications

This is a list of publications, oral and poster presentation realised during this PhD:

Articles

- **Botsyun, S.**, P. Sepulchre, C. Risi, and Y. Donnadieu (2016), Impacts of Tibetan Plateau uplift on atmospheric dynamics and associated precipitation $\delta^{18}O$, Clim. Past Discuss., 2016, 1–46, doi:10.5194/cp-2015-187.

in preparation:

- **Botsyun, S.**, P. Sepulchre, C. Risi, and Y. Donnadieu. Controls of the Eocene stable oxygen isotopes over Himalayas and Tibetan Plateau
- **Botsyun, S.**, P. Sepulchre, Y. Donnadieu, C. Risi, A. Licht and L.K. Caves. Eocene stable oxygen isotopes in the Himalayas and Tibetan Plateau: A record of elevation or of climate change?

Conference Abstracts

- **Svetlana Botsyun**, Pierre Sepulchre, and Yannick Donnadieu Impact of Himalayas and Tibetan plateau uplift on regional climate and isotopic lapse rate, Geophysical Research Abstarcts Vol. 16, EGU2014-5866, 2014 EGU General Assembly **2014, Wien (Austria)**, oral presentation;
- **Svetlana Botsyun**, Pierre Sepulchre, Yannick Donnadieu and Camille Risi. Modelling of Tibetan Plateau uplift impact on climate evolution, The Urbino Summer School in Paleoclimatology, University of Urbino, July 9 - 24, **2014, Urbino (Italy)**, poster presentation;
- **Svetlana Botsyun**, Pierre Sepulchre, and Yannick Donnadieu. Numerical modeling of Asian climat. Eu-Russia researchers' mobility forum **2014, Bruxelles (Belgique)**, poster presentation;
- **Svetlana Botsyun**, Pierre Sepulchre, Yannick Donnadieu, Camille Risi, and Frédéric Fluteau. Changes in Oxygen Isotopes Composition of Precipitation over Tibetan

Plateau during Cenozoic. AGU Fall Meeting **2014, Fan-Francisco (USA)**, poster presentation;

- **Svetlana Botsyun**, Yannick Donnadieu, Pierre Sepulchre, Camille Risi, and Frederic Fluteau. Cenozoic climate evolution in Asian region and its influence on isotopic composition of precipitation. Geophysical Research Abstracts Vol. 17, EGU2015-7214, EGU General Assembly **2015, Wien (Austria)**, poster presentation;

- **Svetlana Botsyun**, Pierre Sepulchre, Camille Risi, and Yannick Donnadieu. Impact of Tibetan Plateau uplift on Asian climate and stable oxygen isotopes in precipitation, Geophysical Research Abstracts Vol. 18, EGU2016-14707, EGU General Assembly **2016, Wien (Austria)**, poster presentation;

- **Svetlana Botsyun**, Pierre Sepulchre, Yannick Donnadieu, Ines Mangolte, and Frederic Fluteau.Impact of the tectonic evolution of Himalayan collision zone on Asian climate during the Cenozoic. The **2016** Himalayan-Karakoram-Tibet Workshop, **Aussois (France)**, poster presentation;

- **Svetlana Botsyun**, Pierre Sepulchre, Yannick Donnadieu, Camille Risi, Alexis Licht, Jeremy K. Caves. Modeling the response of climate and precipitation oxygen stable isotopes to the tectonic development of the Indian collision zone during the Cenozoic. AGU Fall Meeting **2016, Fan-Francisco (USA)**, oral presentation

Bibliography

Abe, M., Kitoh, A., Yasunari, T., 2003. An Evolution of the Asian Summer Monsoon Associated with Mountain Uplift-Simulation with the MRI Atmosphere-Ocean Coupled GCM-. Journal of the Meteorological Society of Japan 81 (5), 909–933. 9, 215

Achache, J., Courtillot, V., Xiu, Z. Y., 1984. Paleogeographic and tectonic evolution of southern Tibet since middle Cretaceous time: new paleomagnetic data and synthesis. Journal of Geophysical Research: Solid Earth 89 (B12), 10311–10339. 22, 23, 192

Aitchison, J. C., Ali, J. R., Davis, A. M., 2008. When and where did India and Asia collide? Geological Bulletin of China 27 (9), 1351–1370. 20

Allegre, C. J. O., Courtillot, V., Tapponnier, P., Hirn, A., Mattauer, M., Coulon, C., Jaeger, J. J., Achache, J., Schärer, U., Marcoux, J., 1984. Structure and evolution of the Himalaya–Tibet orogenic belt. 17

An, Z., Kutzbach, J. E., Prell, W. L., Porter, S. C., 2001. Evolution of Asian monsoons and phased uplift of the Himalaya-Tibetan plateau since Late Miocene times. Nature 411 (6833), 62–66. 9, 14

Araguás-Araguás, L., Froehlich, K., Rozanski, K., 1998. Stable isotope composition of precipitation over southeast Asia. Journal of Geophysical Research 103 (D22), 28721. 76

Arrhenius, S., 1896. On the influence of carbonic acid in the air upon the temperature of the ground. The London, Edinburgh, and Dublin Philosophical Magazine and Journal of Science 41 (251), 237–276. 53

Baatsen, M., van Hinsbergen, D. J. J., von der Heydt, A. S., Dijkstra, H. A., Abels, H. A., Bijl, P. K., 2016. Reconstructing geographical boundary conditions for palaeoclimate modelling during the Cenozoic. Climate of the Past 12 (8), 1635. 212

Baede, A. P. M., Ahlonsou, E., Ding, Y., Schimel, D. S., 2001. The climate system: an overview. In: Climate Change 2001: impacts, adaptation and vulnerability. Cambridge University Press, pp. 87–98. 51

Baldwin, J., Vecchi, G., 2016. Influence of the Tianshan Mountains on Arid Extratropical Asia. Journal of Climate (2016). 6

Barron, E. J., Sloan, J., Harrison, C. G. A., 1980. Potential significance of land—sea distribution and surface albedo variations as a climatic forcing factor; 180 my to the present. Palaeogeography, Palaeoclimatology, Palaeoecology 30, 17–40. 12

Barron, E. J., Washington, W. M., 1985. Warm Cretaceous climates: High atmospheric CO2 as a plausible mechanism. The Carbon Cycle and Atmospheric CO: Natural Variations Archean to Present, 546–553. 14

Beerling, D. J., Royer, D. L., 2011. Convergent Cenozoic CO2 history. Nature Geoscience 4 (7), 418–420. 11, 13, 14, 70, 194

Benetti, M., Reverdin, G., Pierre, C., Merlivat, L., Risi, C., Steen-Larsen, H. C., Vimeux, F., 2014. Deuterium excess in marine water vapor: Dependency on relative humidity and surface wind speed during evaporation. Journal of Geophysical Research: Atmospheres 119 (2), 584–593. 216

Bershaw, J., Penny, S. M., Garzione, C. N., 2012. Stable isotopes of modern water across the Himalaya and eastern Tibetan Plateau: Implications for estimates of paleoelevation and paleoclimate. Journal of Geophysical Research: Atmospheres 117 (2), 1–18. 76, 77, 78, 122, 123, 147, 154

Bershaw, J., Saylor, J. E., Garzione, C. N., Leier, A., Sundell, K. E., 2016. Stable isotope variations (δ18O and δD) in modern waters across the Andean Plateau. Geochimica et Cosmochimica Acta 194, 310–324. 76

Bice, K. L., Marotzke, J., 2002. Could changing ocean circulation have destabilized methane hydrate at the Paleocene/Eocene boundary? Paleoceanography 17 (2). 12

Bijl, P. K., Bendle, J. A. P., Bohaty, S. M., Pross, J., Schouten, S., Tauxe, L., Stickley, C. E., McKay, R. M., Röhl, U., Olney, M., 2013. Eocene cooling linked to early flow across the Tasmanian Gateway. Proceedings of the National Academy of Sciences 110 (24), 9645–9650. 12

Bjerknes, V., 1904. Das Problem der Wettervorhersage: betrachtet vom Standpunkte der Mechanik und der Physik. 56

Bjerknes, V., 1921. On the dynamics of the circular vortex with applications to the atmosphere and atmospheric vortes and wave motions. 57

Blisniuk, P. M., Hacker, B. R., Glodny, J., Ratschbacher, L., Bi, S., Wu, Z., McWilliams, M. O., Calvert, a., 2001. Normal faulting in central Tibet since at least 13.5 Myr ago. Nature 412 (6847), 628–632. 22, 37

Blisniuk, P. M., Stern, L. A., 2005. Stable isotope paleoaltimetry: A critical review. American Journal of Science 305 (10), 1033–1074. 34, 59, 80, 83

Bolin, B., 1950. On the influence of the earth's orography on the general character of the westerlies. Tellus 2 (3), 184–195. 7

Bony, S., Risi, C., Vimeux, F., 2008. Influence of convective processes on the isotopic composition (δ18O and δD) of precipitation and water vapor in the tropics: 1. Radiative-convective equilibrium and Tropical Ocean-Global-Atmosphere-Coupled Ocean-Atmosphere Responce Experiment (TOGA-COARE). Journal of Geophysical Research: Atmospheres 113 (D19). 64, 65, 79, 210

Boos, W. R., Kuang, Z., 2010. Dominant control of the South Asian monsoon by orographic insulation versus plateau heating. Nature 463 (7278), 218–222. 15, 192, 202

Botsyun, S., Sepulchre, P., Risi, C., Donnadieu, Y., jun 2016. Impacts of Tibetan Plateau uplift on atmospheric dynamics and associated precipitation δ18O. Climate of the Past 12 (6), 1401–1420. 62, 65, 122

Bouilhol, P., Jagoutz, O., Hanchar, J. M., Dudas, F. O., 2013. Dating the India-Eurasia collision through arc magmatic records. Earth and Planetary Science Letters 366, 163–175. 20

Braun, J., 2003. Pecube: A new finite-element code to solve the 3D heat transport equation including the effects of a time-varying, finite amplitude surface topography. Computers & Geosciences 29 (6), 787–794. 27, 217

Broccoli, A. J., Manabe, S., 1992. The Effects of Orography on Midlatitude Northern Hemisphere Dry Climates. 9, 15, 192

Brookfield, M. E., 1993. The Himalayan passive margin from Precamprian to Cretaceous times. Sedimentary Geology 84 (1), 1–35. 19

Brovkin, V., Claussen, M., Driesschaert, E., Fichefet, T., Kicklighter, D., Loutre, M.-F., Matthews, H. D., Ramankutty, N., Schaeffer, M., Sokolov, A., 2006. Biogeophysical effects of historical land cover changes simulated by six Earth system models of intermediate complexity. Climate Dynamics 26 (6), 587–600. 57

Budyko, M. I., 1969. The effect of solar radiation variations on the climate of the earth. Tellus 21 (5), 611–619. 56

Burchfiel, B. C., Zhiliang, C., Hodges, K. V., Yuping, L., Royden, L. H., Changrong, D., Jiene, X., 1992. The South Tibetan detachment system, Himalayan orogen: Extension contemporaneous with and parallel to shortening in a collisional mountain belt. Geological Society of America Special Papers 269, 1–41. 19

Burchfiel, B. C., Zhiliang, C., Yupinc, L., Royden, L. H., 1995. Tectonics of the Longmen Shan and adjacent regions, central China. International Geology Review 37 (8), 661–735. 19

Burg, J. P., Chen, G. M., 1984. Tectonics and structural zonation of southern Tibet, China. Nature 311, 219–223. 17, 19

Burov, E., Gerya, T., 2014. Asymmetric three-dimensional topography over mantle plumes. Nature 513 (7516), 85–89. 26

Cai, F., Ding, L., Yue, Y., 2011. Provenance analysis of upper Cretaceous strata in the Tethys Himalaya, southern Tibet: Implications for timing of India-Asia collision. Earth and Planetary Science Letters 305 (1-2), 195–206. 20

Campani, M., Mulch, A., Kempf, O., Schlunegger, F., Mancktelow, N., 2012. Miocene paleotopography of the Central Alps. Earth and Planetary Science Letters 337, 174–185. 28

Caves, J. K., Sjostrom, D. J., Mix, H. T., Winnick, M. J., Chamberlain, C. P., 2014. Aridification of Central Asia and uplift of the Altai and Hangay mountains, Mongolia: Stable isotope evidence. American Journal of Science 314 (8), 1171–1201. 28, 154

Caves, J. K., Winnick, M. J., Graham, S. A., Sjostrom, D. J., Mulch, A., Chamberlain, C. P., 2015. Role of the westerlies in Central Asia climate over the Cenozoic. Earth and Planetary Science Letters 428, 33–43. 123

Chaloner, W., Creber, G., 1990. Do fossil plants give a climatic signal? Journal of the Geological Society 147 (2), 343–350. 28

Chalot-Prat, F., Girbacea, R., 2000. Partial delamination of continental mantle lithosphere, uplift-related crust–mantle decoupling, volcanism and basin formation: a new model for the Pliocene–Quaternary evolution of the southern East-Carpathians, Romania. Tectonophysics 327 (1), 83–107. 21

Chamberlain, C. P., Mix, H. T., Mulch, A., Hren, M. T., Kent-Corson, M. L., Davis, S. J., Horton, T. W., Graham, S. A., 2012. The Cenozoic climatic and topographic evolution of the western North American Cordillera. American Journal of Science 312 (2), 213–262. 28

Chamberlain, C. P., Poage, M. A., Craw, D., Reynolds, R. C., 1999. Topographic development of the Southern Alps recorded by the isotopic composition of authigenic clay minerals, South Island, New Zealand. Chemical Geology 155 (3), 279–294. 28

Chang, C.-F., Pan, Y.-S., Sun, Y.-Y., 1989. The tectonic evolution of Qinghai-Tibet Plateau: a review. In: Tectonic Evolution of the Tethyan Region. Springer, pp. 415–476. 17, 19

Chao, W. C., Chen, B., 2001. Multiple Quasi Equilibria of the ITCZ and the Origin of Monsoon Onset. Part II: Rotational ITCZ Attractors. Journal of the Atmospheric Sciences 58 (18), 2820–2831. 192

Charles, C. D., Rind, D., Healy, R., Webb, R., 2001. Tropical cooling and the isotopic composition of precipitation in general circulation model simulations of the ice age climate. Climate dynamics 17 (7), 489–502. 61, 62

Charney, J., Quirk, W. J., Chow, S.-h., Kornfield, J., 1977. A comparative study of the effects of albedo change on drought in semi-arid regions. Journal of the Atmospheric Sciences 34 (9), 1366–1385. 12

Charney, J. G., Eliassen, A., 1949. A numerical method for predicting the perturbations of the middle latitude westerlies. Tellus 1 (2), 38–54. 7

Charreau, J., Blard, P.-H., Puchol, N., Avouac, J.-P., Lallier-Verges, E., Bourlès, D., Braucher, R., Gallaud, A., Finkel, R., Jolivet, M., 2011. Paleo-erosion rates in Central Asia since 9Ma: A transient increase at the onset of Quaternary glaciations? Earth and Planetary Science Letters 304 (1), 85–92. 216

Chatterjee, S., Goswami, A., Scotese, C. R., 2013. The longest voyage: Tectonic, magmatic, and paleoclimatic evolution of the Indian plate during its northward flight from Gondwana to Asia. Gondwana Research 23 (1), 238–267. 20

Chen, M., Wang, R., Yang, L., Han, J., Lu, J., 2003. Development of east Asian summer monsoon environments in the late Miocene: radiolarian evidence from Site 1143 of ODP Leg 184. Marine Geology 201 (1), 169–177. 191

Chen, Z., Wang, X., Feng, X., Wang, C., Liu, J., 2002. New evidence from stable isotope for the uplift of mountains in northern edge of the Qinghai-Tibetan Plateau. Science in China Series B: Chemistry 45 (1), 1–10. 42, 215

Cherchi, A., Alessandri, A., Masina, S., Navarra, A., 2011. Effects of increased CO2 levels on monsoons. Climate Dynamics 37 (1), 83–101. 193

Chung, S. L., Chu, M. F., Zhang, Y., Xie, Y., Lo, C. H., Lee, T. Y., Lan, C. Y., Li, X., Zhang, Q., Wang, Y., 2005. Tibetan tectonic evolution inferred from spatial and temporal variations in post-collisional magmatism. Earth-Science Reviews 68 (3-4), 173–196. 16, 17, 18, 19, 20, 21, 22, 24, 26, 38, 115

Chung, S.-L., Liu, D., Ji, J., Chu, M.-F., Lee, H.-Y., Wen, D.-J., Lo, C.-H., Lee, T.-Y., Qian, Q., Zhang, Q., 2003. Adakites from continental collision zones: melting of thickened lower crust beneath southern Tibet. Geology 31 (11), 1021–1024. 21, 22

Ciais, P., Jouzel, J., 1994. Deuterium and oxygen 18 in precipitation: Isotopic model, including mixed cloud processes. Journal of Geophysical Research: Atmospheres 99 (D8), 16793–16803. 59

Claussen, M., 2005. Table of EMICS-Earth System Models of Intermediate Complexity. 57

Claussen, M., Mysak, L., Weaver, A., Crucifix, M., Fichefet, T., Loutre, M.-F., Weber, S., Alcamo, J., Alexeev, V., Berger, A., 2002. Earth system models of intermediate complexity: closing the gap in the spectrum of climate system models. Climate Dynamics 18 (7), 579–586. 57

Clift, P., Carter, A., Krol, M., Kirby, E., 2002. Constraints on India-Eurasia Collision in the Arabian Sea Region taken from the Indus Group, Ladakh Himalaya, India. Geological Society, London, Special Publications 195, 97–116. 20

Clift, P. D., Giosan, L., Carter, A., Garzanti, E., Galy, V., Tabrez, A. R., Pringle, M., Campbell, I. H., France-Lanord, C., Blusztajn, J., 2010. Monsoon control over erosion patterns in the western Himalaya: possible feed-back into the tectonic evolution. Geological Society, London, Special Publications 342 (1), 185–218. 191

Clift, P. D., Hodges, K. V., Heslop, D., Hannigan, R., Van Long, H., Calves, G., 2008. Correlation of Himalayan exhumation rates and Asian monsoon intensity. Nature Geoscience 1 (12), 875–880. 20, 191

Clift, P. D., Layne, G. D., Blusztajn, J., 2004. Marine sedimentary evidence for monsoon strengthening, Tibetan uplift and drainage evolution in East Asia. Continent-Ocean Interactions Within East Asian Marginal Seas, 255–282. 191

Clift, P. D., Plumb, R. A., 2008. The Asian monsoon: causes, history and effects. Vol. 288. Cambridge University Press Cambridge. 14

Coplen, T. B., Herczeg, A. L., Barnes, C., 2000. Isotope engineering—using stable isotopes of the water molecule to solve practical problems. In: Environmental tracers in subsurface hydrology. Springer, pp. 79–110. 30

Craig, H., 1961. Isotopic variations in meteoric waters. Science 133 (3465), 1702–1703. 75

Currie, B. S., Polissar, P. J., Rowley, D. B., Ingalls, M., Li, S., Olack, G., Freeman, K. H., 2016. Multiproxy paleoaltimetry of the Late Oligocene-Pliocene Oiyug Basin, southern Tibet. American Journal of Science 316 (5), 401–436. 38, 39, 40, 42, 43, 44, 191, 215

Currie, B. S., Rowley, D. B., Tabor, N. J., 2005. Middle Miocene paleoaltimetry of southern Tibet: Implications for the role of mantle thickening and delamination in the Himalayan orogen. Geology 33 (3), 181–184. 35, 39, 43, 80, 83

Cyr, A. J., Currie, B. S., Rowley, D. B., 2005. Geochemical Evaluation of Fenghuoshan Group Lacustrine Carbonates, North-Central Tibet: Implications for the Paleoaltimetry of the Eocene Tibetan Plateau. The Journal of Geology 113 (5), 517–533. 35, 37, 41, 80, 83, 115, 116

Dana, J. D., 1856. A review of the Classification of Crustacea with reference to certain principles of classification. American Journal of Science and Arts. 10

Dansgaard, W., 1953. The abundance of O18 in atmospheric water and water vapour. Tellus 5 (4), 461–469. 31

Dansgaard, W., 1964. Stable isotopes in precipitation. Tellus 16 (4), 436–468. 31, 59, 75, 76, 78, 216

Day, J. A., Fung, I., Risi, C., 2015. Coupling of South and East Asian Monsoon Precipitation in July-August. Journal of Climate, 150227131327003. 64, 193

DeCelles, P. G., Quade, J., Kapp, P., Fan, M., Dettman, D. L., Ding, L., 2007. High and dry in central Tibet during the Late Oligocene. Earth and Planetary Science Letters 253 (3-4), 389–401. 38, 42, 83, 115

DeConto, R. M., 2009. Plate tectonics and climate change. In: Encyclopedia of paleoclimatology and ancient environments. Springer, pp. 784–798. 5, 13

DeConto, R. M., Pollard, D., 2003. A coupled climate–ice sheet modeling approach to the early Cenozoic history of the Antarctic ice sheet. Palaeogeography, Palaeoclimatology, Palaeoecology 198 (1), 39–52. 10, 191

DeConto, R. M., Pollard, D., Wilson, P. A., Pälike, H., Lear, C. H., Pagani, M., 2008. Thresholds for Cenozoic bipolar glaciation. Nature 455 (7213), 652–656. 61, 62

Deng, T., 2013. Paleo-altimetry of the Tinetan Plateau as indicated by mammalian fossils. Acta Geologica Sinica (English Edition) 87 (s1), 857–893. 40, 44

Deng, T., Wang, S., Xie, G., Li, Q., Hou, S., Sun, B., 2012. A mammalian fossil from the Dingqing Formation in the Lunpola Basin, northern Tibet, and its relevance to age and paleo-altimetry. Chinese Science Bulletin 57 (2-3), 261–269. 28, 39, 40, 42, 43

Dettman, D. L., Fang, X., Garzione, C. N., Li, J., 2003. Uplift-driven climate change at 12 Ma: A long δ18O record from the NE margin of the Tibetan plateau. Earth and Planetary Science Letters 214 (1-2), 267–277. 36, 40, 83

Dettman, D. L., Kohn, M. J., Quade, J., Ryerson, F. J., Ojha, T. P., Hamidullah, S., 2001. Seasonal stable isotope evidence for a strong Asian monsoon throughout the past 10.7 m.y. Geology 29 (1), 31–34. 36, 39, 83, 115

Dewey, J. F., 1988. Extensional collapse of orogens. Tectonics 7 (6), 1123–1139. 19, 20

Dickenson, R., Henderson-Sellers, A., 1988. Modeling tropical deforestation: A study of GCM land-surface parametrizations. Quarterly Journal of the Royal Meteorological Society 114 (480), 439–462. 5

Ding, L., Kapp, P., Wan, X., 2005. Paleocene-Eocene record of ophiolite obduction and initial India-Asia collision, south central Tibet. Tectonics 24 (3). 20

Ding, L., Xu, Q., Yue, Y., Wang, H., Cai, F., Li, S., 2014. The Andean-type Gangdese Mountains: Paleoelevation record from the Paleocene-Eocene Linzhou Basin. Earth and Planetary Science Letters 392, 250–264. 28, 37, 41, 80, 83, 115

Donnadieu, Y., Pierrehumbert, R., Jacob, R., Fluteau, F., 2006. Modelling the primary control of paleogeography on Cretaceous climate. Earth and Planetary Science Letters 248 (1-2), 411–422. 12, 63

Donnadieu, Y., Pucéat, E., Moiroud, M., Guillocheau, F., Deconinck, J.-F., 2016. A better-ventilated ocean triggered by Late Cretaceous changes in continental configuration. Nature communications 7. 12

Doria, G., Royer, D. L., Wolfe, A. P., Fox, A., Westgate, J. A., Beerling, D. J., 2011. Declining atmospheric CO2 during the late Middle Eocene climate transition. American Journal of Science 311 (1), 63–75. 13

Dorodnitsyn, A. A., 1950. Effect of the Earth's Surface Relief on Airflows. Tr. TsIP (21), 3–25. 7

Dupont-Nivet, G., Hoom, C., Konert, M., 2008. Tibetan uplift prior to the Eocene-Oligocene climate transition: Evidence from pollen analysis of the Xining Basin. Geology 36 (12), 987–990. 37, 42, 115

Dupont-Nivet, G., Krijgsman, W., Langereis, C. G., Abels, H. A., Dai, S., Fang, X., 2007. Tibetan plateau aridification linked to global cooling at the Eocene–Oligocene transition. Nature 445 (7128), 635–638. 191

Dupont-Nivet, G., Lippert, P. C., van Hinsbergen, D. J. J., Meijers, M. J. M., Kapp, P., 2010. Palaeolatitude and age of the Indo-Asia collision: Palaeomagnetic constraints. Geophysical Journal International 182 (3), 1189–1198. 20

Duretz, T., Gerya, T. V., May, D. A., 2011. Numerical modelling of spontaneous slab breakoff and subsequent topographic response. Tectonophysics 502 (1), 244–256. 26

Dymnikov, V. P., Lykosov, V. N., Volodin, E. M., 2012. Modeling climate and its changes: Current problems. Herald of the Russian Academy of Sciences 82 (2), 111–119. 51

Eby, M., Weaver, A. J., Alexander, K., Zickfeld, K., Abe-Ouchi, A., Cimatoribus, A. A., Crespin, E., Drijfhout, S. S., Edwards, N. R., Eliseev, A. V., 2013. Historical and idealized climate model experiments: an intercomparison of Earth system models of intermediate complexity. Climate of the Past 9, 1111–1140. 57

Edwards, P. N., 2011. History of climate modeling. Wiley Interdisciplinary Reviews: Climate Change 2 (1), 128–139. 52, 58

Ehlers, T. A., Farley, K. A., 2003. Apatite (U–Th)/He thermochronometry: methods and applications to problems in tectonic and surface processes. Earth and Planetary Science Letters 206 (1), 1–14. 27

Ehlers, T. A., Poulsen, C. J., 2009. Influence of Andean uplift on climate and paleoaltimetry estimates. Earth and Planetary Science Letters 281 (3-4), 238–248. 35, 62, 76, 77, 81, 83, 121

Eiler, J. M., 2011. Paleoclimate reconstruction using carbonate clumped isotope thermometry. Quaternary Science Reviews 30 (25-26), 3575–3588. 34, 35

Elbaradei, M., 2013. Global Network of Isotopes in Precipitation.
URL http://www-naweb.iaea.org/napc/ih/documents/other/GNIPbrochure.pdf 33

Evans, M. N., 2007. Toward forward modeling for paleoclimatic proxy signal calibration: A case study with oxygen isotopic composition of tropical woods. Geochemistry, Geophysics, Geosystems 8 (7). 154

Faccenna, C., Becker, T. W., Miller, M. S., Serpelloni, E., Willett, S. D., 2014. Isostasy, dynamic topography, and the elevation of the Apennines of Italy. Earth and Planetary Science Letters 407, 163–174. 26

Fan, M., Dettman, D. L., Song, C., Fang, X., Garzione, C. N., 2007. Climatic variation in the Linxia basin, NE Tibetan Plateau, from 13.1 to 4.3 Ma: The stable isotope record. Palaeogeography, Palaeoclimatology, Palaeoecology 247 (3-4), 313–328. 36, 83, 115

Fasullo, J., Webster, P. J., 2003. A hydrological definition of Indian Monsoon onset and withdrawal. Journal of Climate 16 (19), 3200–3211. 8, 195, 196

Favre, A., Päckert, M., Pauls, S. U., Jähnig, S. C., Uhl, D., Michalak, I., Muellner-Riehl, A. N., 2014. The role of the uplift of the Qinghai-Tibetan Plateau for the evolution of Tibetan biotas. Biological reviews 90 (1), 236–253. 16, 213

Fielding, E. J., 1996. Tibet uplift and erosion. Tectonophysics 260 (1), 55–84. 21

Flament, N., Gurnis, M., Williams, S., Seton, M., Skogseid, J., Heine, C., Müller, R. D., 2014. Topographic asymmetry of the South Atlantic from global models of mantle flow and lithospheric stretching. Earth and Planetary Science Letters 387, 107–119. 26

Forest, C. E., Wolfe, J. A., Molnar, P., Emanuel, K. A., apr 1999. Paleoaltimetry incorporating atmospheric physics and botanical estimates of paleoclimate. Geological Society of America Bulletin 111 (4), 497–511. 28, 34

France-Lanord, C., Derry, L. A., 1997. Organic carbon burial forcing of the carbon cycle from Himalayan erosion. Nature 390 (6655), 65–67. 10

France-Lanord, C., Sheppard, S. M. F., Le Fort, P., 1988. Hydrogen and oxygen isotope variations in the High Himalaya peraluminous Manaslu leucogranite: evidence for heterogeneous sedimentary source. Geochimica et Cosmochimica Acta 52 (2), 513–526. 39, 43

Frankenberg, C., Yoshimura, K., Warneke, T., Aben, I., Butz, A., Deutscher, N., Griffith, D., Hase, F., Notholt, J., Schneider, M., Schrijver, H., Röckmann, T., sep 2009. Dynamic Processes Governing Lower-Tropospheric HDO/H2O Ratios as Observed from Space and Ground. Science 325 (5946), 1374–1377. 79, 81, 83

Froehlich, K., Gibson, J. J., Aggarwal, P., 2001. Deuterium excess in precipitation and its climatological significance. In: Study of Environmental Change Using Isotope Techniques. Proc. Intern. Conf. Citeseer, pp. 54–66. 216

Galewsky, J., 2009. Rain shadow development during the growth of mountain ranges: An atmospheric dynamics perspective. Journal of Geophysical Research: Earth Surface 114 (F1). 7

Galewsky, J., Hurley, J. V., 2010. An advection-condensation model for subtropical water vapor isotopic ratios. Journal of Geophysical Research: Atmospheres (1984–2012) 115 (D16). 30

Galewsky, J., Sobel, A., Held, I., 2005. Diagnosis of subtropical humidity dynamics using tracers of last saturation. Journal of the atmospheric sciences 62 (9), 3353–3367. 30

Galy, V., France-Lanord, C., Beyssac, O., Faure, P., Kudrass, H., Palhol, F., 2007. Efficient organic carbon burial in the Bengal fan sustained by the Himalayan erosional system. Nature 450 (7168), 407–410. 10

Gan, M. A., Rao, V. B., Moscati, M. C. L., 2005. South American monsoon indices. Atmospheric Science Letters 6 (4), 219–223. 195, 196

Garzione, C. N., Auerbach, D. J., Smith, J. J.-S., Rosario, J. J., Passey, B. H., Jordan, T. E., Eiler, J. M., 2014. Clumped isotope evidence for diachronous surface cooling of the Altiplano and pulsed surface uplift of the Central Andes. Earth and Planetary Science Letters 393, 173–181. 28

Garzione, C. N., Dettman, D. L., Quade, J., De Celles, P. G., Butler, R. F., 2000a. High times on the Tibetan Plateau: Paleoelevation of the Thakkhola graben, Nepal. Geology 28 (4), 339–342. xiii, 33

Garzione, C. N., Hoke, G. D., Libarkin, J. C., Withers, S., MacFadden, B., Eiler, J., Ghosh, P., Mulch, A., 2008. Rise of the Andes. science 320 (5881), 1304–1307. 28

Garzione, C. N., Molnar, P., Libarkin, J. C., MacFadden, B. J., 2006. Rapid late Miocene rise of the Bolivian Altiplano: Evidence for removal of mantle lithosphere. Earth and Planetary Science Letters 241 (3), 543–556. 28

Garzione, C. N., Quade, J., DeCelles, P. G., English, N. B., 2000b. Predicting paleoelevation of Tibet and the Himalaya from δ18O vs. altitude gradients in meteoric water across the Nepal Himalaya. Earth and Planetary Science Letters 183 (1-2), 215–229. 28, 35, 38, 43, 76, 83, 115

Gat, J. R., 1996. Oxygen and hydrogen isotopes in the hydrologic cycle. Annual Review of Earth and Planetary Sciences 24 (1), 225–262. 76, 77

Gébelin, A., Mulch, A., Teyssier, C., Chamberlain, C. P., Heizler, M., 2012. Coupled basin-detachment systems as paleoaltimetry archives of the western North American Cordillera. Earth and Planetary Science Letters 335, 36–47. 28

Gébelin, A., Mulch, A., Teyssier, C., Jessup, M. J., Law, R. D., Brunel, M., 2013. The Miocene elevation of Mount Everest. Geology 41 (7), 799–802. 39, 42

Gerya, T., 2010. Introduction to numerical geodynamic modelling. Cambridge University Press. 217

Goddéris, Y., Donnadieu, Y., Le Hir, G., Lefebvre, V., Nardin, E., 2014. The role of palaeogeography in the Phanerozoic history of atmospheric CO2 and climate. Earth-Science Reviews 128, 122–138. 13, 14

Gonfiantini, R., 1978. Standards for stable isotope measurements in natural compounds. 29

Gonfiantini, R., Roche, M. A., Olivry, J. C., Fontes, J. C., Zuppi, G. M., 2001. The altitude effect on the isotopic composition of tropical rains. Chemical Geology 181 (1-4), 147–167. 35

Grabowski, W. W., 2001. Coupling cloud processes with the large-scale dynamics using the cloud-resolving convection parametrization (CRCP). Journal of the Atmospheric Sciences 58 (9), 978–997. 210

Grossman, E. L., Ku, T.-L., 1986. Oxygen and carbon isotope fractionation in biogenic aragonite: temperature effects. Chemical Geology: Isotope Geoscience Section 59, 59–74. 32

Grujic, D., Coutand, I., Bookhagen, B., Bonnet, S., Blythe, A., Duncan, C., 2006. Climatic forcing of erosion, landscape, and tectonics in the Bhutan Himalayas. Geology 34 (10), 801–804. 191

Guo, Z. T., Ruddiman, W. F., Hao, Q. Z., Wu, H. B., Qiao, Y. S., Zhu, R. X., Peng, S. Z., Wei, J. J., Yuan, B. Y., Liu, T. S., 2002. Onset of Asian desertification by 22 Myr ago inferred from loess deposits in China. Nature 416 (6877), 159–163. 191

Gupta, A. K., Yuvaraja, A., Prakasam, M., Clemens, S. C., Velu, A., 2015. Evolution of the South Asian monsoon wind system since the late Middle Miocene. Palaeogeography, Palaeoclimatology, Palaeoecology 438, 160–167. 9

Gurrola, L. D., Keller, E. A., Chen, J. H., Owen, L. A., Spencer, J. Q., 2014. Tectonic geomorphology of marine terraces; Santa Barbara fold belt, California. Geological Society of America Bulletin 126 (1/2), 219–233. 26

Hamon, N., Sepulchre, P., Lefebvre, V., Ramstein, G., 2013. The role of eastern tethys seaway closure in the middle miocene climatic transition (ca. 14 Ma). Climate of the Past 9 (6), 2687–2702. 12, 63

Harris, N., 2006. The elevation history of the Tibetan Plateau and its implications for the Asian monsoon. Palaeogeography, Palaeoclimatology, Palaeoecology 241 (1), 4–15. 38

Harrison, T. M., Yin, A., Grove, M., Lovera, O. M., Ryerson, F. J., 2000. Displacement history of the Gangdese thrust, southeastern Tibet. J. Geophys. Res 105 (19), 211–219. 21

Hastie, T., Tibshirani, R., Friedman, J., 2009. Unsupervised learning. In: The elements of statistical learning. Springer, pp. 485–585. 82

Haxeltine, A., Prentice, I. C., 1996. BIOME3: An equilibrium terrestrial biosphere model based on ecophysiological constraints, resource availability, and competition among plant functional types. Global Biogeochemical Cycles 10 (4), 693–709. 63

Hay, W. W., 1996. Tectonics and climate. Geologische Rundschau 85 (3), 409–437. 5, 6, 7

Hay, W. W., Shaw, C. A., Wold, C. N., 1989. Mass-balanced paleogeographic reconstructions. Geologische Rundschau 78 (1), 207–242. 27

He, Y., Risi, C., Gao, J., Masson-Delmotte, V., Yao, T., Lai, C.-T., Ding, Y., Worden, J., Frankenberg, C., Chepfer, H., Cesana, G., may 2015. Impact of atmospheric convection on south Tibet summer precipitation isotopologue composition using a combination of in situ measurements, satellite data, and atmospheric general circulation modeling. Journal of Geophysical Research: Atmospheres 120 (9), 3852–3871. 75, 79

Helsen, M. M., Van de Wal, R. S. W., Van den Broeke, M. R., 2007. The isotopic composition of present-day antarctic snow in a lagrangian atmospheric simulation*. Journal of Climate 20 (4), 739–756. 59, 60

Henderson-Sellers, A., Wilson, M. F., 1983. Surface albedo data for climatic modeling. Reviews of Geophysics 21 (8), 1743–1778. 147

Herold, N., Buzan, J., Seton, M., Goldner, A., Green, J. A. M., Müller, R. D., Markwick, P., Huber, M., 2014. A suite of early Eocene (˜ 55 Ma) climate model boundary conditions. Geoscientific Model Development 7 (5), 2077–2090. 66, 68, 69, 71, 193, 195

Herold, N., Seton, M., Müller, R. D., You, Y., Huber, M., 2008. Middle Miocene tectonic boundary conditions for use in climate models. Geochemistry, Geophysics, Geosystems 9 (10). 66, 67, 68, 69, 70, 71, 193, 194, 195

Hide, R., 1953. Some experiments on thermal convection in a rotating liquid. Quarterly Journal of the Royal Meteorological Society 79 (339), 161. 56

Hill, D. J., Haywood, A. M., Valdes, P. J., Francis, J. E., Lunt, D. J., Wade, B. S., Bowman, V. C., 2013. Paleogeographic controls on the onset of the Antarctic circumpolar current. Geophysical Research Letters 40 (19), 5199–5204. 12

Hodges, K. V., Parrish, R. R., Searle, M. P., 1996. Tectonic evolution of the central Annapurna range, Nepalese Himalayas. Tectonics 15 (6), 1264–1291. 19

Hoefs, J., Hoefs, J., 1997. Stable isotope geochemistry. Vol. 201. Springer. 30

Hoffmann, G., Jouzel, J., Masson, V., 2000. Stable water isotopes in atmospheric general circulation models. Hydrological Processes 14 (8), 1385–1406. 58

Hoffmann, G., Werner, M., Heimann, M., 1998. Water isotope module of the ECHAM atmospheric general circulation model: A study on timescales from days to several years. Journal of Geophysical Research: Atmospheres 103 (D14), 16871–16896. 60, 61

Hoke, G. D., Liu-Zeng, J., Hren, M. T., Wissink, G. K., Garzione, C. N., 2014. Stable isotopes reveal high southeast Tibetan Plateau margin since the Paleogene. Earth and Planetary Science Letters 394, 270–278. 29, 35, 40, 41, 43, 44, 80, 83, 115, 215

Hoorn, C., Straathof, J., Abels, H. a., Xu, Y., Utescher, T., Dupont-Nivet, G., 2012. A late Eocene palynological record of climate change and Tibetan Plateau uplift (Xining Basin, China). Palaeogeography, Palaeoclimatology, Palaeoecology 344-345, 16–38. 37, 41

Hourdin, F., Musat, I., Bony, S., Braconnot, P., Codron, F., Dufresne, J. L., Fairhead, L., Filiberti, M. A., Friedlingstein, P., Grandpeix, J. Y., Krinner, G., LeVan, P., Li, Z. X., Lott, F., 2006. The LMDZ4 general circulation model: Climate performance and sensitivity to parametrized physics with emphasis on tropical convection. Climate Dynamics 27 (7-8), 787–813. 63, 193, 209, 210

Hren, M. T., Bookhagen, B., Blisniuk, P. M., Booth, A. L., Chamberlain, C. P., 2009. δ18O and δD of streamwaters across the Himalaya and Tibetan Plateau: Implications for moisture sources and paleoelevation reconstructions. Earth and Planetary Science Letters 288 (1-2), 20–32. 78, 123

Hsu, J., Tao, J. J., Sun, H. J., 1973. On the discovery of a Quercus semicarpifolia bed at Mount Shisha Pangma and its significance in botany and geology. Acta Botanica Sinica. 40, 44

Hu, X., Garzanti, E., Moore, T., Raffi, I., 2015. Direct stratigraphic dating of India-Asia collision onset at the Selandian (middle Paleocene, 59 ± 1 Ma). Geology 43 (10), 859–862. 20

Huber, M., Goldner, A., 2012. Eocene monsoons. Journal of Asian Earth Sciences 44, 3–23. 8, 9, 191, 202

Huntington, K. W., Lechler, A. R., 2015. Carbonate clumped isotope thermometry in continental tectonics. Tectonophysics 647, 1–20. 34, 40

Huntington, K. W., Saylor, J., Quade, J., Hudson, A. M., 2015. High late Miocene-Pliocene elevation of the Zhada Basin, southwestern Tibetan Plateau, from carbonate clumped isotope thermometry. Bulletin of the Geological Society of America 127 (1-2), 181–199. 44

Jacob, R. L., 1997. Low frequency variability in a simulated atmosphere ocean system. 62, 63, 194

Jia, G., Bai, Y., Ma, Y., Sun, J., Peng, P., 2015. Paleoelevation of Tibetan Lunpola basin in the Oligocene–Miocene transition estimated from leaf wax lipid dual isotopes. Global and Planetary Change 126, 14–22. 38, 42

Jiang, D., Yu, G., Zhao, P., Chen, X., Liu, J., Liu, X., Wang, S., Zhang, Z., Yu, Y., Li, Y., Jin, L., Xu, Y., Ju, L., Zhou, T., Yan, X., 2015. Paleoclimate modeling in China: A review. Advances in Atmospheric Sciences 32 (2), 250–275. 212

Jiang, X., Li, Z.-X., Li, H., 2013. Uplift of the West Kunlun Range, northern Tibetan Plateau, dominated by brittle thickening of the upper crust. Geology 41 (4), 439–442. 22

Joussaume, S., Jouzel, J., 1993. Paleoclimatic tracers: An investigation using an atmospheric general circulation model under ice age conditions: 2. Water isotopes. Journal of Geophysical Research: Atmospheres 98 (D2), 2807–2830. 61

Joussaume, S., Sadourny, R., Jouzel, J., 1984. A general circulation model of water isotope cycles in the atmosphere. Nature 311, 24–29. 60, 61

Jouzel, J., Hoffmann, G., Koster, R. D., Masson, V., 2000. Water isotopes in precipitation:: data/model comparison for present-day and past climates. Quaternary Science Reviews 19 (1), 363–379. 59

Jouzel, J., Koster, R. D., Suozzo, R. J., Russell, G. L., 1994. Stable water isotope behavior during the last glacial maximum: A general circulation model analysis. Journal of Geophysical Research: Atmospheres 99 (D12), 25791–25801. 59, 61

Jouzel, J., Merlivat, L., 1984. Deuterium and oxygen 18 in precipitation: Modeling of the isotopic effects during snow formation. Journal of Geophysical Research: Atmospheres 89 (D7), 11749–11757. 59, 65

Jouzel, J., Russell, G. L., Suozzo, R. J., Koster, R. D., White, J. W. C., Broecker, W. S., 1987. Simulations of the HDO and H2 18O atmospheric cycles using the NASA GISS general circulation model: The seasonal cycle for present-day conditions. Journal of Geophysical Research: Atmospheres 92 (D12), 14739–14760. 60, 61

Kar, N., Garzione, C. N., Jaramillo, C., Shanahan, T., Carlotto, V., Pullen, A., Moreno, F., Anderson, V., Moreno, E., Eiler, J., 2016. Rapid regional surface uplift of the northern Altiplano plateau revealed by multiproxy paleoclimate reconstruction. Earth and Planetary Science Letters 447, 33–47. 28

Kent-Corson, M. L., Ritts, B. D., Zhuang, G., Bovet, P. M., Graham, S. A., Page Chamberlain, C., 2009. Stable isotopic constraints on the tectonic, topographic, and climatic evolution of the northern margin of the Tibetan Plateau. Earth and Planetary Science Letters 282 (1-4), 158–166. 35, 36, 83, 115, 212

Khan, S. D., Walker, D. J., Hall, S. A., Burke, K. C., Shah, M. T., Stockli, L., 2009. Did the Kohistan-Ladakh island arc collide first with India? Bulletin of the Geological Society of America 121 (3-4), 366–384. 20

Kim, S. T., O'Neil, J. R., 1997. Equilibrium and nonequilibrium oxygen isotope effects in synthetic carbonates. Geochimica et Cosmochimica Acta 61 (16), 3461–3475. 32, 35

Kitoh, A., 2004. Effects of Mountain Uplift on East Asian Summer Climate Investigated by a Coupled Atmosphere–Ocean GCM. Journal of Climate 17 (4), 783–802. 9, 215

Kohn, M. J., Dettman, D. L., 2007. Paleoaltimetry from Stable Isotope Compositions of Fossils. Reviews in Mineralogy and Geochemistry 66 (1), 119–154. 34, 35, 115

Kripalani, R. H., Oh, J. H., Kulkarni, A., Sabade, S. S., Chaudhari, H. S., 2007. South Asian summer monsoon precipitation variability: coupled climate model simulations and projections under IPCC AR4. Theoretical and Applied Climatology 90 (3-4), 133–159. 216

Krishnan, R., Sabin, T. P., Vellore, R., Mujumdar, M., Sanjay, J., Goswami, B. N., Hourdin, F., Dufresne, J. L., Terray, P., 2015. Deciphering the desiccation trend of the South Asian monsoon hydroclimate in a warming world. Climate Dynamics. 64, 193

Kuhle, M., 1995. Glacial isostatic uplift of Tibet as a consequence of a former ice sheet. GeoJournal 37 (4), 431–449. 27

Kuo, H. L., Qian, Y.-F., 1982. Numerical simulation of the development of mean monsoon circulation in July. Monthly Weather Review 110 (12), 1879–1897. 192

Kurita, N., Noone, D., Risi, C., Schmidt, G. A., Yamada, H., Yoneyama, K., 2011. Intraseasonal isotopic variation associated with the Madden-Julian Oscillation. Journal of Geophysical Research: Atmospheres 116 (D24). 61

Kürschner, W. M., Kvaček, Z., Dilcher, D. L., 2008. The impact of Miocene atmospheric carbon dioxide fluctuations on climate and the evolution of terrestrial ecosystems. Proceedings of the National Academy of Sciences 105 (2), 449–453. 14

Kutzbach, J. E., 1980. Estimates of past climate at Paleolake Chad, North Africa, based on a hydrological and energy-balance model. Quaternary Research 14 (2), 210–223. 9

Kutzbach, J. E., Guetter, P. J., Ruddiman, W. F., Prell, W. L., 1989. Sensitivity of climate to late Cenozoic uplift in southern Asia and the American west: numerical experiments. Journal of Geophysical Research: Atmospheres (1984–2012) 94 (D15), 18393–18407. 1, 5

Kutzbach, J. E., Prell, W. L., Ruddiman, W. F., 1993. Sensitivity of Eurasian climate to surface uplift of the Tibetan Plateau. The Journal of Geology, 177–190. 191, 192

Ladant, J.-B., 2015. Interactions climat-calotte durant la greenhouse Creetace-Paleogene (120-34 Ma) : influence de la paleogeographie et du CO2 atmospherique. Ph.D. thesis, L'UNIVERSITE PARIS-SACLAY. 66

Ladant, J.-B., Donnadieu, Y., Lefebvre, V., Dumas, C., 2014. The respective role of atmospheric carbon dioxide and orbital parameters on ice sheet evolution at the Eocene-Oligocene transition. Paleoceanography 29 (8), 810–823. 64, 65, 193, 194

Lambeck, K., Smither, C., Johnston, P., 1998. Sea-level change, glacial rebound and mantle viscosity for northern Europe. Geophysical Journal International 134 (1), 102–144. 26

Lauderdale, J. M., Garabato, A. C. N., Oliver, K. I. C., Follows, M. J., Williams, R. G., 2013. Wind-driven changes in Southern Ocean residual circulation, ocean carbon reservoirs and atmospheric CO2. Climate dynamics 41 (7-8), 2145–2164. 12

Lechler, A. R., Galewsky, J., 2013. Refining paleoaltimetry reconstructions of the Sierra Nevada: California, using air parcel trajectories. Geology 41 (2), 259–262. 28

Lee, J., Fung, I., 2008. "Amount effect" of water isotopes and quantitative analysis of post-condensation processes. Hydrological Processes 22 (1), 1–8. 65, 75, 77, 78, 79, 210, 211

Lee, J.-E., Fung, I., DePaolo, D. J., Henning, C. C., 2007. Analysis of the global distribution of water isotopes using the NCAR atmospheric general circulation model. Journal of Geophysical Research 112 (D16), D16306. 60, 61

Lee, J. E., Risi, C., Fung, I., Worden, J., Scheepmaker, R. A., Lintner, B., Frankenberg, C., 2012. Asian monsoon hydrometeorology from TES and SCIAMACHY water vapor isotope measurements and LMDZ simulations: Implications for speleothem climate record interpretation. Journal of Geophysical Research: Atmospheres 117 (15), 1–12. 64, 77, 193

Lee, T.-Y., Lawver, L. A., 1995. Cenozoic plate reconstruction of Southeast Asia. Tectonophysics 251 (1), 85–138. 16

Leech, M. L., Singh, S., Jain, A. K., Klemperer, S. L., Manickavasagam, R. M., 2005. The onset of India-Asia continental collision: Early, steep subduction required by the timing of UHP metamorphism in the western Himalaya. Earth and Planetary Science Letters 234 (1-2), 83–97. 20

Lefebvre, V., Donnadieu, Y., Goddéris, Y., Fluteau, F., Hubert-Théou, L., 2013. Was the Antarctic glaciation delayed by a high degassing rate during the early Cenozoic? Earth and Planetary Science Letters 371-372, 203–211. 66

Lefebvre, V., Donnadieu, Y., Sepulchre, P., Swingedouw, D., Zhang, Z. S., 2012. Deciphering the role of southern gateways and carbon dioxide on the onset of the Antarctic Circumpolar Current. Paleoceanography 27 (4), 1–9. 12, 63

LeGrande, A. N., Schmidt, G. A., aug 2009. Sources of Holocene variability of oxygen isotopes in paleoclimate archives. Clim. Past 5 (3), 441–455. 77

Lewis, J. M., 1998. Clarifying the dynamics of the general circulation: Phillips's 1956 experiment. Bulletin of the American Meteorological Society 79 (1), 39. 56

Li, F., Rosa, D., Collins, W. D., Wehner, M. F., 2012. "Super-parameterization": A better way to simulate gerional extrene precipitation? Journal of Advances in Modeling Earth Systems 4 (2). 210

Li, J., Ehlers, T. A., Mutz, S. G., Steger, C., Paeth, H., Werner, M., Poulsen, C. J., Ran, F., 2016. Modern precipitaion δ18O and trajectory analysis over the Himalaya-Tibet Orogen from ECHAM5-wiso simulations. Journal of Geophysical Research: Atmospheres. 62, 78

Liang, M.-M., Bruch, A., Collinson, M., Mosbrugger, V., Li, C.-S., Sun, Q.-G., Hilton, J., 2003. Testing the climatic estimates from different palaeobotanical methods: an example from the Middle Miocene Shanwang flora of China. Palaeogeography, Palaeoclimatology, Palaeoecology 198 (3), 279–301. 28

Licht, A., van Cappelle, M., Abels, H. A., Ladant, J.-B., Trabucho-Alexandre, J., France-Lanord, C., Donnadieu, Y., Vandenberghe, J., Rigaudier, T., Lécuyer, C., Terry Jr, D., Adriaens, R., Boura, A., Guo, Z., Soe, A. N., Quade, J., Dupont-Nivet, G., Jaeger, J.-J., 2014. Asian monsoons in a late Eocene greenhouse world. Nature 513 (7519), 501–506. 64, 66, 67, 68, 69, 70, 71, 146, 191, 193, 194, 195, 202

Lithgow-Bertelloni, C., Silver, P. G., 1998. Dynamic topography, plate driving forces and the African superswell. Nature 395 (6699), 269–272. 26

Liu, X., Sun, H., Miao, Y., Dong, B., Yin, Z.-Y., 2015. Impacts of uplift of northern Tibetan Plateau and formation of Asian inland deserts on regional climate and environment. Quaternary Science Reviews 116, 1–14. 6

Liu, X., Yin, Z. Y., 2002. Sensitivity of East Asian monsoon climate to the uplift of the Tibetan Plateau. Palaeogeography, Palaeoclimatology, Palaeoecology 183 (3-4), 223–245. 196

Liu, X. D., Dong, B. W., 2013. Influence of the Tibetan Plateau uplift on the Asian monsoon-arid environment evolution. Chinese Science Bulletin 58 (34), 4277–4291. 15

Liu, X. Y., Gao, Q., Han, M., Jin, J. H., 2016. Estimates of late middle Eocene pCO2 based on stomatal density of modern and fossil Nageia leaves. Climate of the Past 12 (2), 241–253. 14

Liu, Z., Tian, L., Yao, T., Yu, W., 2008. Seasonal deuterium excess in Nagqu precipitation: influence of moisture transport and recycling in the middle of Tibetan Plateau. Environmental geology 55 (7), 1501–1506. 216

Liu, Z., Tian, L., Yao, T., Yu, W., 2010. Characterization of precipitation δ18O variation in Nagqu, central Tibetan Plateau and its climatic controls. Theoretical and applied climatology 99 (1-2), 95–104. 32

Liu, Z., Wang, C., Yi, H., 2001. Evolution and mass accumulation of the Cenozoic Hoh Xil basin, northern Tibet. Journal of Sedimentary Research 71 (6), 971–984. 21

Lorenz, E. N., 1983. A history of prevailing ideas about the general circulation of the atmosphere. Bulletin of the American Meteorological Society 64 (7), 730–769. 52

Lunt, D. J., Farnsworth, A., Loptson, C., Foster, G. L., Markwick, P., O'Brien, C. L., Pancost, R. D., Robinson, S. A., Wrobel, N., 2015. Palaeogeographic controls on climate and proxy interpretation. Climate of the Past Discussions 11, 5683–5725. 12

Lunt, D. J., Flecker, R., Clift, P. D., 2010. The impacts of Tibetan uplift on palaeoclimate proxies. Geological Society, London, Special Publications 342 (1), 279–291. 9, 192

Lyell, C., 1830. Principles of Geology, 3 vols. London: Murray 33, 163–167. 11

Majoube, M., 1971. Fractionnement en oxygene-18 et en deuterium entre l'eau et sa vapeur. J. Chim. phys 68 (7-8), 1423–1436. 30, 65

Manabe, S., Broccoli, A. J., 1990. Mountains and arid climates of middle latitudes. Science 247 (4939), 192–195. 7, 8, 15

Manabe, S., Bryan, K., 1985. CO2-induced change in a coupled ocean-atmosphere model and its paleoclimatic implications. Journal of Geophysical Research: Oceans 90 (C6), 11689–11707. 14

Manabe, S., Wetherald, R. T., 1967. Thermal equilibrium of the atmosphere with a given distribution of relative humidity. 56

Marti, O., Braconnot, P., Dufresne, J. L., Bellier, J., Benshila, R., Bony, S., Brockmann, P., Cadule, P., Caubel, A., Codron, F., De Noblet, N., Denvil, S., Fairhead, L., Fichefet, T., Foujols, M. A., Friedlingstein, P., Goosse, H., Grandpeix, J. Y., Guilyardi, E., Hourdin, F., Idelkadi, A., Kageyama, M., Krinner, G., Lévy, C., Madec, G., Mignot, J., Musat, I., Swingedouw, D., Talandier, C., 2010. Key features of the IPSL ocean atmosphere model and its sensitivity to atmospheric resolution. Climate Dynamics 34 (1), 1–26. 63

Mathieu, R., Pollard, D., Cole, J. E., White, J. W. C., Webb, R. S., Thompson, S. L., 2002. Simulation of stable water isotope variations by the GENESIS GCM for modern conditions. Journal of Geophysical Research: Atmospheres 107 (D4). 60, 61

Maxbauer, D. P., Royer, D. L., LePage, B. A., 2014. High Arctic forests during the middle Eocene supported by moderate levels of atmospheric CO2. Geology 42 (12), 1027–1030. 13, 14

McElwain, J. C., 2004. Climate-independent paleoaltimetry using stomatal density in fossil leaves as a proxy for CO2 partial pressure. Geology 32 (12), 1017. 28

McGuffie, K., Henderson-Sellers, A., 1997. A climate modeling primer (Research and development in climate and climatology), J. 52, 57

Meehl, G. A., Covey, C., Taylor, K. E., Delworth, T., Stouffer, R. J., Latif, M., McAvaney, B., Mitchell, J. F. B., 2007. The WCRP CMIP3 multimodel dataset: A new era in climate change research. Bulletin of the American Meteorological Society 88 (9), 1383–1394. 63

Meissner, R., Mooney, W., 1998. Weakness of the lower continental crust: a condition for delamination, uplift, and escape. Tectonophysics 296 (1), 47–60. 26

Meng, J., Wang, C., Zhao, X., Coe, R., Li, Y., Finn, D., 2012. India-Asia collision was at 24°N and 50 Ma: palaeomagnetic proof from southernmost Asia. Scientific reports 2, 925. 20

Merlivat, L., Jouzel, J., 1979. Global climatic interpretation of the deuterium-oxygen 18 relationship for precipitation. Journal of Geophysical Research: Oceans 84 (C8), 5029–5033. 30, 65

Merlivat, L., Nief, G., 1967. Fractionnement isotopique lors des changements d'état solide-vapeur et liquide-vapeur de l'eau à des températures inférieures à 0°C. Tellus 19 (1), 122–127. 30, 65

Mix, H. T., Mulch, A., Kent-Corson, M. L., Chamberlain, C. P., 2011. Cenozoic migration of topography in the North American Cordillera. Geology 39 (1), 87–90. 28

Miyake, Y., Matsubaya, O., 1968. Isotopic study on meteoric precipitation. Tech. rep. 78

Molnar, P., 2004. Late Cenozoic increase in accumulation rates of terrestrial sediment: How might climate change have affected erosion rates? Annu. Rev. Earth Planet. Sci. 32, 67–89. 216

Molnar, P., Boos, W. R., Battisti, D. S., 2010. Orographic Controls on Climate and Paleoclimate of Asia: Thermal and Mechanical Roles for the Tibetan Plateau. Annual Review of Earth and Planetary Sciences 38 (1), 77–102. 15, 23, 25, 191, 192

Molnar, P., England, P., 1990. Late Cenozoic uplift of mountain ranges and global climate change: chicken or egg? Nature 346 (6279), 29–34. 10, 15, 191

Molnar, P., England, P., Martinod, J., 1993. Mantle dynamics, uplift of the Tibetan Plateau, and the Indian monsoon. Reviews of Geophysics 31 (4), 357–396. 8, 14, 15, 17, 21, 38, 191

Molnar, P., Stock, J. M., 2009. Slowing of India's convergence with Eurasia since 20 Ma and its implications for Tibetan mantle dynamics. Tectonics 28 (3), 1–11. 17

Mulch, A., 2016. Stable isotope paleoaltimetry and the evolution of landscapes and life. Earth and Planetary Science Letters 433, 180–191. 35, 76

Mulch, A., Chamberlain, C. P., 2006. Earth science: The rise and growth of Tibet. Nature 439 (7077), 670–671. 37, 38, 40

Mulch, a., Chamberlain, C. P., 2007. Stable Isotope Paleoaltimetry in Orogenic Belts The Silicate Record in Surface and Crustal Geological Archives. Reviews in Mineralogy and Geochemistry 66 (1), 89–118. 28, 34

Mulch, A., Uba, C. E., Strecker, M. R., Schoenberg, R., Chamberlain, C. P., 2010. Late Miocene climate variability and surface elevation in the central Andes. Earth and Planetary Science Letters 290 (1), 173–182. 28

Murphy, J. B., Oppliger, G. L., Brimhall, G. H., Hynes, A., 1998. Plume-modified orogeny: An example from the western United States. Geology 26 (8), 731–734. 26

Murphy, M. A., Saylor, J. E., Ding, L., 2009. Late Miocene topographic inversion in southwest Tibet based on integrated paleoelevation reconstructions and structural history. Earth and Planetary Science Letters 282 (1-4), 1–9. 39, 44, 215

Murphy, M. A., Yin, A., Harrison, T. M., Dürr, S. B., Chen, Z., Ryerson, F. J., Kidd, W. S. F., Wang, X., Zhou, X., 1997. Did the Indo-Asian collision alone create the Tibetan plateau? Geology 25 (8), 719–722. 20

Najman, Y., Appel, E., Boudagher-Fadel, M., Bown, P., Carter, A., Garzanti, E., Godin, L., Han, J., Liebke, U., Oliver, G., Parrish, R., Vezzoli, G., 2010. Timing of India-Asia collision: Geological, biostratigraphic, and palaeomagnetic constraints. Journal of Geophysical Research: Solid Earth 115 (12), 1–18. 17, 20

New, M., Lister, D., Hulme, M., Makin, I., 2002. A high-resolution data set of surface climate over global land areas. Climate Research 21 (1), 1–25. 197

Noone, D., Simmonds, I., 2002. Associations between δ18O of Water and Climate Parameters in a Simulation of Atmospheric Circulation for 1979-95. Journal of Climate 15 (22), 3150–3169. 60, 61

North, G. R., Short, D. A., Mengel, J. G., 1983. Simple energy balance model resolving the seasons and the continents- Application to the astronomical theory of the ice ages. Journal of Geophysical Research 88 (C11), 6576–6586. 10

Otto-Bliesner, B. L., 1995. Continental drift, runoff and weathering feedbacks: Implications from climate model e te model e te model experiments. Journal of Geophysical Research 100 (D6), 11–537. 12

Pagani, M., Zachos, J. C., Freeman, K. H., Tipple, B., Bohaty, S., 2005. Marked decline in atmospheric carbon dioxide concentrations during the Paleogene. Science 309 (5734), 600–603. 14

Pan, G., Wang, L., Li, R., Yuan, S., Ji, W., Yin, F., Zhang, W., Wang, B., 2012. Tectonic evolution of the Qinghai-Tibet Plateau. Journal of Asian Earth Sciences 53, 3–14. 17

Parrish, J. T., Ziegler, A. M., Scotese, C. R., 1982. Rainfall patterns and the distribution of coals and evaporites in the Mesozoic and Cenozoic. Palaeogeography, Palaeoclimatology, Palaeoecology 40 (1-3), 67–101. 194, 202, 204

Patriat, P., Achache, J., 1984. India–Eurasia collision chronology has implications for crustal shortening and driving mechanism of plates. Nature 311. 17, 20

Peel, M. C., Finlayson, B. L., McMahon, T. A., 2007. Updated world map of the Koppen-Geiger climate classification. Hydrol. Earth Syst. Sci 11, 1633–1644. 214

Peizhen, Z., Molnar, P., Downs, W. R., 2001. Increased sedimentation rates and grain sizes 2–4 Myr ago due to the influence of climate change on erosion rates. Nature 410 (6831), 891–897. 191

Peltier, W. R., Tarasov, L., Vettoretti, G., Solheim, L. P., 2004. Climate dynamics in deep time: modeling the “snowball bifurcation” and assessing the plausibility of its occurrence. The Extreme Proterozoic: Geology, Geochemistry, and Climate, 107–124. 57

Pfahl, S., Sodemann, H., 2014. What controls deuterium excess in global precipitation? Climate of the Past 10 (2), 771–781. 216

Poage, M. A., Chamberlain, C. P., 2001. Empirical relationships between elevation and the stable isotope composition of precipitation and surface waters: Considerations for studies of paleoelevation change. American Journal of Science 301 (1), 1–15. xii, 33, 34, 76

Pohl, A., Donnadieu, Y., Hir, G. L., Ladant, J.-B., Dumas, C., Alvarez-Solas, J., Vandenbroucke, T. R. A., 2016. Glacial onset predated Late Ordovician climate cooling. Paleoceanography (May). 63, 65

Pohl, A., Donnadieu, Y., Le Hir, G., Buoncristiani, J.-F., Vennin, E., 2014. Effect of the Ordovician paleogeography on the (in)stability of the climate. Climate of the Past 10 (6), 2053–2066. 63

Pohl, A., Nardin, E., Vandenbroucke, T. R., Donnadieu, Y., 2015. High dependence of Ordovician ocean surface circulation on atmospheric CO2 levels. Palaeogeography, Palaeoclimatology, Palaeoecology (October). 63

Polissar, P. J., Freeman, K. H., Rowley, D. B., McInerney, F. a., Currie, B. S., 2009. Paleoaltimetry of the Tibetan Plateau from D/H ratios of lipid biomarkers. Earth and Planetary Science Letters 287 (1-2), 64–76. 34, 40, 43

Potter, P. E., Szatmari, P., 2009. Global Miocene tectonics and the modern world. Earth-Science Reviews 96 (4), 279–295. 27, 37

Poulsen, C. J., Ehlers, T. A., Insel, N., 2010. Onset of convective rainfall during gradual late Miocene rise of the central Andes. Science 328 (5977), 490–493. 35, 62, 76, 83

Poulsen, C. J., Gendaszek, A. S., Jacob, R. L., 2003. Did the rifting of the Atlantic Ocean cause the Cretaceous thermal maximum? Geology 31 (2), 115–118. 12

Poulsen, C. J., Jeffery, M. L., 2011. Climate change imprinting on stable isotopic compositions of high-elevation meteoric water cloaks past surface elevations of major orogens. Geology 39 (6), 595–598. xiv, 62, 80, 83, 121, 126, 152

Poulsen, C. J., Pierrehumbert, R. T., Jacob, R. L., 2001. Impact of ocean dynamics on the simulation of the neoproterozoic "snowball Earth". Geophysical Research Letters 28 (8), 1575. 12, 63

Poulsen, C. J., Pollard, D., White, T. S., 2007. General circulation model simulation of the δ18O content of continental precipitation in the middle Cretaceous: A model-proxy comparison. Geology 35 (3), 199–202. 62, 83, 121

Quade, J., Breecker, D. O., Daëron, M., Eiler, J., 2011. The paleoaltimetry of Tibet: An isotopic perspective. American Journal of Science 311 (2), 77–115. 77, 78, 123

Quade, J., Cerling, T., Bowman, J., 1989. Systematic variations in the carbon and oxygen isotopic composition of pedogenetic carbonate along elevation transects in the suthern Grat Basin, United Satates. Bull. Geol. Soc. Am. 101 (April), 464–475. 39, 115

Quade, J., Cerling, T. E., 1995. Expansion of C4 grasses in the Late Miocene of Northern Pakistan: evidence from stable isotopes in paleosols. Palaeogeography, Palaeoclimatology, Palaeoecology 115 (1), 91–116. 36, 39, 83, 115

Quade, J., Cerling, T. E., Barry, J. C., Morgan, M. E., Pilbeam, D. R., Chivas, A. R., Lee-Thorp, J. A., van der Merwe, N. J., 1992. A 16-Ma record of paleodiet using carbon and oxygen isotopes in fossil teeth from Pakistan. Chemical Geology 94 (3), 183–192. 36

Quade, J., Eiler, J., Daeron, M., Achyuthan, H., 2013. The clumped isotope geothermometer in soil and paleosol carbonate. Geochimica et Cosmochimica Acta 105, 92–107. 212

Quade, J., Garzione, C., Eiler, J., 2007. Paleoelevation Reconstruction using Pedogenic Carbonates. Reviews in Mineralogy and Geochemistry 66 (1), 53–87. 77, 122

Ramanathan, V., Coakley, J. A., 1978. Climate modeling through radiative-convective models. Reviews of Geophysics and Space Physics 16 (4), 465–489. 56

Ramstein, G., Fluteau, F., Besse, J., Joussaume, S., 1997. Effect of orogeny, plate motion and land–sea distribution on Eurasian climate change over the past 30 million years. 15, 17, 147, 192

Raymo, M. E., 1994. The Himalayas, organic carbon burial, and climate in the Miocene. Paleoceanography 9 (3), 399–404. 10

Raymo, M. E., Ruddiman, W. F., 1992. Tectonic forcing of late Cenozoic climate. Nature 359 (6391), 117–122. 1, 5, 10, 15, 37

Richardson, L. F., 1922. Weather prediction by numerical methods. 56

Richardson, L. F., 2007. Weather prediction by numerical process. Cambridge University Press. 56

Rind, D., Russell, G., Ruddiman, W. F., 1997. The effects of uplift on ocean-atmosphere circulation. In: Tectonic Uplift and Climate Change. Springer, pp. 123–147. 9

Rio, C., Hourdin, F., 2015. A thermal plume model for the convective boundary layer: Representation of cumulus clouds. Journal of the Atmospheric Sciences 72 (9). 209, 210

Risi, C., 2009. Les isotopes stables de l 'eau: applications à l'étude du cycle de l ' eau et des variations du climat. Ph.D. thesis, L'universite Paris 6. 32, 58, 59, 64, 65, 75

Risi, C., Bony, S., Vimeux, F., 2008. Influence of convective processes on the isotopic composition (δ18O and δD) of precipitation and water vapor in the tropics: 2. Physical interpretation of the amount effect. Journal of Geophysical Research: Atmospheres 113 (19), 1–12. 75, 79, 81, 82, 210

Risi, C., Bony, S., Vimeux, F., Jouzel, J., 2010. Water-stable isotopes in the LMDZ4 general circulation model: Model evaluation for present-day and past climates and applications to climatic interpretations of tropical isotopic records. Journal of Geophysical Research: Atmospheres 115 (12), 1–27. 60, 61, 64, 65, 75, 77, 210

Risi, C., Noone, D., Frankenberg, C., Worden, J., 2013. Role of continental recycling in intraseasonal variations of continental moisture as deduced from model simulations and water vapor isotopic measurements. Water Resources Research 49 (7), 4136–4156. 65, 75, 76, 77

Roche, D. M., 2013. δ18O water isotope in the iLOVECLIM model (version 1.0)–Part 1: Implementation and verification. Geoscientific Model Development 6 (5), 1481–1491. 60

Roe, G. H., Ding, Q., Battisti, D. S., Molnar, P., Clark, M. K., Garzione, C. N., 2016. A modeling study of the response of Asian summertime climate to the largest geologic forcings of the past 50 Ma. Journal of Geophysical Research: Atmospheres. 8, 61, 62, 122, 191, 192, 202

Rohrmann, A., Strecker, M. R., Bookhagen, B., Mulch, A., Sachse, D., Pingel, H., Alonso, R. N., Schildgen, T. F., Montero, C., 2014. Can stable isotopes ride out the storms ? The role of convection for water isotopes in models , records , and paleoaltimetry studies in the central Andes. Earth and Planetary Science Letters 407, 187–195. 28

Rossignol-Strick, M., 1983. African monsoons, an immediate climate response to orbital insolation. Nature 304 (5921), 46–49. 9

Rowley, D. B., 2007. Stable Isotope-Based Paleoaltimetry: Theory and Validation. Reviews in Mineralogy and Geochemistry 66 (1), 23–52. 81

Rowley, D. B., Currie, B. S., 2006. Palaeo-altimetry of the late Eocene to Miocene Lunpola basin, central Tibet. Nature 439 (7077), 677–681. 29, 35, 37, 39, 41, 42, 80, 83, 115, 116, 154

Rowley, D. B., Garzione, C. N., 2007. Stable Isotope-Based Paleoaltimetry. Annual Review of Earth and Planetary Sciences 35 (1), 463–508. xiii, 33, 39, 59, 76, 81, 82, 122, 124, 125, 212

Rowley, D. B., Pierrehumbert, R. T., Currie, B. S., 2001. A new approach to stable isotope-based paleoaltimetry: Implications for paleoaltimetry and paleohypsometry of the High Himalaya since the late Miocene. Earth and Planetary Science Letters 188 (1-2), 253–268. xiii, 33, 38, 43, 44, 59, 75, 76, 78, 80, 81, 82, 83, 115, 116, 122, 124, 125, 154, 191

Royden, L. H., Burchfiel, B. C., Hilst, R. D. V. D., 2008. The Geological Evolution of the Tibetan Plateau. Science 321 (August), 1054–1058. 20, 21

Rozanski, K., Araguás-Araguás, L., Gonfiantini, R., 1993. Isotopic patterns in modern global precipitation. Climate change in continental isotopic records, 1–36. 75, 76, 77, 78

Ruddiman, W. F., Kutzbach, J. E., 1989. Forcing of late Cenozoic northern hemisphere climate by plateau uplift in southern Asia and the American West. Journal of Geophysical Research: Atmospheres (1984–2012) 94 (D15), 18409–18427. 1, 5, 15, 17, 191

Sahagian, D., Proussevitch, a., 2007. Paleoelevation Measurement on the Basis of Vesicular Basalts. Reviews in Mineralogy and Geochemistry 66 (1), 195–213. 34

Sanyal, P., Bhattacharya, S. K., Kumar, R., Ghosh, S. K., Sangode, S. J., 2004a. Mio-Pliocene monsoonal record from Himalayan foreland basin (Indian Siwalik) and its relation to vegetational change. Palaeogeography, Palaeoclimate, Palaeoecology 205, 23–41. 36, 83, 115

Sanyal, P., Bhattacharya, S. K., Kumar, R., Ghosh, S. K., Sangode, S. J., 2004b. Mio–Pliocene monsoonal record from Himalayan foreland basin (Indian Siwalik) and its relation to vegetational change. Palaeogeography, Palaeoclimatology, Palaeoecology 205 (1), 23–41. 9

Sarnthein, M., Tetzlafil, G., Koopmann, B., Wolter, K., Pflaumann, U., 1981. Glacial and interglacial wind regimes over the eastern subtropical Atlantic and NW Africa. Nature 293, 193. 9

Sato, T., 2005. The TianShan Rain-shadow Influence on the Arid Climate Formation in Northwestern China. Sola 1, 13–16. 6

Saylor, J. E., Quade, J., Dettman, D. L., DeCelles, P. G., Kapp, P. A., Ding, L., 2009. The late Miocene through present paleoelevation history of southwestern Tibet. American Journal of Science 309 (1), 1–42. 39, 43

Schemmel, F., Mikes, T., Rojay, B., Mulch, A., 2013. The impact of topography on isotopes in precipitation across the Central Anatolian Plateau (Turkey). American Journal of Science 313 (February), 61–80. 76

Schmidt, G. A., 1999. Forward modeling of carbonate proxy data from planktonic foraminifera using oxygen isotope tracers in a global ocean model. Paleoceanography 14 (4), 482–497. 154

Schmidt, G. A., LeGrande, A. N., Hoffmann, G., 2007. Water isotope expressions of intrinsic and forced variability in a coupled ocean-atmosphere model. Journal of Geophysical Research: Atmospheres 112 (D10). 60, 61

Schmittner, A., Silva, T. A. M., Fraedrich, K., Kirk, E., Lunkeit, F., 2011. Effects of Mountains and Ice Sheets on Global Ocean Circulation*. Journal of Climate 24 (11), 2814–2829. 9

Schott, B., Schmeling, H., 1998. Delamination and detachment of a lithospheric root. Tectonophysics 296 (3), 225–247. 26

Sellers, W. D., 1969. A global climatic model based on the energy balance of the earth-atmosphere system. Journal of Applied Meteorology 8 (3), 392–400. 56

Sepulchre, P., Ramstein, G., Fluteau, F., Schuster, M., Tiercelin, J.-J., Brunet, M., 2006. Tectonic uplift and Eastern Africa aridification. Science 313 (5792), 1419–1423. 6

Sepulchre, P., Ramstein, G., Schuster, M., 2009a. Modelling the impact of tectonics, surface conditions and sea surface temperatures on Saharan and sub-Saharan climate evolution. Comptes Rendus - Geoscience 341 (8-9), 612–620. 215

Sepulchre, P., Sloan, L. C., Snyder, M., Fiechter, J., 2009b. Impacts of Andean uplift on the Humboldt Current system: A climate model sensitivity study. Paleoceanography 24 (4). 9

Sewall, J. O., Fricke, H. C., 2013. Andean-scale highlands in the Late Cretaceous Cordillera of the North American western margin. Earth and Planetary Science Letters 362, 88–98. 61, 62, 121, 122

Sherwood, S. C., 1996. Maintenance of the free-tropospheric tropical water vapor distribution. Part II: Simulation by large-scale advection. Journal of Climate 9 (11), 2919–2934. 30

Shi, Z., Liu, X., Liu, Y., Sha, Y., Xu, T., 2014. Impact of Mongolian Plateau versus Tibetan Plateau on the westerly jet over North Pacific Ocean. Climate Dynamics 44 (11-12), 3067–3076. 7

Sijp, W. P., Anna, S., Dijkstra, H. A., Flögel, S., Douglas, P. M. J., Bijl, P. K., 2014. The role of ocean gateways on cooling climate on long time scales. Global and Planetary Change 119, 1–22. 12

Sitch, S., 2000. The role of vegetation dynamics in the control of atmospheric CO2 content. Lund University. 63

Sitch, S., Smith, B., Prentice, I. C., Arneth, A., Bondeau, A., Cramer, W., Kaplan, J. O., Levis, S., Lucht, W., Sykes, M. T., Thonicke, K., Venevsky, S., 2003. Evaluation of ecosystem dynamics, plant geography and terrestrial carbon cycling in the LPJ dynamic global vegetation model. Global Change Biology 9, 161–185. 63

Smith, R. Y., Greenwood, D. R., Basinger, J. F., 2010. Estimating paleoatmospheric pCO2 during the early Eocene climatic optimum from stomatal frequency of Ginkgo, Okanagan Highlands, British Columbia, Canada. Palaeogeography, Palaeoclimatology, Palaeoecology 293 (1), 120–131. 13

Solomon, S., Qin, D., Manning, M., Chen, Z., Marquis, M., Averyt, K. B., Tignor, M., Miller, H. L., 2007. Contribution of working group I to the fourth assessment report of the intergovernmental panel on climate change, 2007. 52

Song, X. Y., Spicer, R. A., Yang, J., Yao, Y. F., Li, C. S., 2010. Pollen evidence for an Eocene to Miocene elevation of central southern Tibet predating the rise of the High Himalaya. Palaeogeography, Palaeoclimatology, Palaeoecology 297 (1), 159–168. 37, 39, 41, 42

Spicer, R. A., Harris, N. B. W., Widdowson, M., Herman, A. B., Guo, S., Valdes, P. J., Wolfe, J. a., Kelley, S. P., 2003. Constant elevation of southern Tibet over the past 15 million years. Nature 421 (6923), 622–624. 35, 39, 43

Stern, L. A., Chamberlain, C. P., Reynolds, R. C., Johnson, G. D., 1997. Oxygen isotope evidence of climate change from pedogenic clay minerals in the Himalayan molasse. Geochimica et Cosmochimica Acta 61 (4), 731–744. 36, 39, 83, 115

Stewart, M. K., 1975. Stable isotope fractionation due to evaporation and isotopic exchange of falling waterdrops: Applications to atmospheric processes and evaporation of lakes. Journal of Geophysical Research 80 (9), 1133. 65

Stocker, T. F., Qin, D., Plattner, G.-K., Tignor, M., Allen, S. K., Boschung, J., Nauels, A., Xia, Y., Bex, V., Midgley, P. M., 2014. Climate change 2013: The physical science basis. 14, 51, 52

Sturm, C., Hoffmann, G., Langmann, B., 2007. Simulation of the stable water isotopes in precipitation over South America: Comparing regional to global circulation models. Journal of Climate 20, 3730–3750. 61, 62, 121

Sturm, C., Zhang, Q., Noone, D., 2010. An introduction to stable water isotopes in climate models: benefits of forward proxy modelling for paleoclimatology. Climate of the Past 6 (1), 115–129. 35, 57, 58, 83, 154

Sud, Y. C., Fennessy, M., 1982. A study of the influence of surfece albedo on July circulation in semi-arid regions using the glas GCM. Journal of Climatology 2 (2), 105–125. 12

Sun, B., Wang, Y.-F., Li, C.-S., Yang, J., Li, J.-F., Li, Y.-L., Deng, T., Wang, S.-Q., Zhao, M., Spicer, R. A., Ferguson, D. K., Mehrotra, R. C., 2015. Early Miocene elevation in northern Tibet estimated by palaeobotanical evidence. Scientific Reports 5 (1), 10379. 40, 43

Sun, J., Xu, Q., Liu, W., Zhang, Z., Xue, L., Zhao, P., 2014. Palynological evidence for the latest Oligocene-early Miocene paleoelevation estimate in the Lunpola Basin, central Tibet. Palaeogeography, Palaeoclimatology, Palaeoecology 399, 21–30. 38, 42

Sun, Z., Yang, Z., Pei, J., Ge, X., Wang, X., Yang, T., Li, W., Yuan, S., 2005. Magnetostratigraphy of Paleogene sediments from northern Qaidam Basin, China: implications for tectonic uplift and block rotation in northern Tibetan plateau. Earth and Planetary Science Letters 237 (3), 635–646. 38

Tada, R., Zheng, H., Clift, P. D., 2016. Evolution and variability of the Asian monsoon and its potential linkage with uplift of the Himalaya and Tibetan Plateau. Progress in Earth and Planetary Science 3 (1), 1. 14

Tang, H., Micheels, A., Eronen, J. T., Ahrens, B., Fortelius, M., 2013. Asynchronous responses of East Asian and Indian summer monsoons to mountain uplift shown by regional climate modelling experiments. Climate Dynamics 40 (5-6), 1531–1549. 15, 191, 192

Tang, Z., Ding, Z., White, P. D., Dong, X., Ji, J., Jiang, H., Luo, P., Wang, X., 2011. Late Cenozoic central Asian drying inferred from a palynological record from the northern Tian Shan. Earth and Planetary Science Letters 302 (3-4), 439–447. 204

Tapponnier, P., Peltzer, G., Armijo, R., 1986. On the mechanics of the collision between India and Asia. Geological Society, London, Special Publications 19, 113–157. 17

Tapponnier, P., Zhiqin, X., Roger, F., Meyer, B., Arnaud, N., Wittlinger, G., Jingsui, Y., 2001. Oblique stepwise rise and growth of the Tibet plateau. Science 294 (5547), 1671–1677. 17

Taylor, K. E., Stouffer, R. J., Meehl, G. A., 2012. An overview of CMIP5 and the experiment design. Bulletin of the American Meteorological Society 93 (4), 485. 63

Tharammal, T., Paul, A., Merkel, U., Noone, D., 2013. Influence of Last Glacial Maximum boundary conditions on the global water isotope distribution in an atmospheric general circulation model. Climate of the Past 9 (2), 789–809. 61, 62

Tian, L., 2003. Oxygen-18 concentrations in recent precipitation and ice cores on the Tibetan Plateau. Journal of Geophysical Research 108 (D9), 1–10. 78

Tian, L., Yao, T., MacClune, K., White, J. W. C., Schilla, A., Vaughn, B., Vachon, R., Ichiyanagi, K., 2007. Stable isotopic variations in west China: A consideration of moisture sources. Journal of Geophysical Research: Atmospheres 112 (10), 1–12. 32, 78

Tian, L., Yao, T., Numaguti, A., Sun, W., 2001. Stable Isotope Variations in Monsoon Precipitation on the Tibetan Plateau. Journal of the Meteorological Society of Japan 79 (5), 959–966. 77, 78, 79

Tindall, J., Flecker, R., Valdes, P., Schmidt, D. N., Markwick, P., Harris, J., 2010. Modelling the oxygen isotope distribution of ancient seawater using a coupled ocean-atmosphere GCM: Implications for reconstructing early Eocene climate. Earth and Planetary Science Letters 292 (3-4), 265–273. 61, 62

Tindall, J., Haywood, A., 2015. Modeling oxygen isotopes in the Pliocene: Large-scale features over the land and ocean. Paleoceanography 30 (9), 1183–1201. 61, 62

Tindall, J., Valdes, P., Sime, L., 2009. Stable water isotopes in HadCM3: Isotopic signature of El Nino–Southern Oscillation and the tropical amount effect. Journal of Geophysical Research: Atmospheres 114 (D4). 60, 61

Tobis, M., Schafer, C., Foster, I., Jacob, R., Anderson, J., 1997. FOAM: Expanding the horizons of climate modeling. In: Supercomputing, ACM/IEEE 1997 Conference. IEEE, p. 27. 62

van der Veen, I., Deal, E., Sachse, D., Bookhagen, B., Strecker, M., 2015. Streamwater deltaD and d-excess values in the Sutlej and Alaknandra valley, NW India. In: EGU General Assembly Conference Abstracts. Vol. 17. p. 8641. 216

van Hinsbergen, D. J. J., Lippert, P. C., Dupont-Nivet, G., McQuarrie, N., Doubrovine, P. V., Spakman, W., Torsvik, T. H., 2012. Greater India Basin hypothesis and a two-stage Cenozoic collision between India and Asia. Proceedings of the National Academy of Sciences 109 (20), 7659–7664. 20

Van Leer, B., 1977. Towards the ultimate conservative difference scheme. IV. A new approach to numerical convection. Journal of Computational Physics 23 (3), 276–299. 63, 64

Vimeux, F., Cuffey, K. M., Jouzel, J., 2002. New insights into Southern Hemisphere temperature changes from Vostok ice cores using deuterium excess correction. Earth and Planetary Science Letters 203 (3), 829–843. 59

Walker, J. C. G., Hays, P. B., Kasting, J. F., 1981. A negative feedback mechanism for the long-term stabilization of Earth's surface temperature. Journal of Geophysical Research: Oceans 86 (C10), 9776–9782. 14

Wang, B., Ding, Q., 2006. Changes in global monsoon precipitation over the past 56 years. Geophysical Research Letters 33 (6), 1–4. 8, 39

Wang, B., Wu, Z., Li, J., Liu, J., Chang, C.-P., Ding, Y., Wu, G., 2008a. How to measure the strength of the East Asian summer monsoon. Journal of Climate 21 (17), 4449–4463. 17

Wang, C., Dai, J., Zhao, X., Li, Y., Graham, S. A., He, D., Ran, B., Meng, J., 2014a. Outward-growth of the Tibetan Plateau during the Cenozoic: A review. Tectonophysics 621, 1–43. 17

Wang, C., Zhao, X., Liu, Z., Lippert, P. C., Graham, S. A., Coe, R. S., Yi, H., Zhu, L., Liu, S., Li, Y., 2008b. Constraints on the early uplift history of the Tibetan Plateau. Proceedings of the National Academy of Sciences of the United States of America 105 (13), 4987–4992. 17, 38

Wang, J.-H., Yin, A., Harrison, T. M., Grove, M., Zhang, Y.-Q., Xie, G.-H., 2001. A tectonic model for Cenozoic igneous activities in the eastern Indo–Asian collision zone. Earth and Planetary Science Letters 188 (1), 123–133. 22

Wang, P. X., Wang, B., Cheng, H., Fasullo, J., Guo, Z. T., Kiefer, T., Liu, Z. Y., 2014b. The global monsoon across timescales: Coherent variability of regional monsoons. Climate of the Past 10 (6), 2007–2052. 8

Wang, Q., Wyman, D. A., Xu, J., Dong, Y., Vasconcelos, P. M., Pearson, N., Wan, Y., Dong, H., Li, C., Yu, Y., Zhu, T., Feng, X., Zhang, Q., Zi, F., Chu, Z., 2008c. Eocene melting of subducting continental crust and early uplifting of central Tibet: Evidence from central-western Qiangtang high-K calc-alkaline andesites, dacites and rhyolites. Earth and Planetary Science Letters 272 (1-2), 158–171. 17, 19

Wang, S., Zhang, M., Hughes, C., Zhu, X., Dong, L., Ren, Z., Chen, F., 2016. Factors controlling stable isotope composition of precipitation in arid conditions: an observation network in the Tianshan Mountains, central Asia. Tellus B 1 (February), 1–14. 75

Wang, Y., Deng, T., Biasatti, D., 2006. Ancient diets indicate significant uplift of southern Tibet after ca. 7 Ma. Geology 34 (4), 309–312. 43, 115

Wang, Y., Deng, T., Flynn, L., Wang, X., Yin, A., Xu, Y., Parker, W., Lochner, E., Zhang, C., Biasatti, D., 2012a. Late Neogene environmental changes in the central Himalaya related to tectonic uplift and orbital forcing. Journal of Asian Earth Sciences 44, 62–76. 37, 38

Wang, Y., Huang, C., Sun, B., Quan, C., Wu, J., Lin, Z., 2014c. Paleo-CO 2 variation trends and the Cretaceous greenhouse climate. Earth-Science Reviews 129, 136–147. 13

Wang, Y., Wang, X., Xu, Y., Zhang, C., Li, Q., Tseng, Z. J., Takeuchi, G., Deng, T., 2008d. Stable isotopes in fossil mammals, fish and shells from Kunlun Pass Basin, Tibetan Plateau: Paleo-climatic and paleo-elevation implications. Earth and Planetary Science Letters 270 (1-2), 73–85. 40, 44

Wang, Y., Xu, Y., Khawaja, S., Passey, B. H., Zhang, C., Wang, X., Li, Q., Tseng, Z. J., Takeuchi, G. T., Deng, T., Xie, G., 2013. Diet and environment of a mid-Pliocene fauna from southwestern Himalaya: Paleo-elevation implications. Earth and Planetary Science Letters 376, 43–53. 40, 44

Wang, Y., Zheng, J., Zhang, W., Li, S., Liu, X., Yang, X., Liu, Y., 2012b. Cenozoic uplift of the Tibetan Plateau: Evidence from the tectonic-sedimentary evolution of the western Qaidam Basin. Geoscience Frontiers 3 (2), 175–187. 191

Washington, W. M., Meehl, G. A., 1983. General circulation model experiments on the climatic effects due to a doubling and quadrupling of carbon dioxide concentration. Journal of Geophysical Research: Oceans 88 (C11), 6600–6610. 193

Webster, P. J., Magaña, V. O., Palmer, T. N., Shukla, J., Tomas, R. A., Yanai, M., Yasunari, T., 1998. Monsoons: Processes, predictability, and the prospects for prediction. Journal of Geophysical Research 103 (C7), 14451. 192

Webster, P. J., Yang, S., 1992. Monsoon and Enso: Selectively Interactive Systems. Quarterly Journal of the Royal Meteorological Society 118 (507), 877–926. 196

Wei, Y., Zhang, K., Garzione, C. N., Xu, Y., Song, B., Ji, J., 2016. Low palaeoelevation of the northern Lhasa terrane during late Eocene: Fossil foraminifera and stable isotope evidence from the Gerze Basin. Scientific reports 6, 27508. 37, 41, 191

Wen, J., Zhang, J., Nie, Z.-L., Zhong, Y., Sun, H., 2014. Evolutionary diversifications of plants on the Qinghai-Tibetan Plateau. Frontiers in genetics 5, 4. 213

Williams, H., Turner, S., Kelley, S., Harris, N., 2001. Age and composition of dikes in Southern Tibet: New constraints on the timing of east-west extension and its relationship to postcollisional volcanism. Geology 29 (4), 339–342. 21

Williams, M., 2007. Deep-time perspectives on climate change: Marrying the signal from computer models and biological proxies. Geological Society of London. 69

Worden, J., Noone, D., Bowman, K., 2007. Importance of rain evaporation and continental convection in the tropical water cycle. Nature 445 (7127), 528–532. 60, 75, 78, 122

Wu, F., Herrmann, M., Fang, X., 2014. Early Pliocene paleo-altimetry of the Zanda Basin indicated by a sporopollen record. Palaeogeography, Palaeoclimatology, Palaeoecology 412, 261–268. 20

Wu, G., Duan, A., Liu, Y., Mao, J., Ren, R., Bao, Q., He, B., Liu, B., Hu, W., 2015. Tibetan Plateau climate dynamics: recent research progress and outlook. National Science Review 2 (1), 100–116. 8, 15, 192, 202

Wu, G., Liu, Y., He, B., Bao, Q., Duan, A., Jin, F.-F., 2012. Thermal controls on the Asian summer monsoon. Scientific Reports 2, 404. 15, 192, 202

Wu, G., Liu, Y., Zhang, Q., Duan, A., Wang, T., Wan, R., Liu, X., Li, W., Wang, Z., Liang, X., 2007a. The influence of mechanical and thermal forcing by the Tibetan Plateau on Asian climate. Journal of Hydrometeorology 8 (4), 770–789. 40, 192

Wu, Z., Hu, D., Ye, P., Wu, Z., 2013. Early Cenozoic tectonics of the Tibetan Plateau. Acta Geologica Sinica (English Edition) 87 (2), 289–303. 22, 25

Wu, Z. H., Zhao, X., Ye, P. S., Wu, Z. H., Hu, D. G., Zhou, C. J., 2007b. Paleo-elevation of the Tibetan Plateau inferred from carbon and oxygen isotopes of lacustrine deposits. Acta Geologica Sinica 81 (9), 1277–1288. 42, 43

Xi, X., 2014. A Review of Water Isotopes in Atmospheric General Circulation Models: Recent Advances and Future Prospects. International Journal of Atmospheric Sciences 2014. 58

Xu, Q., Ding, L., Hetzel, R., Yue, Y., Rades, E. F., 2015. Low elevation of the northern Lhasa terrane in the Eocene: Implications for relief development in south Tibet. Terra Nova 27 (6), 458–466. 115

Xu, Q., Ding, L., Zhang, L., Cai, F., Lai, Q., Yang, D., Liu-Zeng, J., 2013. Paleogene high elevations in the Qiangtang Terrane, central Tibetan Plateau. Earth and Planetary Science Letters 362, 31–42. 29, 37, 41, 80, 83, 115

Xu, Z., Fu, C., Qian, Y., 2009. Relative Roles of Land–Sea Distribution and Orography in Asian Monsoon Intensity. Journal of the Atmospheric Sciences 66 (9), 2714–2729. 193

Yan, Z., Li, Y., Li, H., Dong, S., Zhao, G., Li, J., Li, F., Yan, L., Zheng, L., 2015. Application of the Material Balance Method in Paleoelevation Recovery: A Case Study of the Longmen Mountains Foreland Basin on the Eastern Margin of the Tibetan Plateau. Acta Geologica Sinica (English Edition) 89 (2), 598–609. 27

Yanai, M., Wu, G.-X., 2006. Effects of the tibetan plateau. In: The Asian Monsoon. Springer, pp. 513–549. 15, 192

Yang, S., Galbraith, E., Palter, J., 2014. Coupled climate impacts of the Drake Passage and the Panama Seaway. Climate dynamics 43 (1-2), 37–52. 12

Yang, X., Yao, T., Yang, W., Yu, W., Qu, D., 2011. Co-existence of temperature and amount effects on precipitation δ18O in the Asian monsoon region. Geophysical Research Letters 38 (November), 1–6. 82

Yao, T., Masson-Delmotte, V., Gao, J., Yu, W., Yang, X., Risi, C., Sturm, C., Werner, M., Zhao, H., He, Y., Ren, W., Tian, L., Shi, C., Hou, S., 2013. A review of climatic controls on δ18O in precipitation over the Tibetan Plateau: Observations and simulations. Reviews of Geophysics 51 (4), 525–548. 65, 75, 79, 81, 83

Yim, S.-Y., Wang, B., Liu, J., Wu, Z., 2013. A comparison of regional monsoon variability using monsoon indices. Climate Dynamics, 1423–1437. 195

Yin, A., 2006. Cenozoic tectonic evolution of the Himalayan orogen as constrained by along-strike variation of structural geometry, exhumation history, and foreland sedimentation. Earth-Science Reviews 76 (1-2), 1–131. 17

Yin, A., Harrison, T. M., 2000. Geologic Evolution of the Himalayan-Tibet Orogen. Annual Reviews of Earth and Planetary Sciences 28, 211–280. 17, 18, 19, 20, 23, 37

Yoshimura, K., Kanamitsu, M., Noone, D., Oki, T., 2008. Historical isotope simulation using reanalysis atmospheric data. Journal of Geophysical Research: Atmospheres 113 (D19). 60, 61

Yun, K.-S., Seo, Y.-W., Ha, K.-J., Lee, J.-Y., Kitoh, A., 2016. The seasonally varying effect of the Tibetan Plateau on Northern Hemispheric blocking frequency and amplitude. Climate Dynamics, 1–15. 7

Zachos, J. C., Dickens, G. R., Zeebe, R. E., 2008. An early Cenozoic perspective on greenhouse warming and carbon-cycle dynamics. Nature 451 (7176), 279–283. 13, 14

Zachos, J. C., Kump, L. R., 2005. Carbon cycle feedbacks and the initiation of Antarctic glaciation in the earliest Oligocene. Global and Planetary Change 47 (1), 51–66. 16

Zhang, R., Jiang, D., Zhang, Z., Yu, E., 2015. The impact of regional uplift of the Tibetan Plateau on the Asian monsoon climate. Palaeogeography, Palaeoclimatology, Palaeoecology 417, 137–150. 191

Zhang, R., Jiang, D. B., Liu, X. D., Tian, Z. P., 2012. Modeling the climate effects of different subregional uplifts within the Himalaya-Tibetan Plateau on Asian summer monsoon evolution. Chinese Science Bulletin 57 (35), 4617–4626. 191

Zhang, R., Liu, X.-D., 2010. The effects of tectonic uplift on the evolution of Asian summer monsoon climate since Pliocene. Chinese Journal of Geophysics 53 (6), 948–960. 67, 68, 69

Zhang, X., Nakawo, M., Yao, T., Han, J., Xie, Z., 2002. Variations of stable isotopic compositions in precipitation on the Tibetan Plateau and its adjacent regions. Science in China Series D: Earth Sciences 45 (6), 481–493. 77

Zhang, Z., Huijun, W., Zhengtang, G., Dabang, J., 2007a. Impacts of tectonic changes on the reorganization of the Cenozoic paleoclimatic patterns in China. Earth and Planetary Science Letters 257 (3-4), 622–634. 192

Zhang, Z., Klemperer, S., Bai, Z., Chen, Y., Teng, J., 2011. Crustal structure of the Paleozoic Kunlun orogeny from an active-source seismic profile between Moba and Guide in East Tibet, China. Gondwana Research 19 (4), 994–1007. 19

Zhang, Z., Ramstein, G., Schuster, M., Li, C., Contoux, C., Yan, Q., 2014. Aridification of the Sahara desert caused by Tethys Sea shrinkage during the Late Miocene. Nature 513 (7518), 401–404. 66, 70, 71, 193, 194, 195

Zhang, Z., Wang, H., Guo, Z., Jiang, D., 2007b. What triggers the transition of palaeoenvironmental patterns in China, the Tibetan Plateau uplift or the Paratethys Sea retreat? Palaeogeography, Palaeoclimatology, Palaeoecology 245 (3-4), 317–331. 192

Zhou, T., Li, Z., 2002. Simulation of the East Asian summer monsoon using a variable resolution atmospheric GCM. Climate Dynamics 19 (2), 167–180. 64, 193

Zhou, Z., Yang, Q., Xia, K., 2007. Fossils of Quercus sect. Heterobalanus can help explain the uplift of the Himalayas. Chinese Science Bulletin 52 (2), 238–247. 39, 40, 42, 44

Zhuang, G., Brandon, M. T., Pagani, M., Krishnan, S., 2014. Leaf wax stable isotopes from Northern Tibetan Plateau: Implications for uplift and climate since 15 Ma. Earth and Planetary Science Letters 390, 186–198. 40, 43, 216

Ziegler, A., Eshel, G., Rees, P. M., Rothfus, T., Rowley, D., Sunderlin, D., 2003. Tracing the tropics across land and sea: Permian to present. Lethaia 36 (3), 227–254. 194, 202, 204

Titre : Modélisation de l'impact de l'évolution tectonique himalayennes et tibétaines sur le climat et les isotopes stable de l'oxygène au Cénozoïque

Mots-Clés : climat, plateau tibétain, paléo élévation, modélisation climatique, isotopes stable de l'oxygène, Himalaya

Résumé : La vitesse de surrection de l'Himalaya et du plateau tibétain tout au long du Cénozoïque reste encore aujourd'hui largement débattue. L'analyse des isotopes stables de l'oxygène pour reconstruire les paléo-altitudes est considérée comme une technique très efficace et a été largement utilisée. Néanmoins, cette méthode a deux limites principales: 1) les relations entre $\delta^{18}O$ et le climat ne sont pas bien établies et 2) le climat Cénozoïque en Asie est mal contraint. Dans le cadre de cette thèse, nous avons étudié le lien entre la surrection des montagnes, les changements climatiques associés et le $\delta^{18}O$ dans les paléo-précipitations. Nous utilisons le modèle de circulation générale atmosphérique isotopique nommé LMDZ-iso. Avec une expression théorique de la composition isotopique des précipitations fondée sur la distillation de Rayleigh, nous avons montré que seulement 40 % des sites échantillonnés de l'Himalaya et du plateau tibétain contiennent une signature isotopique qui enregistrent des informations sur la topographie. L'utilisation de conditions aux limites réalistes nous permettent de reconstruire le $\delta^{18}O$ des paléo-précipitations pour quatre époques du Cénozoïque (55, 42, 30 et 15 Ma). Dans la mesure où les reconstructions des paléo-altitudes sont particulièrement controversées pour les premières étapes de l'évolution du plateau tibétain, nous avons ensuite approfondi notre étude en nous focalisant sur l'Eocène (en utilisant une paléogéographie qui correspond à 42 Ma). Pour ce cas, nous montrons que le $\delta^{18}O$ des précipitations est insensible à l'altitude en Asie, tandis que le $\delta^{18}O$ dans les archives naturelles (carbonates) enregistre le signal de la paléo-élévation puisque le fractionnement entre la calcite et l'eau est sensible à la température, qui elle-même dépend en partie de l'altitude. La comparaison du $\delta^{18}O$ simulé pour l'Eocène avec les données du $\delta^{18}O$ mesuré dans les carbonates suggère que, pendant l'Eocène, l'Himalaya et le plateau tibétain n'avaient pas encore atteint leur élévation actuelle (> 3000 m).

Title: Modeling the response of climate and precipitation $\delta^{18}O$ to the Cenozoic tectonic evolution of the Himalayas and the Tibetan Plateau

Keywords: climate, Tibetan Plateau, paleoelevation, climate modeling, stable oxygen isotopes, Himalayas

Summary: The timing and rate of surface elevations of the Himalayas and the Tibetan Plateau remain controversial and their impact on Asian climate and the onset of monsoon systems in this area is highly debated. Stable oxygen paleoaltimetry is considered to be a very efficient and widely applied technique, but has limitations from two sides: 1) the link between stable oxygen composition of precipitation and climate is not well established, 2) Cenozoic climate over Asia is poorly reconstructed. With a purpose of filling the gap in our knowledge of climate variability over Asia during the Cenozoic, we use the isotope-enabled atmospheric general circulation model LMDZ-iso to understand the links between the growth of mountains, associated climate changes and $\delta^{18}O$ in paleo-precipitation. Our results show a significant influence of the Paratethys retreat, the latitudinal displacement of India and the height of the Tibetan Plateau on Asian hydrological cycle. We develop a theoretical expression for the precipitation composition based on the Rayleigh distillation and show that only 40% of sampled sites for paleoaltimetry depict signal attributed to topography changes. Realistic boundary conditions allow us reconstructing $\delta^{18}O$ for several periods during the Cenozoic (for 55 Ma, 42 Ma, 30 Ma and 15 Ma). The focus has been put on the Eocene (42 Ma), since paleoelevation reconstructions are particularly controversial for this time. We show that Eocene precipitation $\delta^{18}O$ is rather insensitive to topographic height in Asia. However, carbonate $\delta^{18}O$ still records paleo-elevation because the fractionation between calcite and water is sensitive to temperature, which partly depends on altitude. Comparison of simulated Eocene $\delta^{18}O$ patterns with data from the carbonate archives suggest that the Himalayas and the Tibetan Plateau did not reach present-day (> 3000 m) elevations during the Eocene.